STUDIES ON FABRICATION OF FIBER BRAGG GRATINGS USING HIGH REPETITION RATE ULTRAVIOLET RADIATION FROM FREQUENCY CONVERTED COPPER VAPOUR LASER

By

RAMAKANTA MAHAKUD

PHYS03200904003

Raja Ramanna Centre for Advanced Technology, Indore

A thesis submitted to the

Board of Studies in Physical Sciences

In partial fulfillment of requirements

for the Degree of

DOCTOR OF PHILOSOPHY

of

HOMI BHABHA NATIONAL INSTITUTE

March, 2014

Homi Bhabha National Institute

Recommendations of the Viva Voce Committee

As members of the Viva Voce Committee, we certify that we have read the dissertation prepared by **Ramakanta Mahakud** entitled **"Studies on fabrication of Fiber Bragg Gratings using high repetition rate ultraviolet radiation from frequency converted copper vapour laser"** and recommend that it may be accepted as fulfilling the thesis requirement for the award of Degree of Doctor of Philosophy.

8/8/2014.

Chairman - Dr. L. M. Kukreja — Date

08-08-2014

Guide/Convener - Dr. S. K. Dixit — Date

08-08-2014

Member 1 - Dr. H. S. Rawat — Date

Member 2 - Dr. K. Dasgupta — Date

08.08.2014

Member 3 - Dr. P. K. Mukhopadhyay — Date

08.08.2014

External examiner: Dr. S. K. Bhadra — Date

Final approval and acceptance of this thesis is contingent upon the candidate's submission of the final copies of the thesis to HBNI.

I hereby certify that I have read this thesis prepared under my direction and recommend that it may be accepted as fulfilling the thesis requirement.

Date: 8th August, 2014

Place: RRACT, Indore

Guide: (Dr. S. K. Dixit)

STATEMENT BY AUTHOR

This dissertation has been submitted in partial fulfillment of requirements for an advanced degree at Homi Bhabha National Institute (HBNI) and is deposited in the Library to be made available to borrowers under rules of the HBNI.

Brief quotations from this dissertation are allowable without special permission, provided that accurate acknowledgement of source is made. Requests for permission for extended quotation from or reproduction of this manuscript in whole or in part may be granted by the Competent Authority of HBNI when in his or her judgment the proposed use of the material is in the interests of scholarship. In all other instances, however, permission must be obtained from the author.

RMahakud

Ramakanta Mahakud

DECLARATION

I, hereby declare that the investigation presented in the thesis has been carried out by me. The work is original and has not been submitted earlier as a whole or in part for a degree / diploma at this or any other Institution / University.

Rmahakud

Ramakanta Mahakud

List of Publications arising from the thesis

Journal

1. "A study on the non-uniform behavior of temperature sensitivity of bare and embedded fiber Bragg gratings: Experimental results and analysis" **R. Mahakud**, J. Kumar, O. Prakash and S. K. Dixit, Applied Optics, **2013,** 52, 7570-7579.
2. "Analysis of ultraviolet fringes contrast on first and second order Fiber Bragg gratings written by prism interferometers" **R. Mahakud**, J. Kumar, O. Prakash and S. K. Dixit, Optical Engineering, **2013**, 52, 0761141-6.
3. "Analysis on the effect of UV beam intensity profile on the refractive index modulation in phase mask based fiber Bragg grating writing" **R. Mahakud**, O. Prakash, J. Kumar, S. V. Nakhe and S. K. Dixit, Optics Communications, **2012**, 285, 5351-5358.
4. "Analysis on the saturation of refractive index modulation in fiber Bragg gratings (FBGs) written by partially coherent UV beams", **R. Mahakud**, O. Prakash, S.V. Nakhe and S. K. Dixit, Applied Optics, **2012**, 51, 1828-1835.
5. "Analysis on the laser beam pointing instability induced fringe shift and contrast dilution from different interferometers used for writing fiber Bragg grating" **R. Mahakud**, O. Prakash, S.K. Dixit and J.K. Mittal, Optics Communications, **2009**, 282, 2204 – 2211.
6. "Enhanced temperature (~ 800 ^{0}C) stability of type IIa fiber Bragg grating written in Ge doped photosensitive fiber", O. Prakash, J. Kumar, **R. Mahakud**, S. K. Agrawal, S. K. Dixit and S. V. Nakhe, IEEE photonics technology letters, **2014**, 26, 93-95.

7. “Studies on thermal regeneration and temperature stability of type-I FBGs written in Ge- B codoped and Ge-doped fibers by a kHz repetition rate nanosecond 255nm beam” J. Kumar, **R. Mahakud**, A. Mokhariwale, O. Prakash, S. K. Dixit and S. V. Nakhe, Optics Communications, **2014**, 320, 109–113.
8. “HF based clad etching of Fiber Bragg grating and its utilization in concentration sensing of laser dye in dye-ethanol solution”, J. Kumar, **R. Mahakud**, O. Prakash and S. K. Dixit, Pramana Journal of Physics **2014,** 82, 265-71.
9. “A study on HF based clad etching and chemical sensing characteristics of FBGs of different reflectivity fabricated under different UV exposure times,” J. Kumar, **R. Mahakud**, O. Prakash and S. K. Dixit, Optical Engineering **2013,** 52, 054402-7.
10. “Effect of pulse to pulse variation of divergence, pointing and amplitude of copper vapour laser radiations on their second harmonic and sum frequency conversion” O. Prakash, **R. Mahakud**, S. V. Nakhe and S. K. Dixit, Optics & Laser Technology, **2013,** 50, 43-50.
11. “Comparative study on second harmonic conversion and saturation characteristics of three copper vapor laser beams of same average power and different spatial coherence”, O.Prakash, **R. Mahakud** and S.K. Dixit, Optical Engineering, **2011**, **50,** 114201-6.
12. “Role of optical resonator on the pointing stability of copper vapour laser” S. K Dixit, **R. Mahakud, O.** Prakash, R. Biswal and J. K. Mittal, Optics Communications, **2008,** 281, 2590-2597.

Rmahakud

Ramakanta Mahakud

ACKNOWLEDGEMENTS

It is a matter of great pleasure for me to express my gratitude to all those who have contributed to this thesis work, directly or indirectly.

With profound honour and ardent faith, I express my sincere gratitude to Dr. S. K Dixit for his overall guidance, support and direction in planning and execution of the various experiments and analysis of the results.

I thank Dr. P. D. Gupta, Director, RRCAT, for allowing me to pursue Ph.D. in HBNI. I thank all the members of Ph.D. advisory committee (Dr. L.M. Kukreja, Dr. K. Dasgupta and Dr. H. S. Rawat) for their valuable suggestions during the yearly review presentations. Special thanks to Dr. S. C. Mehendale (ex-member) for his inputs during the planning stages. I am grateful to Shri. S. V. Nakhe, head, LSES, for his constant encouragement. I am greatly indebted to Dr. Om Prakash, my senior colleague, for his numerous inputs and advice and for his immense help in different stages of experiment and analytical works.

I must also thank Shri U. Nundy, ex-head, LSES for encouraging to initiate work in the field of Fiber Bragg Gratings. Special thanks are due to Dr. R. Bhatnagar, Shri J.K. Mittal and Shri B. Singh for their contributions in CVL technology. I am especially thankful to Shri H. S. Vora for providing the beam analysing software.

Many thanks are due to Jitendra Kumar for his enthusiastic participation in the experimental work. I wish to acknowledge the support of colleagues J. Kumar, U. Kumbhakar, S. Agrawal, A. Mokhriwale, S. Singh, R. Biswal, P. Agarwal, P. Kumar, S. Gurram and others for supporting me in different ways, in different stages of work. I express my appreciation to my family for their whole hearted support during the period of my thesis work.

CONTENTS

Page No

SYNOPSIS **1**

LIST OF FIGURES **9**

LIST OF TABLES **17**

CHAPTER 1: REVIEW ON FIBER BRAGG GRATING **19**

1.0 Introduction …………………… ………………………………………………. 19

1.1 Evolution of FBG field ……………………………………………………………. 20

1.2 Photosensitivity of optical fibers …………………………………………………. 21

1.2.1 Defects in optical fiber ……………………..……..…………………… 21

1.2.2 Techniques of photosensitivity enhancement …………..………………. 22

1.2.3 Mechanism of photo induced refractive index change………………… 23

1.3 FBG fabrication techniques ……………………………………………………… 25

1.4 Wave propagation in optical fiber …..…………………………………. ………….25

1.5 Fiber grating theory……………………………………………………………… 28

1.5.1 Mode coupling……………..…………..……………………………. 29

1.5.2 Fiber Bragg gratings …………………………………………………. 30

1.5.3 Long period gratings (co-directional coupling) ……….………………. 34

1.6 Analytical techniques to characterize non uniform fiber Bragg gratings…………… 36

1.6.1 Transfer matrix method………………………………………………. 36

1.6.2 Multiple layer analysis……………..…………………………………..…37

1.7 Fiber Bragg gratings structures………………………………………………………. 38

1.7.1 Tilted fiber Bragg grating ………………… …………………………….38

1.7.2 Chirped fiber Bragg grating……………….……………………………. 39

1.7.3 Apodised fiber Bragg grating…………………………………………….. 40

1.7.4 Superimposed and superstructure multiple Bragg gratings ……………. 41

1.7.5 Phase-shifted Bragg gratings…………………………………………… 41

1.8 Grating types ……………………………………………………………………. 41

1.9 Laser sources for Bragg grating fabrication…………………………………………. 43

1.9.1 Copper vapour laser (CVL)……………………………………………. 44

1.10 Current status of FBG technology and applications……………………………… 47

CHAPTER 2: STUDIES ON FREQUENCY CONVERTED COPPER VAPOUR LASER UV (255 nm) RADIATION 49

2.0 Introduction ………………………………………………………………………. 49

2.1 Visible /UV beam diagnostic techniques…………………………...…………… 50

2.1.1 Cylindrical lens based reversal shear interferometer for spatial coherence measurement ……………… ………………………………. 50

2.1.2 Measurement of divergence and pointing stability ……………………. 53

2.1.3 Line-width measurement……………………………………………….. 55

2.1.4 Measuring optical power ………………………………………………. 56

2.1.5 Recording Laser beam temporal profile ……………………...………… 56

2.2 CVL optical resonators …………………………………………………………….. 56

2.2.1 Unstable resonator……………………………………………………. 56

2.2.2 Diffraction filtered resonator…………………………………………... 57

2.3 Results on CVL beam characteristics with different resonator configurations ……. 59

2.4 Discussion of results on CVL beam parameters ……………………….……….. 65

2.5 Non-linear frequency conversion of copper vapour laser to UV (255 nm) radiation 69

2.6 Experimental studies on second SHG of fundamental CVL beams ……………….. 73

2.6.1 Experimental method ………………………………………………….. 73

2.6.2 Results and discussion ………………………………………………… 75

2.7 Conclusion ………………………………………………………….................. 81

CHAPTER 3: ANALYSIS ON THE CONTRAST AND STABILITY OF UV FRINGES OF DIFFERENT FBG WRITING INTERFEROMETERS 83

3.0 Introduction………………………………..……………………………………… 83

3.1 Analysis on the spatial coherence of writing UV beam on interferometer fringe contrast ………………………………………………………………. 84

3.1.1 General considerations ……………………………………………… 84

3.1.2 Fringe contrast of phase mask and phase mask –Talbot interferometers……………………….………………………………… 85

3.1.3 Fringe contrast of prism interferometers ………………………………. 89

3.2 Effect of beam pointing stability on fringe stability…………………………………. 93

3.2.1 General considerations ……. ………………………………………. 93

3.2.2 Fringe stability/contrast of phase mask interferometer………………… 96

3.2.3 Phase mask-Talbot interferometer’s fringe stability…………………… 97

3.2.4 Bi-prism interferometer fringe stability……………………….............. 99

3.3 Test (experimental) results on fringes instability and contrast dilution…………… 102

3.4 Conclusion …………………….…………………………………………………….. 107

CHAPTER 4: EXPERIMENTAL STUDIES ON WRITING OF FBGs BY PHASE MASK TECHNIQUE USING CVL-UV BEAM **109**

4.0 Introduction …………………………………………………………………… 109

4.1 Experimental arrangement for FBG fabrication …………………………………… 111

4.2 General discussion on optimizing FBG writing ……………………………………. 114

4.3 Arrangement for FBG spectra recording …………………………………………… 115

4.3.1 Measurement and calculation of different FBG parameters…………….. 117

4.4 Experimental results and discussion on FBG fabrication …………………………….119

4.4.1 FBG growth characteristics……………………………………………. 119

4.4.2 Effect of UV beam spatial coherence ………………..…………………..123

4.4.3 Effect of fiber composition on refractive index modulation…………. 128

4.4.4 Effect of long exposure (Type II A gratings)…………………………… 130

4.5 Tilted Fiber Bragg gratings (TFBGs] ……………………………………………. 133

4.6 Effect of phase mask pitch on refractive index modulation ………… …………….. 137

4.7 Conclusion ………………………………………………. ………………………. 139

CHAPTER 5: THEORETICAL ANALYSIS OF PHASE MASK BASED FBG FABRICATION **141**

5.1 Introduction ……………………………………………………………………… 141

5.2 Effect of UV beam spatial coherence on refractive index modulation…………… 142

5.2.1 UV photon induced excitation ……………………………………….. 142

5.2.2 Induced refractive index change in the photosensitive fiber…….……. 144

5.2.3 UV fringes (sinusoidal) induced refractive index distribution…………. 145

5.2.4 Fourier harmonics of refractive index change ………………………… 148

5.2.5 Fiber Bragg grating reflection in first order ………………………….. 151

5.3 Effect of non-uniform UV beam profile on evolution of Bragg reflection spectrum .. 153

5.3.1 Fringe intensity distribution …………………….................................. 153

5.3.2 Fringe modulation due to beam focusing ………………………………. 155

5.3.3 Dynamic evolution of refractive index modulation profile…………….. 159

5.3.4 Dynamic evolution of FBG reflection spectra …………………………. 162

5.3.5 Effect of nonlinear growth on apodisation of grating profile…………….165

5.4 Effect of phase mask residual orders on fringe intensity distribution……………….. 167

5.5 Conclusion……………………………………………………………………. 169

CHAPTER 6: STUDIES ON FBG FABRICATION AND BRAGG WAVELENGTH TUNING BY PRISM INTERFEROMETERS 171

6.0 Introduction ……………………………………………………………………….. 171

6.1 Analysis of FBG inscription by bi-prism interferometer………… ………………… 173

6.1.1 Optimization of FBG reflection ……………………………………… 173

6.2 Bragg wavelength tuning ………………………………………………………..177

6.2.1 By incidence angle tuning of incident collimated UV beam ………….. 177

6.2.2 Bragg wavelength tuning by a diverging UV beam……………………. 179

6.3 Analysis of FBG inscription by single (Lloyd) prism interferometer ……………… 182

6.4 Experimental method, results and discussion …………………………………….. 185

6.5 Conclusion …………………………………………………………………… 191

CHAPTER 7: STUDIES ON TEMPERATURE SENSITIVITY AND STABILITY FOR FBG BASED TEMPERATURE SENSING 193

7.0 Introduction ……………………………………………………………………. 193

7.1 Experimental methodology ……………………………………………………….. 194

7.1.1 For investigation of temperature sensitivity in bare FBG……….. 194

7.1.2 For investigation of temperature sensitivity in embedded FBG ……… 196

7.1.3 For study on thermal sustainability …………………………………… 196

7.2 Non-uniformity of sensitivity of FBG based temperature sensors ………………..…. 197

7.2.1 Experimental results and discussion on bare FBG

temperature sensitivity…………………………………………..…… 199

7.2.2 Results and discussion on embedded FBG temperature sensitivity..….. 205

7.3 Studies on thermal sustainability of FBG ……………………………………….. 209

7.3.1 Experimental results ………………………………….………………… 209

A) Studies on thermal behavior of FGBs with temperature elevation………… 210

B) Thermal decay of FBGs for high and low reflectivity (in same fiber)…….. 212

C) Studies on thermal decay of Type I and Type IIA FBG (in same fiber)…. 213

D) Studies on thermal regeneration of FBG reflectivity……………………… 214

7.4 Discussion on FBG temperature stability … ……………………………………….. 216

7.5 Conclusion ……………………………………………………………..…………. 223

CHAPTER 8: SUMMARY AND FUTURE SCOPE 223

8.1 Summary of the thesis ……………………………………………………………. 225

8.2 Future scope of work ……………………………………………………………… 235

REFERENCES …………………………………………………………………….. 236

Homi Bhabha National Institute

Ph. D. PROGRAMME

1.	**Name of the Student**	**:**	**Ramakanta Mahakud**
2.	**Name of the Constituent Institution**	**:**	**Raja Ramanna Centre for Advanced Technology, Indore-452 013**
3.	**Enrolment Number**	**:**	**PHYS 03200904003**
4.	**Title of the Thesis**	**:**	Studies on fabrication of Fiber Bragg Gratings using high repetition rate ultraviolet radiation from frequency converted copper vapour laser
5.	**Board of Studies**	**:**	**Physical Sciences**

SYNOPSIS

A fiber Bragg grating (FBG) consists of a periodic modulation of the core refractive index in an optical fiber. The FBGs are now extensively utilized as fiber optic components for telecommunication, as mirrors in fiber lasers and as fiber based temperature, strain and chemical sensors. The advantages of fiber gratings over competing technologies include their all-fiber geometry, immunity from EMI (electromagnetic interference), low insertion loss, flexibility for obtaining desired spectral characteristics, capability to work in harsh environments, compactnessand lightweight. The refractive index modulation is imprinted in the photosensitive fiber core by exposing it to UV interference pattern of submicron period. The contrast and stability of the UV fringes are crucial in deciding the FBG characteristics, which in turn depend on specifics of the laser system and interferometer used for FBG writing. The magnitude and profile of refractive index modulation along the fiber length determine the FBG reflectivity and spectrum. These spatial variations are the combined effect of beam profile, beam focusing and interferometer type. Highly coherent UV beam is required for inducing large refractive index modulation. High UV beam pointing stability is also essential to avoid the wash out of induced refractive index modulation, as FBGs are usually written over a period of time. The phase mask technique is most commonly used for FBG writing. On the other hand, the prism (interferometric) based FBG fabrication is particularly a convenient choice for writing FBGs at different Bragg wavelengths, as required in distributive sensing. The sensitivity and thermal sustainability of the written FBGs are crucial for high temperature sensing. Highly coherent, high repetition rate (5-6 kHz), low pointing stability UV pulses at 255 nm, obtained from second harmonic (SH) generationof copper vapor laser (CVL), has emerged as a potential source for fast writing of FBGs, typically in a few minutes. The low pulse energy FBG writing from CVL based UV sources also lead to higher fiber strength/lifetime.

The present thesis work comprises of the experimental and analysis works on FBG fabrication as well as its utilization in temperature sensing. The experimental works consisted of studies on the spatial coherence and beam pointing stability of CVL and its second harmonic; contrast and stability of UV fringes; FBG writing by phase mask and prism interferometers by UV beams of different beam quality; studies on temperature sensitivity, thermal sustainability and the development of FBG based high temperature sensor. The effect of various parameters on FBG fabrication, temperature sensitivity and thermal sustainability has been thoroughly analyzed. The characteristics of UV beam generated from frequency conversion depend on beam parameters of fundamental CVL beam. Hence for improving efficacy of FBG writing, the parameters such as spatial coherence, divergence and pointing stability of CVL laser beam with different resonator configurations and corresponding frequency converted UV beams are studied. Using these UV beams, the FBGs are written by phase mask and prism interferometers. The effect of writing UV beam parameters such as fluence, profile, focusing, spatial coherence and pointing stability on the FBG fabrication are studied. A theoretical model based on single photon absorption explained the experimental trends on the growth and saturation of refractive index modulation of type I FBGs written by partially coherent UV beams. This analysis was further extended to study the effect of UV beam profiles such as Gaussian and top hat intensity distribution on the evolution of FBG spectrum. The effect of fractional radiation present in the phase mask's residual orders on fringe intensity distribution and FBG fabrication is analyzed and discussed. A numerical analysis and experiments on the reflectivity and Bragg wavelength tuning of prism based FBG fabrication are carried out. The FBG based high temperature sensor has been studied. For temperature sensing, the grating strength was stabilized by annealing. The factors affecting temperature sustainability, temperature sensitivity were theoretically analyzed. The theoretical and experimental study on the strain transfer coefficient and its effect on temperature sensitivity of embedded FBGs have been carried out. The present work supplements a very limited literature available in FBG fabrication using high repetition rate 255 nm UV sources, that too without any detailed experimental study or analysis. Also the CVL based kHz repetition rate, ns pulse width and kW range peak power UV sources are very interesting complimentary sources for FBG fabrication amongst the most common low repetition rate, nano-second, high pulse energy Excimer, low average power CW and also recently investigated IR fs laser sources.

The overall thesis work is organized into eight chapters as follows,

Chapter 1: Review on Fiber Bragg Grating

The first chapter begins with the fundamentals of Fiber gratings and ends with current status on FBG technology and applications. The fundamentals of FBG cover the physics of light propagation, photosensitivity, FBG types and fabrication techniques. After a short introduction to light propagation in step index fibers and fiber gratings, the parameters influencing the grating reflectivity of a uniform FBG are discussed using coupled-mode theory. Transfer matrix and multilayer analysis are incorporated to characterize non uniform grating profiles. The laser sources for writing FBGs are discussed. The applications of FBGs in research, technology and industrial areas are presented. The review ends with presentation of current status of this rapidly evolving field.

Chapter 2: Studies on the frequency converted copper vapour laser UV (255 nm) radiation

The UV beam properties important for FBG fabrications are intensity, spatial coherence, beam profile, pointing and power stability. These UV beam characteristics are guided by the fundamental (CVL) beam properties. This chapter presents the detailed experimental results on the second harmonic of CVL leading to generation of UV (255 nm) beams. The UV beam characteristics are correlated with that of fundamental CVL beams. The CVL has been equipped with unstable and spatial filtering optical resonators. The diagnostic tools, methodological formulation of techniques and its analysis on measuring spatial coherence and pointing stability of the UV/CVL laser beams are presented. The spatial coherence was measured by a homemade cylindrical lens based reversible shear interferometer. The pointing stability was measured by recording the single pulse spatial shift of the far-field intensity distribution from the mean position. The effect of laser beam spatial coherence and pointing stability of the CVL beam on the conversion efficiency and UV beam parameters are discussed.

Chapter 3: Analysis on the contrast and stability of UV fringes of different FBG writing interferometers

Fiber Bragg gratings are made by inducing refractive index modulation in the photosensitive fiber core by a UV interference pattern of submicron period. The contrast and stability of UV fringes are crucial for FBG inscription efficiency. In this chapter, the effect of spatial coherence and beam pointing stability on the contrast and stability of sub-micron UV fringes produced by different interferometric techniques such as phase mask, biprism, Lloyd prism and phase mask -Talbot interferometers has been theoretically analyzed. It is shown that fringe contrast, at a point in the fringe plane, decreases with increase in beam divergence as well as with increase in separation between two points on the incident wave front. The spatial variation of fringe contrast also depends on interferometer type. The fringe stability decreased with increase in beam pointing instability as well as with distance of the fringe plane from the beam splitter. The theoretical formulation is verified by correlating with experimentally measured contrast and stability of fringes generated by a 2^0 biprism by 255 nm UV beams of different spatial coherence and pointing stability. This chapter provided guidelines for the effective FBG fabrication for the present thesis work as well as supplementing the published literature in the field.

Chapter 4: Experimental studies on writing of FBGs by phase mask technique using CVL-UV beam

This chapter presents the experimental investigations on FBG fabrication by phase mask technique, using 255 nm UV beams of different spatial coherence and pointing stability characteristics. Both the germanium and germanium- boron co-doped photosensitive fibers are employed in the FBG fabrication. In thephase mask technique, refractive index modulation is induced in the photosensitive fiber core by exposure of UV interference pattern, formed by the overlap of the +1 and -1 order beam of the phase mask. The UV beam was focused by a cylindrical lens on the fiber. The average power, average power density and energy density of the UV beam varied approximately in the range of 200 - 400 mW , 8 - 16 W/cm^2 and 1.4 -2.8 mJ/cm^2, respectively. The fiber was placed at different distances from the phase mask to write FBGs of different length, bandwidth and reflectivity. The growth trends of refractive index modulation, average effective refractive index and bandwidth are studied. The growth characteristics of gratings written by the UV beams of different spatial coherence and pointing stability are compared. Gratings were written at different wavelengths (~ 1535 nm, ~ 1024 nm, ~ 1054 nm) by phase masks of different pitch. The fabrication of tilted gratings, with grating planes at angles 0 to 5^0 to the fiber axis, is studied. The effect of fiber composition on FBG fabrication efficiency is studied. The evolution of FBG spectrum with UV fringes exposure is studied. Overall, the FBGs of different length (2 to 10 mm), different Bragg wavelengths, different reflectivity (up to 99.9 %) and different bandwidth (up to 1 nm) have been written and studied in different fiber types. The effect of various parameters on grating growth, saturation and evolution of FBG spectrum has been outlined for the analysis.

Chapter 5: Theoretical analysis of phase mask based FBG fabrication

This chapter presents the theoretical analysis of FBG fabrication in terms of the refractive index modulation in the fiber core and its subsequent saturation. The implication of experimental results on growth and saturation of refractive index modulation are analyzed by a physical model based on single photon absorption. It is shown that the evolution of refractive index modulation in different Fourier harmonics is due to nonlinear growth of UV radiation induced refractive index change in the fiber core. The growth and saturation of refractive index modulation depends on the fringe contrast and fiber composition. The effect of residual phase mask orders in FBG fabrication is analyzed and discussed.

This analysis is further extended to study the reflection spectrum of the fiber Bragg gratings written by the UV beam profiles of different intensity distributions, particularly cylindrically focused top hat and Gaussian beams. It is analytically shown that while writing FBG by UV fringes of non-uniform intensity distribution, the refractive index distribution envelope evolves with exposure time. The average refractive index and refractive index modulation profiles change due to nonlinear growth and saturation of UV induced refractive index, at different sections of the grating occurring at different times of exposure. Effect of average refractive index and refractive index modulation profile dynamics on the reflection spectra of fiber Bragg gratings, are discussed. The analysis explained the observed experimental results on FBG fabrication and its post fabrication erasure by fringeless UV exposure.

Chapter 6: Studies on FBG fabrication and Bragg wavelength tuning by prism interferometers

This chapter presents analysis and experimental results on the fiber Bragg gratings fabrication by wave front splitting prism interferometers. The analysis of FBG writing by biprism interferometers has been carried out to optimize the FBG writing position in order to maximize the FBG reflectivity. It is analytically shown that the fiber position of maximum reflectivity and inscribed grating length varied with change in UV beam spatial coherence and beam diameter. The evolution, reflectivity, bandwidth and saturation fluence of FBGs written by biprism and Lloyd prism are compared. The techniques of Bragg wavelength tuning of FBGs written by prism interferometers are discussed. A 24^0 apex angle biprism is employed to write FBGs by the 255nm UV radiation. The peak FBGs wavelength was around 1550 nm and their performance was studied with various parameters. The experimental results qualitatively agreed with the analysis.

Chapter 7: Studies on temperature sensitivity and stability for FBG based temperature sensing

The temperature sensitivity and thermal stability are the two important parameters for the FBGs to be used as sensor in high temperature applications. This chapter presents the studies on the Bragg wavelength shift with change in temperature and thermal sustainability of FBG reflection in the temperature range 25 ^{0}C to 800 ^{0}C. The FBG temperature sensitivity increased with temperature elevation. However, the sensitivity was different for FBGs written in different fiber types. The experiment on thermal sustainability of FBGs showed that the FBG written in low photosensitive fiber was able to tolerate higher temperature.

A theoretical analysis on the factors affecting the shift of Bragg wavelength with change in temperature, in typical bare and embedded FBG based temperature sensors, has been carried out. It is shown that the non-uniform behavior of temperature sensitivity in bare FBG is a combined effect of thermal expansion coefficient of fiber and temperature derivatives of effective refractive index. The temperature sensitivity of embedded FBGs increased with the increase in fractional strain transfer from the substrate to FBG. It is analytically shown that the thermal stability is the cumulative effect of factors such as thermo optic coefficient, UV induced defect distribution, release rate/fiber composition of the trapped defects and grating strength. Based on these studies, FBG based single point high temperature sensors have been developed.

Chapter 8: Summary and future scope

This chapter is a summary of the experimental and analytical investigations on the FBGs as carried out during the thesis work. The scope for the future work is discussed.

LIST OF FIGURES

1.1:	Schematic of an optical waveguide	26
1.2:	(a) Schematic fiber Bragg grating structure (b) Simulated reflection spectrum of a uniform FBG of length 10 mm and Δn_{eff}= 0.0004	32
	(c) Transmission spectrum of a LPG of length 40 mm and period 320 µm	35
1.3:	Schematic of the concatenation of several short reflection gratings	36
1.4:	Refractive index layers	37
1.5:	(a) Schematic and (b) Representative spectrum of a tilted FGB, written by phase mask technique using 255 nm UV beam as presented in chapter 4	38
1.6:	Representative spectrum of (a) chirp FGB (b) apodised FBG (c) superstructure (d) phase shifted FBG	40
1.7:	(a) Energy levels of copper involved in lasing action	44
	(b) Schematic of CVL assembly with excitation circuit	45
2.1:	(a) Schematic of wavefront reversal shear interferometer (b) A typical reversal shear interferogram of highly spatially coherent CVL beam	51
2.2:	(a) Schematic for measuring pulse to pulse divergence, pointing and intensity stabilities (b) A drifted far field spot from the reference spot	54
2.3:	CVL in unstable resonator (PBUR) configuration	57
2.4:	CVL in diffraction filtered (GDFR) resonator configuration	58
2.5:	Variation of CVL line width in time	60
2.6:	Interferogram of (a) PBUR1 (c) PBUR2 (e) GDFR CVL beams; Intensity profile of (b) PBUR1 (d) PBUR2 (f) GDFR interferograms	61
2.7:	Variation of degree of coherence (fringe visibility) along radial distance	62

2.8:	Composite pictures of CVL far-field line images (at cursor position) for 650 s for (a) PBUR1 (b) PBUR2 and (c) GDFR CVL beams	63
2.9:	Pulse to pulse far-field intensity profile for (a) PBUR1 (b) PBUR2 (c) GDFR CVL beams	63
2.10	(a) Angular wandering of far field peak intensity position of GDFR beam (b) Probability distribution of beam pointing of three beams	64
2.11	Pulse to pulse CVL (a) far field peak intensity and (b) divergence	64
2.12:	(a) Schematic of the experimental set up for SH generation (b) Experimental set up of CVL based SH generation	74
2.13:	Variation of second harmonic (a) power (b) conversion efficiency with fundamental input power	75
2.14:	Temporal pulse shapes of fundamental and the second harmonic beam for (a) PBUR1 (b) PBUR2 (c) GDFR CVL	76
2.15:	Relative variation in UV average power for (a) PBUR2 and GDFR CVL as fundamental beam with time (b) change in UV3 power with time for 22 minutes	77
2.16:	Near field of (a) UV2 (b) UV3 beams	79
2.17:	Typical interferogram of (a) UV1 (b) UV2 (c) UV3 beams	79
2.18:	Line intensity variation across interferogram of (a) UV1 (c) UV2 (d) UV3 beams ; Degree of coherence of (b) UV1 (d) UV2 (f) UV3 beams	80
3.1:	Schematic of overlap of +1/-1 order beams of a phase mask	85
3.2:	Simulated variation (a) fringe contrast for constant divergence (b) pulse averaged contrast for different round trip divergence values for incident beam	87

on phase mask

3.3: Schematic of phase mask –Talbot interferometer 88

3.4: (a) Schematic of a biprism interferometer (b) simulated fringe intensity distribution for beam divergence of (b) $\Delta\phi$ = 63 μrad and (c) 150 μrad 90

3.5: (a) Schematic of FBG inscription by Lloyd prism interferometer (b) Variation of fringe contrast in the FBG writing plane 91

3.6: Schematic of (a) two beam interference and (b) UV beam incident at different angles on the phase mask 94

3.7: Simulated (a) fringe intensity positional fluctuation for different pointing angles (b) average fringe contrast [$\nu_S(x, \Delta\phi)$] vs distance from phase mask (x) 97

3.8: (a) Schematic of UV beam incident on phase mask at different angles, simulated (b) phase variation vs. pointing angle (c) fringe intensity positional fluctuation for different pointing angles (d) average fringe contrast vs distance from phase mask for different beam pointing angles 0-20 μrad in Talbot region 98

3.9: (a) Schematic of UV beam incident on biprism at different pointing angles; simulated (b) phase variation vs. pointing angle (c) fringe intensity positional fluctuation for different pointing angles (d) average fringe contrast vs distance from biprism for different pointing angles 0-40 μrad 100

3.10: Schematic of experimental set up to measure fringe stability 103

3.11: Composite picture of interference pattern for beam pointing stability of (a) 8 μrad (b) 22 μrad and (c) 45 μrad at x=125 mm 103

3.12: Intensity profile of interference pattern for beam pointing stability of (a) 8 μrad (b) 22 μrad and (c) 45 μrad at x=125 mm 104

3.13: Positional jitter of interference pattern at distance of (a) x= 50 mm (b) 150 mm for pointing stability of 22 μrad 105

3.14: Theoretical (line) and experimental (data points) variation of fringe instability with the distance from the apex of a 2^0 biprism for the beam pointing angle of 8 μrad, 22 μrad and 45 μrad and λ = 510 nm 105

3.15: Time stacked picture of horizontal cursor at x = 100 mm for (a) exposure time 172 μsec (single pulse) (b) 50 msec (250 pulses) (c) Variation of single pulse and time average visibility (averaged over 250 pulses) of fringes with distance from biprism for 10mm diameter PBUR2 CVL beam 106

4.1: (a) Schematic and (b) Experimental set-up for FBG inscription 111

4.2: Diffraction of light in different orders by phase mask of pitch 1.060 μm 113

4.3: Schematic of recording of FBG spectra 115

4.4: Evolution of transmission dip of a FBG with increase in fringe exposure time 119

4.5: (a) Change in average RI (b) modulation contrast with growth of RI modulation 120

4.6: Transmission of FBG written at distance of (a) 3 mm (b) 5mm from phase mask 121

4.7: (a) FBG reflectivity (b) refractive index modulation for different FBG lengths 122

4.8: Reflection spectrum of FBG at cumulative fluence of (a) 0.2 kJ/cm^2 (b) 0.8 kJ/cm^2 (c) 1.6 kJ/cm^2 (d) 3.2 kJ/cm^2 122

4.9: (a) Growth of transmission dip with UV exposure time and transmission spectrum of FBGs written by (b) UV1 beam (c) UV2 beam (d) UV3 beam 124

4.10: Change in FBG (a) reflectivity (b) refractive index modulation with fluence 125

4.11: (a) Evolution of refractive index modulation (b) average refractive index with increase in UV fluence 128

4.12: Transmission of the FBG written in (a) CMS-1550-R1 (b) PS-270 fiber 129

4.13: (a) Transmission spectrum at different fluence (b) Variation of reflectivity, average index and index modulation with increase in accumulated fluence 131

4.14: Variation of RI index modulation with increase in accumulated fluence 131

4.15: Transmission spectra of a tilted FBG (for $\theta = 0.5^0$) 133

4.16: Transmission spectra of tilted FBGs for (a) $\theta = 2^0$ (b) $\theta = 4^0$ 134

4.17: (a) Bragg wavelength tuning by tilting the fiber in the fringe plane (b) Variation in coupling coefficient with increase in tilt angle 135

4.18: Transmission of FBGs written by phase mask of pitch 0.725 μm 136

5.1: Simulated normalized RI change along FBG length for (a) γ (x) = 1 and (b) γ (x) = 0.5 for different normalized fluence (F_{n0}) (c) Change of δn_n^{max} and δn_n^{min} with F_{n0} for $\gamma(x) =1$ and $\gamma (x) = 0$ 146 147

5.2: variation of harmonic coefficients (a) $<\delta n_n>$ (b) $\delta n_n^{(1)}$ (c) $\delta n_n^{(2)}$ and (d) $\delta n_n^{(3)}$ of RI change with change in F_{n0} and γ (x) 149

5.3: a) Change of $<\delta n_n>$, $\delta n_n^{(1)}$, $\delta n_n^{(2)}$ and $\delta n_n^{(3)}$ with F_{n0} for γ (x) =1 (b) Change of $\delta n_n^{(1)}$ and $\delta n_n^{(2)}$ for γ (x) = 0.7 and γ (x) =1 (c) Spatial variation of first three harmonics of normalized refractive index change [$\delta n_n(z)$] 150

5.4: Simulated variation of (a) FBG reflectivity (b) Bragg wavelength shift (c) Bandwidth with increase in accumulated normalized fluence for a FBG of length 5 mm 152

5.5: (a) Schematic of FBG writing by phase mask technique with non uniform UV beam profile and (b) Typical beam profiles 154

5.6: Variation of maximum and minimum fringe intensity in the fringe depth 157 by superposition of +1 and -1 order of phase mask with (a) UVG (b) UVT beam illumination

5.7: Mean fringe intensity and (b) fringe modulating parameter at different phase mask to fiber distance (indicated in mm) for UVG beam illumination 157

5.8: (a) Change of mean fringe intensity and (b) Fringe modulating parameter at different phase mask fiber distance (indicated in mm) for UVT beam illumination 158

5.9: Variation of normalized (a) $\delta n^1(x,z)$ (b) $<\delta n\ (x,z)>$ for UVG beam; (c) $\delta n^1(x,z)$ (d) $<\delta n\ (x,z)>$ for UVT beam with normalized accumulated fluence 160

5.10: Simulated (a) $\delta n_n^1(x,z)$ (b) $<\delta n_n\ (x,z)>$ for UVG beam written FBG at different normalized accumulated fluence for $x = 5$ mm 161

5.11: Simulated reflection spectra of FBGs at different normalized fluence written by (a) UVG (b) UVT beam for phase mask fiber distance (x) of 0.2 mm 163

5.12: Simulated reflection spectra of FBG for phase mask fiber distance (x) of 5 mm 163

5.13: Simulated spectra for fiber phase mask distance of 0.2 mm and $\gamma_1(x) = 0.7$ 164

5.14: (a) Simulated growth of FBG reflectivity with fringe exposure and decay with fringeless UV illumination (b) Growth of a FBG reflection with fringe exposure (c) Decay of FBG transmission dip with UV illumination 166

5.15: (a) Phase mask diffracting in different orders; Fringe intensity distributions for (a) $f_0 = 0.01$, $f_{\pm1} = 0.42$, $f_{\pm2} = 0.075$, $f_{\pm3} = 0$ and $f_{\pm4} = 0$ and for (b) $f_0 = 0.01$, $f_{\pm1} = 0.40$, $f_{\pm2} = 0.025$, $f_{\pm3} = 0.055$ and $f_{\pm4} = 0.015$ 168

6.1: (a) Schematic of biprism interferometer for FBG inscription (b) Change in Bragg wavelength with change in refracting angle of the prism 173

6.2: Variation of (a) fringe contrast [γ_{bp} (x)] (b) FBG length (L_g) (c) product of Fringe contrast and FBG length [γ_{bp} (x). L_g] with distance (x) from the biprism 174

6.3: Variation of simulated FBG reflectivity with distance from the apex of the biprism for different beam divergence angle 176

6.4: Variation of simulated FBG reflectivity with distance from the apex of the biprism (a) for a diffraction limited uniform UV beam (b) for a Gaussian UV beam 177

6.5: (a) Schematic of UV beam incidence at anlge θ on the biprism (b) Bragg wavelength change with increase in incidence angle (θ) 178

6.6: (a) Schematic of the interference by geometrically diverging UV beam (b) Change in fringe width with increase in distance from the apex of the prism 179

6.7: (a) Variation of Bragg wavelength with increase in fiber to biprism distance for different cone angles (b) Schematic of FBG fabrication by using a diverging beam incidence on the biprism 181

6.8: Refractive index distribution at positions z = 0.2 mm and 2.5 mm 183

6.9: Simulated (a) fringe contrast and refractive index modulation along FBG Length; reflection spectrum of a FBG in (b) first (R_1) and (b) second (R_2) order 184

6.10: (a) Bragg resonant wavelength shift with change in incidence angle (b) Chirp band width with change in incidence beam cone angle 185

6.11: Biprism based FBG writing set up 186

6.12: Transmission spectrum of FBGs written by (a) UV1 (b) UV2 (c) UV3 beams 187

6.13: Composite picture and intensity profile of a 2° biprism fringes for (a) UV1 beam (b) UV3 beam 187

6.14: Reflection spectra of gratings written at 2 mm (G1), 5 mm (G2) and 7.5 mm (G3) from biprism 188

6.15: Reflection spectrum of (a) grating arrays written by moving the collimating lens (b) grating arrays with partial overlap of their spectrum bandwidth 189

6.16: Transmission spectra of FBG written by UV3 beam in (a) GF1 (b) PS270 fibers 190

7.1: (a) Schematic of temperature controlled oven (b) Oven photograph 194

7.2: (a) Bare FBG sensor (encapsulated) (b) Schematic of embedded FBG sensor 195

7.3: Reflection spectrum of FBG (a) during annealing (b) during data recording 200

7.4: (a) Bragg wavelength at different temperature for FBG in fiber (a) A (c) B (e) C and variation of average temperature sensitivity [<S(T)>] with change in temperature ($T-T_0$) for FBG in fiber (d) A (e) B (f) C 201

7.5: Simulated Bragg wavelength shift ($\Delta\lambda$) vs. temperature change (ΔT) for FBGs written in fiber A, B and C (a) $\Delta\lambda$ from 0 to 6 nm (b) $\Delta\lambda$ from 4 to 6 nm 204

7.6: Simulated (a) Bragg wavelength shift (b) sensitivity with change in temperature for different strain transfer coefficients (c) Experimental Bragg wavelength shift with change in temperature for embedded length 20 mm, 40 mm and 60 mm 205

7.7: Figure 7.7: Change in FBG transmission with (a) increase in temperature (b) increase in time at fixed temperature 210

7.8: Growth of (a) refractive index modulation (b) average index with UV fluence 211

7.9: (a) Decay of NICC [η (t,T)] and (b) increase of average temperature sensitivity with temperature elevation 211

7.10: (a) Variation of temperature and reflectivity of type I and type IIA FBG with time during annealing (b) Variation of Bragg wavelength shift and reflectivity 213 of post annealed FBG with increase in temperature

7.11: (a) Variation of temperature and FBG reflectivity with time during annealing 215
(b) Variation of post annealed FBG reflectivity with increase in temperature

7.12: Simulated (a) trap energy distributions of d_1 and d_2 [(d_1: $\varepsilon_0 = 2$ eV, $\Delta\varepsilon = 1$ eV; d_2: $\varepsilon_0 = 3$ eV, $\Delta\varepsilon = 1.5$ eV] (b) η (ε_d) vs. T (c) Change in demarcation energy with time 217

7.13: Simulated η (ε_d) vs. T (a) for distributions A ($\varepsilon_{0A} = 3.15$ eV, $\Delta\varepsilon_{0A} = 1.1$ eV) and B: ($\varepsilon_{0B} = 2.8$ eV , $\Delta\varepsilon_{0B} = 1.2$ eV) (b) based on different variation of effective refractive index in bright and dark fringe regions 222

LIST OF TABLES

2.1 Parameters of BBO (β-BaB_2O_4) crystal 72

3.1 Comparative data on interferometers of different length for beam pointing angle of 20 μrad (± 10 μrad) and fringe pitch of 0.530 μm 101

4.1 UV (255 nm) beam parameters and FBG results 128

4.2 Results of FBG fabrication in different fiber types 130

7.1 Coefficients of temperature sensitivity and effective refractive index for fibers A, B and C 202

Chapter 1

Review on Fiber Bragg Grating

1.0 Introduction

The advancement in the fiber Bragg grating (FBG) systems has made significant impact in the field of telecommunication and sensor technologies. A fiber Bragg grating (FBG) is wavelength encoded device. FBGs are the core components in wavelength division multiplexing (WDM) based optical communications systems. In the field of sensing, FBG based optic sensors are compact, robust, chemically inert, nonconductive and potential to operate in high EMI and hazardous environments. The FBGs have contributed significantly in the development of point as well as distributed sensors measuring temperature, strain, vibration, flow, pressure, etc. These sensors are being utilized in many major industries such as aviation, oil, gas, mining, railways, seismology, structure health monitoring, smart structures, nuclear and medical fields. The FBGs are also been extensively used in fiber lasers as mirror, gain flattener for dispersion compensation and pulse compression. This review chapter begins with tracing the evolution of FBG field. A brief discussion on fundamentals of fiber gratings such as light propagation, photosensitivity, FBG types and fabrication techniques is presented. The parameters influencing the grating reflectivity of a uniform FBG are discussed using coupled-mode theory. Transfer matrix and multilayer analysis are described for characterization of non-uniform gratings. The laser sources, for writing FBGs, are discussed. The copper vapour laser (CVL) source, the FBG writing fundamental source of present thesis, is presented separately. The applications of FBGs in research, technology and industrial areas are presented. The review ends with the current status of this rapidly evolving field.

1.1 Evolution of FBG field

A fiber Bragg grating (FBG) in its most basic form, is a phase grating, consisting of periodic modulation of refractive index in a small segment of the fiber core. In 1978, Hill and co-workers [1-2] first discovered photosensitivity by forming a standing wave in the core of Ge-doped optical fiber. In the original experiment, laser radiation at 488 nm was reflected from the fiber end producing a standing wave pattern. This led to formation of the internal grating known as “Hill’s grating”. The grating strength increased as the square of light intensity, suggesting a two-photon process as the responsible mechanism [3]. The investigation on photosensitivity remained academic [4-5] for many years. In 1989, Meltz *et al*. [5] showed that 244 nm UV photon, close to the absorption peak of a germanium-related defect in the wavelength range of 240–250 nm, could be used to form gratings by illuminating the fiber through the side of the fiber by an interference pattern. This was a single photon process at 244 nm. Moreover, the grating formation was found to be orders-of-magnitude more efficient [5] than that observed in internal gratings. The permanent change of refractive index, in optical fiber upon exposure of ultraviolet radiation, is described as fiber photosensitivity. Stone observed photosensitivity in many different fibers with relatively high concentration of germanium [6]. The germanium oxygen deficient centers (GODCs), existing in the oxygen-deficient type glass, are thought to be responsible for the refractive-index changes [7-11]. Germanosilicate glass fibers exhibit photo-induced refractive index change initiated by UV light from the lasers tuned to wavelengths lying in the 5.1eV germanium oxygen vacancy defect band [8-11]. Kashyap *et al*. wrote Bragg gratings in the C-band in germanosilicate fibers by exposing the core by a two-beam UV interference pattern [12]. The UV induced index change in untreated optical fibers was of the order of 10^{-4}. Lemaire *et al*. [13] showed that the loading of molecular hydrogen induced refractive index modulation even in standard telecommunication fiber. Several developments have taken place that has pushed the fabrication of FBGs of different variants, written in different fibers for application in varied fields [14-16].

1.2 Photosensitivity of optical fibers

Since the discovery of photosensitivity in germanium-doped silica fiber by Hill *et al.*, various methods and techniques to enhance photosensitivity in silica fibers has appeared in numerous publications. Fibers doped other than germanium such europium [17], cerium [18], and erbium [19] also exhibited photosensitivity phenomena of different degree. The germanium–boron co-doping in silica fiber produce large index modulation of the order of 10^{-3}. The hydrogen loading of standard single mode fibers enhanced the photo induced refractive index modulation in fiber Bragg gratings [20-21]. The FBG can also be written in standard telecom fibers by multi-photon process with fs lasers [20-25]. The refractive index change in the fiber core has gone up to the order of 10^{-1} [16].

1.2.1 Defects in optical fiber

The refractive index change is induced by 240 nm (~ 5.1 eV) photons, below the band gap energy (~ 8.5 eV) of Ge-doped silica glass [16-17]. This implied that the point defects in the ideal tetrahedral network of glass are responsible for the FBG inscription. During the high-temperature gas-phase oxidation process of modified chemical vapor deposition technique (MCVD), GeO_2 dissociates to GeO due to its higher stability at elevated temperature. This manifests in the form of oxygen vacancy Ge–Si and Ge–Ge bonds [26-30]. These defects, normally caused during the fiber drawing process, are called color centers due to their strong absorption [31-33]. Experimental results suggest that Ge–Si, Ge-Gewrong bonds are mainly responsible for the photosensitivity, though may not be the only trigger mechanism. In 1986, Friebele and Griscom first reported $Ge(1)^-$, $Ge(2)^-$ and $GeE^/$defect centers [34-35]. The Ge–Si wrong bond has an absorption band at ~240 nm [14]. The bleaching of this absorption band [36] results in the evolution of new absorption bands on creation of new defects [36-38]. Irradiation with 240 nm UV light ionizes a wrong bond to form a $GeE^/$ center [36-38]. The electron released may recombine immediately with its $GeE^/$ center to give recombination luminescence, or it may diffuse through the matrix until it is trapped at a Ge(1) or Ge(2) center to form a $Ge(1)^-$or $Ge(2)^-$ center, respectively [36-38].

1.2.2 Techniques of photosensitivity enhancement

Optical fibers fabricated with high germanium dopant levels and/or under reduced oxidizing conditions were proven to be highly photosensitive. This is due to the presence of higher concentration of UV bleachable germanium oxygen deficiency centers (GODC) in the fiber core [16-17]. Hydrogen loading, flame brushing and boron co-doping have been used for enhancing the photosensitivity. Hydrogen loading [39-41] is carried out by diffusing hydrogen molecules into fiber core at high pressure and temperature. Hydrogen molecules react in the glass at normal Si–O–Ge sites, forming OH species and UV bleachable GODCs, responsible for photosensitivity. Hydrogenation allows the fabrication of strong Bragg gratings in germanosilica fiber including in intrinsically low photosensitive standard telecom fibers [13]. In flame brushing [42], the region of the optical waveguide, to be photosensitized, is brushed repeatedly by a flame fueled with hydrogen and a small amount of oxygen. At flame temperature of approximately 1700 ^{0}C, hydrogen diffuses into the core of the fiber very quickly and reacts with the germane-silica glass to produce germaniumGODCs. Boron co-doping increases photosensitivity [43-45]. The absorption measurements suggest that boron co-doping does not affect the peak absorption characteristics at 240 nm [45]. The addition of boron reduces the core index of refraction due to buildup of thermo-elastic stresses [44]. The boron co-doping increases the photosensitivity of the fiber through photo induced stress relaxation initiated by the breaking of wrong bonds by UV light [44].

1.2.3 Mechanism of photo induced refractive index change

The underlying mechanism of photo induced refractive index change is not well settled and still under the subject of discussion [16-17]. The grating formation dynamics is complex and involves at least two processes. During UV illumination, the existing germanium oxygen deficient centers in the fiber core are thought to act as gates for transfer of energy from the UV light to the glass matrix [46-47]. The excitation induces forbidden transitions [47] to trapped states [called as defect induced defects (DIDs)]. The creation of new defect sites leads to change in absorption spectrum and accompanied structural modifications. It is believed that the growth of photo induced refractive index is a cumulative effect of change in absorption spectrum, compaction and photo-elastic changes produced by structural modification of the fiber core illuminated by UV fluence [48-51]. The radiation absorption is of one and/or two photon [52-56] nature. The approach of two-photon absorption, through an intermediate virtual state [55-56], utilizes high-intensity (100 GW/cm^2) 264 (or 267) nm fs pulses in low-UV-absorbing telecom [52-53], silica-core [52] and holey fibers [54]. The two-step excitation [56-57] involves the absorption of two light quanta, in consecutive steps and proceeds at much lower intensities, i.e. at about 10 MW/cm^2 in the case of a germanosilicate fiber core, exposed to 193 nm radiation [56-57]. The refractive index of silica fiber core is affected by the number density, orientation and electronic absorption spectra of defects. The color center model, proposed by Hand and Russell [49], is based on the change in absorption spectrum of the fiber core subject to UV illumination. It relates the real (ε_r) and imaginary (ε_i) part of the dielectric constant (ε) through Kramers–Kronig relation, given as [14],

$$\epsilon_r(\lambda) = 1 + \int \frac{\epsilon_i(\lambda)}{\lambda' - \lambda} d\lambda',$$ (1.1)

The color center model is the most widely accepted for the formation mechanism of Bragg gratings. However, it is not clear whether this model alone can always account for all the observed index changes [14].

The compaction model is based on laser irradiation induced density changes, which lead to changes in index of refraction. Compaction was considered as an important component of fiber photosensitivity. The increase in tension on UV illumination was linearly proportional to the refractive index modulation [58-59]. Illumination of 800 nm femtosecond laser light increased core stress in a SMF-28 fiber [60]. The FBG inscription by high-intensity fs (264 nm) irradiation in H_2-free standard telecom fiber is accompanied by stress induction whereas no stress was generated in hydrogenated fiber [61]. Increase in tension lowers the induced refractive index through the photo elastic effect. Fiori *et al*. reported compaction in fused silica slab waveguides that lead to positive refractive index changes on UV illumination [62]. The compaction model proposed by Bernardin and Lavandy [63] considered a two photon activated Ge-Si bond breakage that leads to the compaction of the glass network. Glass compaction was thought to occur via the collapse of higher order ring structures into 2-or 3-membered rings [64]. A differential form of the Lorentz-Lorenz equation shows that the change in refractive index is associated with the change in densification by the relation [51]

$$\frac{\Delta n}{n} = \left(\frac{\Delta \rho}{\rho}\right)(1 + \Omega)\frac{(n^2-1)(n^2+2)}{6n} \tag{1.2}$$

where n is the refractive index of silica clad (~1.45) and Ω is the ratio of the relative change of the polarizability to the relative density change (~ -0.18 for fused silica) [1.28]. The UV-induced increase of the refractive index in the fiber core, due to both color-center and compaction effects, exceeds the decrease caused by the photo-elastic effect. The amount of each contribution might vary strongly as a function of fiber content, pre-irradiation treatment and irradiation wavelength.The stress relief model [65] is based on the hypothesis that the refractive-index change arises from the alleviation of built-in thermo-elastic stresses in the core of the fiber. The UV irradiation breaks the wrong bonds and promotes relaxation in the tensioned glass, thus reducing frozen-in thermal stresses in the core. It is believed that stress relief is one of the reasons of type IIA grating formation [66].

1.3 FBG fabrication techniques

The fabrication of a FBG requires inducing refractive index modulation of submicron period in the fiber core. The requirement of such a short period makes the stability a severe constraint on the FBG fabrication techniques. The externally written FBG fabrication techniques include phase mask [67-70], interferometric [71-72], and point-by-point [73]. The holographic writing involves side exposure of UV fringes on the photosensitive fiber core which photo prints fiber Bragg grating [6]. These techniques and discussion on fringe modulation are provided in detail in chapters 3 and 6 of the thesis on FBG fabrication by phase mask and prism interferometer by UV (255 nm) radiation.

1.4 Wave propagation in optical fiber

Optical fiber is a waveguide for transmission of information at optical frequencies, particularly in near infrared region. An optical fiber has a cylindrical symmetry (though not always). A typical fiber consists of a germanium doped silica (GeO_2:SiO_2) core of higher refractive index surrounded by a silica (SiO_2) cladding, though exact composition may vary for fibers intended for different applications. The cladding is surrounded by a protective plastic jacket. Fig. 1.1 shows a standard step index fiber consisting of a cylindrical core of radius 'a' of refractive index n_1 surrounded by a cladding with index of refraction n_2 ($< n_1$). The rays undergo multiple reflections at the core/cladding interface. For the rays, incident upon the interface at angles greater than the critical angle, the total internal reflection occur.

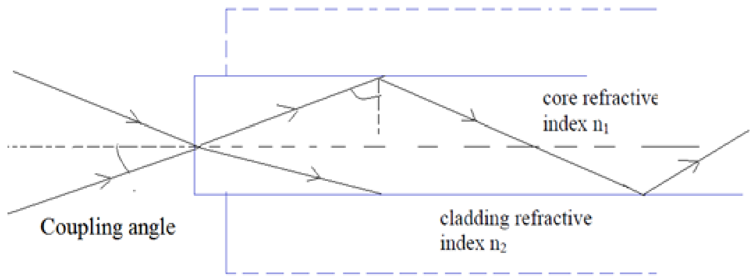

$$n(r) = \begin{cases} n_1, & r \le a \\ n_2, & r > a \end{cases}$$

Figure 1.1: Schematic of an optical waveguide

Light propagating this way is thought of as being lossless in an ideal fiber with no absorption. This sets a limit on the coupling angle at boundaries. The propagation of electromagnetic radiation is governed by Maxwell's equations, solution of which provides information on the propagation, dispersion and energy confinement of each mode. The exhaustive treatment of wave propagation and mode field distribution are well developed. The general form of wave equation in the optical fiber is described as,

$$\nabla^2 \mathbf{E}(\mathbf{r},t) - \epsilon_0 \mu_0 \frac{\partial^2 \mathbf{E}(\mathbf{r},t)}{\partial t^2} - \mu_0 \frac{\partial^2 \mathbf{P}(\mathbf{r},t)}{\partial t^2} = 0 \tag{1.3}$$

where E (r, t) is the electric field, ε_0 is the dielectric constant and μ_0 is the magnetic permeability of the medium. The induced polarization (P) reflects the material response to electric field and highly depends of the field frequency. For a linear isotropic medium, the induced polarization is linear. The polarization and electric displacement vector are given as,

$$P(r,t) = \varepsilon_0 \chi E(r,t) ; \qquad D = \varepsilon_0 (1+\chi) E = \varepsilon_0 \varepsilon_r E = \varepsilon E \tag{1.4}$$

where χ is susceptibility and ε_r (= $1+\chi$) is the relative permittivity. The electric field of a wave propagating in the z-directions is given as [76]

$$E(r,z,\phi,t) = \xi_t(r,\phi)e^{(\omega t \pm \beta_v z)} \tag{1.5}$$

where β_v is propagation constant of v^{th} mode, ω- frequency and $\xi_t(r,\phi)$ is the transverse component of the propagating wave. The exact solution of the wave equation, for a step index fiber, is very complicated involving all six non-zero field components in the so called hybrid modes. A simplification to the solution is arrived by using the approximation for the so called 'weak guidance' where the fractional refractive index difference is assumed to be small [Δ = ($1-n_2/n_1$) <<1]. In such a case, the electric and magnetic fields are approximately transverse to the fiber axis and can have any arbitrary state of polarization. These linearly polarized waves are usually referred as LP modes. The mode fields of a cylindrical waveguide are J-Bessel functions in the core and K-Bessel functions in the cladding, expressed as [16]

$$\xi_{vt}(r,\phi) = \begin{array}{ll} \dfrac{A}{J_v(U)} J_v(U\dfrac{r}{a}) \begin{pmatrix} \cos v\phi \\ \sin v\phi \end{pmatrix}, & r < a \\ \dfrac{A}{K_v(U)} K_v(W\dfrac{r}{a}) \begin{pmatrix} \cos v\phi \\ \sin v\phi \end{pmatrix}, & r > a \end{array} \tag{1.6a}$$

where v (= 0,1,2..) is the mode number. The waveguide parameters are,

$$U = k_0 a(n_1^2 - n_{eff}^2)^{1/2}; \quad V = k_0 a(n_1^2 - n_2^2)^{1/2}; \; W = (V^2 - U^2)^{1/2} \tag{1.6b}$$

$$n_{eff} = n_2[b(n_1 - n_2)/n_2 + 1]; \; b = W^2/U^2 \tag{1.6c}$$

where n_{eff} (= β/ k_0) is effective index of the mode. The guided modes correspond to discrete β values,

$$k_0^2 n_2^2 < \beta^2 < k_0^2 n_1^2 \tag{1.7}$$

The guided modes are oscillatory in the core and decay in the cladding. For a given value of v, there will be several guided modes which are designated as LP_{vm} modes (m=1,2,3..). For

$\beta^2 < k_0^2 n_2^2$, the fields are oscillatory even in the cladding and β can assume a continuum of values known as radiation modes. The guided and radiation modes form a complete set of orthogonal modes. Hence any arbitrary field distribution can be expanded as [16],

$$E_t(r,\phi,z,t) = \frac{1}{2}\sum_{\nu=1}^{m}[A_\nu(z)\xi_{\nu t}(r,\phi)e^{i(\omega t-\beta_l z)} + cc] \tag{1.8}$$

where ξ_ν are normalized transverse mode field with propagation constants $\beta_\nu$satisfying the orthogonality condition. The summation sums over all discrete indices (ν) of the guided modes and integrates over all continuous indices of the radiation and evanescent modes. The mode fields of an unperturbed wave guide remain unchanged. Except for evanescent fields, the energy of the fields in a waveguide flows only in the longitudinal direction. In an ideal waveguide, the normal modes do not couple i.e. $A_\nu(z)$ are constants. Optical fibers are classified as single mode or multimode depending on the radial dimension of the core. The number of modes supported by an optical fiber is reduced as the fiber core diameter is decreased and/or operated at a longer wavelength. In a step index fiber with $0 < V \leq 2.408$, there exist only the lowest order guided mode, namely LP_{01} mode. Such a single mode fiber necessitates the core diameters of only a few microns. Fiber Bragg gratings are usually written in single mode step index photosensitive fibers.

1.5 Fiber grating theory

The coupled-mode theory [74-78] is applied to solve the wave propagation in a FBG. Wave propagation in optical fibers is analyzed by solving Maxwell's equations with appropriate boundary conditions. The wave-propagation equations are simplified by assuming weak guidance approximation. This allows the decomposition of the modes into an orthogonal set of transversely polarized modes [79-80]. These modes propagate without coupling in the absence of any perturbation. Coupling of specific propagating modes can occur if the wave guide has a phase and/or amplitude perturbation. The coupled-mode method assumes that the mode field distribution of the unperturbed waveguide remain unchanged in the presence of weak perturbation. This approach provides a set of first-order differential equations for the change in the amplitude of the fields along the fiber, which have analytical solutions for uniform sinusoidal periodic perturbations. A complex grating may be considered to be a concatenation of several small sections, each of constant period and unique refractive index modulation. The mathematical tools that have been used to analyze complex grating structures include transfer matrix method [81], multilayer analysis [82] and Bloch theory [83]. The solutions provide the basic field distributions of the bound and radiation modes of the waveguide.

1.5.1 Mode coupling

The modes defined by the ideal waveguide are no longer exact normal modes of the perturbed waveguide. The modes can be coupled by the perturbation while propagating along the fiber. If the total field is still expanded (eqn 1.8) in terms of the normal modes of the unperturbed waveguide, the expansion coefficients A_ν (z) are no longer constants of propagation but vary with z as the fields propagate in the waveguide. The spatially dependent perturbation to the waveguide can be represented by a perturbing polarization. When the wave propagation takes place in a perturbed system, the total polarization response of the dielectric medium can be expressed as [16]

$$\vec{P} = \vec{P}_0 + \vec{P}_{gr} \tag{1.9}$$

where P_0 ($= \varepsilon_0 \chi E_\nu$) is unperturbed polarization and P_{gr} is termed as perturbation part. The coupling to radiation modes is ignored. Thus, the wave equation (1.3) in perturbed system is expressed as,

$$\nabla^2 \vec{E} = \mu_0 \varepsilon_0 \varepsilon_r \frac{\partial^2 \vec{E}}{\partial t^2} + \mu_0 \frac{\partial^2 \vec{P}_{gr}}{\partial t^2} \tag{1.10}$$

For weak coupling, the slowly varying envelope approximation (SEVA) is applied [16]. The amplitude of a mode slowly changes over the distance of wavelength of light such that $\frac{\partial^2 A_\nu}{\partial z^2} << \beta_g \frac{\partial A_\nu}{\partial z}$, where ν refers to transverse mode number. With these conditions, the coupled modes can be expressed as,

$$\sum_{g=1}^{l} \left[-2i\mu_0 \omega \frac{\partial A_g}{\partial z} \xi_{gt} e^{i(\omega t - \beta_g z)} + cc \right] = \int_{-\infty}^{\infty}\int_{-\infty}^{\infty} \mu_0 \frac{\partial^2 P_{gr}}{\partial t^2} \xi_{\mu t}^* \, dxdy \tag{1.11}$$

Thus the amplitude of modes are coupled which applies to a set of forward and backward propagating modes. However, coupling takes place between two modes, in most of the applications. This includes coupling in the same waveguide such as FBG and LPG (Long period grating) or between two parallel waveguides, as in a directional coupler. For coupling between two modes, the coupled mode equations are written in a simple form that can be solved analytically. For two-mode coupling, the field expansion consists of only two modes with amplitudes A(z) and B (z).

1.5.2 Fiber Bragg gratings (Coupling of counter propagating guided modes)

In a fiber Bragg grating, the perturbation Δε (permittivity) is a periodic function of z. The phase fronts are perpendicular to the fiber longitudinal axis. Assume that A(z) and B(z) are the amplitudes of the forward and backward propagating modes, respectively. These amplitudes change during propagation in the grating, due to exchange energy. The total transverse field is described as,

$$E(x,y,z,t) = \frac{1}{2}[A(z)\xi_t e^{i(\omega t - \beta z)} + B(z)\xi_t e^{i(\omega t + \beta z)} + cc] \tag{1.12}$$

The polarization can be expressed as [16],

$$P_{gr}(z) = 2n\varepsilon_0 \delta n(z) E\,(x,y,z) \tag{1.13}$$

where $\delta n(z)$ is the refractive index perturbation. In a normal grating, the grating planes are of a constant period (Λ) with a wave number K (= 2 π/Λ). The refractive index modulation is described as [16]

$$\delta n(z) = <\Delta n> [1 + \frac{\nu}{2}(e^{i(2\pi .z/\Lambda)+\phi(z)} + cc)] \tag{1.14}$$

where γ is refractive index modulation contrast, $<\Delta n>$ is average index change (dc index) and $\gamma <\Delta n>$ is index modulation (ac index). The coupled mode equations are given as [16]

$$\frac{dA(z)}{dz} = -i\kappa_{dc} A(z) - i\kappa_{ac}^{*} B(z) e^{i(\Delta\beta z - \phi(z))} \tag{1.15a}$$

$$\frac{dB(z)}{dz} = i\kappa_{dc} B(z) + i\kappa_{ac} A(z) e^{-i(\Delta\beta z - \phi(z))} \tag{1.15b}$$

where $\Delta\beta$ is phase mismatch, given as $\Delta\beta = 2\beta - 2\pi/\Lambda$ (1.16)

and κ_{ac} and κ_{dc} are termed as ac and dc coupling coefficients, given as [16]

$$\kappa_{dc} = n\omega\varepsilon_0 \iint <\Delta n> \xi_t \xi_t^{*} dxdy\,; \quad \kappa_{ac} = \frac{\gamma}{2} k_{dc} \tag{1.17}$$

κ_{dc} influences propagation due to change in average index. The rate of change of $\phi(z)$ is measure of chirp in the grating. The analytical solution of coupled mode equations with boundary conditions, yields reflection coefficient (ρ) of the grating given as,

$$\rho = \frac{-\kappa_{ac} \sinh\,(\alpha L)}{\delta \sinh(\alpha L) - i\alpha \cosh(\alpha L)} \tag{1.18a}$$

where α and δ are given as

$$\delta = \kappa_{dc} + \frac{1}{2}(\Delta\beta - \frac{d\phi}{dz})\,; \qquad \alpha = \sqrt{\kappa_{ac}^2 - \delta^2} \tag{1.18b}$$

Uniform fiber Bragg gratings - In a normal grating (Fig. 1.2a), the grating planes are of a constant period (Λ) with a wave number K = 2 π/Λ. Light guided along the core of an optical fiber will be scattered by each grating plane. At phase matching, $\Delta\beta = 0$, the field couples to the generated wave over infinite distance. The wavelength at which phase matching condition satisfied is given as [16-17]

$$\lambda = 2\, n_{eff}\Lambda \qquad (1.19)$$

where n_{eff} is the effective index of the fiber. If the Bragg condition is satisfied, the contributions of reflected light from each grating plane add constructively in the backward direction to form a back-reflected peak with a center wavelength defined by eqn (1.20). Otherwise, the reflected light from each of the subsequent planes becomes progressively out of phase and will eventually cancel out.

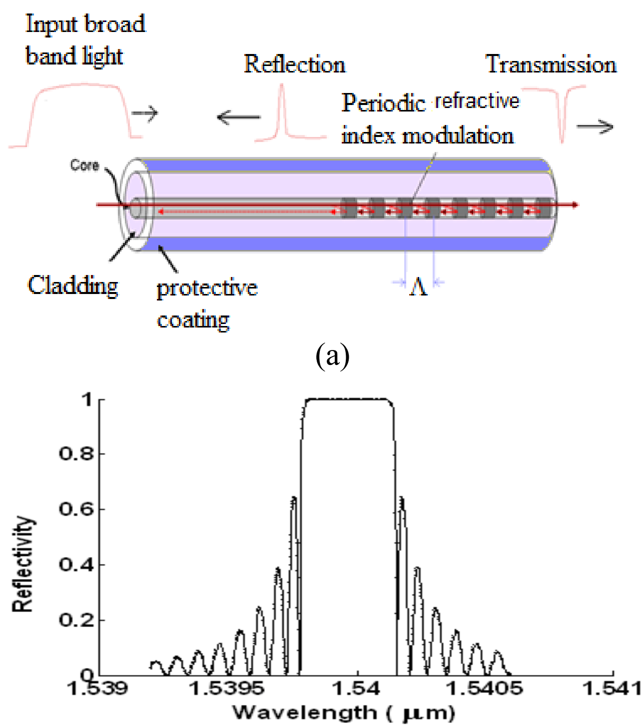

Figure 1.2: (a) Schematic of a fiber Bragg grating structure (b)Simulated reflection spectrum of a uniform FBG of length 10 mm and Δn_{eff}= 0.0004

The phase matching condition is requirement for satisfaction of energy and momentum conservation. The frequency of the incident radiation and the reflected radiation are the same. The vector sum of the incident wave vector and the grating vector is equal the wave vector of the scattered radiation. For a uniform FBG with grating planes normal to the fiber axis, the diffracted wave vector is equal in magnitude but opposite in direction to the incident wave vector. For a uniform grating, $d\phi/dz = 0$. The ac coupling coefficient at phase matching ($\Delta\beta = 0$) is a real quantity. The power of the reflection coefficient is [16]

$$R = |\rho|^2 = \frac{\kappa_{ac}^2 \sinh^2(\alpha L)}{\kappa_{ac}^2 \sinh^2(\alpha L) - \delta^2} \tag{1.20a}$$

The peak reflectivity occurs at a wavelength at which $\delta = 0$ (and therefore $\delta = \kappa_{ac}$), given as

$$R = \tanh^2(\kappa_{ac} L) \tag{1.20b}$$

Wavelength (λ_{max}) at which peak reflectivity occurs is $\lambda_{max} = \lambda\ (1 + \langle\Delta n_{eff}\rangle/n_{eff})$ where λ_b is the design wavelength. The Bragg peak occurs at slightly longer wavelength than defined by the grating period and effective index of the pristine fiber. This is because the average index of the mode index in the FBG continuously increases with increase in photo induced refractive index change. Fig. 1.2b shows the typical reflection spectrum of a uniform FBG. The central peak is bounded on either side by a number of sub peaks. The bandwidth of the FBG reflection spectrum increase with increase in modulation and decrease with increase in FBG length. For wavelengths outside the band gap, the boundaries of the uniform grating (at $z = \pm L/2$) act like abrupt interfaces, thus forming a Fabry–Perot-like cavity [16]. The nulls in the reflection spectrum are analogous to Fabry–Perot resonances. The light is trapped inside the cavity for many round trips at these frequencies, thus experiencing enhanced delay. The dispersion is zero near λ_{max} and becomes appreciable near the band edges where it tends to vary rapidly with wavelength [16-17].

The Bragg wavelength (λ) of a FBG is susceptible to external perturbations such as temperature and strain. The Bragg wavelength shift (Δλ) of a FBG subjected to temperature and axial strain is given as [16-17]

$$\Delta\lambda = \lambda(\kappa_T + \alpha_f)\Delta T + \lambda k \varepsilon_g \tag{1.21}$$

where ΔT is change in temperature, ε_g is axial strain, κ_T [= ($1/n_{eff}$ .dn_{eff}/dT)] is thermo-optic coefficient of the fiber material (~ $8.6\text{x}10^{-6}$ /^{0}C for silica fiber), n_{eff} is effective refractive index of the fiber (~ 1.456), α_f is thermal expansion coefficient of the fiber (~ $0.55\text{x}10^{-6}$ /^{0}C) and k = (1- P_e) where P_e (~ 0.22) is effective photo elastic constant of the fiber.

1.5.3 Long period gratings (co-directional coupling)

The refractive index modulation in the long-period grating (LPG) has a period typically in the range 100 μm to 1 mm. The coupling is between the propagating core mode and co-propagating cladding modes. The high attenuation of the cladding modes results in the transmission spectrum of the fiber containing a series of attenuation bands centered at discrete wavelengths. Each attenuation band corresponds to the coupling to a different cladding mode [84-86]. The phase matching for efficient coupling is given by

$$\beta_1 - \beta_2 = 2\pi/\Lambda \tag{1.22}$$

The phase matching is achieved at the wavelength, λ, where the expression [84]

$$\lambda = [n_{eff}(\lambda) - n_{clad}^{i}(\lambda)]\Lambda \tag{1.23}$$

where $n_{eff}(\lambda)$ and $n_{clad}^{i}(\lambda)$ are the effective indices of co propagating fundamental core mode and ith cladding mode. The minimum transmission of the attenuation bands is given by the expression [85]

$$T_i = 1 - \sin^2(\kappa_{ac} L) \tag{1.24}$$

where κ_{ac} is ac coupling coefficient. A co-directional coupler requires careful fabrication for maximum coupling as the forward coupled mode re-couples to the input mode at $\alpha L > \pi/2$.Fig.1.2c shows the typical transmission spectrum of a LPG of length 40 mm and period 320 μm, fabricated in Corning SMF-28 fiber [85]. The long period fiber gratings (LPFGs) found application for gain equalizing /flattening of Erbium doped fiber amplifiers (EDFAs), for multi-channel filtering in WDM applications, and for temperature/strain/refractive-index sensing [16].

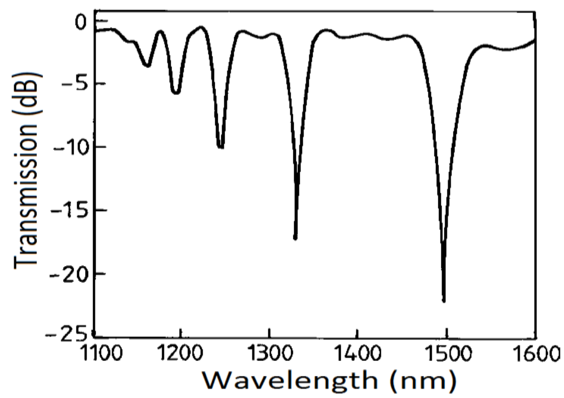

Figure 1.2: (c) Transmission spectrum of a LPG of length 40 mm with period 320 μm fabricated in Corning SMF-28 fiber [85]

1.6 Analytical techniques to characterize non uniform fiber Bragg gratings

1.6.1 Transfer matrix method

Transfer matrix method is used to calculate the reflectivity, transmission and phase [5, 81] of nonuniform gratings. This method relies on sectioning the grating into short segments for which the coupling constant $\kappa(z)$ and chirp $\phi(z)$ are assumed to be constant in each segment. The grating is considered as a four port device with four fields: input field $R(-\delta l_j/2)$ and $R(\delta l_j/2)$ and output field $S(-\delta l_j/2)$ and $S(\delta l_j/2)$ for a segment of FBG with length δl_j. A (2x2) transfer matrix T^j represents the amplitude and phase response of section δl_j[16]

$$\begin{bmatrix} R_j(-\delta l_j/2) \\ S_j(-\delta l_j/2) \end{bmatrix} = \begin{bmatrix} T_{11}^j & T_{12}^j \\ T_{21}^j & T_{22}^j \end{bmatrix} \begin{bmatrix} R_j(\delta l_j/2) \\ S_j(\delta l_j/2) \end{bmatrix} \tag{1.25}$$

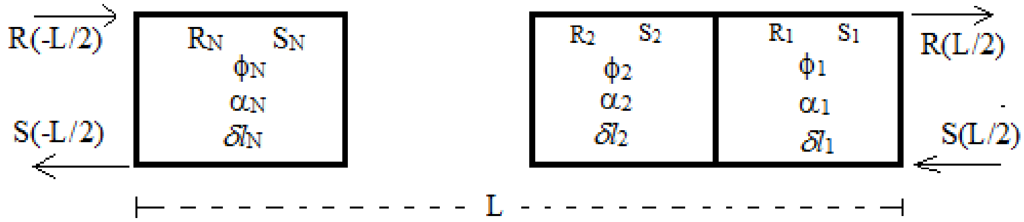

Figure 1.3: Schematic of the concatenation of several short reflection gratings [16]

The coupled mode equations are used to calculate the output fields of each segment. The transfer matrix elements of Jth section are [16]

$$T_{11}^j = \cosh(\alpha\delta l_j) - \frac{i\delta\sinh(\alpha\delta l_j)}{\alpha} \;;\; T_{12}^j = -i\kappa_{ac}\frac{\sinh(\alpha\delta l_j)}{\alpha}$$
$$T_{21}^j = i\kappa_{ac}\frac{\sinh(\alpha\delta l_j)}{\alpha} \;;\; T_{22}^j = \cosh(\alpha\delta l_j) + \frac{i\delta\sinh(\alpha\delta l_j)}{\alpha} \tag{1.26}$$

The closed-form solutions for each uniform piece are combined by multiplying matrices associated with the pieces. The fields of the entire grating (after the N^{th}section) can be expressed as,

$$\begin{bmatrix} R(-L/2) \\ S(-L/2) \end{bmatrix} = [T] \begin{bmatrix} R(L/2) \\ S(L/2) \end{bmatrix} \tag{1.27}$$

where L =$\sum\delta l_j$. The transfer function of the whole grating is given by,

$$[T] = \prod_{j=1}^{N}[T^j] = \begin{bmatrix} T_{11} & T_{12} \\ T_{21} & T_{22} \end{bmatrix} \tag{1.28}$$

For a reflection grating, R (-L/2) = 1 and S(L/2) = 0. The transmission coefficient (τ) and reflection coefficient (ρ) of the whole grating is

$$\tau = 1-\rho = \frac{R(L/2)}{R(-L/2)} = \frac{1}{T_{11}} \;;\; \rho = \frac{S(-L/2)}{R(-L/2)} = \frac{T_{21}}{T_{11}} \tag{1.29}$$

In the thesis work, transfer matrix has been used for synthesis of gratings written by UV beam profiles of non-uniform intensity, presented in chapter 5 and chapter 6.

1.6.2 Multiple layer analysis

This method relies on sectioning the grating into multiple layers and replacing each layer by an interface with a complex reflectivity, which includes the phase change through the layer [82]. The processes are repeated for *N* single-period sections. The basic analysis is similar to the T-matrix approach. However, the reflectivity is simply calculated from the difference in the refractive index between two adjacent layers. Fig. 1.4 shows a thin film on a substrate with light propagating at normal incidence. The transverse field components and the refractive index of each section are indicated. The field in each region (E_j) is the sum of the forward (R_j) and backward (S_j) traveling fields.

$$\overrightarrow{E_j} = \overrightarrow{R_j} + \overrightarrow{S_j} \tag{1.30}$$

Typically the two adjacent layers could be spaced by separation of $\delta l_j = \Lambda/2$, starting from z = 0. The refractive index of the jth layer is, $n_j(z) = n_0 + \langle \Delta n(z) \rangle + (-1)^j \gamma(z) \langle \Delta n(z) \rangle$.

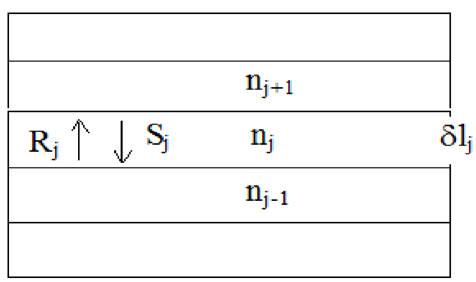

Figure 1.4: Refractive index layers

Applying continuity of the transverse field components (which are tangential to the interface), the matrix equation is given as [16],

$$\begin{bmatrix} R_j \\ S_j \end{bmatrix} = \frac{1}{t_j} \begin{bmatrix} e^{i\varphi_j} & r_j e^{i\varphi_j} \\ r_j e^{i\varphi_j} & e^{-i\varphi_j} \end{bmatrix} \begin{bmatrix} R_{j+1} \\ S_{j+1} \end{bmatrix} = [T^j] \begin{bmatrix} R_{j+1} \\ S_{j+1} \end{bmatrix} \tag{1.31}$$

where $\varphi_j = \beta_j \delta l_j = 2\pi n_j \delta l_j/\lambda$; $r_j=(n_j-n_{j+1})/(n_j+n_{j+1})$; $t_j =2n_j/(n_j+n_{j+1})$ (1.32)

The transfer matrix (T) is given as, $$T = \prod_{j=1}^{N}[T^j] = \begin{bmatrix} T_{11} & T_{12} \\ T_{21} & T_{22} \end{bmatrix} \quad (1.33a)$$

The reflectivity (R) is given as, $$R_{FBG}= |T_{21}/T_{11}|^2 \quad (1.33b)$$

1.7 Fiber Bragg gratings structures

The fiber Bragg gratings are distinguished by pitch (Λ), tilt of grating planes and also refractive index profile along FBG length. There are number of novel refractive index structures besides uniform Bragg grating, most commonly used.

1.7.1 Tilted fiber Bragg grating

Tilting of Bragg grating planes (fig 1.5a) couples light from a forward-propagating guided mode to a back- ward-propagating cladding mode, or to a continuum of radiation modes [87-89].

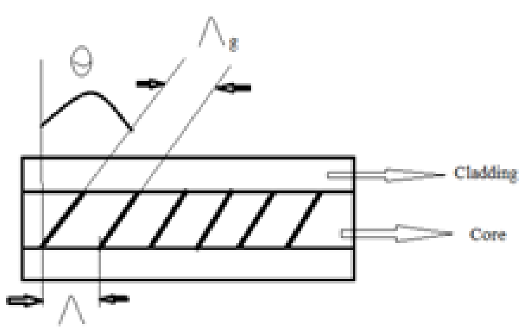

(a)

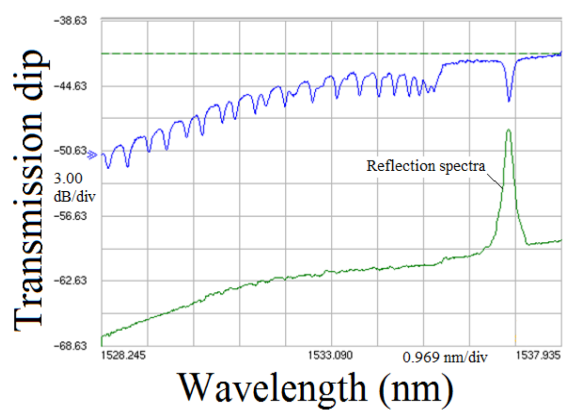

(b)

Figure 1.5: (a) Schematic of a titled FBG (b) Representative spectrum of a tilted FGB written by phase mask technique using 255 nm UV beam, as presented in chapter 4

The transmitted spectra of such gratings exhibit attenuation band related to the coupling with the counter propagating core mode and cladding modes [87-90]. The resonance wavelengths depend on the effective refractive indices of core and cladding modes and on the grating pitch. The dips in the transmission spectra, related to the coupling of discrete bounded cladding modes, are achieved for wavelengths shorter than the Bragg resonance wavelength. In tilted (blazed) gratings, not only different wavelengths emerge at different angles, but different modes of the same wavelength also emerge at slightly different angles due to their different propagation constants [14]. The reflectivity in main mode decreases with increase in tilt angle due to decrease in coupling coefficient [88]. Important properties of blazed gratings are their stability and low intrinsic temperature sensitivity [91]. Tilt grating are used to flatten the gain spectrum of erbium-doped fiber amplifiers. Different grating periods are used for mode conversion at different wavelengths. Hill *et al.* demonstrated efficient mode conversion between forward propagation LP_{01} and LP_{11} modes [92].

1.7.2 Chirped fiber Bragg grating

Gratings that have a non-uniform period along their length are known as chirped. The chirp in the gratings may take many different forms.Fig.1.6a shows the spectrum of typical chirp FBGs having different chirp [14].The period may vary symmetrically, either increasing or decreasing in period around a pitch in the middle of a grating. The chirp may be linear, i.e., the period varies linearly with length of the grating [93], may be quadratic [94], or may even have jumps in the period [95]. A grating could also have a period that varies randomly along its length. Chirp may be imparted in several ways: by exposure to UV beams of non-uniform intensity of the fringe pattern, varying the refractive index along the length of a uniform period grating [96], altering the coupling constant $k_{ac}$of the grating as a function of position [97], incorporating a chirp in the inscribed grating [98], fabricating gratings in a tapered fiber [99], applying of non-uniform strain [100]. In a linearly chirped grating, the resonant frequency is a linear function of the axial position along the grating so that different frequencies, present in the pulse, are reflected at different points and, thus, acquire different delay times. Chirped gratings are used as dispersion compensators [101-103], sensing [104-105], ASE suppression [106], amplifier gain flattening [107], and band-blocking/ band-pass filters [108].

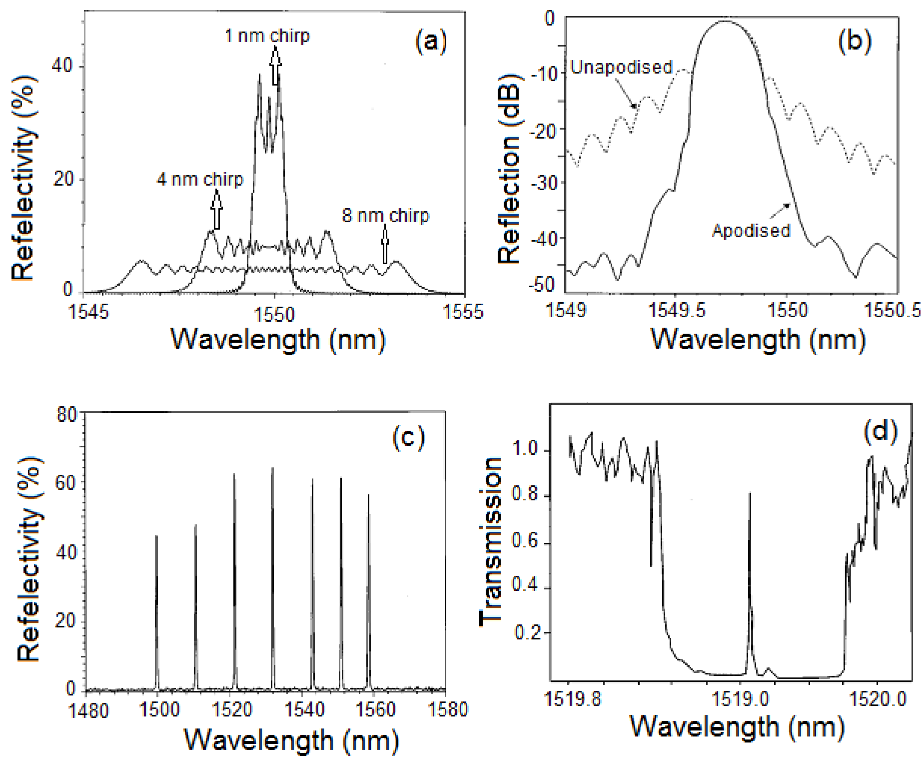

Figure 1.6: Representative spectrum of (a) chirp FGB (b) apodised FBG (c) superstructure multiple FBG (d) phase shifted FBG [14]

1.7.3 Apodised fiber Bragg grating

The reflection spectrum of a finite-length Bragg grating with uniform modulation is accompanied by a series of side lobes [109-112]. High rejection of the non- resonant light in typical systems requires suppression of side lobe reflection.Fig.1.6b shows the reflection spectrum of a typical apodised FBG profile in compared to un-apodised FBG spectrum [14]. Various apodisation techniques have been used to suppress side lobes. Amplitude shading of the intensity profile of the interference pattern helps reducing the side lobes of the spectrum. The various techniques include stamping of short overlapping gratings to build a composite spectrum. Mechanical techniques rely on physically blurring out the fringes in a controlled manner. Apodisation of Bragg gratings allow closer positioning of optical channels in wavelength division multiplexed (WDM) systems.

1.7.4 Superimposed and superstructure multiple Bragg gratings

The inscription of several Bragg gratings at the same location on an optical fiber performs a comb function. However, each time a new grating is formed, the reflectivity of the existing gratings gets reduced [113].Fig. 1.6c shows the spectrum of thesuperstructure Bragg grating, fabricated with a modulated exposure over the length of the gratings by Eggleton *et al.* [14, 114] by the translation of the UV writing beam along a fiber and phase-mask assembly while the intensity of the beam was modulated. This type of grating structure is suited for multiplexing and de-multiplexing of signals.

1.7.5 Phase-shifted Bragg gratings

The phase-shifted Bragg gratings could be designed as a narrow-band transmission filter. The technique consists of the introduction of phase shift across the fiber grating whose location and magnitude can be adjusted to design a specific transmission spectrum. Fig. 1.6d shows the spectrum of typical phase-shifted FBG [14].The techniques include using phase masks, in which phase-shift regions have been written into the mask design [115], post fabrication processing by exposure of the grating region to pulses of UV laser radiation [116], using localized heat treatment [117]. Such processing produces two gratings out of phase with each other. Multiple phase shifts can be introduced to produce devices such as comb filters. They can also be used to obtain single-mode operation of DFB fiber lasers.

1.8 Grating types

The FBG are classified into four distinct growth regimes: type I, IIA (or type In), II and type IA on the basis of intensity of the incidence beam and accumulated UV fluence. Type I FBGs are formed in most photosensitive fibers exposed to continuous wave (CW) or relatively low pulse energy UV radiation. In some fiber types, prolonged exposure of UV fringes can result in partial or complete grating erasure of type I FBGs, followed by a new spectral formation known as a type IIA FBG [118]. In this regime, the Bragg wavelength undergoes blue shift. The induced average index decreases. Type IA FBGs are similar to type IIA in terms of formation except, during the prolonged exposure after the initial grating erasure; the Bragg wavelength undergoes red shift. Type II FBGs are formed when single high-energy pulse causes physical damage to the glass in the core of the exposed fiber on the side of the writing beams [119-120]. The sudden growth of the refractive index is accompanied by a large short-wavelength loss due to the coupling of the guided mode to the radiation field [14]. Type II Bragg gratings have a very high reflectivity and large bandwidth. The gratings generally tend to have an irregular reflection spectrum due to "hot spots" in the laser beam profile. The origin of the process is not fully understood. Russell *et al.* [121] proposed that the process is initiated by high single-photon absorption, exciting electrons into the conduction band of silica, where they seed the formation of free electron plasma. This would then produce an abrupt surge in UV absorption, and permanent damage in the glass. In addition, type II gratings transmit wavelengths longer than the Bragg center wavelengths but strongly couple shorter wavelengths into the cladding, permitting the gratings to act as effective wavelength selective taps. Type IIA and type II FBGs have high sustainability of temperature.

1.9 Laser sources for Bragg grating fabrication

The UV laser sources, both CW and pulsed, have been used for writing holographic Bragg gratings [16-17]. The first source used in FBG fabrication was excimer laser pumped frequency doubled dye laser operating in 240 nm window [122]. The low repetition rate and low coherence sources used in FBG fabrication include excimer lasers [KrF (248nm), ArF (193nm)] [42, 70] and femtosecond UV radiation at 264 (267) nm [22, 52]. Due to high pulse energy of excimer laser sources, single pulse FBG writing in fiber draw tower has also been possible [119]. However, the pulse to pulse transverse beam variation affects single pulse writing of gratings. The hot spots and non-uniformity in the beam profile causes multiple peaks and chirp in the grating spectrum. Low coherence length affects fabrication efficiency in interferometric technique of FBG writing. The CW and high coherence sources used include Argon ion laser (257, 244nm; intra cavity frequency doubled in KFD/BBO) [16, 123], 262 nm QS frequency quadrupled Nd^{3+}: YLF laser [124], line narrowed frequency doubled pumped dye laser [122], Argon ion laser (302 nm) [16], Krypton ion laser (323.5 nm, frequency doubled in BBO) [16]. These lasers have been successful for inducing large index changes though having the disadvantage of lower peak power densities. In the past, only a few reports appeared on utilization of high repetition rate (~ kHz) UV sources for writing FBGs [125-128]. These are the second harmonic of copper vapour laser (CVL) based sources. Since the present thesis is based on FBG fabrication by CVL source, the energy level and technological aspects of CVL are presented, briefly, in the next section. The detailed CVL and its second harmonic beam characteristics are presented and discussed in the next chapter.

1.9.1 Copper vapour laser (CVL)

The high repetition rate (5-10 kHz) UV pulses at 255 nm obtained from second harmonic generation (SHG) of copper vapor laser has emerged as a fast writing source of Bragg gratings, typically in few minutes [125-128]. The copper vapor laser (CVL) is a high repetition rate (5-10 KHz) high gain (~ 10^4), high average power self- terminating pulsed laser with three laser levels [129-133]. Fig. 1.7a shows the energy levels of copper involved in lasing action. The upper laser levels are at 3.79 eV ($4p^2\ P_{1/2}$) and 3.82 eV ($4p^2\ P_{3/2}$) and lower laser levels (metastable) are at 1.39 eV ($4s^2\ D_{5/2}$) and 1.64 eV ($4s^2\ D_{3/2}$) from the ground state respectively [129].The gain competition restricts oscillation to 510.6 nm ($4p^2\ P_{3/2} \rightarrow 4s^2\ D_{5/3}$) and 578.2 nm ($4p^2\ P_{1/2} \rightarrow 4s^2\ D_{5/2}$). The gain duration (inversion) is about 50-60 ns [129-130].The repetition rate is limited by de-excitation of lower laser level ($D_{3/2,5/2}$) life time (~ 180 μsec) [131-133].

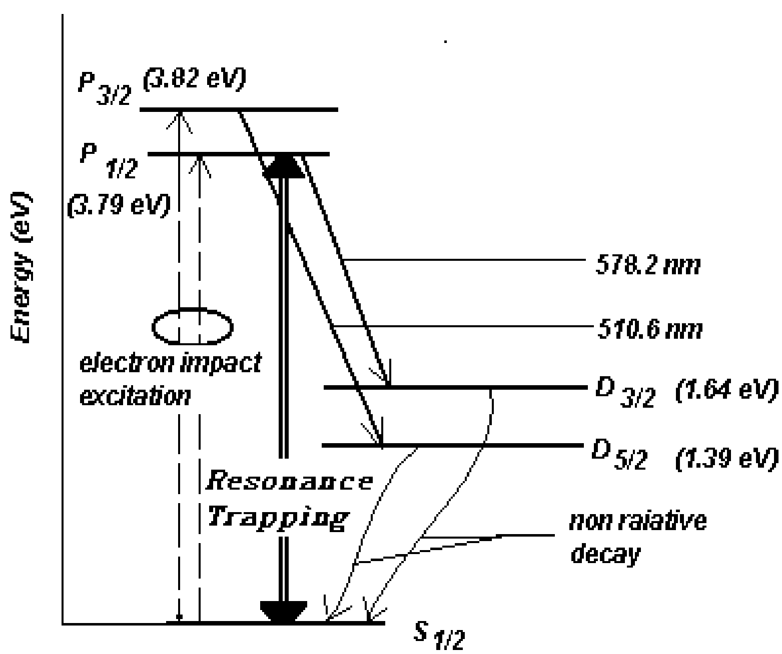

(a)

Figure 1.7: (a) Energy levels of copper involved in lasing action

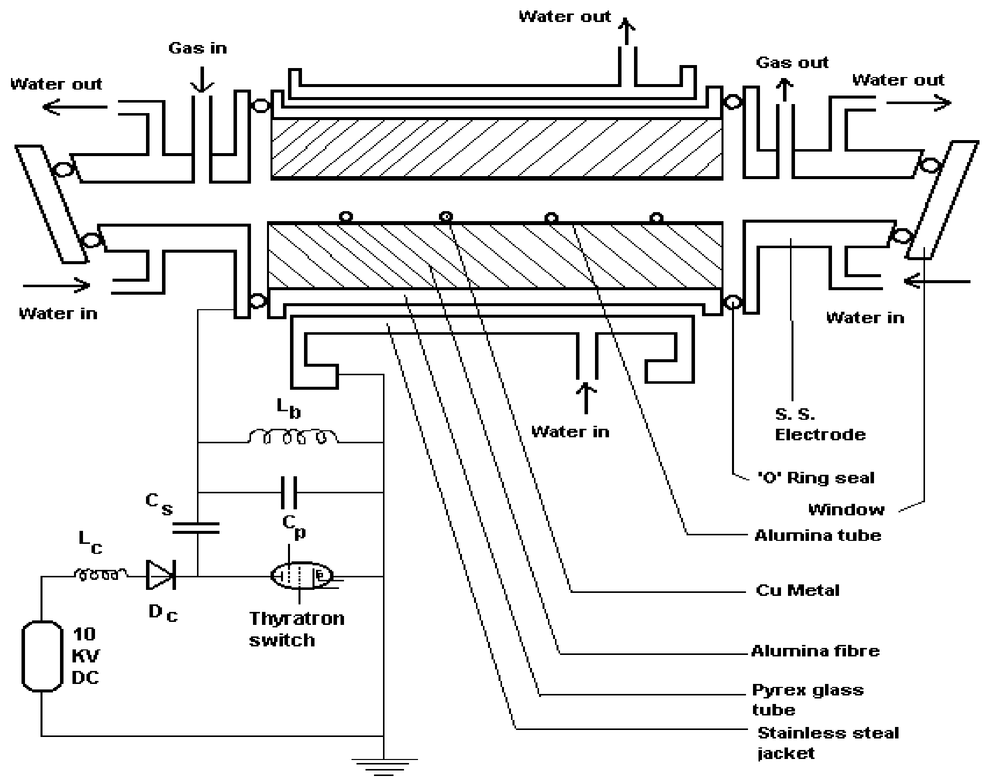

(b)

Figure 1.7: (b) Schematic of CVL assembly with excitation circuit

Fig.1.7b shows the schematic of CVL assembly. The copper vapor laser is a self- discharge heated system in which high repetition rate and high voltage discharge pulse itself heats and excites the copper atoms from ground state ($S_{1/2}$) to upper laser levels ($P_{3/2,\ 5/2}$) .

A medium scale CVL with discharge tube of diameter 28 mm and length of 150 cm was assembled in house to carry out the thesis work. The laser consisted of an alumina tube wrapped with insulating alumina fiber mat and placed co-axially in the glass jacket [133]. The thermal insulation confines the heat in the tube to maintain the operating temperature (~ 1500^0 C). Water cooled doubled wall jacket, confining the glass discharge tube, was used to remove to excess heat flowing out of the glass surface. The ends of glass jacket were sealed by water cooled stainless steel electrodes. The water jacket also provides the coaxial current return path needed to minimize the discharge circuit inductance for faster rise time of current pulse. The discharge energy is supplied through by a high voltage pulser (~ 20 to 25 kV) with sharp rise time (~ 60 ns), heating the laser tube as well as to provide the optimum electron temperature required for efficient excitation. Neon as buffer gas is used to help in initiating the discharge. Water as a coolant is circulated to maintain thermal equilibrium in the discharge tube. A high voltage switch in the modulator circuit generates fast rise time voltage pulse. A hydrogen-filled gas discharge device, namely a thyratron, is used for switching purpose.

The unstable and filtering resonators are used to control CVL beam quality as described in chapter 2. The frequency conversion was carried our using a nonlinear BBO crystal. The UV beam (255 nm) quality is controlled by fundamental CVL parameters which in turn depend on resonator configuration. The spatial coherence and pointing stability of the FBG writing beam is crucial in FBG fabrication. The detailed discussion about 255 nm UV beams of different spatial characteristics generated from SH of CVL radiation (510 nm) is presented in the next chapter. The effect of beam pointing stability on stability of fringes of different interferometers, used in FBG writing, has been not been adequately addressed. The effect of beam spatial characteristics on contrast and stability of fringes formed by different FBG writing interferometers is discussed in chapter 3. Using second harmonic of CVL beams of different characteristics, the experiment and analysis on FBG fabrication by phase mask technique is presented in chapter 4 and 5 and that by biprism interferometer is presented in chapter 6. The temperature sensitivity and stability of FBGs written by high repetition rate and low pulse energy 255 nm UV beam is discussed in chapter 7.

1.10 Current status of FBG technology and applications

The current trends include writing of FBGs in polymer fibers [134], microstructure optical fibers (MOFs) [135-137] and photonic crystal fibers (PCF) [138]. Fiber Bragg Gratings (FBGs) writing in pure-silica MOF was reported by Groothoff *et al.* [137] using 193 nm UV beam. Eggleton *et al.* [135] photo-write FBGs and LPGs in Ge-doped air-silica micro-structured optical photosensitive fibers using a phase mask setup, with a frequency-doubled excimer pumped dye laser. Tilted Fiber Bragg Gratings photo written in a micro-structured optical fiber for refractive index measurement [136]. Canning *et al.* [138] wrote gratings in Er^{3+}-doped alumino-silicate core photonic crystal fiber.

The sensitiveness to external perturbations is exploited for various applications in the field of fiber optic sensors and tuning of fiber lasers. High temperature sustainable FBGs have been achieved by various methods such as type IIA FBG inscription [139] and inscription of Sapphire fiber Bragg grating using femtosecond radiation [140], FBG inscription in nitrogen doped silica fiber [141], chemical composition [142] and regenerative gratings [143-145]. Regenerated gratings were observed to survive to temperature cycles reaching extremes above 1000 °C [144]. The femtosecond (fs) laser technology is exploited to write FBGs in optical fibers without the requirement of the material photosensitivity [145]. The regenerative gratings possesses features of good spectral shape of a Type I grating with a Type II like temperature stability. Regenerative gratings are obtained by annealing the initially type I gratings written in non-hydrogen loaded photosensitive fibers at defined high temperatures [144]. The processes responsible for the regeneration effect are not yet fully understood. The sapphire FBG can work up to 1700 ^{0}C [146]. The pressure and temperature sensitivities of a fibre Bragg grating (FBG) can be increased by as much as 30 and 8 times, respectively, by coating the FBG with a polymer [134]. A single FBG can be used for simultaneous measurement of pressure and temperature with good sensitivities [147].

The application of FBG for different purposes has broadened considerably. FBGs have found application in medicine [134, 148] and gamma ray dosimetry [149]. Bragg gratings (FBGs) are suitable for the measurement of high dose γ-radiation levels above 10^4–10^5 Gy. The measured wavelength shift was fairly independent of the radiation dose rate [149]. FBGs are increasingly being used as refractive index sensors based on itching the cladding [150]. Gas sensing is also a potential application by coating the FBG with a gas absorbing medium. FBG quasi-distributed sensors have already found extensive application in civil engineering, automotive and aerospace for structural health monitoring [151-152]. The WDM interrogation method allows for multiplexing single element FBG sensors in arrays within a single fiber to form 1-D multipoint quasi-distributed sensing systems.

Chapter 2

Studies on frequency converted copper vapor laser UV (255 nm) radiation

2.0 Introduction

The high repetition rate (5-10 kHz) copper vapor lasers (CVL) produce radiation at 510 nm (green) and 578 nm (yellow) with larger fraction of power in green beam. The non-linear, second harmonic and sum frequency conversion of these visible radiations, generate ultraviolet (UV) radiations at wavelength of 255 nm, 271 nm, and 289 nm. The FBGs have been written by 255 nm and 289 nm UV beams [125–128]. However, the fabrication efficiency is higher for 255 nm UV beam as the wavelength lies closer to 240 nm absorption band of germanium doped silica fibers. Hence, the frequency conversion studies for present thesis will be limited to 510 nm CVL radiation. The attained FBG parameters such as reflectivity and bandwidth are crucially linked to writing UV beam coherence, pointing stability and fluence [16, 69-70]. In turn, the second harmonic beam characteristics such as power, coherence, beam profiles and pointing stability are controlled by fundamental beam parameters [153-156]. The present thesis chapter focuses on a comprehensive study on the second harmonic UV (255 nm) beam characteristics for different fundamental CVL (510 nm) beams. This includes the spatial, temporal and power characteristics of both the beams. The diagnostic techniques for measuring the beam parameters, including in-house developed reversal shear interferometer, are concisely presented.

2.1 Visible/UV laser beam diagnostic techniques

2.1.1 Cylindrical lens based reversal shear interferometer for spatial coherence measurement

In the past, several techniques such as Young's double slit/pinhole [157-158], Fresnel biprism [159] and double-grating shearing interferometers [160] have been used to measure the laser beam spatial coherence. However these techniques require a collection of a large number of data points and hence an extensive data analysis procedure and time to correctly map the spatial coherence of laser beam. In contrast, the self-referencing reversal shear interferometer is a very good design to quickly measure the spatial coherence, in a single shot [161-162]. However, these wavefront reversing interferometers based either on roof prisms 161-162] or cemented cube beam splitters or wedges [163-165] employ a large number of optical components. This is particularly serious for deep UV beams for their high absorption in optics and consequently the distortion of measuring wavefront itself. We proposed a cylindrical-lens-based reversal shear interferometer [165] which employed only four optical components namely a wedge, a cylindrical lens and two reflecting plane mirrors, as a modified version of Michelson interferometer. The proposed interferometer was developed in-house and used to measure spatial coherence of UV/Visible radiations [165].

The schematic of the developed interferometer is shown in fig. 2.1a. It consists of a ghost less wedge beam splitter W, a cylindrical lens L (focal length ~ 30 cm) and two plane mirrors M_1 and M_2 (reflectivity = 100 %), mounted in tilt mounts for ease of alignment. The wavefront is reversed in one of interferometer's arm by the retro-reflection by the plane mirror located at the focal plane of a cylindrical lens. The mirrors M_1 and M_2 are placed on precision linear stages. This is for positioning mirror M_1 precisely at the focal plane of cylindrical lens in retro-reflecting mode and adjusting the length of another arm by translating M_2 to keep both the interferometer's arms of almost equal length.

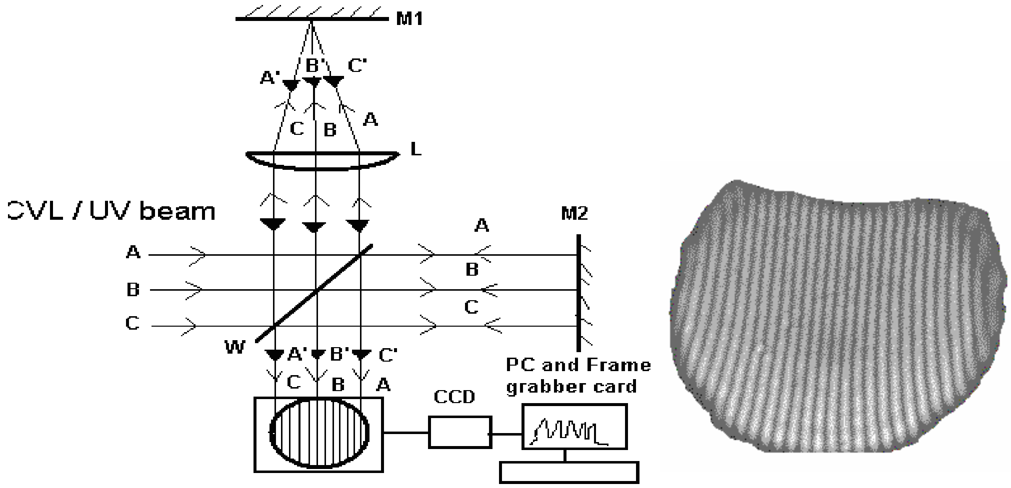

(a) (b)

Figure 2.1: (a) Schematic of wavefront reversal shear interferometer (b) A typical reversal shear interferogram of highly spatially coherent CVL beam

To avoid the multiple transmitted beams after the beam splitter, a ghost less-type wedge beam splitter (W) is used in which the reflected beam inside the wedge suffers total internal reflection and allows only one beam in the forward direction.The wedge angle (α) for ghost less operation, for the incident beam at an angle of incidence i_1, is given by [165]

$$\alpha \geq [\sin^{-1}(1/n) - \sin^{-1}\{(\sin i)/n\}] / 2 \tag{2.1}$$

where n is the refractive index of the wedge material. For fused silica (n=1.5084 at λ = 248 nm) and i = 45^0, the wedge angle is $\alpha \sim 6.78^0$ to allow only one beam in the forward direction. In the present set up, the wedge of angle of 7.5^0 was chosen. In this interferometer design, the wavefront reversal can be obtained along any axis perpendicular to the direction of beam propagation simply by rotating the cylindrical lens. This means that the original wavefront can interfere with its own rotated (by a chosen angle) replica, ideal for 2-D or 3-D evaluation of the wavefront. Thus in addition to for circularly symmetric laser beam such as from CVL, this interferometer can also be used for spatial coherence evaluation of rectangular beams from excimer and solid state slab lasers, where the coherence characteristics along the perpendicular directions are widely different. This design can also be used for the temporal coherence measurement. The cylindrical lens also reduces the focal point density to prevent the optical damage of mirror. The operating principle of the interferometer is as follows. The amplitude of incident wavefront ABC splits into two parts at the first surface of the wedge W. The reflected beam travels towards the cylindrical lens L, is line focused at the plane mirror M_1, and is reflected back to the cylindrical lens. This wavefront is reversed ($C^I B^I A^I$) as it is reflected from mirror M_1.This reversed beam is again collimated by lens Land proceeds to the wedge for further transmission. The beam directly transmitted through the wedge proceed to mirror M_2, is reflected by it, then proceeds to wedge to be partially reflected and combined with the wavefront-reversed beam coming from another arm. Both the overlapping beams are of the same size as could be understood from ray tracing in the wedge. The fringe intensity distribution in a fringe plane is given as,

$$I = \left| A(x,y) \exp(i\mathbf{k_1}.\mathbf{r}) + A(-x,y) \exp(i\mathbf{k_2}.\mathbf{r}) \right|^2 \tag{2.2}$$

where A (x,y) and A (-x,y) are amplitude distributions and $k_1 = k_2$ (= $2\pi/\lambda$) magnitude of propagation constant. Assume that the shear is such that the fringes are formed along x-axis. The eqn (2.2) can be expressed as,

$$I = I_0 [1 + \gamma (x,\Delta\phi) \cos (2kx \sin\theta)] \tag{2.3}$$

where 2θ is angle of intersection between two beams in the fringe plane, $\Delta\phi$ is beam divergence and $\gamma (x,\Delta\phi)$ is degree of coherence. The value of $I_0 = I_1 + I_2$, where I_1 and I_2 are intensities in each arm with $I_1 \approx I_2$ in case of AR coated cylindrical lens. Assuming equal intensity distribution in all the spatial frequency components, $\gamma(x,\Delta\phi) \sim \mathrm{sinc}(k\, x\, \Delta\phi \cos\theta)$. Since θ is very small, $\cos\theta \sim 1$. The fringe contrast will be zero at a distance, x [= $(x_2-x_1)/2$]$\approx\lambda/(2\Delta\phi)$, from the center of fringe system. Thus the coherence width, $(x_2-x_1) \approx\lambda/\Delta\phi$.

The data recording for estimation of spatial coherence is as follows. First the alignment of the interferometer is carried out. For this, a cross wire is inserted in the incident beam with its lines in the horizontal and vertical directions and its center coinciding with the center of the incident beam. The vertical line of the cross wire serves as the reference axis across which the wavefront is to be reversed. The vertical line of the cross wire of the two interfering arm beam was matched by the suitably tilting the axis of the mounts (cylindrical lens and plane mirror). In this aligned condition, the output shear interferogram of the input CVL beam is recorded by imaging it on a visible CCD camera. The recorded interference pattern was analyzed by image-processing software. For recording UV fringes, the fringe pattern was first put on UV fluorescent LUMI glass (M/S Sumita Glasses, Japan) slab of thickness 500 μm. Then the visible fluorescence (green) was recorded with visible range CCD. Fig 2.1b is a typical reversible shear interferogram of a highly spatially coherent visible (CVL) beam. The fringe visibility is calculated by the relation

$$\langle \nu(x) \rangle = [\langle I_{max} \rangle - \langle I_{min} \rangle] / [\langle I_{max} \rangle + \langle I_{min} \rangle] \qquad (2.4)$$

where $\langle I_{max} \rangle$ and $\langle I_{min} \rangle$ are intensity of fringe maxima and minima respectively. The degree of coherence is estimated from the plot of fringe visibility vs. distance.

2.1.2 Measurement of divergence and pointing stability

Fig. 2.2a shows the schematic of experimental setup for measuring pulse to pulse divergence, pointing and intensity stabilities of a high repetition rate laser. For the CVL studies, a part of green beam (4%) was selected by a wedge. This beam was focused by lens L_1 (f_1= 150 cm). The amplified spontaneous emission (ASE) was removed by placing an aperture, A_1, at the focal plane of lens L_1. This ASE filtered far field spot is imaged (with suitable magnification, M) by another lens L_2 (f=25 cm) on to CCD. The ND filters were used to attenuate the beam intensity below saturation of CCD. The beam divergence was estimated from width of far-field spot. The pointing stability of different pulses of the laser beam is determined by the displacement (wandering) of the far field intensity peak from their modal position (Fig. 2.2b). The pulse to pulse measurement was only possible by employing a gated CCD camera with selectable time gatesfrom 5μs to 65 s with a minimal time interval of 1μs. Such a camera (pixelfly PCO, AG), with a PCI bus based Frame Grabber card, was employed for recording the focal spot intensity distribution.

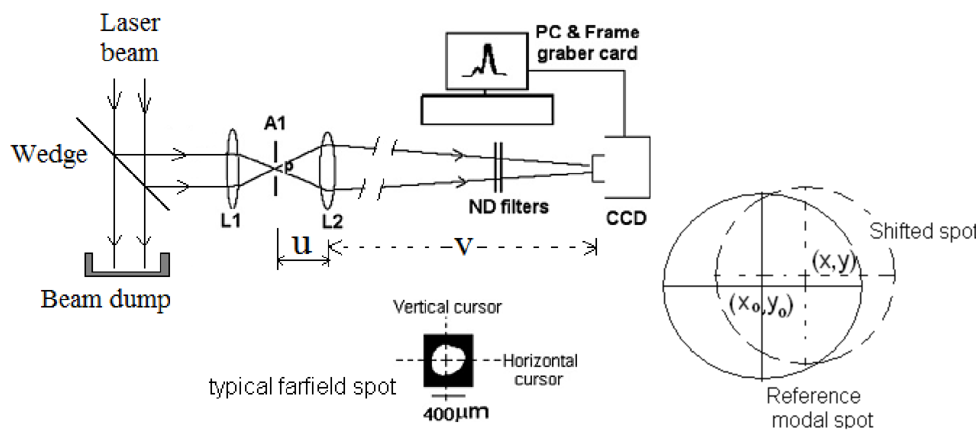

(a) (b)

Figure 2.2: (a) Schematic of measuring pulse to pulse divergence, pointing and intensity stabilities (b) A drifted far field spot from reference spot with centre (x_0,y_0)

In these experiments, the CCD acquiring time was set to 174μs, little less than the pulse separation of 179μs at 5.6 kHz laser repetition rate. This ensured single pulse recording each time. The subsequent images (pulses) were acquired after time interval of about 1sec. A typical CVL far field spot is shown in Fig. 2.2a. An orthogonal pair of cursors is centered on this spot. The placed cursors provide the reference position to save line profile of the subsequently acquired images, in a dynamically allocated memory of the PC. Each stored line (both horizontal and vertical) in the composite picture is acquired at preset time interval [166-167]. At the end of acquiring preset number of images, the individual line profiles stored in the allocated memory is saved as an image, which is named as a composite (stacked) picture [166-167]. Since each image line is acquired after pre-decided time interval, therefore, the time information (from top to bottom) is inherently associated in the composite picture itself. The horizontal and vertical pixel position of the intensity peak for each pulse is determined by the software which provides information about drifted position of the peak. This reveals the stability in the position of the far-field intensity distribution, divergence and the relative magnitude of the intensity peak. The pointing stability was estimated from the spatial displacement of the intensity peak on either side of the judiciously chosen mid value. The angular pointing angle drift $\delta\theta_x$ (along x), $\delta\theta_y$ (along y) from mean position were estimated as

$$\delta\theta_x = \Delta x / Mf_l \quad ; \quad \delta\theta_y = \Delta y / Mf_l \tag{2.5}$$

Where Δx (= $x-x_0$) and Δy (= $y-y_0$) are components of focal spot displacement along X and Y direction respectively. The beam divergence fluctuation of different pulses $\Delta\phi_x$ and $\Delta\phi_y$ were estimated as [167],

$$\delta(\Delta\phi_x)_n = \Delta\phi_{xn} - \langle\Delta\phi_x\rangle \quad ; \quad \delta(\Delta\phi_y)_n = \Delta\phi_{yn} - \langle\Delta\phi_y\rangle \tag{2.6}$$

where $\Delta\phi_{xn} = 2w_{xn} / Mf_l$, $\Delta\phi_{yn} = 2w_{yn} / Mf_l$, $\langle\Delta\phi_x\rangle = \langle 2w_x\rangle / Mf_l$ and $\langle\Delta\phi_y\rangle = \langle 2w_y\rangle / Mf_l$. The term w_{xn} and w_{yn} are beam diameter of n^{th} pulse along X and Y axis respectively. The fractional peak intensity fluctuation is given as, $\delta I_n/\langle I\rangle = (I_n - \langle I\rangle)/\langle I\rangle$, where I_n is peak intensity of n^{th} pulse and $\langle I\rangle$ is the average intensity.

2.1.3 Line-width measurement

The laser line width could be estimated from conventional Fabry–Perot etalon-based measurements. In the present study, the real-time spectral line-width of the CVL radiation was recorded by linewidth measuring module of the wavelength meter based on Fizeau interferometers. The CVL green line (separated from yellow line by dichroic beam splitter) was sampled to the wavelength meter (high finesse: Angstrom WS-7). In the wavemeter, the interference pattern produced by the Fizeau interferometer is recorded by two photodiodes arrays and transferred to the PC in real time. The laser line-width is calculated from the fringe contrast. These results are displayed on the monitor of the PC. The maximum upper limit of the line-width that could be measured in the wavelength meter was 10 GHz with an accuracy of about 100 MHz.

2.1.4 Measuring optical power

The average power of the CVL/UV laser beam was measured by a pyro-electric detector based laser power meter. The radiation incident on a conical shaped detector raises its temperature which is measured by thermocouples or temperature dependent resisters attached to the body of the cone. The difference in the temperature with respect to fixed reference temperature gives rise to an e.m.f. proportional to the incident power. Average output power in this study was measured by a commercially available power meter (Gentech, PS-310 WB).

2.1.5 Recording Laser beam temporal profile

Temporal variation of the intensity of the fundamental and the second harmonic (SH) pulses were recorded using bi-planer photodiodes (Hamamatsu, R1193U-02, rise time ~ 270 ps) and a fast oscilloscope (500 MHz, Tekronix TDS-540C). The bi-planar photodiode is a vacuum photo tube consisting of a photo-cathode and a mesh type anode, aligned parallel to each other. The photo induced electrons generated on the photo-cathode are collected at the anode. The bi-planar configuration generates high linear output current with sub ns response time.

2.2 CVL optical resonators

2.2.1 Unstable resonator

In high gain, large aperture (high Fresnel number) lasers such as CVL, the unstable resonators (UR) are most commonly used to obtain good spatial coherence (low beam divergence) while utilizing the large gain volume [153-155, 168]. Fig. 2.3 shows schematic of CVL with con-focal positive branch unstable resonator (PBUR), provided collimated output laser beam.

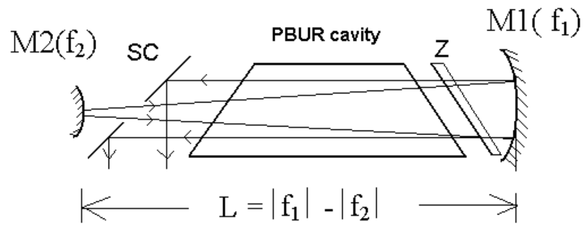

Figure 2.3: CVL in unstable resonator (PBUR) configuration

The resonator consists of a concave mirror M_1 of focal length f_1 and a convex mirror M_2 of focal length f_2, incorporating the CVL discharge tube. The feedback is given by mirror M_2. The beam is plane polarized by an intra-cavity polarizer. The cavity length (L) is, $L = |f_1| - |f_2|$ and resonator magnification (M) is, $M = |f_1| / |f_2|$. The output is taken through scraper mirror. It is well known that in high gain pulsed lasers, increasing the unstable resonator magnification (M) leads to improved beam quality at the cost of reduced laser power due to reduced feedback [153-155]. Hence to compare the effect of unstable resonator magnification on fundamental and second harmonic characteristics and finally on FBG fabrication, two unstable resonators one of low (M=12.5, PBUR1) and another of high (M= 100, PBUR2) magnification (M) were used with CVL. The resonator parameters are, PBUR1 (M = 12.5, F1 = 250 cm, F2 = -20 cm, L = 230 cm) and PBUR2 (M = 100, F1 = 250 cm, F2 = -2.5 cm, L = 247.5 cm). The performance of CVL is studied with these resonators.

2.2.2 Diffraction filtered resonator

The unstable resonators, though worked very well with CVLs, have their own drawbacks especially when applied to frequency conversions. The CVL, being a short inversion time (40-50 ns) self-terminating laser, the resonator mode is not established in the available time. This dictates that the beam divergence varies significantly within a CVL pulse, as our own experiments have confirmed [155]. This means that when such a CVL pulse is focused on a nonlinear crystal (for frequency conversion), the focal spot varies in time. Such a situation compromises both the conversion efficiency as well as beam quality of frequency converted UV output. Both the factors adversely affect the fiber grating writing. The new class of laser cavities, known as filtering resonators [169-171] based on spatial filtering of circulating radiation largely circumvented these issues. In a filtering resonator [170-171], only the spatially filtered central lobe of far-field intensity distribution (Airy's pattern) is allowed to build up as the resonator mode, right from the onset of laser pulse. This dictates that the laser divergence is diffracted limited and constant throughout the pulse, as also demonstrated with CVL [155,170-171]. The extensively utilized filtering resonators are mainly low mode volume self-filtering unstable resonator (SFUR) and large mode volume generalized diffraction filtered resonator (GDFR) [170-171]. In the present thesis, CVL based on GDFR is extensively studied and utilized.

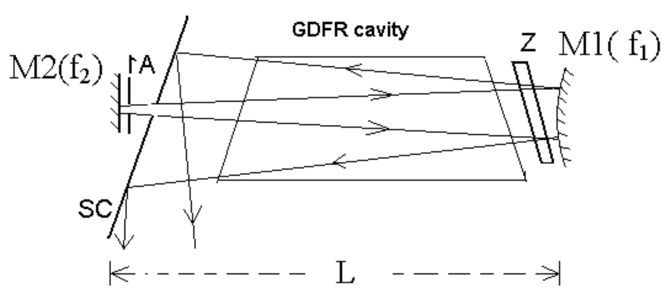

Figure 2.4: CVL in diffraction filtered resonator (GDFR) configuration

Fig. 2.4 shows schematic of a generalized diffraction filtered resonator (GDFR). In the GDFR, M_1 is a convex mirror and $M_2$is a plane mirror. An aperture 'A' (radius = a) was placed in front of M_2. The radiation diffracted by 'A' attains the far field distribution at M_1

after traversing the cavity length (L) provided L >> $\pi a^2/\lambda$ [171]. The central lobe of the Airy's pattern is filtered and allowed to build-up as mode. The CVL gain medium itself acts as the second filtering aperture. The beam expanded by convex mirror again fall on aperture 'A' (as a plane wave over a very small aperture size)) to start another cycle. The round trip magnification, $M_g = 0.61\ \lambda L\ (2 + L/f_1)\ /a^2$ [171]. The laser output from the GDFR resonator CVL is geometrically diverging. The output is taken through scraper mirror. The output laser beam can be collimated by suitable lens. The resonator parameters employed in the study are: GDFR (M = 107, f_1 = -20 cm, $f_2=\infty$, L = 230 cm, diameter of hard aperture, A, at plane mirror = 0.6 mm).

2.3 Results on CVL beam characteristics with different resonator configurations

The homemade laser is based on discharge tube diameter 28 mm and length 1500 mm [172]. In the present study, all the input conditions (input power, repetition rate, buffer gas pressure, etc) as well as mechanical and physical environment for the laser were almost identical for all the sets of optical resonators. The CVL was first optimized with a plane - plane resonator which utilizes maximum gain volume. The output power was optimized at buffer gas (Neon) pressure of ~ 22 mb and at pulse repetition rate of 5.6 kHz. The CVL produced an average optical power 18 W (10 W green and 8 W yellow) at 3.6 kW of electrical input power. The CVL gain pulse (amplified spontaneous emission, ASE) duration was ~ 60 ns at $1/e^2$ points. After optimizing the repetition rate and buffer gas pressure, the plane - plane resonator was replaced by PBUR1, PBUR2 and GDFR successively to study the CVL green (510 nm) beam characteristics after separating yellow (578 nm) by a dichroic mirror. Because of high gain, the unstable and diffraction filtered resonators optical output possesses significant amplified spontaneous emission (ASE) superposed on low divergence laser beam. The ASE in the output beam was externally filtered by an aperture (A1, Fig 2.2 a) of 0.7

mmdiameter, placed at the common focal plane of the telescopic combination of lenses. The results on line-width, spatial coherence, divergence, pointing stability and pulse shape are discussed. The whole study pertains to 510 nm CVL beams only.

(a) Power, pulse shape and line-width

Fig. 2.5 shows the wavemeter line-width trace for CVL 510 nm radiation. The emission line-width of green beam is approximately 4.5 GHz, almost same for all resonators from plane–plane to PBURs/GDFR. This is expected in view of high gain nature of CVL transition. To improve beam quality, the CVL was operated with three resonators namely PBUR1, PBUR2 and GDFR. The ASE was filtered externally. The average powers observed at 510 nm were 7.5 Watt, 6 Watt and 3.5 Watt for resonator configurations of PBUR1, PBUR2 and GDFR respectively. This is to be compared with 10 W power (green) observed from the plane-plane resonator. Fig. 2.14 (a–c) (in section 2.6.2 of this chapter) show the typical temporal pulse profiles of PBUR1, PBUR2 and GDFR CVL beam respectively. Deeply modulated temporal structures are typical of short inversion time, high gain lasers.

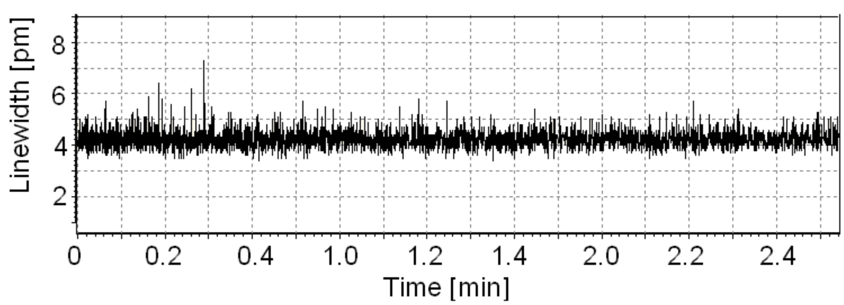

Figure 2.5: Variation of CVL line width in time

(b) Spatial coherence and divergence

Figs. 2.6(a-b), 2.6 (c-d) and 2.6(d-e) show the reversal shear interferogram and intensity profile across a line for PBUR1, PBUR2 and GDFR CVL beams respectively. Fig. 2.7 shows the variation of degree of coherence (fringe visibility) of interferogram across the beam diameter for all three CVL beams. The fringes of appreciable contrast are confined into a small region for low magnification (M=12.5) PBUR1 CVL beam. The fringe contrast decreased with increase in separation between two points on the wavefront. The region of fringes of good contrast increased for higher magnification (M=100) PBUR2 CVL beam. In case of GDFR CVL, the fringes of vey high contrast were observed across whole cross section of the beam, signifying a high degree of spatial coherence across the whole beam cross section. The coherence radius is defined as the radial distance at which the fringe visibility decreases by (1/e) times from that at the centre of interferogram.

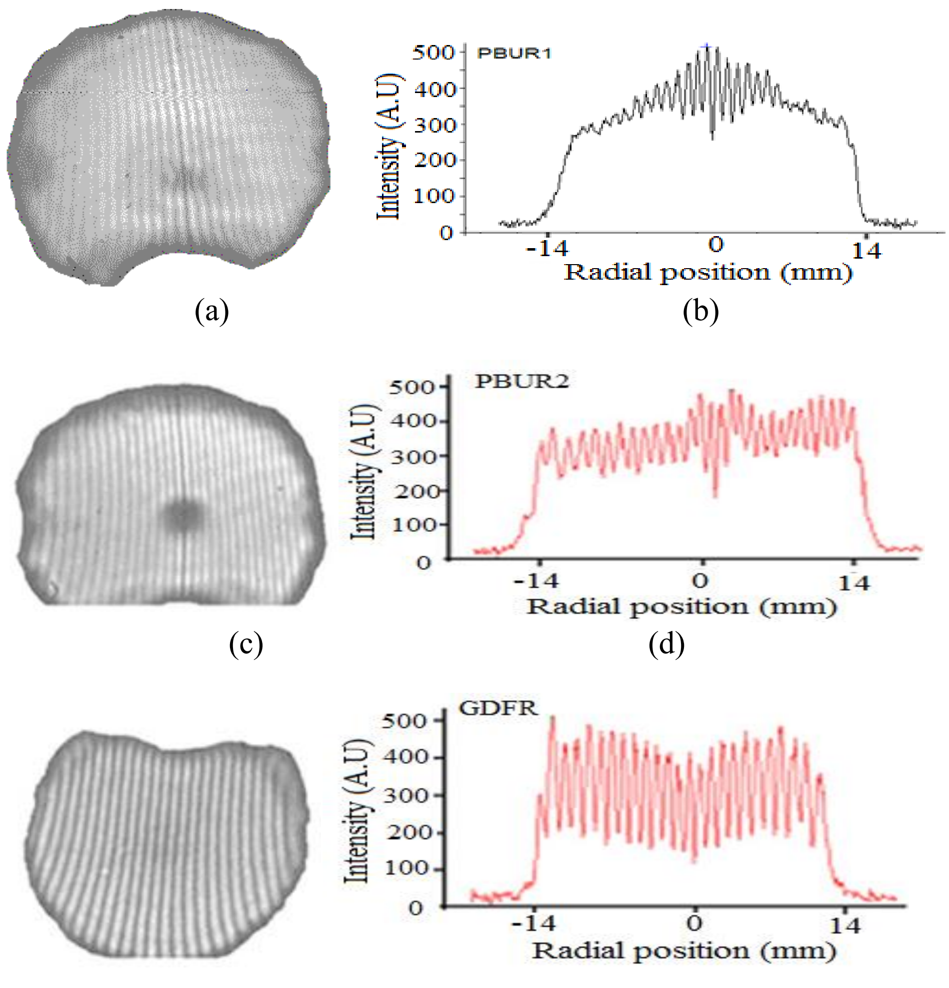

(a) (b)

(c) (d)

(e) (f)

Figure 2.6: Interferogram of (a) PBUR1 (c) PBUR2 (e) GDFR CVL beams; and intensity profile of (b) PBUR1 (d) PBUR2 (f) GDFR corresponding interferogram

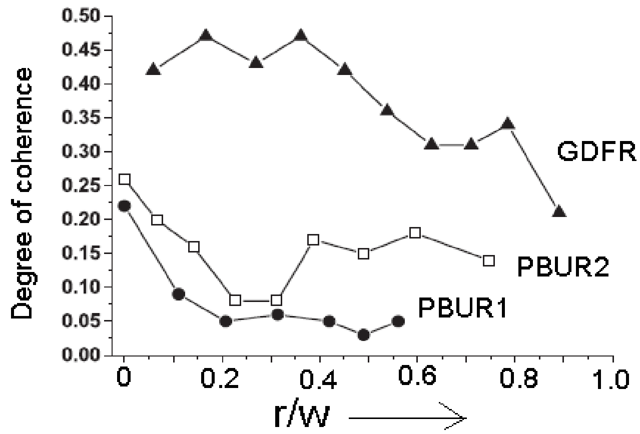

Figure 2.7: Variation of degree of coherence (fringe visibility) along radial distance

The coherence width and degree of coherence of the CVL beam increased with increase in unstable resonator magnification. This established that spatial coherence of CVL beam enhances with increase in UR magnification. However the best coherence was obtained from GDFR, as expected. This was also directly confirmed by measuring divergence of these beams. The average divergence ($1/e^2$ intensity point) measured for PBUR1, PBUR2 and GDFR CVL green beam of about 25 mm diameter (D) were approximately 150 μrad, 110 μrad and 54 μrad respectively. These figures represents 3 DL, 2.2 DL, 1.1 DL beams from PBUR1, PBUR2 and GDFR, where DL is diffraction limited divergence (= 2.44 λ/D, for flat top beam ~ 50 μrad). It is worth mentioning here that though the fringes of high contrast are formed across whole beam diameter for PBUR2 and GDFR CVL, the time average fringe contrast is never unity even at the centre of interferogram. The divergence of CVL decreases with successive round trips within the pulse [153-155]. The experimentally observed single pulse fringe visibility will be weighted average of time resolved divergence angles. The pointing stability of different pulses will also dilute time average fringe visibility. The non-uniform near field distribution, typical of high gain CVL characteristics and the presence of remnant ASE may also dilute the time average fringe contrast.

(d) Pulse to pulse beam pointing, divergence and intensity stabilities

The pulse to pulse far-field beam pointing, divergence and intensity stability were measured for CVL (λ = 510 nm) with PBUR1, PBUR2 and GDFR configurations over the time duration of about 650 s.

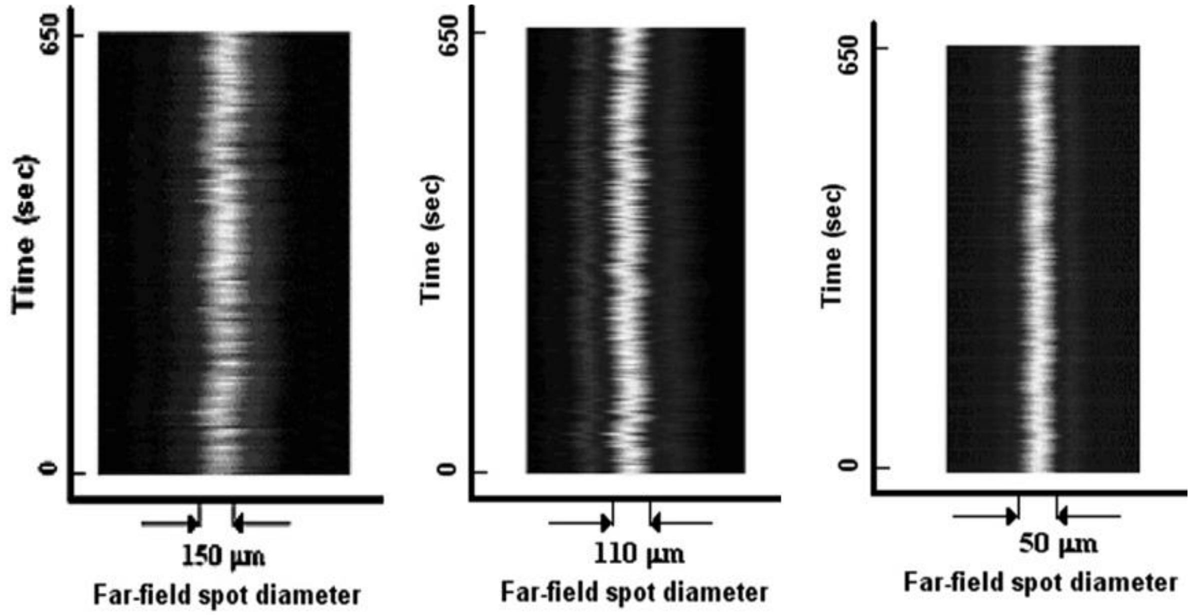

(a) (b) (c)

Figure 2.8: Composite pictures of CVL far-field line images (at cursor position) for 650 s for (a) PBUR1 (b) PBUR2 and (c) GDFR CVL beams

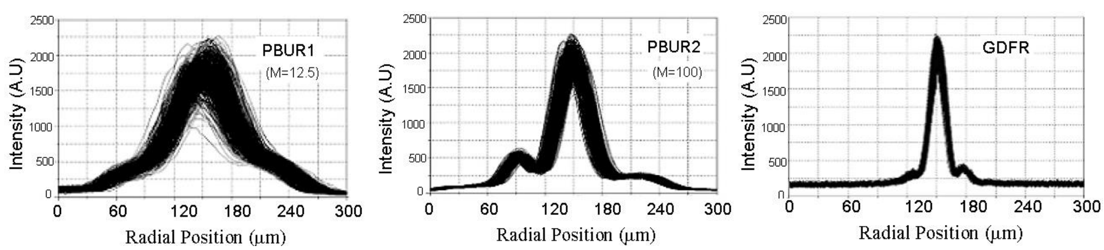

(a) (b) (c)

Figure 2.9: Pulse to pulse far-field intensity profile for (a) PBUR1 (b) PBUR2 and (c) GDFR CVL beams

Fig. 2.8 (a-c) shows the typical composite pictures of CVL far field line images for 650 s. As already mentioned, the gated CCD operated to capture single pulse with pulse to pulse separation was about 1s. Fig. 2.9 (a-c) shows the stacked far field intensity profile (normalized at focal plane of lens L1, f = 100 cm) for same 650 s.

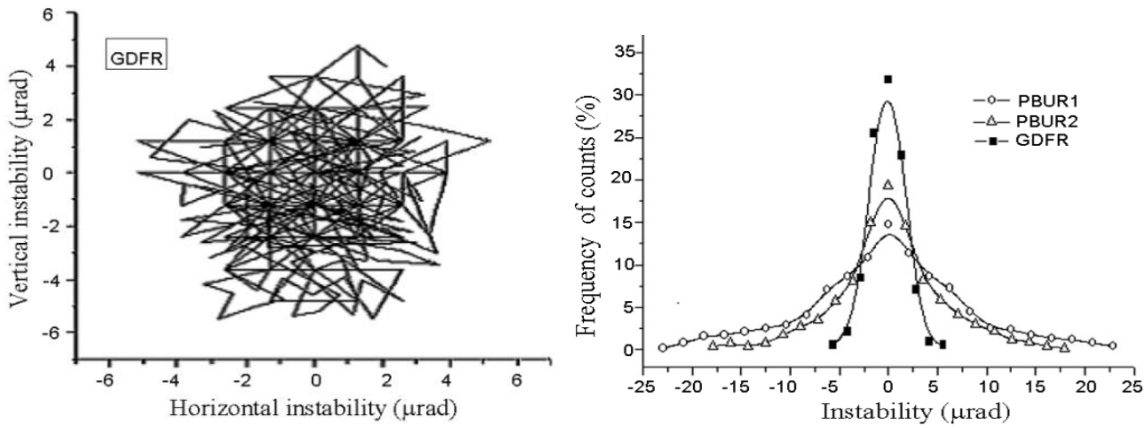

(a) (b)

Figure 2.10: (a) Angular wandering of far field peak intensity position of GDFR beam (b) Probability distribution of beam pointing of three beams

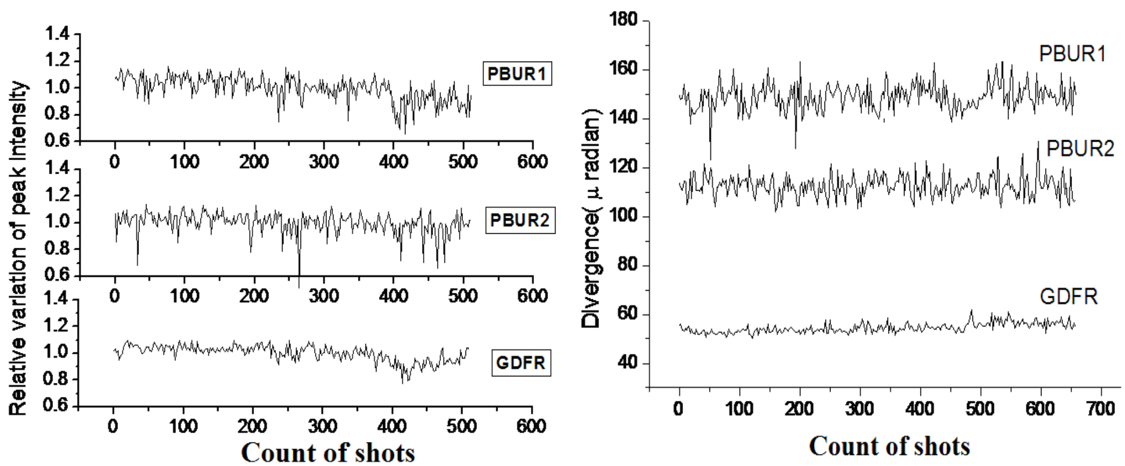

(a) (b)

Figure 2.11: Pulse to pulse CVL (a) far field peak intensity and (b) divergence

The laser beam pointing stability was estimated by mapping pulse to pulse shift in peak of far field distributions. Similarly divergence fluctuation was estimated by pulse to pulse change in $1/e^2$ width of far-field intensity distributions. Fig 2.10 shows typical angular wandering of far field peak of GDFR beam.The estimated maximum pointing instability were approximately ± 22 μrad, ± 11 μrad,± 4 μrad for PBUR1, PBUR2 and GDFR CVL beams respectively (fig.2.10b). Figs. 2.11a and 2.11b show the estimated pulse to pulse variation of peak intensity and divergence about their mean value for three different resonator configurations. These data clearly shows that GDFR resonator out performs PBURs in all the aspect of CVL beam quality fluctuations. The pulse to pulse far-field divergence and peak intensity fluctuations are least for GDFR CVL as compared to PBUR CVLs. The reasons for this excellent performance of GDFR CVL are discussed in the next section.

2.4 Discussion of results on CVL beam parameters

From the results, four mutually related facts have emerged. First, the optical resonator has a definite role to play in influencing beam divergence, spatial coherence and pointing instability. Second, the spatial coherence and pointing stability is the best for GDFR. Third, in the case of PBURs, the spatial coherence and pointing stability was better for higher magnification. Fourth, the improved spatial coherence and pointing stability seems to be linked to decrease in beam divergence. These facts need to be explained. In addition, the different trends in peak intensity variation for different resonators need to be explained.

In copper vapor laser, the laser beam spatial coherence and pointing stability are the cumulative effect of optical resonator, resonator mode evolution, gain medium thermal fluctuation, temperature gradient in optical windows, ambient temperature fluctuations, acoustic noise, mechanical vibrations, air currents, etc [167]. In addition, in the present experiment, the beam stability is studied over10 min encompassing over 10^6 pulses. This necessitates the beam disturbances/wave-front distortions originating in different time slots, to be taken into account. These timeslots are (1) optical resonator build up time (laser pulse width ~ 60 ns), (2) inter-pulse period (laser repetition rate ~ 180 μs), (3) CVL plasma thermal relaxation time (10s of ms), (4) short (10s of seconds) and long term (100s of seconds) thermally driven fluctuations in CVL plasma. Since all the input and environment conditions were identical for all the three sets of optical resonators, the difference in beam parameters could be mainly attributed to how a particular resonator modifies the intra-cavity circulating radiation and its capability to clean out the wave-front distortions accumulated in different time slots as mentioned above. For clarity of discussion, two issues related to optical resonators which affect beam parameters namely, (i) action of optical resonator on initial random amplitude and phase noise (spontaneous emission) in a limited number of transits as in CVL, and (ii) effect of thermally induced wave-front distortions, are discussed separately. Ultimately, the results are combined to draw the common inference.

(i) *Effect of resonator mode build up time* - The CVL being ASE dominated short inversion time high gain laser, the single pulse laser characteristics are controlled by the initial optical noise (ASE) from which the resonator mode build up. This optical noise is highly random in phase and amplitude distribution across the beam. Due to highly random nature, the starting optical noise is also different from pulse to pulse. The extent to which the random phase distribution of the noise pulses affect the single pulse laser divergence and pointing stability, is closely linked to the fact as to how close is a single starting noise pulse reaches the steady state in the available inversion time. The equations 2.7 give the estimate of the resonator mode establishment time T [167, 173-174] for different resonators for the CVL (D = 28 mm, L = 2.3 m) used in present experiment. After time, T, the steady state is reached and the phase and amplitude profile of the radiation field do not change in subsequent transits. The resonator mode establishment time (T) is given as [167],

$$T_{PBUR} = 2L\{1+(\ln M_0)/(\ln M)\}/C \quad \text{where } M_0= D^2/[2.44\lambda(2L-L^2/f_1)$$

$$= 50 \text{ ns (PBUR1) and } 34 \text{ ns (PBUR2)} \tag{2.7a}$$

$$T_{GDFR} = 2L/C = 15 \text{ ns (one round trip time)} \tag{2.7b}$$

where C is velocity of light. Faster resonators build up leads to higher beam quality of the laser output. The beam quality of GDFR CVL is comparatively higher. The observed spatial coherence, divergence and beam pointing stability trends are in tune with resonator build up time. Since the round trip time and resonator build up time are almost same in GDFR, the steady state reached very fast due to intra- cavity spatial filtering of radiation, thus reducing beam divergence. Any single pulse randomness, in starting noise pulses, is washed out well within the inversion time resulting in vastly improved laser beam spatial coherence. The intra pulse and pulse to pulse distortion in wavefront and phase profile and beam tilt (pointing) will be minimized. This resulted in a high quality, single pulses repeatable wavefront with highly stable beam. The higher magnification PBUR2 performing better than lower magnification PBUR1 both in beam divergence and pointing. This is again mainly due to faster mode buildup time and hence better temporal integrity of wavefront in PBUR2 as compared to PBUR1.

(ii) *Effect of thermally induced wave-front distortion*- Highly heated CVL plasma tube is a source of thermally induced optical wave-front distortions. The temperature at the tube center (peak gas temperature) is in range 3000–4000 ^{0}C while the discharge tube wall is around 1500 ^{0}C, a trend almost same over central 90% of the tube length [167]. The radial temperature gradient leads to refractive index [n(r)] which can be expressed in Taylor series as,

$$n(r) = n_0+n_1r+n_2r^2+n_3r^3+\ldots \tag{2.8}$$

where r is the radial coordinate. The terms $n_1$represent wedge type wave-front aberration, n_2-lens type in-homogeneity and coefficients n_3,n_4,.. represent higher order components affecting phase profile. The thermally driven fluctuations in CVL plasma lead to disturbed and fluctuating refractive index distribution [n(r)], thereby leading to wave-front distortions which degrades beam spatial coherence and pointing. The cleaning of distorted wave-front is equivalent to filtering of higher spatial frequency components. From the point of view thermally induced turbulence in the discharge tube, the ultimate figure for spatial coherence and beam pointing of output beam is linked to how effectively an optical resonator cleans the phase distortion introduced by thermal effects. In PBURs, the magnifying action of convex mirror together with apertures offered by the hole in scraper mirror and the laser tube, the circulating radiation is spatially filtered in each round-trip. Since the apertures offered by scraper mirror hole (~ 3 mm) and tube aperture (~ 28 mm) are relatively large, spatial filtering is not very efficient. This is due to the fact that in PBUR the radiation is always in near field where spatial frequency spectrum has poor resolution. However, the larger magnification resonator e.g. PBUR2,is expected to accomplish better spatial cleaning of wavefront which lead to better beam quality. As compared to PBURs, the vastly improved performance of GDFR beam is largely attributed to the excellent round-trip spatial filtering action within the resonator. The intra-cavity beam (diameter, ~ 30 mm) falling on the aperture A (at plane mirror) is about 50 times larger than the aperture. Hence the internal beam is strongly diffracted by the aperture, A. This diffracted radiation reaches into far-field, moving from aperture A to convex mirror, and hence evolves into very well defined spatial frequency spectrum. This spatial frequency spectrum, as it travels back to aperture, A, after expanded by convex mirror, is very efficiently spatially filtered by the limiting aperture of laser tube. Hence in GDFR CVL, the excellent spatial cleaning of circulating radiation in every round-trip, makes sure that the beam disturbances do not build up cumulatively and almost same conditions are maintained in different time intervals. This repetitive cleaning of phase profile leads to much better spatial coherence and beam pointing stability from GDFR as observed.

(iii) *Effect of resonator on variation of single pulse divergence and far-field intensity*- The observed pulse to pulse far-field intensity variation may be attributed to single pulse variation of factors namely, laser peak power, pulse energy, pulse duration and pulse divergence. The single pulse beam divergence, as measured in the present experiments, is in fact an averaged value over variation within a pulse. However, the CVL beam divergence varies within the single pulse [153-155] whose nature is different for different resonators. In laser far-field intensity [proportional to pulse energy/(pulse duration x divergence^2)] estimation, the divergence occurring in denominator as a square term, affect the peak intensity significantly even with a small change. In CVL with an optical resonator, the pulse duration is not likely to change from pulse to pulse. Pulse to pulse energy fluctuations is also not significant in CVL with different resonators. Hence pulse to pulse intensity variation is mainly due to corresponding pulse divergence fluctuations (Fig. 2.11b). The observed increasing sequence of pulse to pulse far field intensity variation from GDFR to PBUR2 to PBUR1 may be explained as follows. In GDFR, excellent single pulse divergence stability is expected as divergence is constant throughout the pulse [155], close to diffraction limit (DL) value. In PBUR2, single pulse divergence stability is expected to be much poorer due to much larger intra-pulse divergence variation from 4.7 DL to 2.3 DL in a 50 ns pulse [155]. Hence the poorer far-field intensity variation performance of PBUR2 as compared to GDFR. The worst performance of PBUR1 is attributed to very poor single pulse divergence stability due to a very large intra-pulse pulse divergence variation from 23 DL to 2.7 DL in a 50 ns pulse [155].

2.5 Non-linear frequency conversion of copper vapour laser to UV (255 nm) radiation

Isaeve *et al.* [173] reported, first time, the studies on frequency conversion of copper vapor laser, using KDP crystal. However, this crystal was not phase matched for 510 nm beam at room temperature. High conversion efficiency of CVL radiations has been observed in β-BBO crystal [174-176]. More than one watt UV (255 nm) power was achieved using line focusing pump geometry [177-178]. The beam qualities of second harmonic (SH) of CVL are controlled by that of the fundamental CVL beam. This in turn depends on optical resonator configuration of CVL [153-155]. The relative merit of unstable and filtering resonators, as applied to CVL, with a specific aim of frequency conversion has already been discussed in section 2.2. The experimental results on CVL beam quality are adequately presented in section 2.3. The present section focuses on experimental results and discussion of UV (255) generation with CVL beams obtained from different optical resonators. To start with, the relevant physics of second harmonic generation (SHG) is introduced very briefly. The overall study, in this section, is geared up for application of UV beams in FBG writing as continued in later chapters of the thesis.

The induced polarization (P), in a crystal, is nonlinear when the incident electric field (E) is sufficiently high. The second order nonlinear polarization is, $P^{(2)}(t) = \chi^{(2)} E^2(t)$, where $\chi^{(2)}$ is second order nonlinear susceptibility. The nonlinear material response is utilized for second harmonic and sum frequency generation of copper vapor laser in nonlinear non-centro symmetric ($\chi^{(2)} \neq 0$) medium. The technique of second harmonic generation (SHG) converts the fundamental wave of frequency ω to 2ω. The SH conversion efficiency is given as [179]

$$\eta_{\mathrm{SHG}} = \frac{P_{2\omega}}{P_\omega} = 8\left(\frac{\mu_0}{\varepsilon_0}\right)^{3/2} \frac{\omega^2 d_e^2 l^2}{n^3} \left(\frac{P^\omega}{A}\right) \frac{\sin^2(\Delta k l/2)}{(\Delta k l/2)^2} \tag{2.9}$$

where ω is the frequency of the fundamental wave, d_e is the effective nonlinear coefficient, lies the length of crystal, $P_\omega$and $P_{2\omega}$are the power (peak) at fundamental and second harmonic respectively, n is the index of refraction of the nonlinear crystal and Δk [$= k_{2\omega} - 2k_\omega$] is the mismatching quantity of the wave vectors, A is overlap area of interacting waves in the crystal. k_ω and $k_{2\omega}$are propagation constants of fundamental wave at ω and second harmonic at 2ω respectively. The SH conversion efficiency, with depleted input in case of high conversion, is given as [179]

$$\eta_{\mathrm{SHG}} = \frac{P_{2\omega}}{P_\omega} = \tanh^2\left[2\omega d_e l \left(\frac{\mu_0}{\varepsilon}\right)^{3/4} \left(\frac{P^\omega}{A}\right)^{1/2} \frac{\sin(\Delta k l/2)}{(\Delta k l/2)}\right] \tag{2.10}$$

The crystals such as BBO, KDP, DKDP, CLBO etc have been used for frequency conversion of CVL radiations [176-178]. The reported highest conversion efficiency in CLBO crystal is attributed to larger acceptance angle and higher UV transmission [176]. However, the rapid degradation in transmission with time is a limitation. The negative uni-axial Beta Barium Borate (β-BBO) crystal has wide transparency and phase matching ranges, large non-linear coefficient, high damage threshold and excellent optical homogeneity. In the present experiments, β-BBO has been used. The relevant BBO parameters for SH conversion of 510 nm to 255 nm, in type-I phase matching, are listed in the table 2.1. The type I (ooe) phase matching condition (for $\Delta k=0$) is given as [179-180],

$$n_0\,(\omega) = n_e\,(2\omega, \theta_m) \tag{2.11}$$

where θ_m is phase matching angle, n_0 is ordinary refractive index of fundamental and n_e is extra ordinary refractive index of the SH wave. The peak power (~ 20-100 kW) of CVL is comparatively low. In order to achieve high conversion efficiency, the CVL radiation is focused into the β-BBO crystal [153-155]. The observed conversion efficiency in cylindrical focusing is higher than that in spherical focusing geometry [155]. The spherical focusing geometry suffers from the disadvantages associated with the beam walk-off and non-uniform thermal detuning. Line-focusing geometry takes the advantage of large acceptance angle along azimuthal direction of BBO crystal, hence adds to conversion efficiency. The cylindrical focusing geometry ensures efficient utilization of high power fundamental beam and also reduces the chances of damage to the crystal due to lower flux density [180]. The conversion efficiency is highest for perfect phase matching ($\Delta k = 0$). In practice, it is difficult to satisfy perfect phase matching because of beam coherence/divergence parameters, thermal detuning and beam walk off. The phase mismatch due to beam divergence ($\Delta\phi$) is given as,

$$\Delta k = \gamma \sin 2\theta_m \Delta\theta_m = \gamma \sin 2\theta_m \Delta\phi \tag{2.12}$$

where $\gamma = -\omega n_0^3(\omega)[n_e^{-2}(2\omega) - n_0^{-2}(2\omega)]/c$. The SH conversion efficiency is high for diffraction limited fundamental beam. In general, the fundamental CVL is partially spatially coherent. The beam divergence [$\Delta\phi(t)$] decreases with successive transits within the resonator [155]. Thus instantaneous peak power changes with time. The evolution of coherence radius leads to variation in the fundamental beam flux and the utilized crystal length (l_u) even within the pulse. Thus, the instantaneous SH power [$P_{2\omega}(t)$] within a pulse changes due to change in change in phase mismatch ($\Delta k l_u$) factor.

Table 2.1 Parameters of BBO (β-BaB_2O_4) crystal

Transferency range	189-3500 nm
Phase matchable wavelength	189 nm -1750 nm
Refractive indices At 0.5106 µm At 0.2553µm	 n_e=1.5561, n_0=1.6762 n_e=1.6208, n_0=1.7706
Phase matching	Type I (oo-e)
Phase matching angle at 510.6 nm	50.7^0
Thermo optoc coefficient	$dn_0/dT=-9.3x10^{-6}$, $dn_e/dT=-16.6x10^{-6}$
Effective nonlinear coefficient	2.5 pm/V
Damage threshold	~ $1GW/cm^2$
Crystal structure	Trigonal, space group R_{3c}
Density	3.85 gm/cm^3
Absorption coefficient	~ $0.01cm^{-1}$ at 510 nm
Specific heat	1.91 J/cm^3
Thermal conductivity	0.08 W/mK
Angular acceptance	~ 0.26 mrad-cm (at 255 nm) in critical plane and 1.0 mard in azimuthal plane
Temperature acceptance	0.044 mrad/^{0}C
Spectral acceptance	1.1 nm-cm
Walk off	2.7° (Type I 1064 SHG)

In cylindrical focusing, the focal spot area in the crystal, A(t) [= f h $\Delta\theta(t)$, where $\Delta\theta(t)$ is instantaneous divergence, f is focal length of cylindrical lens and h is width of focused beam], changes within the pulse and is different for CVLs with different resonator configurations. Thus SH conversion efficiency and SH beam parameters will depend on the on choice of CVL resonator. In critical phase matching, the crystal length is limited by beam walk off effects. For SHG of CVL, normally observed conditions is $L_f >> L >> L_a$, where L_f is focal depth (Rayleigh range), L_a is aperture length and L is crystal length. The utilized crystal length (L_u) is given as, $L_u = (L.L_a)^{1/2}$. The aperture length (L_a) for the TEM_{00} Gaussian mode is given as, $L_a = \pi^{1/2} D_0/2\rho$, where D_0 is focal spot diameter and ρ is walk off angle. Due to strong saturation of CVL gain medium, the near field distribution of fundamental CVL beam is close to top hat. The single transverse mode divergence and therefore focal spot diameter is larger by factor of two as compared to Gaussian beam profile. Due to larger beam waist, the fundamental and second harmonic will overlap over larger length in the crystal before walk off, thus, $L_a \sim 4\pi^{1/2} D_0/2\rho \sim 2\pi^{1/2} f \Delta\phi(t)/\rho$ [155].

2.6 Experimental studies on second SHG of fundamental CVL beams

2.6.1 Experimental method

A comparative study on the second harmonic (SH) conversion efficiency and beam quality of second harmonic (255 nm) beams generated from fundamental PBUR1, PBUR2 and GDFR CVL beams was carried out. Further in the thesis, the SH UV beams generated from PBUR1, PBUR2 and GDFR CVL beams are designated as UV1, UV2 and UV3 respectively further in the thesis. Fig.2.12a shows the schematic of experimental set up for SH generation of CVL (510 nm) in line focusing geometry. The phase matching for normal incidence is 50.6^0 for SHG of 510 nm. Fig.2.12b shows the photograph of the set up. The fundamental beam was polarized by an intra-cavity plane or cube polarizer. The PBUR CVL beam was compressed from 28 mm to 2.8 mm by lenses, and GDFR beam were compressed from 30 mm to 1.9 mm by using lenses.

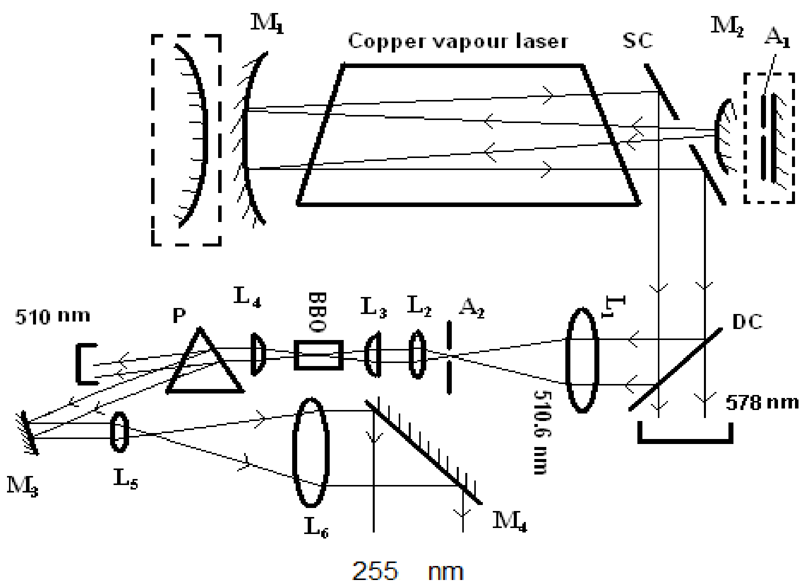

(a)

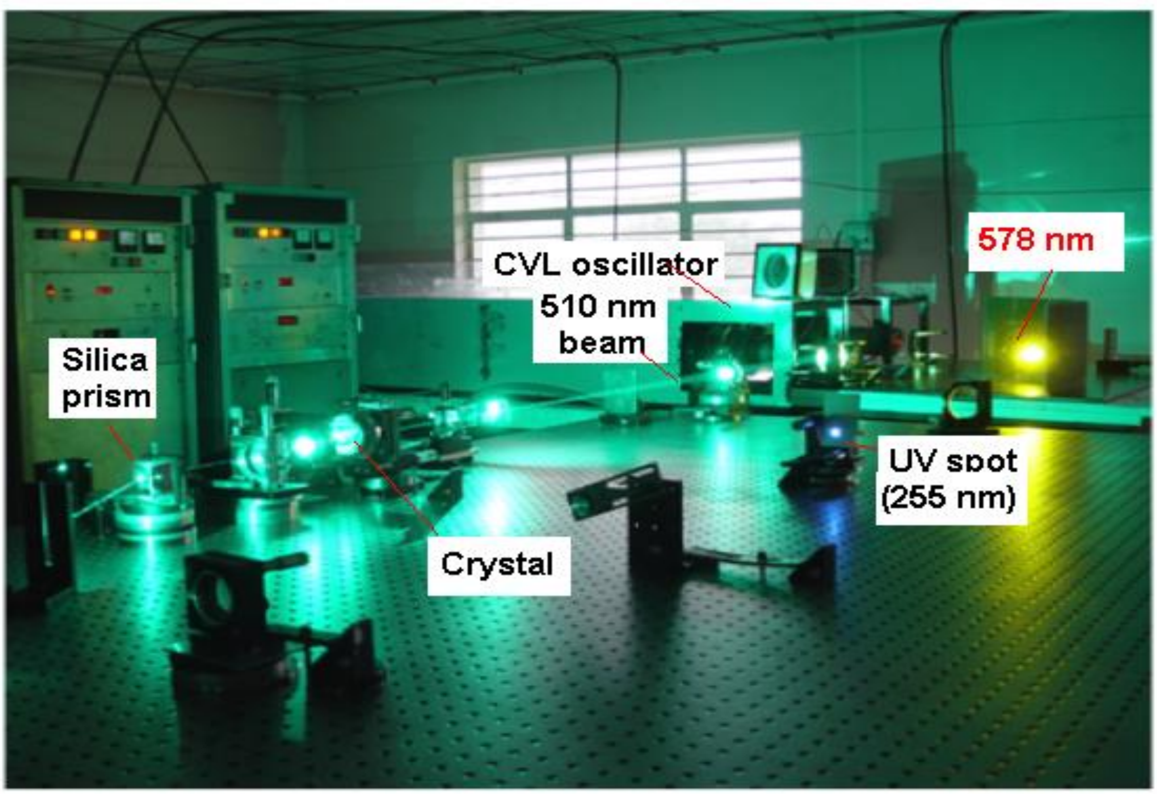

(b)

Figure 2.12: (a) Schematic and (b) Experimental set up of CVL based SH generation

The collimated fundamental beam was line focused by a cylindrical lens, L_3, on a β-BBO crystal (M/s Casix, 4 x 4x 7 mm cut at 51° corresponding to type-I phase matching at λ = 510 nm). The crystal was mounted on a 5-axis micro-positioner and was suitably aligned for SH of 510 nm radiation. The fundamental and the second harmonic beams were re-collimated by a fused silica cylindrical lens, L_4, and separated by a silica prism, P. The SH power was optimum for focal length of 6 cm of cylindrical lens L_3. The average second harmonic conversion efficiency was estimated as, $\eta_{SH} = P_{SH} / P_g \times 100$ %, where the P_{SH} is average second harmonic UV power and P_g is average power of 510 nm green beam.

2.6.2 Results and discussion

(a) Average UV (255 nm) power, conversion efficiency and pulse shape

Fig. 2.13a and 2.13b show the SH (255 nm) average power and conversion efficiency ($\langle P_{2\omega} \rangle / \langle P_{\omega} \rangle$) with increase in fundamental average power (510 nm) respectively, for UV1, UV2 and UV3 beams. The CVL average power was measured just at the entrance of BBO crystal while the UV power was measured at the exit point of prism P (Fig. 2.13a).

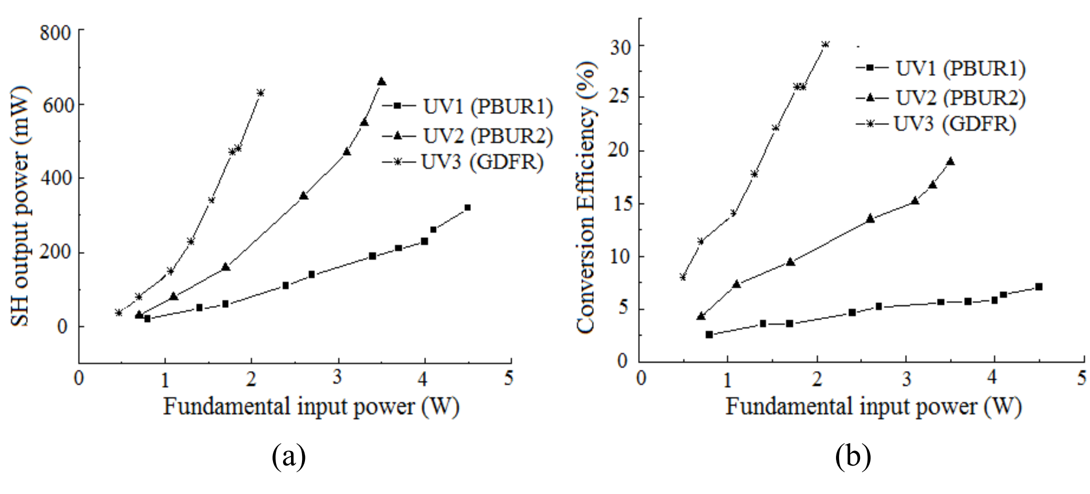

Figure 2.13: Variation of second harmonic (a) power (b) conversion efficiency with fundamental input power

The plot is up to the maximum CVL average power obtained from different resonators under same input conditions. These maximum CVL average powers were 2.1 W, 3.5 W, 4.5W for PBUR1, PBUR2 and GDFR CVLs respectively. With GDFR CVL as fundamental, the SH (UV3) conversion efficiency increased from 7.5 % to about 30 % as the input power increased from 0.5 W to 2.1 W. For PBUR2 CVL, the SH (UV2) conversion efficiency increased from 4 % to 19 % as the fundamental power increased from 0.7 W to 3.5 W. In case of PBUR1 CVL, the SH (UV1) conversion efficiency increased was 7 % at the fundamental power of 4.5 W. The maximum UV powers obtained were 600 mW (UV1) at 2.1 W GDFR CVL, 650 mW (UV2) at 3.5 W PBUR2 CVL and 325 mW (UV3) at 4.5 W PBUR1 CVL.

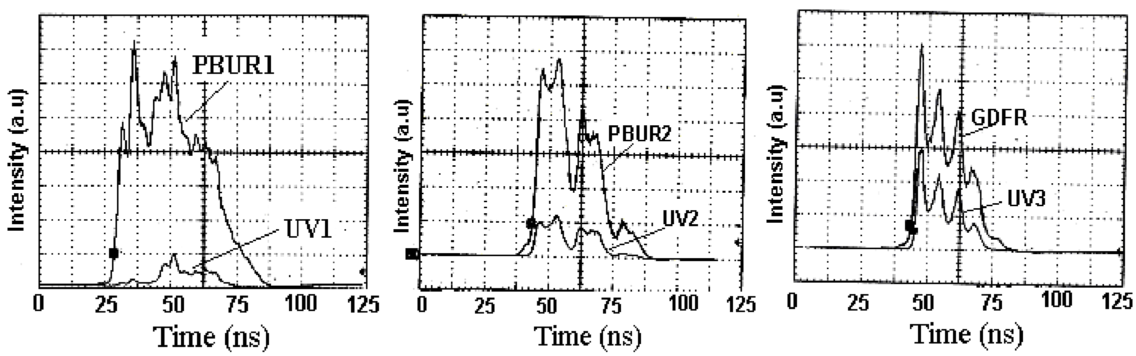

(a) (b) (c)

Figure 2.14: Temporal pulse shapes of fundamental (upper trace) and the second harmonic beam (lower trace) for (a) PBUR1 (b) PBUR2 (c) GDFR CVL beams

Figure 2.14(a-c) shows the pulse shapes of fundamental and the second harmonic beam for PBUR1, PBUR2 and GDFR CVL and corresponding UV1, UV2 and UV3 beams respectively. For PBUR1 (M=12.5) and PBUR2 (M=100) fundamental beam; the efficient frequency conversion starts about 18 ns and 6 ns from the onset of the fundamental pulse. However for GDFR fundamental beam, the time delay between the fundamental and SH pulse is almost negligible. Also the intensity variation of SH pulse follows the variation of fundamental pulse. The UV power and SH conversion efficiency increased with increase in fundamental input power without showing any saturation effect. However, the saturation in

SH conversion efficiency observed at higher input power [180]. The frequency conversion efficiency increased with fundamental beam coherence width. These trends can be explained as follows. The SH frequency conversion efficiency increases with increase in pump beam peak intensity (I_{peak}) and decrease in phase mismatch (Δk). The phase mismatching improves with decrease in beam divergence and beam pointing instability. The peak intensity can be expressed as, $I_{peak} = P_{\omega i}/r\ \tau hf\Delta\phi$; (where r is pulse repetition rate; τ is pulse width; h is line focus length; f is focal length of the cylindrical lens; and $\Delta\phi$ is fundamental beam divergence). The peak intensity is controlled by the factor $P_\omega/\Delta\phi$ (proportional to $\sigma\ P_\omega$ where σ is beam coherence width). The coherence property of GDFR CVL is far superior to other resonator geometries. The pulse averaged divergence and beam pointing instability is lowest for GDFR CVL beam and highest for PBUR1 CVL beam while these parameters for PBUR2 CVL was in between. Therefore, as expected, at same input power, the observed SH conversion efficiency was highest for UV3 beams. The average UV power under different pump beams closely followed the trend. The delay between fundamental and UV pulse for PBUR1 and PBUR2 configurations is attributed to evolution of CVL beam divergence within the pulse [155].

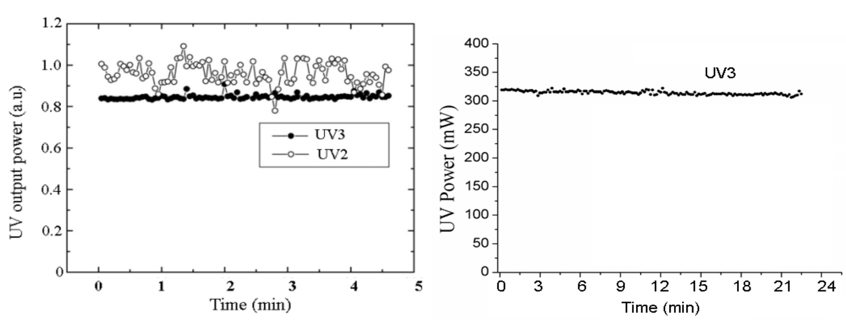

(a) (b)

Figure 2.15: Relative variation in UV average power for (a) PBUR2 and GDFR CVL as fundamental beam with time for 5 minutes (b) change in UV3 power with time for 22 minutes

The beam divergence and its variation within a single pulse (40–60 ns) in unstable resonator (PBUR1 and PBUR2) configurations are significantly higher than that in diffraction filtered resonator (GDFR). The phase matching condition is satisfied over the full GDFR CVL pulse, while it is satisfied for only a part of the pulse for UR CVL. Fig. 2.15a shows the stability of UV2 and UV3 average power, recorded over a period of 300 s with the help of a power meter (Gentec, PS– 310 WB). The fluctuation of UV3 power was within 5% while that of UV2 was close to 30%. However, the CVL average output power is almost constant within 5% over a long operating period of hours [155], irrespective of the optical resonator geometry of the oscillator. The different UV power stabilities may be attributed to the processes specific to SH generation. The most likely cause is the disturbance in fundamental to SH phase matching conditions, within the nonlinear crystal. The CVL beam pointing stability (beam wandering at nonlinear crystal) in disturbing phase matching conditions and leads to UV power fluctuations. For PBUR2 beam, the input CVL beam wandering coupled with large variation of intra pulse divergence leads to significant phase matching disturbances which caused 30% variation in UV power. On the other hand, much smaller GDFR CVL beam wandering and CVL beam divergence, being constant throughout the pulse, both the advantageous facts, lead to an almost constant UVGDFR beam power. The same trend is reflected in UV3 power stability studies up to 22 minutes (fig. 2.15b).It is worth mentioning that whole SH set up was in air conditioned (~ 25 ^{0}C) clean room. The long term ambient temperature fluctuations (< 2 ^{0}C) did not produce any observable change in the performance of second harmonic process and associated FBG writing. This is consistent with the fact that operating temperature of non-linear crystal, due to absorption of high repetition rate CVL/UV radiations, was higher than the ambient temperature.

(b) Spatial characteristics of UV

Figs. 2.16a and 2.16b show the near field profiles of UV2 and UV3 beams respectively. The near field profile is neither uniform nor Gaussian, but nearly top hat. However, the non-uniformities and local hot spots exists. The measured far-field average divergence of UV1, UV2 and UV3 beams are about 1.2 DL, 2.2 DL and 3.2 DL respectively.

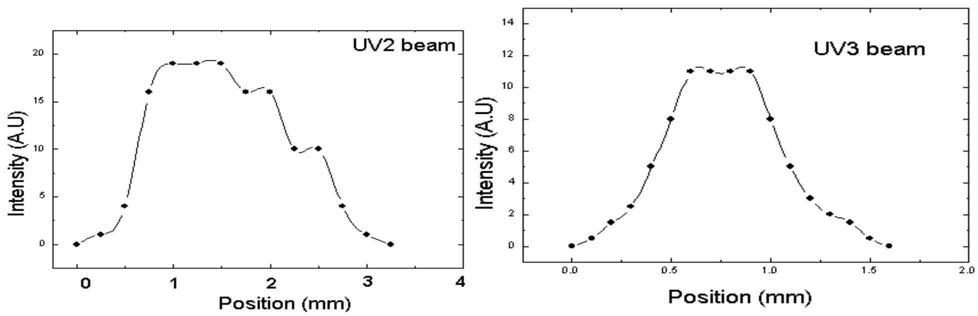

(a) (b)

Figure 2.16: Near field of (a) UV2 (b) UV3 beams

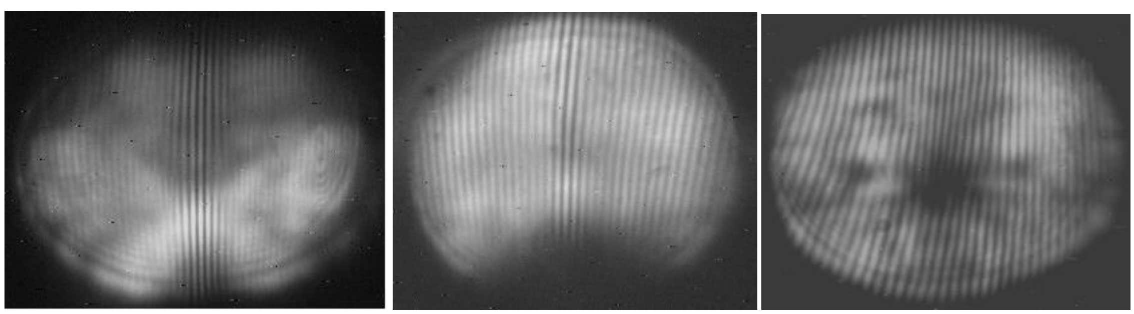

(a) (b) (c)

Figure 2.17: Typical interferogram of (a) UV1 (b) UV2 (c) UV3 beams

Figs. 2.17 (a-c) show the typical reversal shear interferogram recorded for the UV1, UV2 and UV3 beams respectively.The exposure time on CCD was 10 msec. Thus the intensity distribution is averaged over 56 pulses at 5.6 kHz repetition rate. Figs.2.18a, 2.18c and2.18e show the line intensity for the interferogram of UV1, UV2 and UV3 beams respectively. As apparent from the figure, the fringes are limited to only central portion for UV1 beam. The region of fringes as well as the fringes contrast increased for the UV2 beam. The fringes across the whole beam cross section are observed UV2 and UV3 beam. Therefore for UV2 and UV3 beam, the phase correlation exists across the whole cross section of the beam. However, the importance difference between UV2 and UV3 beam is the fringes contrast (degree of coherence). The variations of fringe visibility along the radial distance are shown in figs.2.18b, 2.18d and 2.18e for UV1, UV2 and UV3 beams respectively.

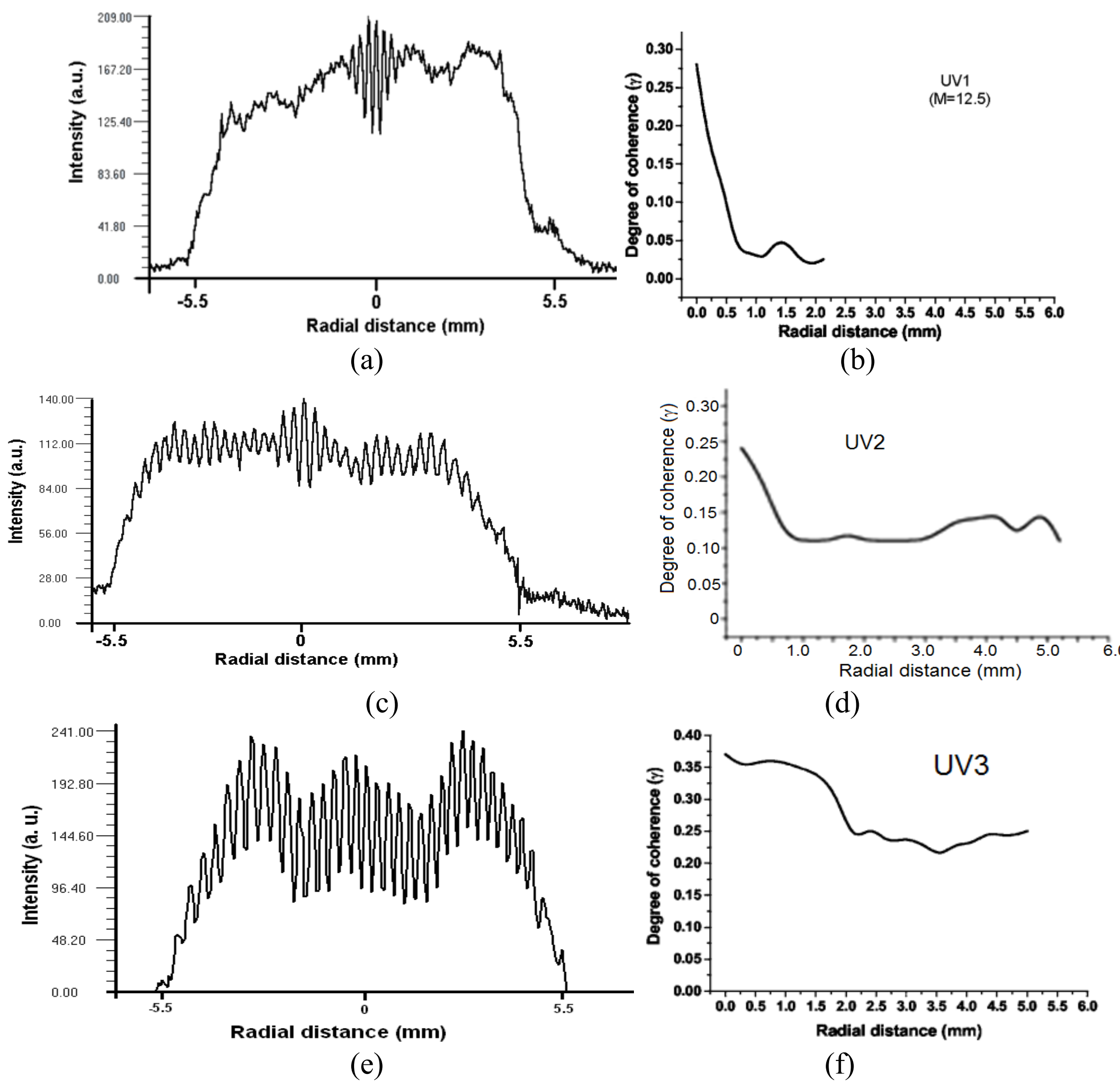

Figure 2.18: Line intensity variation across of (a) UV1 (c) UV2 (e) UV3 beams; Degree of coherence of (b) UV1 (d) UV2 (f) UV3 beams

Highest degree of coherence (~ 0.36) is observed the for UV3 beam as compared to 0.24 for UV2 beam. It is clear from the results that the coherence width and degree of coherence of the SH beam (255 nm) followed that of the fundamental beam (510 nm) which in turn depend on resonator type [180-181] and resonator magnification. These UV beam characteristics and average power level are good enough to write high reflectivity FBGs. The UV fringes' stability is also studied, in a test set up, with about 8 μm spacing UV (255 nm) fringes formed by a 2^0 biprism, as detailed in chapter 6 on prism based FBG writing. As expected the UV3 beam produced the fringes of much better contrast and positional stability as compared to UV1 & UV2 beams. All the studied UV beams, though of different characteristics and power levels, were good enough to write high reflectivity FBGs.These are the UV beams that are employed in writing FBGs as detailed in subsequent chapters.

2.7 Conclusion

This chapter presented a detailed study on the high repetition rate second harmonic UV (255 nm) beam characteristics vis-à-vis the fundamental CVL (510 nm) beamwith an aim to applying the UV beam for FBG fabrication. The chapter starts with presentationof diagnostic tools and methodological formulation of techniques used in the characterization UV/CVL beams. This includes in house proposed and developed compact reversal shear interferometer for spatial coherence measurement as well as gated CCD set up for single pulse data acquisition. Next, the fundamental CVL(510 nm) beam properties such as spatial coherence, divergence, line-width, pulse shape and pointing stability are studied in detail for CVL with unstable and filtering resonator geometries. The CVL beam quality improved with increase in unstable resonator magnification from 12.5 to 100. However the best CVL spatial coherence and pointing stability was obtained in spatial filtering (GDFR) resonator. This was suitably explained. These CVL beams were frequency converted (second harmonic) to UV (255 nm) radiations in a homemade set up. The UV beams (UV1, UV2 and UV3) characteristics such as average power, spatial coherence, beam profile, pulse shape and power stability are studied in detail. The UV beam characteristics are correlated with that of fundamental CVL beam. The beam quality of UV3 was best among the three beams. The overall study led to establishing the credentials of high (~ kHz) repetition rate, short (~ 10s of ns) pulse duration, low average power (~100s of mW) and good coherence properties UV (255 nm) pulses for an effective writing of FBG sources. This was aptly demonstrated in the next few chapters on phase mask and biprism based FBG writing with 255 nm UV1, UV2 and UV3 sources.

Publications based on this chapter

1. "Effect of pulse to pulse variation of divergence, pointing and amplitude of copper vapour laser radiations on their second harmonic and sum frequency conversion" O. Prakash, **R. Mahakud,** S.V. Nakhe , S.K Dixit, Opt & Laser Technology, **2013**, 50, 43-50.
2. "Comparative study on second harmonic conversion and saturation characteristics of three copper vapor laser beams of same average power and different spatial coherence", O. Prakash , **R.Mahakud,** S.K.Dixit, Optical Engg., **2011**, 50, 114201 –6.
3. "Role of optical resonator on the pointing stability of copper vapor laser beam" S.K. Dixit, **R. Mahakud**, O. Prakash, R. Biswal, J.K. Mittal , Optics Commun. , **2008**, 281, 2590–2597.
4. "Cylindrical-lens-based wavefront-reversing shear interferometer for the spatial coherence measurement of UV radiations" O. Prakash, **R. Mahakud**, H. S. Vora and S.K. Dixit Optical Engg., **2006**, 45, 055601-6

Chapter 3

Analysis on the contrast and stability of UV fringes of different FBG writing interferometers

3.0 Introduction

The properties of fiber Bragg grating (FBG) are decided by the strength of induced periodic refractive index modulation in the doped optical fiber core [16]. This is crucially linked to net contrast of the superposed UV laser fringes, averaged over FBG writing period, made by a suitable interferometer. This in turn is guided by the spatial coherence and pointing stability of the writing UV laser beam [182-186]. The effect of these parameters on the contrast and stability of UV fringes will be different for different FBG writing interferometers, which are based on mirrors, phase mask or prisms [185]. The phase mask technique requires the fiber to be placed in close proximity [16]. This however has a possibility of damaging the phase mask. Placing the fiber at a safe distance led to the dominating effect of spatial coherence of the writing beam on dictating FBG characteristics [128,182-183]. The phase mask -Talbot interferometer [187-189] is good choice for safe FBG writing, however involve long path length, necessitating the use of very low pointing instability writing UV beam. The same is true for long path length mirror based UV interferometer. The prism based interferometers [71-72] are cost effective with ease in FBG wavelength tunability. However the demand on UV beam spatial coherence and beam pointing stability are stringent. Though the importance of spatial coherence and pointing stability of writing laser beam in FBG fabrication has been duly recognized [186], the detailed numerical quantification was lacking for different FBG writing interferometers.

In this chapter, the effect of UV beam spatial coherence and beam pointing stability, on the contrast and stability of sub-micron UV fringes produced by different interferometric techniques such as phase mask, phase mask -Talbot and prism interferometers, have been theoretically analyzed [185]. The theoretical formulation is verified by correlating with experimentally measured contrast and stability of 14.6 μm pitch fringes generated by a 2^0 biprism using 510 nm laser beams of different spatial coherence and pointing stability characteristics [185].

3.1 Analysis on the spatial coherence of writing UV beam on interferometer fringe contrast

3.1.1 General considerations

A normal FBG is written by side exposure of interference pattern of submicron period typically produced by a two beam interference pattern. The fringes are produced either by amplitude or wavefront splitting interferometer [16]. The fringe intensity distribution in a two beam interference pattern can be expressed as [190],

$$I(x,z) = I_0(x,z)[1+\gamma(x,z)\cos(\frac{2\pi}{\Lambda}z)] \tag{3.1}$$

where $I_0(x, z)$ is fringes' mean intensity and γ (x, z) is fringe contrast. The fringe contrast depends on temporal and spatial coherence of the laser beam from which two interfering waves are generated. Fringe visibility decreases with increase in laser beam line-width**.** The line width of CVL-UV (255 nm) is narrow (~ 9 GHz). The coherence length is about 37 mm. Since this coherence length is much larger than the path length difference in FBG fabrication, the fringe contrast [γ(x, z)] dilution mainly depends on spatial coherence of the 255 nm writing beam.

3.1.2 Fringe contrast of phase mask and phase mask –Talbot interferometers

A phase mask, used in transmission, is a relief grating etched in UV transmitting silica plate [67-70]. The UV radiation incident on the phase mask is diffracted into different orders to form a three dimensional interference field. The etched sections' depth of the grating is a function of the wavelength of incident UV beam. To minimize the 0^{th} order transmission, the smallest depth etched on the silica plate is given as, $d(n_{uv}-1) = \lambda_{uv}/2$ [16], where d is phase mask period, n_{uv} is the refractive index of phase mask material at UV wavelength and λ_{uv} is wavelength of the incident UV beam. Let us assume an ideal phase mask diffracting in +1 and -1 orders only. Figure 3.1 represents the schematic of UV beam of diameter 2W incident normally on the phase mask in the YZ plane (x=0). The first order diffraction angles (α) are, $\alpha = \sin^{-1}(\lambda_{uv}/d)$. The interference is produced in the beam overlap region of ± 1 order. The fringe separation (Λ) is equal to half the phase mask period (d) i.e. $\Lambda=d/2$. For FBG writing, the fiber is placed in a plane x = constant, parallel to z-axis (fiber axis).

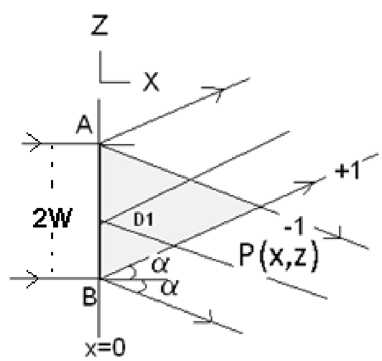

Figure 3.1: Schematic of overlap of +1/-1 order beam of a phase mask

For the interference of ±1 order diffracted beam at P(x,z), the separation (Δs) distance between interfering points is given as $\Delta s(x) = 2x \tan\alpha$. Assuming spatial coherence of a laser beam as a Gaussian correlation function, the degree of coherence (γ_s) between two points separated by distance Δs on the incident wave front is described as [191-192]

$$\gamma_s(\Delta s) = \exp[-(\Delta s)^2 / 2\sigma^2] \tag{3.2}$$

whereσ is the coherence width of the laser beam. The separation (Δs) increases with increase inangle of intersection (α) and the distance (x) of the fringe plane from the phase mask. The interference fringe contrast in the fringe plane, x, decreases with decrease in coherence width and increase in x. The degree of coherence (γ_s) is constant along z (fiber axis). The coherence width (σ) decreases ($\sigma \sim \lambda_{uv}/\Delta\phi$) with increase in beam divergence ($\Delta\phi$).The effect of spatial coherence on the phase mask fringe pattern was analyzed by implicitly incorporating the angular divergence of incident beam on the phase mask as angle of incidence of set of plane waves [182] varying within the envelope of $-\Delta\Phi/2 < m\varepsilon < \Delta\Phi/2$ where$\varepsilon \to 0$ as $m \to \infty$.For uniform distribution over all incident angles, the fringe visibility [γ (x)] is given as [182-185]

$$\gamma\ (x, \Delta\phi) = \mathrm{sinc}\ (k\ x\ \Delta\phi\ \tan\alpha) \tag{3.3}$$

The fringe visibility is a sinc correlation function which decreases with increase in $\Delta\phi$, x and α. The variation of fringe contrast along fringe depth, simulated for two different divergence values $\Delta\phi$ = 1 mrad and $\Delta\phi$ = 0.063 mrad (correspond to diffraction limited (DL) divergence of uniform beam for 2W= 10 mm, λ= 255 nm) is shown in fig.3.2a. The fringe visibility is zero at distance x_0, given as $x_0 = \lambda/ (2\Delta\phi \tan\alpha) = \sigma/ 2\tan\alpha$.

The effect of divergence on interference fringe contrast is negligible for small x (<1 mm), as is typical with phase mask based FBG writing. The visibility plot of fig.3.2a is for constant divergence within the pulse. However, it is worth mentioning here that the divergence of the CVL beam, used in UV generation, evolves within the pulse [155]. The time resolved divergence varies from 4.7 DL to 2.3 DL in PBUR2 and 23 DL to 2.7 DL in a 50 ns pulse [155]. The data are for ASE reduced beam. The CVL ASE divergence is of the order of 10 mrad (~ 200 DL) [155]. The part of this CVL ASE, though filtered by a spatial filter, is always present in second harmonic process. The second harmonic beam characteristics follow that of the fundamental beam [193-195]. This has been established for SHG of CVL [chapter 2]. The fractional power in each round trip of CVL and therefore that of SH beam changes, as apparent from the temporal pulse profile (fig.2.14). Thus the single pulse fringe contrast is weighted average of various round trips in the laser cavity, given as,

$$< \gamma(x) > = \sum_i f_i \gamma_i (x, \Delta\phi_i) \tag{3.4}$$

where f_i is the fractional power and $\Delta\phi_i$ is the divergence in a round trip.

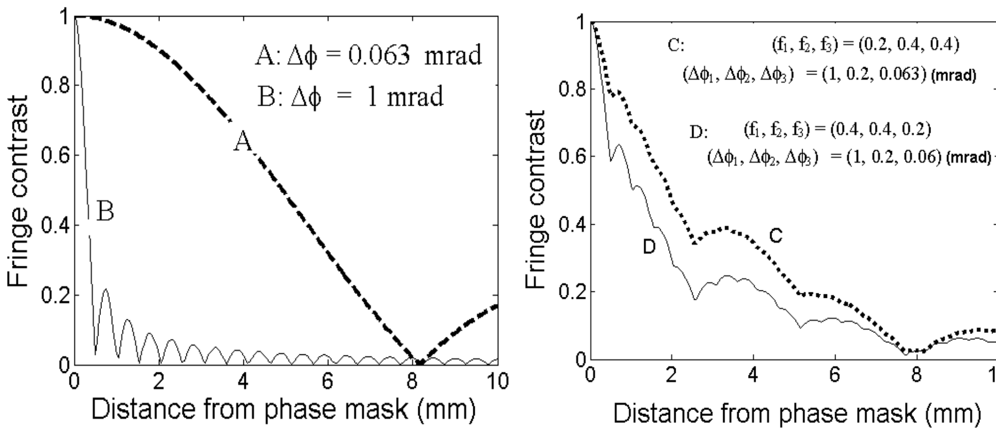

(a) (b)

Figure 3.2: Simulated variation (a) fringe contrast for constant divergence beam (b) pulse averaged contrast for different round trip divergence values for incident beam on phase mask

Fig. 3.2b shows the variation of fringe contrast for typical round trip divergence: $\Delta\phi_1$ = 1 mrad, $\Delta\phi_1$ = 0.2mrad, $\Delta\phi_1$ = 0.063 mrad with fractional power f_1 =0.2, f_2 =0.4, f_3 =0.4 respectively, marked as C. With change in fractional power distribution, typically with f_1 =0.4, f_2 =0.4, f_3 =0.2, the fringe contrast variation changed (marked as D in fig. 3.2b) for same round trip divergence values. The fringe visibility plots in fig.3.2b are typical representations. Larger the fraction of power in higher divergence angle, worsen will be average fringe contrast at a given location, even at very closer to the phase mask. Besides, the presence of remnant ASE will increase the overall intensity level across the fringe pattern thus diluting the fringe contrast. Additionally, fringe pattern drift attributed to beam pointing instability will also reduce time average fringe contrast (discussed in next session 3.2).

In a standard phase mask, approximately 25 % of incident power is distributed in residual zero and higher orders (±2, ±3,..). If we simply consider the residual overlap as background, then the fringe contrast will be diluted by a factor ~ 0.75 [= $(I_{+1}+ I_{-1})/ ((I_{+1}+I_{-1}+ I_r)$, where I_{+1}, I_{-1} and I_r are intensity distribution in +1, -1 and residual orders).The case of fringe contrast for phase mask–Talbot interferometer (Fig. 3.3) fringes is not different from the earlier case except that FBG writing is carried out in the imaged Talbot region D_2.

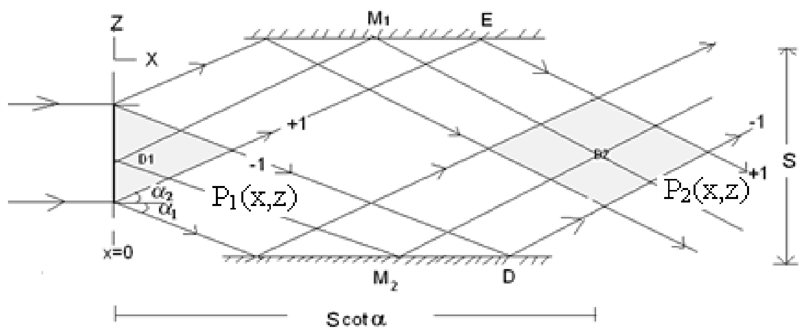

Figure 3.3: Phase mask –Talbot interferometer

After diffraction by the phase mask, +1 and -1 beams again recombine in the region D_2, reflected by two plane mirrors. The FBG is intended to written in shaded region D_2. In an ideal situation (with no pointing disturbance), the refractive index modulation/reflectivity of a FBG being written in the region D_2will be exactly same as in region D_1. The fringe visibility [$\gamma (x, \Delta\phi)$] in a plane at a distance x from the phase mask is given as [183, 185],

$$\gamma (x, \Delta\phi) = \mathrm{sinc}\, [k (x-S \cot\alpha)\Delta\phi \tan\alpha] \tag{3.5}$$

where S is separation distance between two the mirrors as shown in fig. 3.3.

The simulated variation of fringe contrast for different beam divergence values in this case will be same as in fig. 3.2 except for positional translation. However this equivalence will no longer hold if the input UV beam of a given pointing instability is considered as detailed in the next section 3.2.

3.1.3 Fringe contrast of prism interferometers

This interferometric technique of FBG writing is suitable for Bragg wavelength tuning. The biprism [71-72] and single prism (Lloyd prism) [16] interferometers have been used in FBG fabrication. The nature of beam overlap in biprism and Lloyd prism interferometers are opposite. The biprism divides the incident beam into two refracted beams which intersect without wavefront reversal. In contrast, in single prism (Lloyd prism/mirror), half of the wavefront reverses before overlapping with the other half. Thus, the effect of spatial coherence on fringe modulation of these two interferometers will be of different nature which needs analysis [196].

(a) Biprism interferometer

In this configuration, the collimated UV beam of wavelength (λ_{uv}) incident normal to the hypotenuse of the biprism, as shown in Fig.3.4a. The biprism splits the incident wave front into two and these two beams leave the prism, each making an angle α with the initial direction of beam. The interference fringes produced in the rhombus shaped overlap region are parallel to the apex edge of the prism. In the schematic, the fringes are formed in the x-z plane and modulated along z (fiber axis). The distance of separation (Δs) between two points on the incident wave front for interfering at P(x,z) is given as [196]

$$\Delta s_{bp} = 2x \tan\alpha / (1 - \tan\alpha . \tan A) \tag{3.6}$$

where $\alpha = \sin^{-1}$ [n_p sin A]-A. The terms, A is the refraction angle of the biprism, n_p is the refractive index of the prism material.

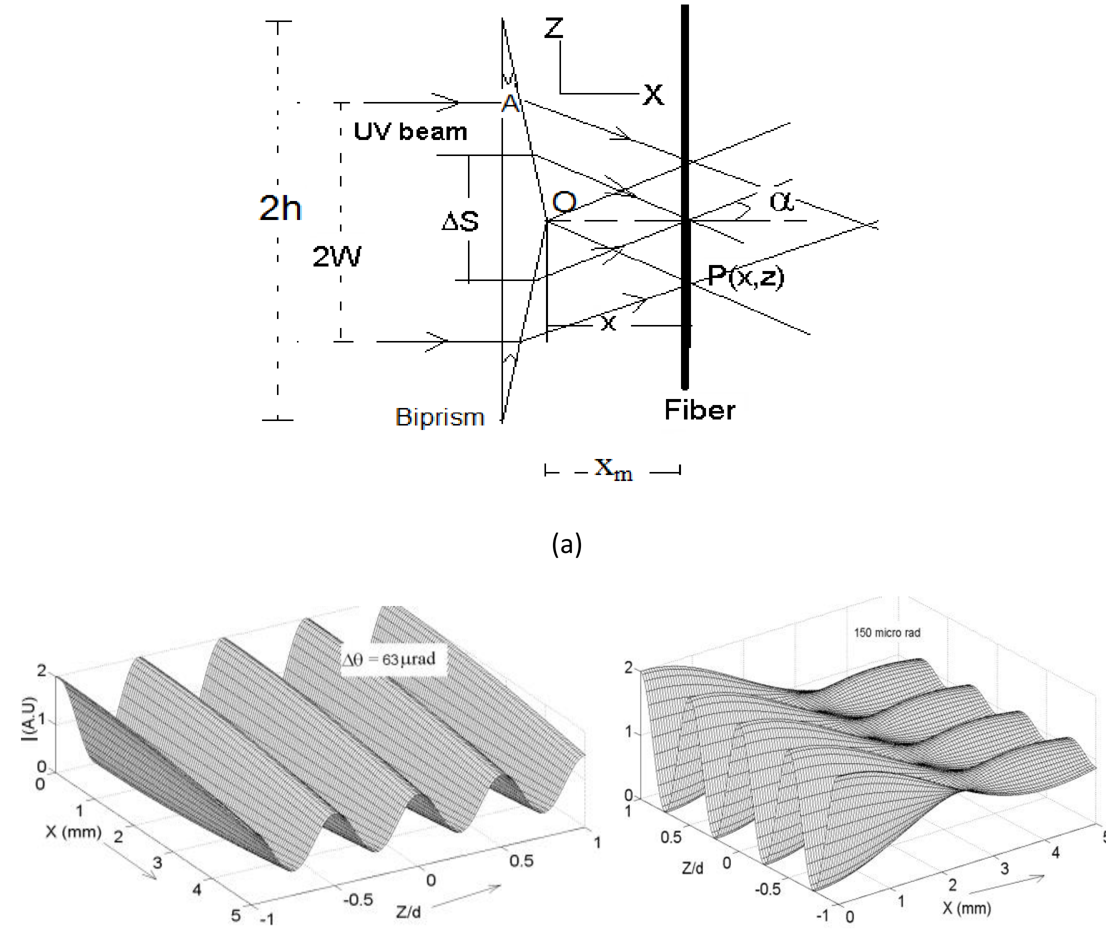

(a)

(b) (c)

Figure 3.4: (a) Schematic of a biprism interferometer (b) Simulated fringe intensity distribution for beam divergence of (b) $\Delta\phi$ = 63 μrad and (c) 150 μrad

In a typical FBG writing plane (x = constant), Δs_{bp} is constant but increases with increase in distance of writing plane (x) from the biprism. The effect of UV beam spatial coherence on biprism fringes was analyzed implicitly by incorporating the uncorrectable beam divergence as incident angle on the biprism. When the incidence angle of a plane wavefront changes from 0 to $\delta\theta$, where $\delta\theta$ belongs to $(-\Delta\phi/2, +\Delta\phi/2)$ corresponding to a full-angle divergence angle $\Delta\phi$, then the refracted angle changes from α to $(\alpha+\delta\alpha)$ where [185]

$$\delta\alpha = [\cos A / \cos(\alpha+A)]\ \delta\theta \tag{3.7}$$

The net intensity is sum of intensity contributions from all values of $\delta\theta$. The distribution of $\delta\theta$ within the divergence envelope will determine the fringe contrast. Assuming uniform distribution for simplicity, the fringes contrast [γ_{bp} (x, z)] in the FBG writing plane (along z) at a distance x from the biprism can be expressed as [196],

$$\gamma_{bp}(x, z) = \text{sinc}\,[k\, x\, \Delta\phi\eta_{bp}] \tag{3.8}$$

where $\eta_{bp} = \sin\alpha \cos A/\cos(\alpha+A)$ and $k = 2\pi/\lambda_{uv}$. For typical values, $A = 24^0$, $n_p = 1.5$, λ_{uv} = 255 nm, 2d = 20 mm, 2W = 10 mm, the simulated fringe intensity distribution for $\Delta\phi$ = 63 μrad and $\Delta\phi$ = 150 μrad are shown in fig. 3.4b and 3.4c respectively. The variation of fringe constant attributed to spatial coherence is similar to that of phase mask. The fringe contrast is constant in a specific FBG writing plane (x). However, it decreases with increase in UV beam divergence ($\Delta\phi$) and/or biprism to fiber distance (x) as expected. Further discussion about FBG refractive index modulation is in prism based FBG fabrication is discussed in chapter 6.

(b) Single (Lloyd) prism interferometer

Fig. 3.5a shows the schematic of Lloyd prism based FBG writing. The writing UV beam is directed at hypotenuse face of a right angled silica prism.

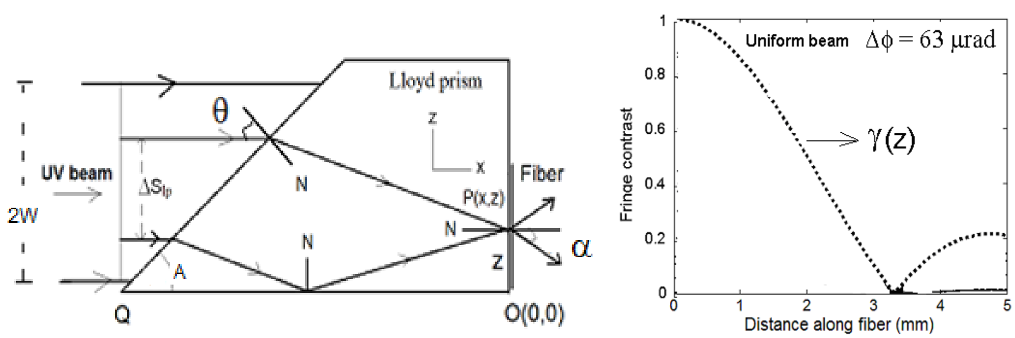

(a) (b)

Figure 3.5: (a) Schematic of FBG inscription by Lloyd prism interferometer (b) Variation of fringe contrast in the FBG writing plane.

The beam is folded about the centre with half of the wavefront leaves the prism after internally reflected from face OQ and overlap with other half to produce interference. The superposition is like reversible shear since one half undergoes internal reflection. At the exit face of the prism, the fiber is aligned for exposure. The prism angle (A) and angle of incidence (θ) of the UV beam on the hypotenuse of the prism fix the fringe periodicity (Λ) which is imprinted in the fiber core to form the FBG.The angle (α) trace by refracted rays with x–axis is given as,

$$\alpha = \sin^{-1}[n_p \,.\, \cos\{A+\sin^{-1}((\sin\theta)/n_p)\}] \tag{3.9}$$

where n_p is refractive index of prism material. The fringe periodicity (Λ) is, $\Lambda = \lambda_{uv}/ 2\sin\alpha$.

The distance of separation (Δs_{lp}) between points on the wavefront for interfering in the plane x= 0 at P(x,z), at a distance z from O (0,0) (fig.3.5a) is given as [196],

$$\Delta s_{lp} = 2nz\sqrt{\frac{1-\sin^2\theta}{n^2-\sin^2\theta}} \tag{3.10}$$

In the FBG writing plane, Δs_{lp} increases along fiber length z = 0 to z = L, where L is beam overlap length [= w (sin α+ cosα tanα) /cosθ] in the plane x=0. The nature of variation of Δs_{lp} in this case is different from that biprism interferometer. The effect of beam divergence on fringe contrast is analyzed, similarly as in biprism. When the incident angle changes by δθ, where δθ belongs to (-Δϕ/2, + Δϕ/2) corresponding to divergence envelope (=Δϕ), then the refracted angle changes from α to (α - δα) where $\delta\alpha = \delta\theta\,[\sin\{\sin^{-1}((\sin\theta)/n_p)+A\}\cos\theta]/[\cos\{\sin^{-1}((\sin\theta)/n_p)\}\cos A]$. The contrast [$\gamma_{lp}$ (x, z)] of fringe intensity distribution in the FBG writing plane (x = 0) can be expressed as [196]

$$\gamma_{lp}(x, z) = \mathrm{sinc}\,[kz\Delta\phi\eta_{lp}] \tag{3.11}$$

where η_{lp} = cosθ sin{A+ $\sin^{-1}$((sin θ)/n_p)} /cos{$\sin^{-1}$ (sin θ/n_p)}.Fig. 3.5 shows variation of fringe contrast [γ_{lp}(x, z] for typical values, A = 45^0, θ=58^0, n_p=1.5, Δϕ =63μrad and λ_{uv} =255 nm. It is clear from Eq. (3.11) that the fringe contrast (fig.3.5b) decreases along the fiber length unlike the case of biprism/phase mask interferometer. The fringe formation of a Lloyd mirror arrangement is similar to the single prism interferometer. Lloyd prism/mirror interferometer based on wavefront reversal requires source intensity and coherence constant across the beam. Otherwise, fringes visibility will be poor. Further discussion about FBG refractive index modulation is in chapter 6.

3.2.1 Effect of beam pointing stability on fringe stability

3.2.1 General considerations

The laser pointing instability is aggregate of all the laser direction fluctuation effects such as intrinsic laser beam dithering, mechanical vibration and environmental disturbances. The effect of beam pointing instability on the refractive index modulation of FBG in case of single pulse FBG writing could be ignored [119]. However, in case of low pulse energy or CW lasers, the FBG writing involves tens of thousands to a million of superposed UV pulses or tens of minutes of CW UV radiation [16]. The refractive index modulation along the length in fiber core will be guided by an average contrast of fringes over writing time. The instability of fringes attributed to various disturbances will inhibit the grating growth which requires fringes of submicron period. Because of pointing instability induced fringe spatial shift in the writing plane, time averaged fringe contrast on that plane will be reduced. In this section, the effect of beam pointing instability on fringe contrast is analyzed for phase mask, phase mask - Talbot and biprism interferometers. The intensity distribution at a point in the overlap (shaded) region (Fig. 3.7a) of two monochromatic partially coherent plane polarized waves of equal amplitude propagating along the vectors defined by vectors $\overline{k_1}$ and $\overline{k_2}$, is given by [179, 190]

$$\begin{aligned} I(x,z) &= 2I_0[1+\gamma_C \cos(\vec{k_2}-\vec{k_1}).\vec{r}+\delta] \\ &= 2I_0[1+\gamma_C \cos\{kz(\sin\alpha_1+\sin\alpha_2)-kx(\cos\alpha_1-\cos\alpha_2)+\delta\}] \end{aligned} \tag{3.12}$$

where α_1 and α_2 are angles traced by propagation vectors $\overline{k_1}$ and $\overline{k_2}$ with x-axis respectively. δ is the initial phase difference between the two overlapping wave front. γ_c is the visibility of the single pulse fringe pattern, which depends on the spatial coherence of the beam.

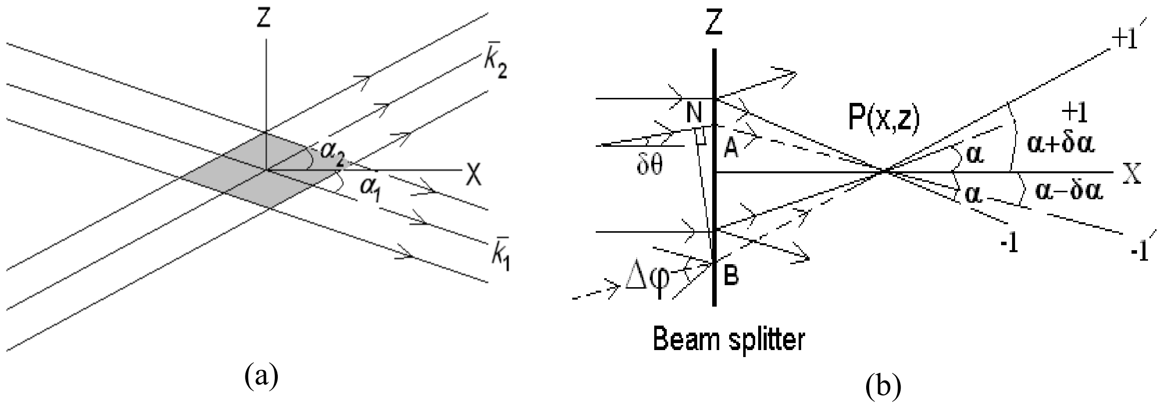

Figure 3.6: Schematic of (a) two beam interference (b) UV beam incident at two different angles on the phase mask

The two beams are derived from a single beam by means of a beam splitter. The laser beam is assumed to incident normally on the beam splitter which is either a phase mask or a biprism. The effect of beam pointing instability of incident beam is analyzed by considering the parallel rays incident on the beam splitting optical element with incident angle fluctuating within the angular pointing instability ($-\Delta\varphi/2<\delta\theta<\Delta\varphi/2$) where $\Delta\varphi$ is the envelope of beam pointing angle. Fig. 3.6b shows this representatively in case of a phase mask. Due to change in angle of incidence of beams on the beam splitter within the angular envelope of pointing instability [$\Delta\varphi$], there will be slight change in angles α_1 and α_2 of the diffracted/refracted beams with x- axis. If the beam incident angle changes by $\delta\theta$due to beam pointing instability, the change in the angle of two interfering rays trace with x-axis are $\delta\alpha_1$ and $\delta\alpha_2$ with opposite sign for typical interferometers such as phase mask and biprism.For small values of$\delta\theta$, the magnitude of change ($\delta\alpha_1 \approx \delta\alpha_2 \approx\delta\alpha$) are approximately equal. Hence, $\alpha_1 = \alpha + \delta\alpha$ and $\alpha_2 = \alpha - \delta\alpha$ (Fig. 3.7b). Assuming, δ=0, the intensity distribution [eqn (3.12)] can be expressed as [185],

$$I(x,y) = 2 I_0[1+\gamma_C (x,z) \cos\{2k \sin\alpha \cos\delta\alpha (z + x \tan \delta\alpha)\}] \quad (3.13)$$

The direction of stratification/fringe axis for $\delta\alpha \neq 0$, can be calculated by,

$$\cos\{2k \sin\alpha \cos\delta\alpha (z+ x \tan\delta\alpha)\}=1 \quad (3.14)$$

The direction of stratification is,

$$z+ x \tan\delta\alpha = N\lambda/ (2 \sin\alpha. \cos\delta\alpha) \quad (3.15)$$

N is an integer. From equation (3.15), the pitch, P, of the fringe system is given as,

$$P = \lambda / (2 \sin\alpha.\cos\delta\alpha) \quad (3.16)$$

Since the pointing angle of FBG writing UV beams usually very small (~ 10-50μrad), $\delta\alpha$ will also be correspondingly small. i.e. $\cos (\delta\alpha)\approx 1$ and $\tan \delta\alpha\approx\delta\alpha$. The direction of stratification and pitch of fringe system, are modified as [185],

$$z + x \ \delta\alpha = N \lambda / (2 \sin\alpha) \quad (3.17)$$

$$P = \lambda / (2 \sin\alpha) \quad (3.18)$$

Equations (3.17) & (3.18) show that the changes in fringes pitch due to 10s of μrad of beam pointing instability is negligible. The fringe axis is at angle $\delta\alpha$ with x-axis [eqn (3.17)]. As incident beam angle changes within the beam pointing envelope $-\Delta\varphi/2<\delta\theta<\Delta\varphi/2$, the phase shift will lead to spatial shift of the fringe pattern at any observation plane (x = constant) beyond beam splitter. The angular drift of the fringe pattern takes place with respect to fringe axis (of $\delta\alpha=0$). The linear fringe shift, Δz, at the above reference plane with change in the beam pointing angle from zero to $\delta\theta$ which causes change in α by $\delta\alpha$ is given as [185],

$$\text{Fringe shift } (\Delta z) = x\ \delta\alpha \tag{3.19}$$

The fringe instability, S, is given as,

$$S = \text{Fringe shift/ Fringe pitch} = 2x\,(\sin\alpha)\,\delta\alpha/\lambda \tag{3.20}$$

It is clear that the fringe shift at the reference plane is directly proportional to magnitude of beam pointing angle and to the distance of the observation plane x but is independent of angle between two beams. However, fringe instability will be higher for smaller pitch fringes (or for larger angle between two beams). The CVL beam pointing has nearly a normal distribution (fig.2.10b, chapter 2). For simplicity in estimation of time average fringe contrast, a uniform distribution of beam pointing angle within the envelope ($-\Delta\varphi/2<\delta\theta<\Delta\varphi/2$) is assumed. The time average intensity due to instability envelope $\Delta\phi$ ($-\Delta\phi/2\leq\delta\alpha\leq\Delta\phi/2$) is then given as,

$$\langle I\rangle = 2I_0\,\{1+\gamma_C\,\nu_S(x,\Delta\phi)\cos(2\,k\,y\sin\alpha)\} \tag{3.21}$$

$$\text{where}\ \ \nu_S\,(x,\Delta\phi) = \mathrm{sinc}[k\,x\,\Delta\phi\sin\alpha] \tag{3.22}$$

ν_S is the time averaged fringe contrast. The relation between $\Delta\phi$ and $\Delta\varphi$ will determine fringe contrast dilution for different interferometers. Further discussion is for few special cases.

3.2.2Fringe stability/contrast of phase mask interferometer

From grating equations, +1 and -1 diffraction angles are given as,

$$\alpha_1 = \sin^{-1}(\lambda/d - \sin\delta\theta\,) \tag{3.23}$$

$$\alpha_2 = \sin^{-1}(\lambda/d + \sin\delta\theta\,) \tag{3.24}$$

For$\delta\theta=0$, $\alpha_1= \alpha_2=\alpha= \sin^{-1}(\lambda/d)$ and the optical path difference (NA+AP-BP) is zero (Fig. 3.6b).Fringe stratification is along x-axis. When $\delta\theta\neq0$, the intensity distribution is given by equation (3.12). Since $\delta\theta$ is very small, $\sin\delta\theta\approx\delta\theta$, and $k.x.\,(\cos\alpha_1-\cos\alpha_2)\approx2\ k.x.\delta\theta.\tan\alpha$. The intensity distribution is given as,

$$I=2I_0\,[1+\gamma_C \cos[(2\,k\,z\,\lambda/d)-2\,k\,x\,\delta\theta\,\tan\alpha+\delta] \qquad (3.25)$$

It is the net phase difference, (δ- 2 k$x\delta\theta$ tanα), that decides the fringe shift. Assuming $\gamma_C = 1$, figure 3.7a shows the fringe intensity distribution for different pointing angles (within the envelope of ± 20 μrad) for typical values, d =1.06 μm, λ = 0.255 μm, x=1mm.This distance is judiciously chosen as in phase mask based proximity FGB writing, the phase mask- fiber distance is within 1000 μm and any distance ≥ 1 mm would be the worst possible case. It was found for phase mask based FBG writing, even in the worst pointing angle of ± 20 μrad, the phase shift (at x≤ 1mm) is very small, being < ± 0.08 π. The time average contrast in phase mask fringes is obtained by replacing $\Delta\phi=\Delta\varphi/\cos\alpha$ in equation (3.22)

$$\nu_S(x, \Delta\phi) = \gamma(x,\Delta\varphi) = \mathrm{sinc}\,[kx\Delta\varphi\,\tan\alpha] \qquad (3.26)$$

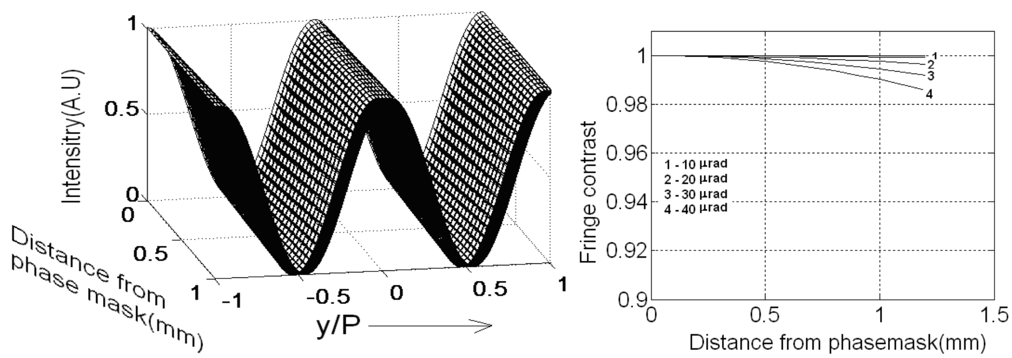

(a) (b)

Figure3.7: Simulated (a) fringe intensity positional fluctuation for different pointing angles (b) average fringe contrast[$\nu_S(x,\Delta\phi)$] vs. distance from phase mask (x)

The loss in superposed fringes contrast (eqn. 3.22) for beam pointing of 0, 10, 20, 30, 40 μrad for phase-mask fiber plane distance from 0 to 1.2 mm are plotted in Fig. 3.7b. In all the cases, the superposed fringes contrast was > 0.97. The data presented in figures 3.7(a-b) conclusively show that in phase mask based proximity mode writing of FBG, the writing beam pointing has insignificant role to decide the net induced refractive index modulation. The more serious issue is the spatial coherence of UV writing beams, discussed in section 3.1.

3.2.3 Phase mask-Talbot interferometer's fringe stability

In an ideal situation of zero pointing ($\delta\theta$ =0), FBG writing i.e. refractive index modulation/Bragg reflectivity in region D_2(fig.3.8a) will be same as in region D_1 However, in view of finite beam pointing, the situation is very different. Significant fringe shifts are likely to occur in region D_2 in view of long optical path length involved.For $\delta\theta$ =0, the midpoint of region D_2 is located at a distance x = S cot α from phase mask where S is the separation distance between two parallel mirrors M_1-M_2 and $\alpha = \sin^{-1}$ (λ/d). Fluctuation of angle of incidence around $\delta\theta$ = 0 leads to path difference variation at point $P_2(x,y)$ between the two ray paths.

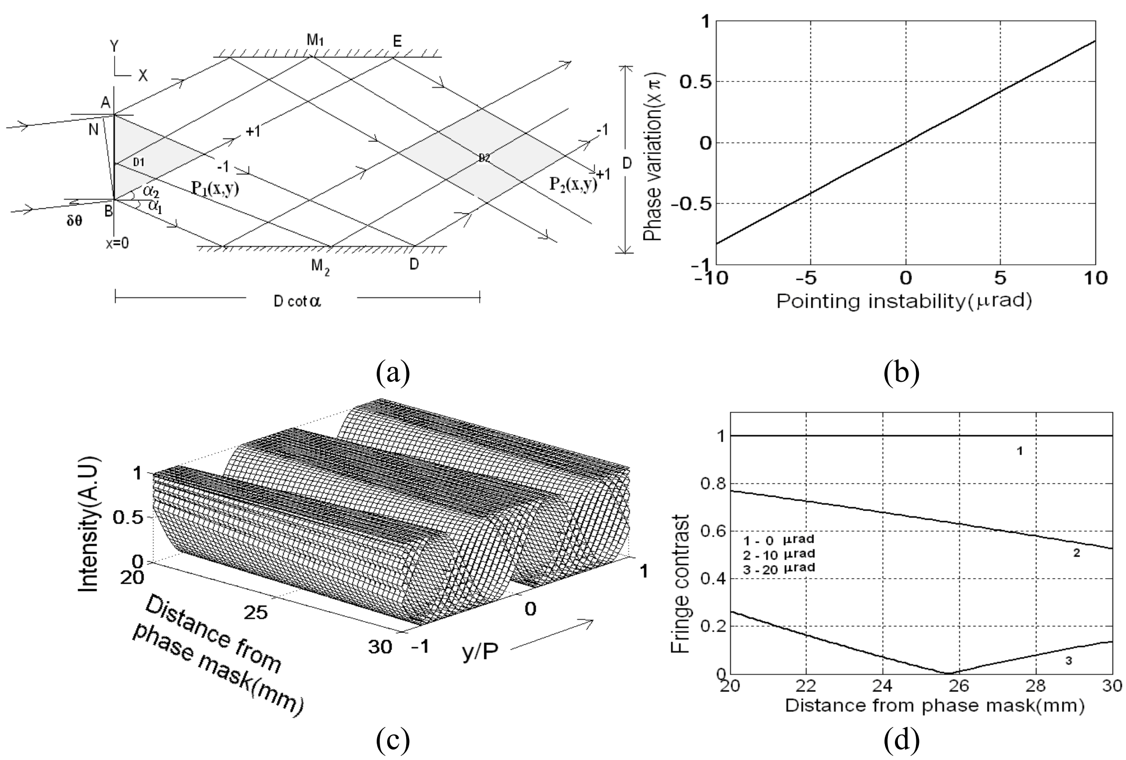

Figure 3.8: (a) Schematic of UV beam incident on phase mask at different angles; simulated (b) phase variation vs. pointing angle in Talbot region (c) fringe intensity positional fluctuation for pointing angles up to ± 5 μrad (d) average fringe contrast vs. distance from phase mask for different beam pointing angles 0-20 μrad.

The intensity distribution in the region D_2 is given by equation (3.12) as,

$$I = 2I_0 (1+ \gamma_C \cos [2ky\lambda/d - k.(x - S \cot \alpha) (\cos\alpha_2 - \cos\alpha_1) +\delta] \tag{3.27}$$

$$\text{where} \quad \delta = -k [\{x (\tan \alpha_1 + \tan \alpha_2) - 2S\} \delta\theta + x (\sec \alpha_1 - \sec\alpha_2)] \tag{3.28}$$

where α_1 and α_2 are given by equation (3.23) & (3.24). Fig. 3.8b shows the plot of net phase shift $[\delta - k.(x - S \cot \alpha) (\cos\alpha_2 - \cos\alpha_1)]$ with the beam pointing instability ($\delta\theta$) at the middle of region D_2 at y=0 and $x = S \cot \alpha = 24.2$mm (S =6mm, $\alpha = \sin^{-1}(\lambda/d)$). For $\delta\theta = \pm 10$ μrad, the phase shift is of the order of $\pm 0.9 \pi$. The D_2 region extends from $x = (S - W/2) \cot\alpha$ to $x = (S + W/2) \cot\alpha$, where W (= 5 mm) is width of incident beam. Fig. 3.8c shows fringes shift in the range of x from 20 to 30 mm for beam pointing of ± 5μrad. Increase in fringes shift with the distance of FBG plane from the phase mask is obvious. Fig.3.8d shows the fringe contrast estimated from equation (3.22). In view of large optical path length, there is significant loss of fringes contrast even for small beam pointing angle of less than < 10 μrad [185]. The same calculations holds for UV beam splitter and UV reflecting mirrors based conventional two arm interferometer.

3.2.4 Biprism interferometer fringe stability

Assume that a plane wave incident at an angle $\delta\theta$ (with x-axis) on the biprism (fig 3.9a). The refracted beams trace angle α_1 and α_2 with x-axis. Each ray passes through three regions: before the prism, in the prism, and after the prism. Using Snell's law,

$$\alpha_1 = \sin^{-1}(n \sin (A - \sin^{-1}(\sin \delta\theta/n))) - A \tag{3.29}$$

$$\alpha_2 = \sin^{-1}(n \sin (A + \sin^{-1}(\sin \delta\theta/n))) - A \tag{3.30}$$

The intensity distribution in overlapping region is expressed as,

$$I = 2I_0 [1+ \cos\{k\, y\ (\sin\alpha_1 + \sin\alpha_2) - k\, x\, (\cos\alpha_1 - \cos\alpha_2) + \delta\}] \tag{3.31}$$

$$\text{where,} \quad \delta = k\{[n\, DE + OE \sin (A + \sin^{-1}(\sin \delta\theta/n)] - [FB + nBC + OC \sin (A - \sin^{-1}(\sin \delta\theta/n)]\} \tag{3.32}$$

It is the net phase difference, [δ - kx (cosα_1 - cosα_2)], that decides the fringe shift at FBG plane. For the typical values, A = 24^0, n_p =1.5, λ = 255 nm, the fringe width is about 0.53 μm. Fig. 3.9b shows the net phase shift vs. beam pointing angle ($\delta\theta$) at a fringe plane located at x = 10 mm for the given parameters (A = 24^0, n_p =1.5, λ = 255 nm, biprism height 2d= 20 mm, incident beam width 2W = 10 mm).

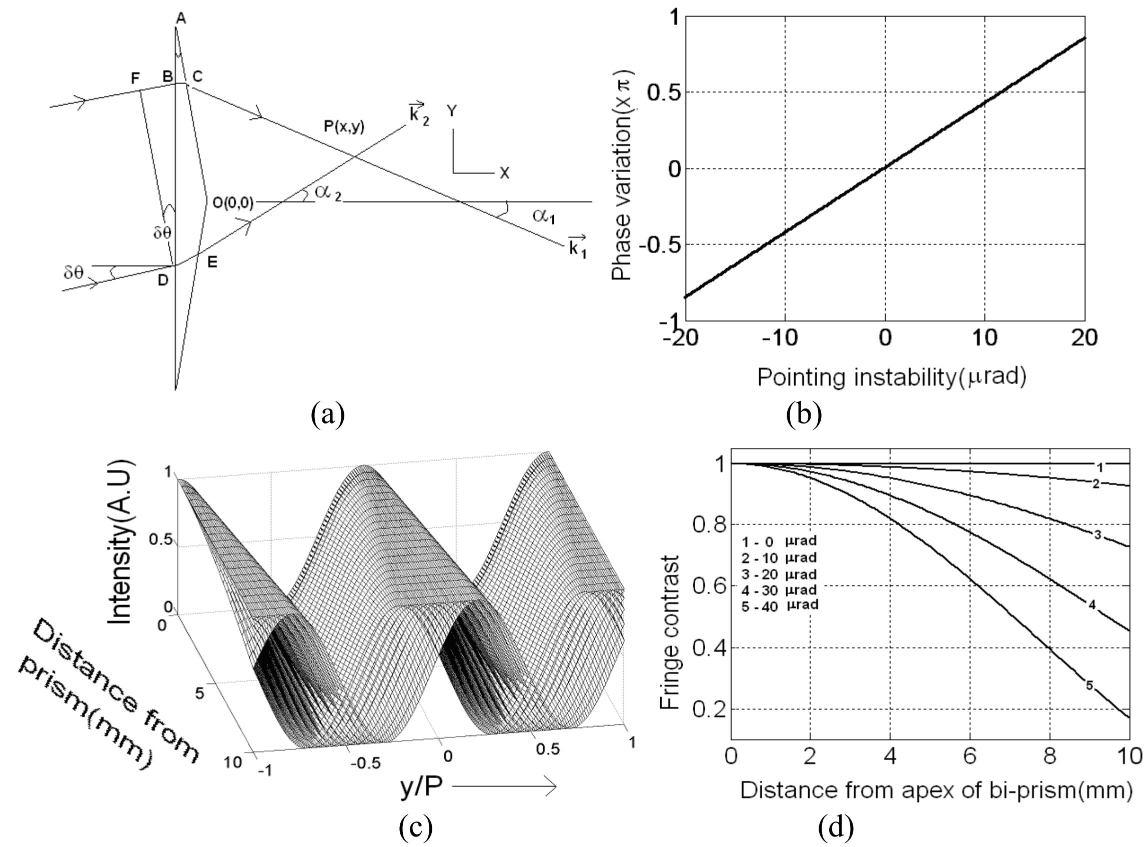

Figure 3.9: (a) Schematic of UV beam incident on biprism at different pointing angles; simulated (b) phase variation vs. pointing angle (c) fringe intensity positional fluctuation for pointing angles± 10 μrad (d) average fringe contrast vs. distance from biprism for different pointing angles 0-40 μrad.

The particular FBG writing plane is chosen as it represents the plane of maximum beam overlap [x = W (cot α - tan A)/2], beyond apex (x = 0) of biprism. The fringe width is about 0.53 μm. As expected, at same location, the phase shift (hence fringe shift) linearly increased with increase in beam pointing angle. It is of order of ± 0.5 π for beam pointing of ± 10 μrad and ± 0.8 π for ± 20 μrad.For a given beam pointing, the fringe shift increases as the fiber location (x) is moved from biprism apex (x = 0, phase shift =0) to further beyond (fig. 3.9c). The resultant fringe instability $(\Delta i)_{BP}$ is given as [185],

$$S_{BP}=2x\,(\sin\alpha)\,\delta\alpha / \lambda = 2x\,(\sin\alpha)\,[\cos A / \cos(\alpha+A)]\,\delta\theta/\lambda \qquad (3.33)$$

where $\alpha = \sin^{-1}(n \sin A) - A$. From x = 0 to 10 mm, the fringe instability increased from 0% to ~ 37 % for beam pointing of ± 10 μrad. At x = 10 mm, the fringe instability increased from about 18.6 % to 80 % as beam pointing of is increased from ± 5 μrad to ± 20 μrad. At higher beam pointing instability, the UV fringes induced refractive index modulation contrast will be diluted. The average fringe contrast of superposed fringes can be obtained from eqn. 3.22 by replacing the $\Delta\phi$ by $[\cos A / \cos(\alpha + A)]\Delta\varphi$. Hence [185],

$$\gamma(x, \Delta\phi) = \mathrm{sinc}\,[k\, x\, \Delta\varphi \sin\alpha \cos A / \cos(\alpha+A)] \qquad (3.34)$$

Fig. 3.9d show the variation of average fringe contrast with the variation of phase-mask fiber plane distance for the beam of different pointing of 0, 10, 20, 30, 40 μrad. It is seen that the larger the beam pointing angle/ phase-mask fiber plane distance, greater is the loss in fringes contrast as expected. At x = 10 mm, for ± 5 μrad beam pointing, the contrast is still high at 0.92, however it drastically drops to < 0.2 for ± 20 μrad beam pointing.

Table 3.1: Comparative data on interferometers of different length for beam pointing angle of 20 μrad (± 10 μrad) and fringe pitch of 0.530μm

Interferometer length	1 mm	10 mm	24 mm
Phase shift	0.077π	0.85π	1.997π
Fringe instability	3.7%	42%	99.8%
Averaged fringe contrast	0.98	0.728	0.07

It is worth pointing that in Biprism based FBG writing, in the region within maximum overlap ($x \approx$ 10 mm, for 2W= 10 mm), there is a compromise between the grating strength and grating length. Closer the fiber to prism apex, higher is the fringes contrast (higher refractive index modulation) but lower is the grating length. Maximum grating length is obtained at maximal overlap region, however fringes contrast is moderate. Beyond maximal overlap region (x> 10 mm) there is continuous fall in both fringes contrast and gating length significantly affecting grating reflectivity. The conclusions arrived in this section are also valid for all other interferometers of long path length such as pure mirror based two arm interferometer with initial beam spitted by a partially reflecting mirror, also known as holographic interferometer. The picture so far emerged from the theoretical analysis is summarized in table 3.1. Length of interferometer is chosen as the guiding parameter rather than differentiation based on their different types. The beam pointing angle of ± 10 μrad was chosen, a typical value for CW or pulsed lasers used in FBG writing. The conclusion from this table is self explanatory.It is worth mentioning that the actual measurement of beam pointing stability will be prone to some errorsdue to least count (± 1 pixel/ ± 6.45 μm) of the measuring CCD, fluctuation in air path and mechanical vibrations. These errors are of the order of ± 1 μrad. The computed relative error in the fringe instability [ΔS/S] due to measurement error of (±)1 μradfor the three beams of pointing stability 8 μrad, 22μrad and 45 μradare ±0.125, and ±0.045 and ±0.02 respectively. The relative error is higher for laser beam of lower beam pointing instability.

3.3 Test (experimental) results on fringes instability and contrast dilution

The results presented in analysis section for different interferometers, are for fringe pitch of about 0.5 μm in order to have C –band (≈ 1550 nm) FBG writing. These small separation fringes are difficult to resolve by imaging on the CCD due to practical limitations on resolution of optics. Hence about 14.6 μm separation fringes produced by a 2^0 angle biprism, with 510 nm incident wavelength were studied (Fig. 3.10) to see the role of beam pointing instability on the fringe shift of the interference pattern.

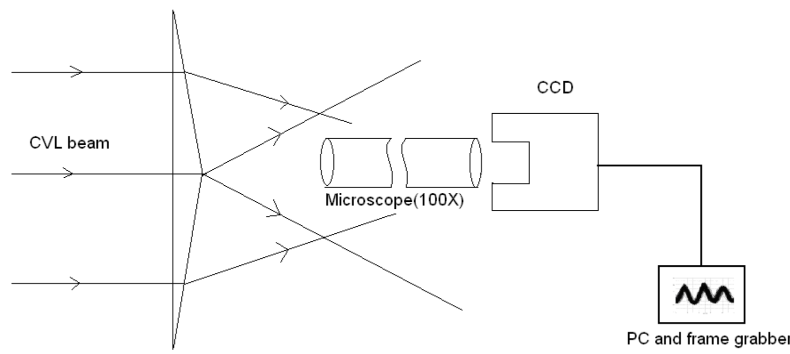

Figure 3.10: Schematic of experimental set up to measure fringe stability

The PBUR1, PBUR2 and GDFR CVL beams of pointing instability of 8, 22, and 45 μrad (fig.2.10b, Chapter 2) were employed [185] in the study. The collimated CVL beams of diameter 10 mm were made to incident on the biprism. The fringes thus formed beyond biprism apex, were magnified by a 100x microscope and recording on CCD (Pixelfly, qe, PCO AG, with user selectable acquiring time and pixel sizes of 6.45 μm x 6.45 μm). The ND filters were used to attenuate the intensity below the saturation of CCD.To estimate the magnitude of fringe shift vs. the distance from the apex of the biprism, it is essential to record the single pulse spatial shift of intensity distribution of interference pattern from the mean position. The single pulses were selected by a suitable gate period of CCD [166,185]. The stacked pictures of pulses were recorded as per the procedure described in (Chapter 2). By changing camera exposure time, the single pulse fringe contrast and average fringe contrast and fringe stability of different pulses could be estimated. The fringe instability was estimated as the ratio of the maximum shift in fringe peak from a chosen central position to fringes separation and studied at various locations in the fringe depth from the apex of the biprism.

For a beam diameter of 10 mm, the maximum overlap occurred about a distance of 143 mm from the apex of the biprism. Figs.3.11 (a-c) show the typical composite pictures of interference pattern of duration 650 s at a distance of 125 mm from the apex for the CVL beams of pointing instability of 8, 22 and 45 μrad respectively.

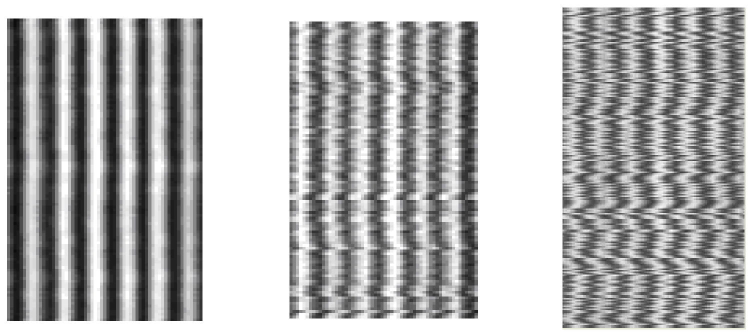

(a) (b) (c)

Figure 3.11: Composite pictures of interference pattern for beam pointing stability of (a) 8 μrad (b) 22 μrad and (c) 45 μrad at x=125 mm

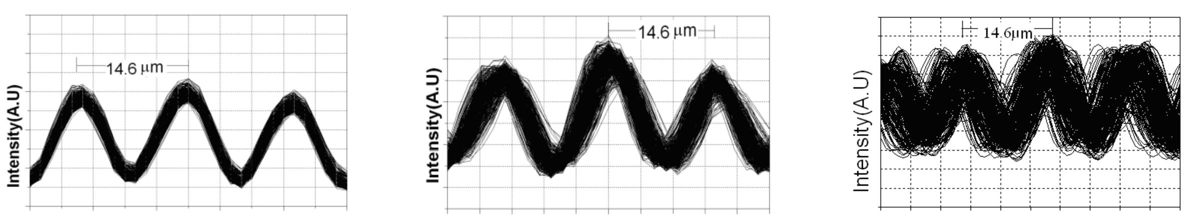

(a) (b) (c)

Figure 3.12: Intensity profile of interference pattern for beam pointing stability of (a) 8 μrad (b) 22 μrad and (c) 45 μrad at x=125 mm

The zigzag shape of the stacked picture is an indicative of fringe positional jitter which occurred due to the laser beam pointing instability. Figs. 3.12 (a-c) show the corresponding intensity profiles of composite pictures. The maximum position jitter is observed for the beam of pointing instability of 45 μrad. As the beam pointing stability reduced to 22 μrad, the jitter in the position of the maximum of interference pattern reduces. The lowest variation in the intensity maximum is observed for beam of pointing instability of 8 μrad. The fringe instability increased with increase in distance from the apex of the prism [185].

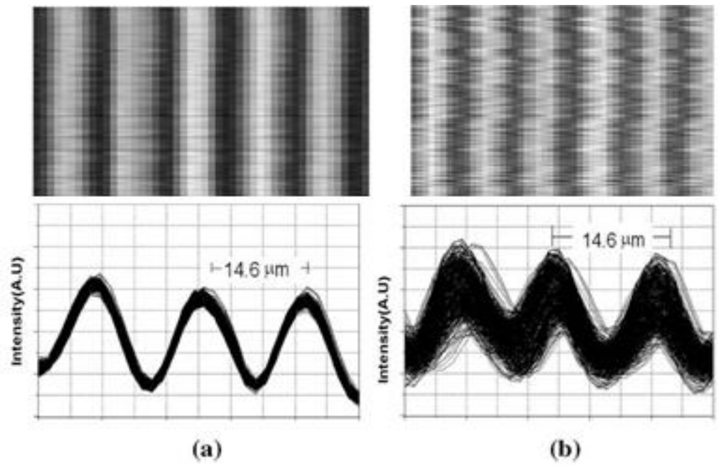

Figure 3.13: Positional jitter of interference pattern at distance of (a) x= 50 mm (b) 150 mm for pointing stability of 22 µrad.

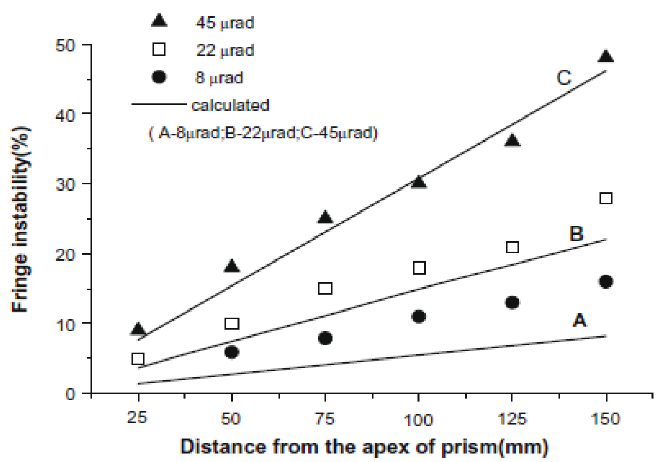

Figure 3.14: Theoretical (line) and experimental (data points) variation of fringe instability with the distance from the apex of a 2^0biprism for the beam pointing angle of 8 µrad, 22µrad and 45 µrad and λ = 510 nm

Figs. 3.13a and 3.13b show the positional jitter and intensity for the CVL beam of pointing angle 22 µrad at distance of 50 mm and 150 mm from the apex of the biprism, respectively. It is clear that the fringe instability increased as the distance of fringe recording plane increased from the apex. Fig. 3.14 shows the plot of data points on fringe instability vs. distance from apex of biprism for different beam pointing disturbance. The fringe instability was estimated as the ratio of the maximum shift in fringe peak (over recording time of 650 sec) from a chosen central position to fringes separation of 14.6 μm. The corresponding theoretical results from equation (3.33) were overlaid as straight lines on the experimental points in Fig. 3.14.

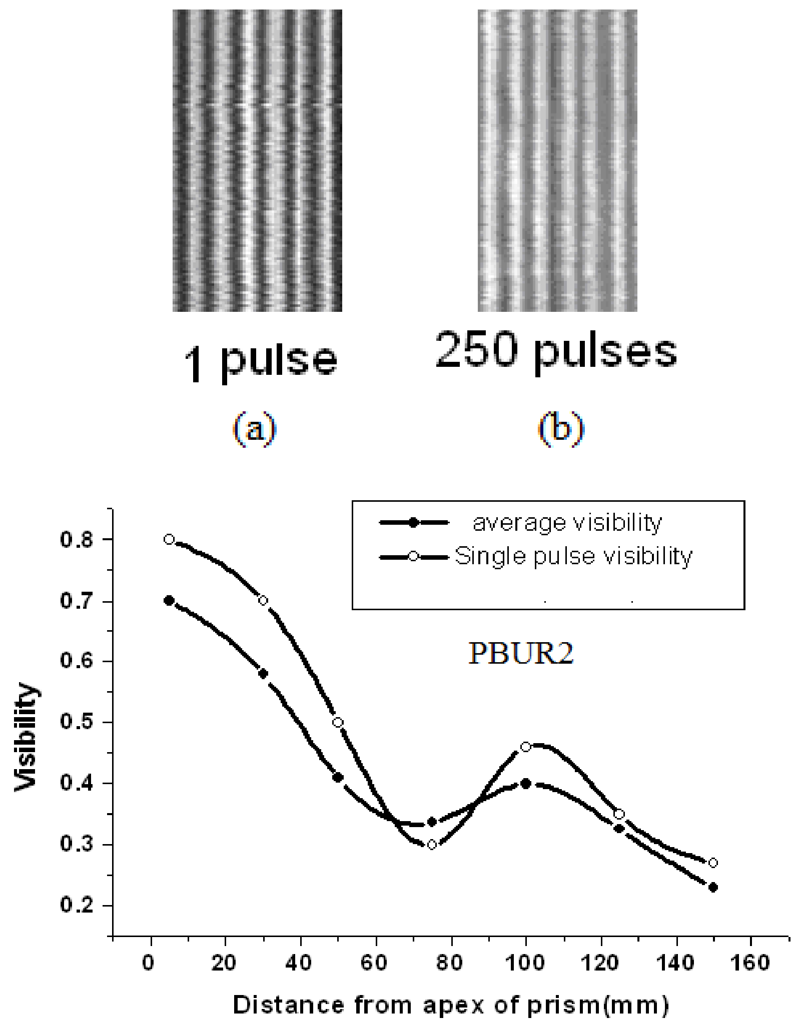

(c)

Figure 3.15: Time stacked picture of horizontal cursor at x = 100 mm for (a) exposure time 172 μsec (single pulse) (b) 45 msec (250 pulses) (c) Variation of single pulse and time average visibility (averaged over 250 pulses) of fringes with distance from biprism for PBUR2 CVL beam.

The trends in experimental results are in good agreement with that calculated. There is a little discrepancy in the exact calculated and experimental fringes instability values, especially for lowest beam pointing of 8μrad. This is probably due to the assumption, in the theoretical calculation, of uniform distribution of beam pointing angle within the envelope ($-\Delta\varphi/2<\delta\theta<\Delta\varphi/2$) while in the experimental case this distribution is more like a peaked Gaussian [fig. 2.10b].

It is clear that the beam pointing instability of significantly affects fringe stability, particularly at larger distance employed in prism based FBG writing from phase mask. The time average fringe contrast is diluted due to fringe positional zitter. Fig.3.14a and3.14b show composite stacked picture of line image for single pulse and that of 250 pulses (camera exposure time 45 msec). It is apparent from the figure that the multi pulses average fringe contrast decreased in compared to single pulse fringes contrast as expected. Fig. 3.15c shows the single pulse and time averaged visibility (averaged over 250 pulses) of fringes at with increase in distance of fringe plane from the biprism for 10 mm diameter PBUR2 CVL beam. Same trends are observed for all CVL beams. The inferences drawn for the test are directly extrapolable to UVs beam utilized for FBG writing.

3.4 Conclusion

The fringe contrast and fringe stability attributed to incidence laser beam spatial coherence and pointing stability are analyzed for FBG writing phase mask and prism interferometers. The fringe contrast is significantly affected by partial spatial coherence of the UV beam. Poorer the spatial coherence, larger will be the fringe contrast dilution. For a given spatial coherence, the net fringe contrast also depends on the location of the fiber from the interferometer. In general, the fringe contrast dilution is higher for larger distance from the beam splitter. For practical case of CVL-UV beams, the fringe contrast distribution is further complicated by the time evolution of spatial coherence within the pulse. In these cases, time averaged contrast dictates FBG writing capabilities. A qualitative analysis on the effect of beam pointing instability on the positional fluctuation of interference pattern formed is presented. In this analysis, the effect of beam pointing instability on fringe shift, at a spatial location, is incorporated as slightly change in the angles between the two interfering beams. It is shown that the spatial shift increases as the position of FBG writing plane move away from the beam splitter. The fringe shift is directly proportional to variation in beam pointing angle and distance of FBG writing plane from the beam splitter. For typical FBG writing position, the effect of the angular beam pointing instability on fringe shift is minimum for phase mask and maximum for phase mask-Talbot interferometer fringes. For the Biprism, the effect of pointing stability was in between. Theoretical predictions are verified experimentally by studying the instability of fringes of 14.6 μm spacing formed by a 2^0biprism andPBUR1, PBUR2 and GDFR CVL beams (510 nm) of pointing instability 8 μrad, 22 μrad and 45 μrad respectively. This chapter provided guidelines for the effective FBG fabrication for the present thesis work, as described in next few chapters, as well as supplementing the published literature in the field.

Publications based on this chapter

1. "Analysis of ultraviolet fringes contrast on first and second order Fiber Bragg gratings written by prism interferometers" **R. Mahakud**, J. Kumar, O. Prakash and S. K. Dixit Opt. Engg. **2013**, 52, 0761141-6.
2. "Analysis on the laser beam pointing instability induced fringe shift and contrast dilution from different interferometers used for writing fiber Bragg grating" **R. Mahakud**, O. Prakash, S.K. Dixit and J.K. Mittal, Optics Commun., **2009,** 282, 2204–2211.

Chapter 4

Experimental studies on writing of FBGs by phase mask technique using CVL-UV beam

4.0 Introduction

The phase mask technique is the most common method of FBG fabrication [197-198]. This easy to handle, single optical element interferometer is a very robust and stable setup for wavelength reproducible Bragg grating writing as required in mass production [67-70]. As brought out in chapter 3 and also from previous published works, the spatial coherence of the writing beam plays a critical role in phase mask based FBG fabrication [182-183]. This issue is particularly relevant in case of a partially coherent CVL-UV (255 nm) source which has also pulse to pulse divergence and pointing fluctuations as discussed in Chapter 2. Also, the FBG fabrication by kHz repetition rate but low energy (10s of μJ) 255 nm pulses require millions of UV pulses in typical writing period of 10 minutes. This is because the 255 nm photon energy lies at the edge of 240 nm absorption band of Ge-or B/Ge co-doped photosensitive fibers. This fact also puts constrains on the short/long term stability of high repetition rate UV source. The above discussed FBG writing complications are further compounded if the aim is to write the grating at a safe distance from the phase mask, to prevent its damage. In this case as well as in writing tilted Bragg gratings, the demand on the coherence of UV source is stringent. In addition the strategy of planning FBG writing experiment is different depending upon which grating types i.e. I, IIA or II is to be written [197-200]. These FBG types have different temperature sustainability [201-202]. The writing of FBG is a dynamic process passing through stages such as growth, saturation and decay of refractive index modulation [203-205]. The process dynamics is crucially linked to writing beam spatial coherence and fluence. Type I grating are usually first grating to be written in normal writing conditions [16]. In some fiber types, prolonged exposure of type I FBGs can result in partial or complete grating erasure, followed by a new spectral formation known as a type IIA FBG [206-207]. Type II FBGs are generally produced as a result of a single high-energy pulse such as from Excimer laser, which causes damage to the glass in the core of the exposed fiber [208-210]. This is not feasible from low pulse energy CVL UV radiations. The present chapter focuses on writing of Type I, type IIA and tilted FBGs with in house developed CVL UV sources as described in chapter 2.

This chapter presents the experimental investigations on FBG fabrication by phase mask technique, using 255 nm UV beams of different spatial coherence. Both the germanium and germanium – boron co-doped photosensitive fibers are employed in the FBG study. The chapter starts with brief description of experimental arrangement, FBG interrogation technique and experimental method. The growth trends of refractive index modulation and average effective refractive index are studied for type I/IIA gratings. The growth characteristics of gratings written by the UV beams of different spatial coherence are compared. The fabrication of tilted gratings is studied. The fiber was placed at different distances from the phase mask to write FBGs of different characteristics. Gratings were written at different wavelengths (~ 1540 nm, ~ 1054 nm) by phase masks of different pitch. The effect of fiber composition on FBG fabrication efficiency is studied. The evolution of FBG spectrum with UV fringes exposure is studied. The effect of various parameters on grating growth, saturation and evolution of FBG spectrum has been outlined for the analysis which is presented in the next chapter.

4.1 Experimental arrangement for FBG fabrication

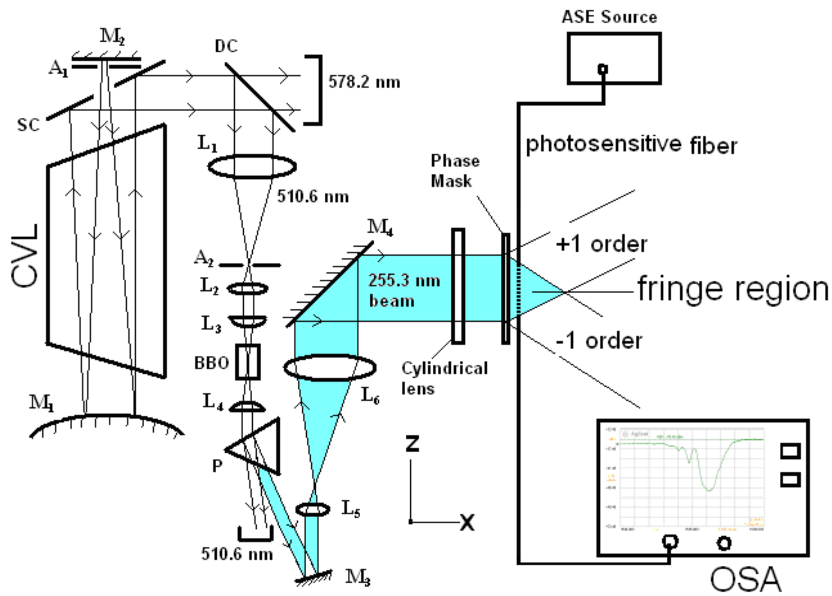

(a)

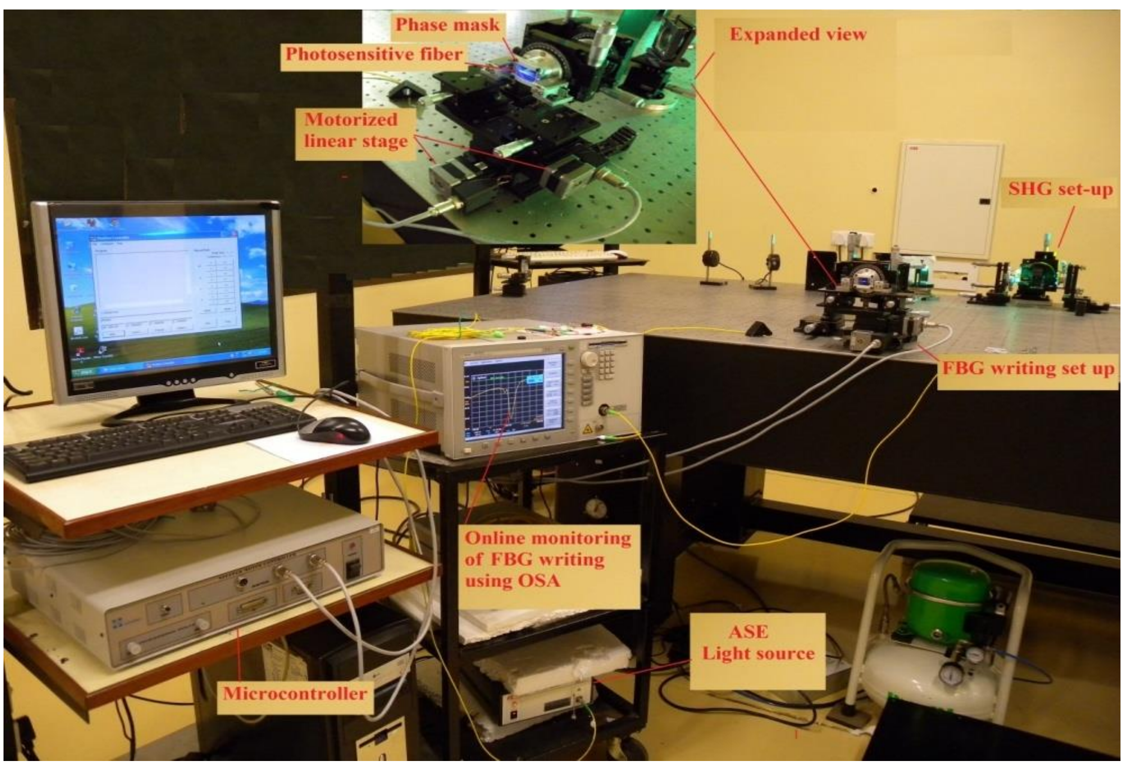

(b)

Figure 4.1: (a) Schematic and (b) experimental set-up for FBG writing

The FBGs were written in different photosensitive fibers by standard phase mask technique. Fig. 4.1a shows the schematic of experimental set-up for FBG inscription. Fig 4.1b shows the experimental system photograph. The UV beam (wavelength $\approx$ 255 nm, pulse repetition rate = 5.6 kHz, pulse width ($1/e^2$) $\approx$ 30 ns) was generated from SH of CVL. The UV beam was magnified and collimated (to about 5 to 10 mm) diameter using UV-grade fused silica lenses L_5 and L_6 (fig. 4.1a). The magnified UV beam was focused by a cylindrical lens of focal length 75 mm to increase the UV energy density on the fiber core. The cylindrical lens focal length is not likely to have significant effect the FBG writing efficiency as long as the UV spot size on the fiber is kept same. The real time growth of transmission dip and shift in Bragg wavelength, with exposure time, was recorded for type I, type II and tilted gratings. The UV beams of different spatial properties were used in FBG fabrication. The important components used in FBG fabrication are described below.

(a) ***Writing UV beams-*** The UV1, UV2 and UV3 beams (255 nm) generated from second harmonic of PBUR1, PBUR2 and GDFR CVL beams, respectively, were used in FBG fabrication. As discussed in chapter 2, these UV beams are partially spatially coherent. FBGs were written by UV1, UV2 and UV3 beams to study the effect of spatial coherence and pointing stability on refractive index modulation saturation. Most of the other experiments focused on achieving high FBG reflectivity, were carried out using highly spatially coherent UV3 beam.

(b) ***Photosensitive fibers –***FBGs were written in non-hydrogenated germanium boron codoped and germanium doped single mode optical fibers, procured from different commercial farms, as tabulated in table 4.2. The doping concentration was different for different fibers. The typical fiber parameters are, core diameter 7-8µm, cladding diameter 125 µm, coating diameter 245 µm and cut-off wavelength 1100–1260 nm.

(c) ***Phase mask-*** The FBG writing in C-band has been carried out by a standard phase mask (manufactured by Isben, zero order suppression at 248 nm) of pitch 1.060 μm. At the normal incidence, there existed nine diffracted orders (0, ±1, ±2, ±3, ±4). The diffraction efficiency of different orders of the phase mask, illuminated by a UV beam of wavelength 255 nm, was measured by placing an optical detector behind the phase mask. The measured phase mask diffraction efficiency in zero, ±1, ±2, ±3, and ±4 orders with respect to total power in all the orders were approximately 0.5 %, 40.0 %, 2.5 %, 5.5% and 1.5 % respectively. Another phase mask of pitch 0.725 μm, which diffracts up to ± 2 orders, has been used in to write FBG at Bragg wavelength of ~ 1054 nm. The measured diffraction efficiency in zero, ±1, ±2 orders are 1.0 %, 42.0 %, and 7.5 %respectively.

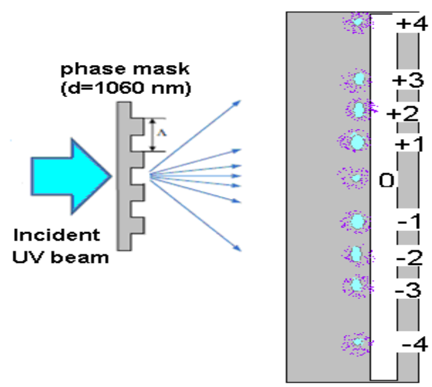

Figure 4.2: Diffraction of light in different orders by phase mask of pitch 1.060 μmwith 255 nm incident beam

(d) ***Mountings*** – The CVL UV based FBG fabrication requires millions UV pulses over a time period of 2-10 minutes. The precision in design and fixing of the optical mounts is critical in FBG writing. In the present experiment, fiber ends were mounted on two translation stages to provide movement in vertical and horizontal movement. The fiber is supported over the entire length of the grating to be fabricated in a long V-groove, kept firm by magnetic clamp. The V-groove is fabricated in two pieces of brass slab, assembled together with a small gap between them. The phase mask mount was additionally placed on rotational mount, which can move in vertical direction. For writing multiple gratings in the same fiber, the fiber is translated across the fringes, both backward and forward. The fiber holding translation stage based mounts, both in X and Y direction, could be moved precisely. For this, a microcontroller based computer controlled FBG writing set up was installed and used. The least count of the movement in X and Y direction was 2μm. The maximum ranges that could be moved, in both directions were 25 mm each. The cylindrical lens was mounted on three axis translation stage for alignment of focal spot along the fiber. The FBG fabrication efficiency is crucially linked to relative movement (vibration) of the CVL laser source, SHG set up and FBG writing set up. All the major systems in FBG fabrication namely the CVL, the second harmonic setup, phase mask writing set and fiber manipulator are mounted on a single vibration free table (Standa, Lithuania, table top dimension: 1.5 m x2.4 m x 0.3 m, table top first resonance frequency: ~ 200 Hz, pneumatic isolator resonance frequency: 2 Hz). Both these resonance frequencies were far away from the floor/ ambient vibrations (~ 10–50 Hz) and the acoustic noise from laser repetition rate (5.6 kHz). The whole experiment was carried out in a clean room.

4.2 General discussion on optimizing FBG writing

The FBG fabrication efficiency is sensitive to mutual alignment of fiber, phase mask, cylindrical lens and incident UV beam [16]. The misalignment affects wavelength repeatability and FBG reflectivity. The UV beams are line focused by a cylindrical lens to increase the power density on the fiber. When the line focus and fiber are misaligned, the effective grating length decreases due to partial overlaps. The tilt of the grating planes cause loss in the main mode reflection [207]. The FBG reflectivity will be reduced. The cladding (of diameter 125 μm) also acts like a cylindrical lens. For a plane wave incident on the phase mask, the incidence +1/-1 beams are oblique (~ 13^0) to the fiber cross-section. Thus +1/-1 beams focusing are highly astigmatic in the fiber core. However, the interference fringe patterns formed in the fiber core are a series of planes with an equal spacing due to symmetry. If incident plane UV wave front on the phase mask is not parallel to the normal of the phase mask, then +1 and -1 beams are not symmetrical to the fiber. The fringe planes will be tilted to the fiber axis. The Bragg resonant wavelength differs from the designed wavelength affecting the wavelength repeatability. The tilting of refractive index planes increases loss in the main mode due to decrease in coupling coefficient. For a diverging UV beam incident symmetrically on the phase mask, the fringe tilt increases from centre of the FBG towards edges introducing chirp in the FBG spectrum. These considerations are kept in mind while writing FBG in the present work.

4.3 Arrangement for FBG spectra recording

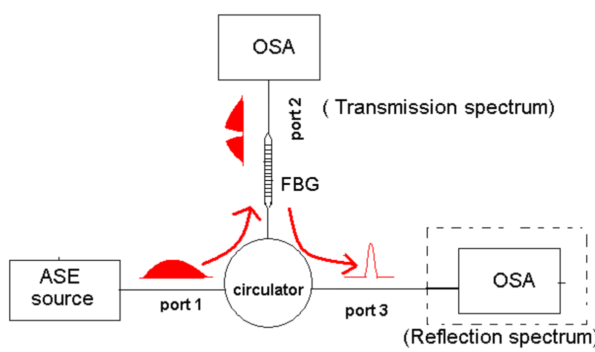

Figure 4.3: Schematic of recording of FBG spectra

The FBG spectra were recorded with the help of an optical spectrum analyzer (OSA), a broadband amplified spontaneous emission (ASE) source and a three port circulator in suitable configuration. A schematic of the optical arrangement is shown in fig 4.3. All the connections in the system are through single mode optical fibers. The broadband light source is connected to one of the three port circulator. The second arm of the circulator is connected to OSA. The light from the broadband source enters the optical circulator through port 1 and leaves through port 2. The FBG, in the fiber segment, is connected to port 2 of the circulator. To record transmission spectrum, one end of the fiber segment incorporating FBG is connected to the OSA and the other end to the port 2 of the circulator. To observe reflection spectrum, the fiber attached to port is connected with OSA. The FBG is illuminated by a light source with a broad spectrum to observe reflection / transmission spectrum.

(a) ***ASE source-*** An Amplified Spontaneous Emission (ASE) broadband light source [ASE-FL-7002, Fiberlabs] was used for C-band FBG interrogation. The output power of this source, based on erbium doped fiber, is 20 mW distributed over the range of 1525 nm to 1600 nm (C+ L band). The Ytterbium-doped fiber based 1050 nm ASE light source (Opto link Corp Ltd) with wavelength range 1030 nm ~ 1070 nm was used to detect the transmission spectrum of the FBG written at Bragg wavelength 1054 nm.

(b) ***Optical circulator*** - In the experiment, three port optical circulators (Optolink corporation) operating in the wavelength range 1520-1625 were used. Light entering in port 1 is emitted from port 2. If some of the emitted light is reflected back to the circulator, it exits from port 3.

(c) ***Optical spectrum Analyzer (OSA)*** **-** The OSA used in the experiments was manufactured by Agilent [86142 B]. The specification of Optical spectrum analyzer (Agilent 86142B) are range - 600 nm to 1700 nm , resolution – 0.06, 0.1, 0.2, 0.5, 1, 2, 5, 10 nm, amplitude sensitivity : - 90 dBm (1250-1610 nm wavelength range) and -75 dBm (900-1250 nm wavelength range), applied input fiber: single mode (9/125 μm) and maximum measurement power: +15 dBm. The wavelength measurement accuracy of OSA is ± 10 pm.

The shape of the intensity vs. wavelength diagram (i. e. the light spectrum) is displayed on the OSA monitor. The spectrum analysis is carried out by sweeping over a wavelength range, defined preliminarily by the operator. The principal parameters for the OSA are: (a) Centre wavelength: central value of the wavelength interval to be swept (b) Sweep width: amplitude of the wavelength interval to be swept (c) Resolution: amplitude of the wavelength interval to which a single intensity data point is assigned and (d) Reference level: noise level for the current analysis. All the above listed commands are adjusted by operating on the instrument's built-in control panel.

(e) ***Fusion splicing*** – For continuous optical path of transmission, single mode optical fibers are joined in the FBG interrogation network. In the experiment, the photosensitive fiber segments in which FBGs written were joined to patch cords by Arc fusion splicer (SWIFT S3, ISLINTECH).

4.3.1 Measurement and calculation of different FBG parameters

The written FBG length (L), when the fiber is placed in the plane at a distance x, from the phase mask is given as,

$$L(x) = 2(W\text{-}x \tan \alpha) \tag{4.1}$$

where α [$=\sin^{-1}(\lambda_{uv}/d)$] is diffraction angle, d is phase mask period and 2W is UV beam diameter incident on the phase mask. The depth (D) of fringe region behind the phase mask is given as, $D = W \cot\alpha$. When the fiber is tilted by angle (θ) in the fringe plane with one end of the FBG at distance x_o from the phase mask, grating planes are tilted. The length of tilted (blazed) grating is given as,

$$L= [2W \cos\alpha\text{-}2x_o] /\cos (\alpha\text{-}\theta) \tag{4.2}$$

The reflectivity of the fiber Bragg grating is calculated from the observed transmission dip (T_d), given as

$$R = [1\text{-}10^{(-Td/10)}] \qquad (4.3)$$

The amplitude of refractive index modulation (RIM),Δn,in the fiber core is calculated from FBG reflectivity R, grating length L and Bragg wavelength λ_B, using the relation [16]

$$\Delta n = (\lambda_B/\pi\eta L)\tanh^{-1}(R^{1/2}) \qquad (4.4)$$

The change of mean refractive index (<Δn>) was estimated from the relation

$$<\Delta n> = \Delta\lambda_B.\ n_{eff}/(\eta\lambda_B) \qquad (4.5)$$

where $\Delta\lambda$ is Bragg wavelength shift measured during writing. Where η is mode overlap integral [14-16]. Assuming the field distribution in the fiber as Gaussian, the parameter, η ~ 1-exp $(-2a^2/w^2)$, where $2a$ is core diameter and $2w$ is the mode field diameter [211]. The parameter η can be estimated from the expression [52]

$$\eta = \pi^2 a^2 K^2 / (\lambda_b^2 + \pi^2 a^2 K^2) \qquad (4.6)$$

where K is the numerical aperture (N.A) of the fibre. For typical fibers used, the parameter η is about 0.85. This value has been taken for calculation in the experimental studies. The refractive index modulation contrast (Δn_{mod}/ <Δn>) is defined as the ratio of refractive index modulation to induced average refractive index. The bandwidth of the FBG was estimated from the first zeros on both side of the FBG reflection spectrum. The UV power incidence on the phase mask was measured by placing a power meter before the phase mask. The spot size of the UV beam at fiber position was measured by putting a fluorescent Lumi glass (M/S Sumita Glasses, Japan) at the fiber location. The accumulated UV fluence was estimated from the relation $F = NI\tau$; where I – peak intensity, τ - pulse duration, N = No of pulses = f x t [f is pulse repetition rate (5.6 kHz), t is time of exposure in sec].

4.4 Experimental results and discussion on FBG fabrication

4.4.1 FBG growth characteristics

Figure 4.4 shows the evolution of transmission spectrum of a typical FBG at different exposure times. The types I FBG have been written in non-hydrogenated single mode photosensitive fiber (CMS-1550-R1) by standard phase mask (pitch 1060 nm) technique. The FBG was written at phase mask fiber distance of a ~ 0.8 mm. The FBG length was about 7 mm. Both the transmission dip and spectrum bandwidth increased with exposure time. The traces marked as 1, 2, 3 and 4 in the fig.4.4 corresponds to UV fluence of 0.1 kJ/cm^2, 0.5 kJ/cm^2, 1 kJ/cm^2 and 2 kJ/cm^2 respectively.

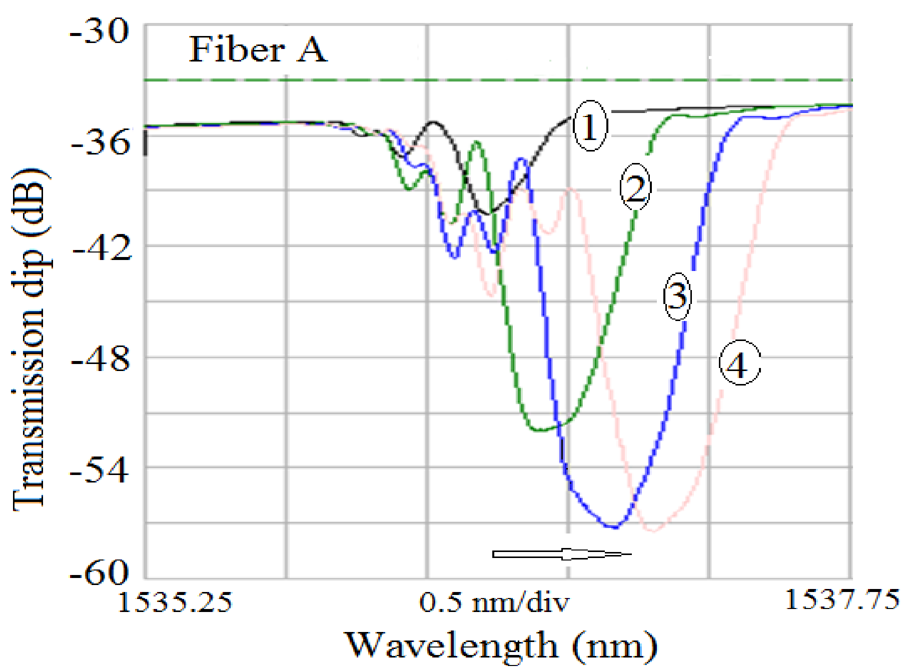

Figure 4.4: Evolution of transmission spectrum of a FBG with increase in fringe exposure

The Bragg resonant wavelength shifted towards red side during fabrication. The RIM was estimated from observed transmission dip (T_d).The average refractive index (RI) change ($<\Delta n>$) was estimated from Bragg wavelength shift ($\Delta\lambda_b$). The refractive index modulation contrast is defined as the ratio of Δn to $<\Delta n>$. Figs. 4.5a and 4.5b show the change in average

RI and RIM contrast with increase in refractive index modulation (increase in exposure time) respectively. With increase in accumulated fluence, the refractive index modulation contrast [= Δn/<Δn>] decreased. The Bragg resonant wavelength shifted by ~ 0.6 nm as the transmission dip increased from 5 dB (trace1) to 23 dB (trace 3) (fig.4.4). The estimated induced average refractive index increased by (6×10^{-4}) where as the refractive index modulation increased by (1.6×10^{-4}).

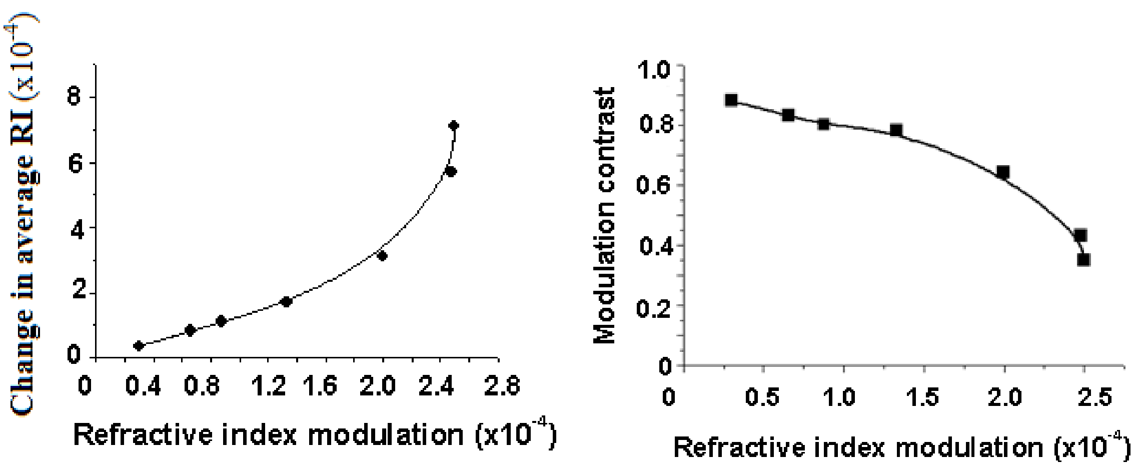

(a) (b)

Figure 4.5 (a) Change in average RI (b) modulation contrastwith growth of RI modulation

Thus the change of average refractive index was higher in compared to growth of refractive index modulation. The Bragg wavelength shift between trace 3 and trace 4 (fig. 4.4) is about 0.15 nm while the transmission dip was almost constant. Thus the growth of refractive index modulation with continuous UV exposure is in saturation phase. With further exposure, the induced average index increased and modulation decreased. The bandwidth of FBG increased with increase in refractive index modulation as apparent from the figure 4.4. The bandwidth increased from about 0.35 nm (trace1) to 0.65 nm (trace 3) as the cumulative fluence increased from 0.1 kJ/cm^{2}to 1 kJ/cm^2.

The gratings of different length could be written by changing the fiber position within the fringe depth. Typically, for highly coherent UV3 beam of 10 mm, the +1 and -1 beam overlap length extends up to 20 mm from the phase mask. However, the fringe contrast, fringe stability and FBG length decrease with increase in phase mask to fiber distance. Thus it is not sensible to write FBGs at higher phase mask to fiber distance as the expected refractive index modulation will decrease. However, the thermal stability of FBGs improves, when written by fringes of low contrast [191]. Figs.4.6a and 4.6b show the transmission spectrum of FBGs written at distance of 3 mm and 5 mm from the phase mask. The observed reflectivity and thus the saturated refractive index modulation of FBGs decreased with increase in phase mask to fiber distance, as expected.

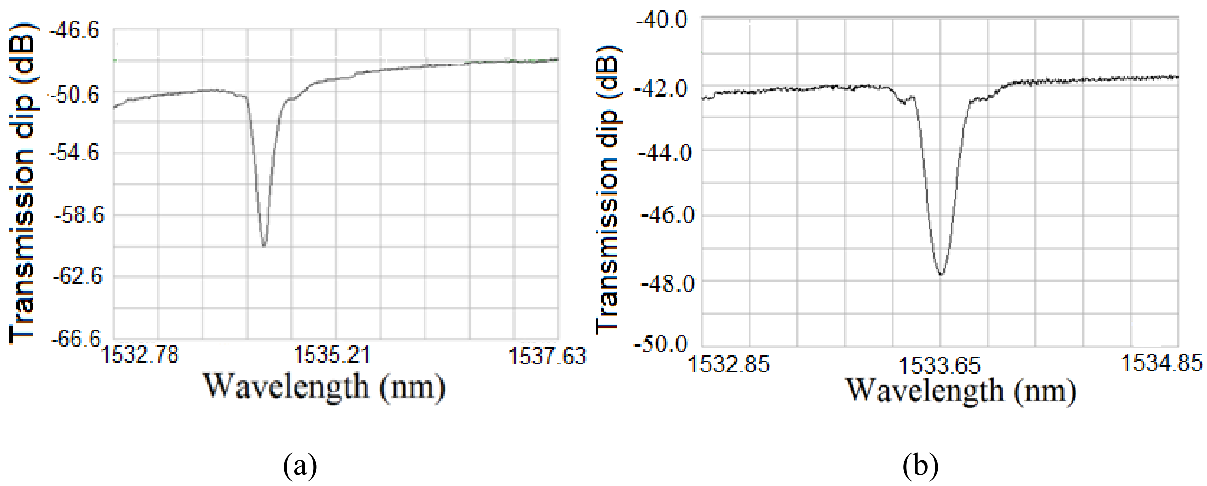

Figure 4.6 Transmission of FBG written at distance of (a) 3 mm (b) 5mm from phase mask

The observed transmission dips at saturation were 10 dB and 5 dB for FBGs, written at distance of 3 mm and 5 mm from phase mask respectively. However, it was observed that the increase in average index during fabrication, at same accumulated fluence, in both cases were almost same. This is because; the average refractive index change depends on exposure time while the induced RI modulation depends on both exposure time and fringes contrast.

To write FBGs of different length, the incident beam diameter was controlled by a variable aperture placed before the phase mask. The aperture selected the central portion of the beam. Fig.4.7a shows the observed reflectivity with increase in FBG length. The observed maximum reflectivity increased with FBG length (increase in diameter of the aperture). Fig.4.7b shows the RI modulation with increase in FBG length. The refractive index modulation was marginally higher for small aperture diameter. This is due to higher intensity at central portion of the UV beam where the beam uniformity is also better.

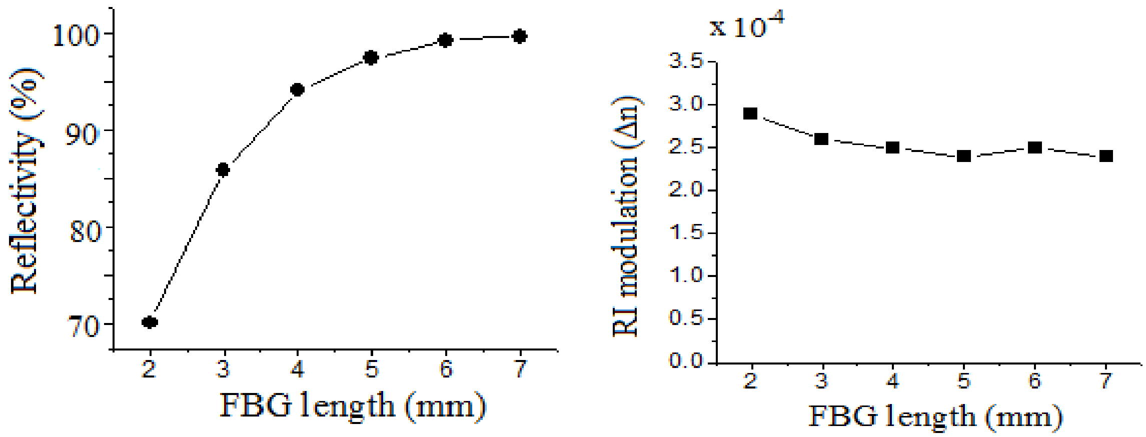

(a) (b)

Figure 4.7: (a) FBG reflectivity (b) refractive index modulation for different FBG length

Evolution of reflection spectrum – The evolution of reflection spectrum of a typical FBG at different UV exposure times are shown in fig. 4.8 (approximately at accumulated fluence of 0.2 kJ/cm^2, 0.8 kJ/cm^2, 1.6 kJ/cm^2, 3.2 kJ/cm^2 marked as a, b, c, d respectively) [212]. The FBG was written by UV2 beam in non-hydrogenated boron-germanium co-doped single mode fiber (GF1, Neufern), placed about 0.2 mm behind phase mask. The UV2 beam was chosen for this study as the beam uniformity was higher than that of UV3 beam. The reflection spectrum evolved with exposure time. The structure and strength of side lobes of the FBG changed with increase in UV fringes exposure. The spectrum profile of a low reflectivity FBG is smooth. The side lobes on the blue side of the spectrum appeared first. However as the UV exposure continued, the side lobes on red side of Bragg resonant wavelength appeared [fig.

4.8d].The saturated FBGs have side lobes on both side of the spectrum. The Bragg gratings with uniform index modulation have strong side lobes at either side of the central filtering spectral band [14-16].

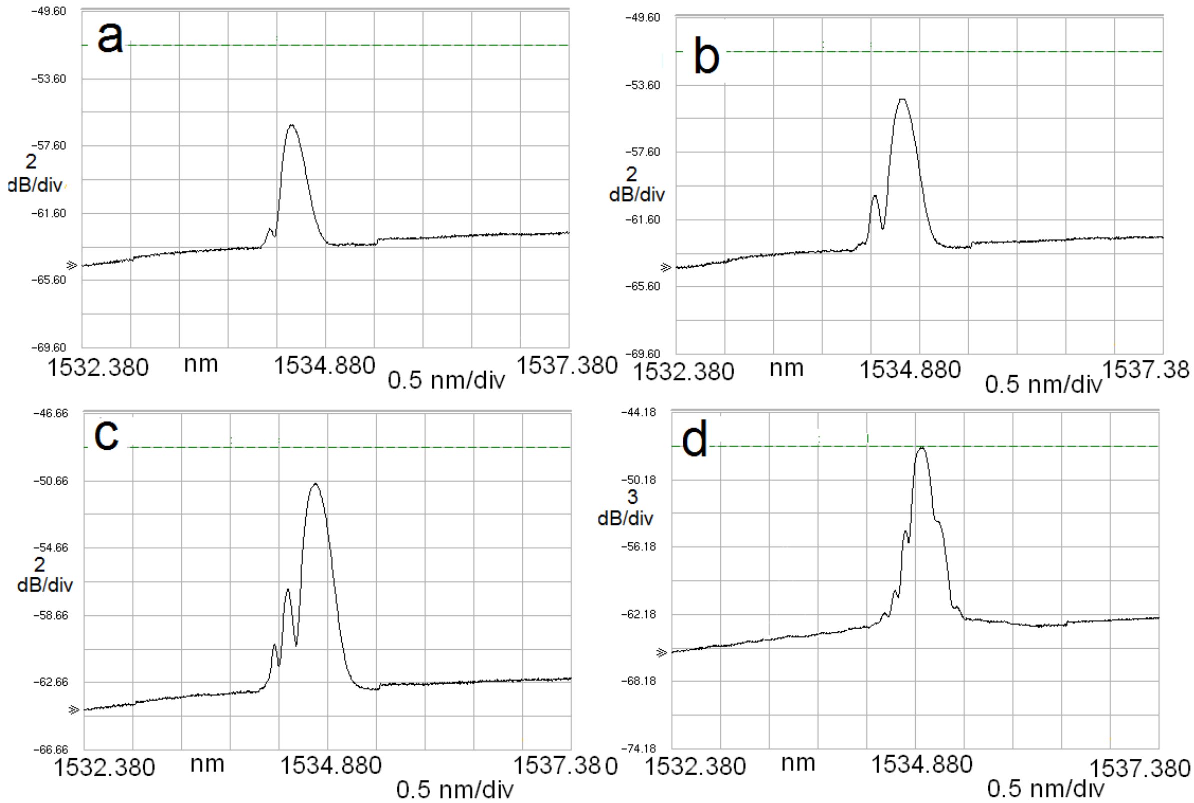

Figure 4.8: Reflection spectrum of FBG at different fluence at (a) 0.2 kJ/cm^2 (b) 0.8 kJ/cm^2 (c) 1.6 kJ/cm^2 (d) 3.2 kJ/cm^2

Bragg grating with Gaussian index modulation profile is smooth, but a structure appears on blue side of the spectrum [16]. However, the dynamic FBG spectral evolution may be attributed to nonlinear growth of UV induced refractive index with continuous exposure [213].The induced refractive index modulation and average index profile will be similar to the UV fringes contrast and mean intensity profile provided that the induced index change is linear. Because of nonlinear growth of photo induced refractive index, the modulation profile will change dynamically due to non uniform fringe intensity profile. This in turn will affect the evolution of FBG spectrum with increase in accumulated UV fluence. Some of these issues are discussed in the next chapter on theoretical analysis on FBG fabrication.

4.4.2 Effect of UV beam spatial coherence on refractive index modulation saturation

A comparative study was carried out on fiber Bragg gratings fabrication efficiency namely the peak reflectivity and rate of growth for UV1, UV2 and UV3 writing beams of different spatial coherence characteristics. The average UV power (220 mW) and phase mask to fiber distance of 0.8 mm and fiber type were kept the same. The type I FBGs were written in non-hydrogenated single mode photosensitive fiber (PS-RMS-50, core dopants: B_2O_3 and GeO_2) fiber.

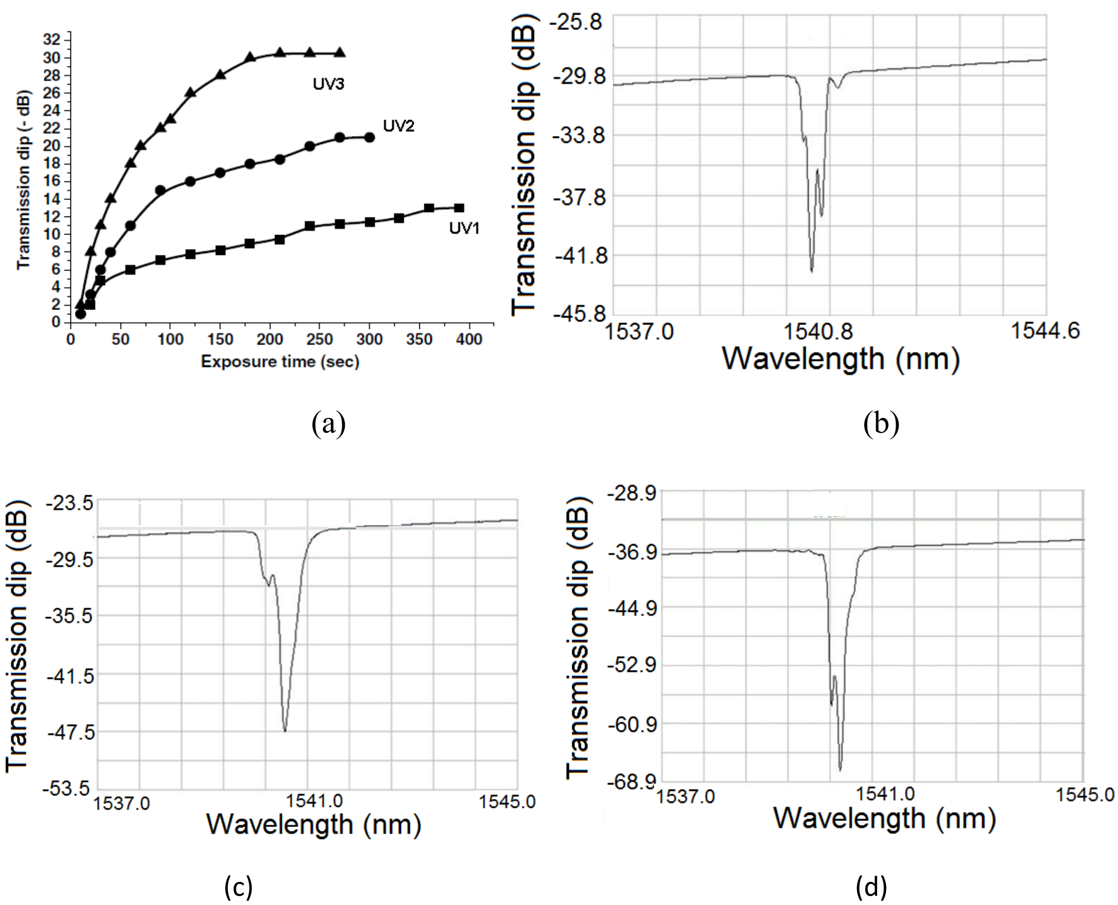

Figure 4.9: (a) Growth of transmission dip with UV exposure time and transmission spectrum of FBGs written by (b) UV1 beam (c) UV2 beam (d) UV3 beam

The phase mask of pitch 1060 nm, cylindrical lens of focal length 75 mm and collimated UV of diameter 10 mm were used in FBG fabrication. Fig. 4.9a shows the growth trends of transmission dip with UV fringes exposure time. These are different for different beams. The growth rate was initially steep. Typically in first 50 seconds, the observed transmission dip increased to 6 dB, 10 dB and 16 dB for UV1, UV2 and UV3 beams respectively. Beyond 50 s, the grating growth rate slowed down for UV1 beam, reaching maximum transmission of 13 dB in 400s. For UV2 beam, maximum transmission dip of 21 dB was obtained in 300 s. The highest transmission of 30.5 dB was observed in 210 s [128] for UV 3 beam. In every case, the growth rate reduced with continuous exposure as the induced refractive index modulation approached saturation. The typical transmission spectrum of typical FBGs written by UV1, UV2 and UV3 beams are shown in figs 4.9b, 4.9c and 4.9d respectively. The calculated inscribed FBG length at distance of 0.8 mm from the phase mask is 9.6mm. The near field profiles of all the UV beams are nearly top hat. However non uniformities exist in the beam cross section. The cylindrical focusing of a top hat beam will increase the beam intensity at the centre than at the edges.

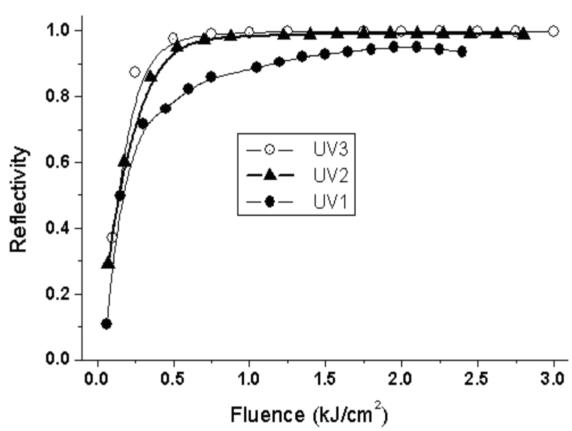

(a)

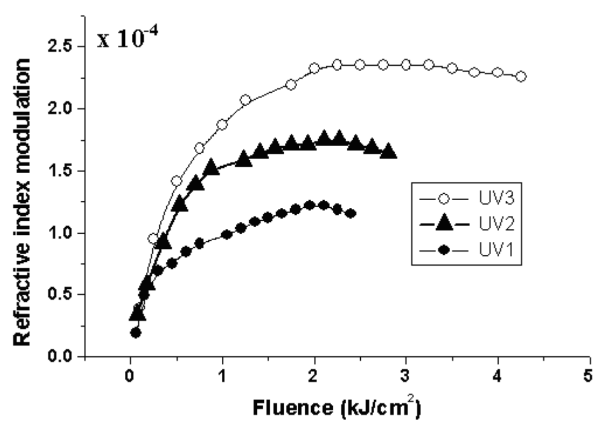

(b)

Figure 4.10: Change in (a) reflectivity (b) refractive index modulation with fluence

For calculation of refractive index modulation and average refractive index, uniform modulation is assumed with the effective length of the FBG as 80 % of beam overlap length. The estimated variation of reflectivity with UV fluence of FBGs written by UV1, UV2 and UV3 beam are shown in Fig. 4.10a. The estimated refractive index modulation with UV fluence of FBGs written by UV1, UV2 and UV_3 beam are shown in Fig. 4.10b. The FBG growth rate was fastest for UV3 writing beam. At same fluence, the induced refractive index modulation was higher for UV3 writing beam in compared to UV1 and UV2 beam. The saturated value of refractive index modulation estimated from observed transmission dip are 1.25 $\times 10^{-4}$, 1.75 $\times 10^{-4}$ and 2.37 $\times 10^{-4}$ for FBGs written by UV1, UV2 and UV3 beams respectively. For a particular UV beam, the index modulation increased non-linearly to saturation with UV fluence. With increase in number of pulses, the growth rate decreased and approached zero at saturation. The maximum (saturated) value of refractive index modulation of FBGs was observed for the UV3 writing beam and minimum for UV1 beam. It is clear that the spatial coherence of the writing beam predominantly decides the refractive index modulation in fiber core as expected for finite phase mask to fiber distance. The maximum affordable phase mask-fiber distance (x_m) is linked to writing beam spatial coherence width as [182],

$$x_m = W_{coh} / \tan \alpha \tag{4.7}$$

where W_{coh} is coherence radius and α is phase mask diffraction angle. The UV beam parameters and FBG results are summarized in table 4.1. The coherence width of UV1 is 30% of whole beam cross section (~ 10mm). The coherence width of UV_2 and UV3 beams are ~ 100% of full beam cross section. The calculated distances, x_m is 6.8, 20 and 20 mm for UV1, UV2 and UV3 beams respectively. For phase mask fiber distance of x= 0.8 mm is well within the upper limit x_m. Hence, the frequency doubled CVL put less stringent requirement

[128] on the distance between the fiber and the mask as compared to Excimer laser, due to high spatial coherence. However the time average degree of coherence at centre of reversal interferogram of UV3 , UV2 and UV1 beam are 0.42 , 0.37 and 0.3 respectively which are much less than theoretical value of unity. This is due to evolution of beam spatial coherence/divergence within the pulse. Further, dilution of time average fringe contrast is attributed to pulse to pulse variation of beam divergence and fringe instability. The results point to the strong role of degree of spatial coherence of the writing beam in the FBG fabrication efficiency. Thus under similar conditions of FBG writing in the same fiber, the spatial characteristics of the UV beam determined the refractive index modulation saturation of the FBGs written. The growth of FBG strength is faster for UV beams of high degree of spatial coherence and low pointing stability. The Bragg wavelength shifted towards red side during inscription. The Bragg wavelength of the FBG written by UV3 beam shifted by about 0.6 nm which correspond to induced average index of about 6.5×10^{-4}. This is due to increase in average refractive index. The shift in Bragg wavelength with accumulated fluence was approximately same for all three beams even though the induced refractive index modulation was different. Thus the induced refractive index modulation contrast ($\Delta n/\langle\Delta n\rangle$) decreased with decrease in beam spatial coherence. The bandwidth of the FBG written by UV3 beam was higher than the FBG written by UV1 beam. This is due to higher refractive index modulation obtained for FBGs written by UV3 beam. The saturation of refractive index modulation occurred at higher accumulated fluence for UV beams of higher spatial coherence. The analysis on effect of UV beam coherence on evolution of refractive index modulation / saturation and the effect of beam profile on evolution FBG spectrum is presented in chapter 5.

Table-4.1: UV (255) beam parameters and FBG results

UV beam	W_{coh}/W	γ_0	<Δφ> (DL)	T_d (dB)	R (%)	$\Delta\lambda_{bw}$ (nm)	Δn ($x10^{-4}$)	<Δn> ($x10^{-4}$)	ν	Fn (kJ/cm^2)
UV1	0.3	0.3	1.1	13	94.98	0.6	1.25	~ 6.4	0.2	2.25
UV2	1	0.37	2.2	21	99.20	0.7	1.75	~ 6.45	0.27	1.8
UV3	1	0.42	3.2	30.5	99.90	0.8	2.37	~ 6.5	0.36	1.5

W_{coh} – coherence width, γ_0 = reversal shear interferogram fringe contrast , Δφ- average divergence, T_d- Transmission, Δn_{mod}- Refractive index modulation, <Δn> - average refractive index change, ν- refractive index modulation contrast, $\Delta\lambda_{bw}$- FBG band width, Fn- saturation fluence, R- reflectivity

4.4.3 Effect of fiber composition on refractive index modulation

In the present work, FBG fabrications are studied in different commercially available photosensitive fibers. The growth trends of FBGs written in different fibers showed that the observed growth and saturation of refractive index modulation, average change in refractive index and required UV fluence to saturate the FBG reflectivity are different for different fibers.

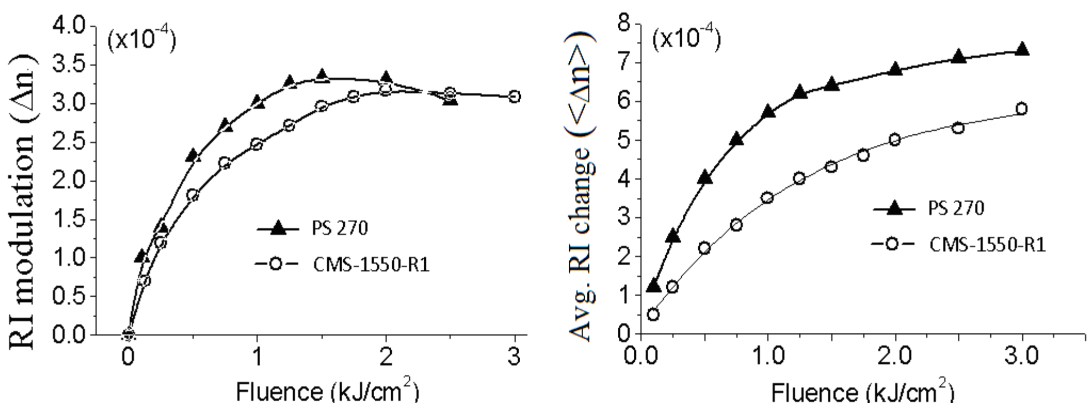

(a) (b)

Figure 4.11: (a) Evolution of refractive index modulation (b) average refractive index with increase in UV fluence

The growth characteristic of FBG written in two different fibers, namely PS 270 (manufactured by CGCRI, Ge-B codoped) and CMS-1550-R1 (manufactured by Stocker Yale, Ge doped), as illustration. The FBGs were written using UV3 beam written under similar conditions to study the effect of fiber photosensitivity. The grating length was ~ 7 mm. The growth of UV fringes induced refractive index modulation (Δn) and average index $<\Delta n>$ with UV fluence (F) are shown in figs.4.11a and 4.11b respectively. The refractive index modulation approached saturation with initial fast growth. With continuous exposure, the FBG transmission dip started to decay at higher accumulated fluence. The refractive index modulation of the FBG written in PS 270 fibersaturated at 3.32×10^{-4}, at the incidence cumulative fluence of about 1.5 kJ/cm^2. At the same fluence, the induced average refractive index was $6.5\text{x}10^{-4}$. With further exposure, the refractive index modulation decreased whereas the average refractive index continued to increase to saturation. For FBGs written in CMS-1550-R1 fiber, the saturated refractive index modulation observed was 3.2×10^{-4}, at incidence cumulative fluence of 2.5 kJ/cm^2. The induced average refractive index at this fluence was 5.5×10^{-4}. The refractive index modulation contrast ($\Delta n/<\Delta n>$) decreased with UV exposure for both fibers.Fig. 4.12a shows the typical transmission spectrum of the FBG written in fiber CMS-1550-R1 at saturation, in which the maximum observed dip and spectrum width were 32 dB and 1 nm respectively. The maximum transmission dip of 38 dB was observed for a FBG written in fiber PS-270 (fig. 4.12b) fiber.Table 4.2 presents typical data of observed transmission dip, reflectivity and refractive index modulation saturation for FBGs written in different fibers. The difference in the refractive index modulation saturation and required saturation fluence is due to different fiber photosensitivity 14-16, 214].

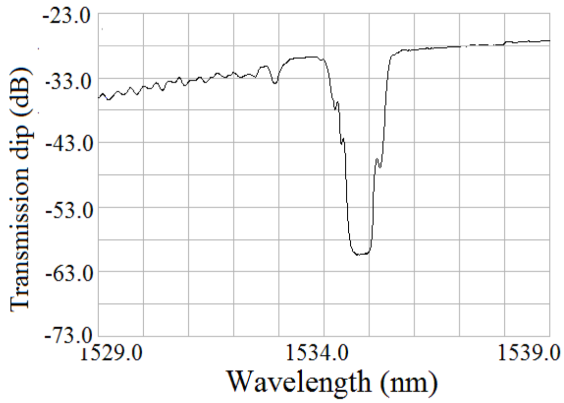

(a)

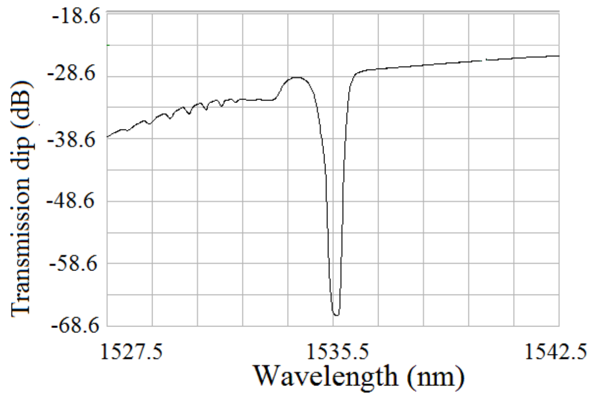

(b)

Figure 4.12: Transmission of the FBG written in (a) CMS-1550-R1 (b) PS-270 fiber

Table 4.2: Results of FBG fabrication in different fiber types

Fiber	Core doping	Bragg resonant wavelength (λ_B)	T_d (dB), (R)	Max. Δn
PS-270 (CGCRI)	Ge-8 mol% ,B- 6 mol%	1534 nm	38 (99.984%)	2.83×10^{-4}
SM-1500 (Fiber core)	Ge- mol 18%	1546 nm	32 (99.936 %)	2.32×10^{-4}
NM-113 (CGCRI)	Ge-10 mol %	1536 nm	30 (99.9 %)	2.32×10^{-4}
GF-1 (Neufern)	Ge-B codoped	1534 nm	30 (99.9 %)	2.32×10^{-4}
CMS-1550-R1 (Stocker Yale)	Ge- doped	1536 nm	26 (99.74 %)	2.06×10^{-4}
PS-RMS-50 (Stocker Yale)	Ge- B codoped	1540 nm	30.5 (99.91 %)	2.35×10^{-4}
SMF-28	Ge – 3 mol %	1534 nm	0.5 (10.8 %)	0.2×10^{-4}

4.4.4 Effect of long exposure (Type II A gratings)

With continuous exposure of UV fringes, the FBG refractive index modulation change goes through three phases, namely, growth, saturation and decay. However, the prolonged exposure of fringes result in partial or complete grating erasure of type I FBG, followed by a new spectral formation, known as a type IIA FBG, which is more thermally stable[118]. In order to develop FBG based high temperature sensor, the experiment was carried out to study the growth of type IIA FBG, with 255 nm exposure [215]. The Ge- doped photosensitive fibers, NM-113 and SM-1500, were used in the study.

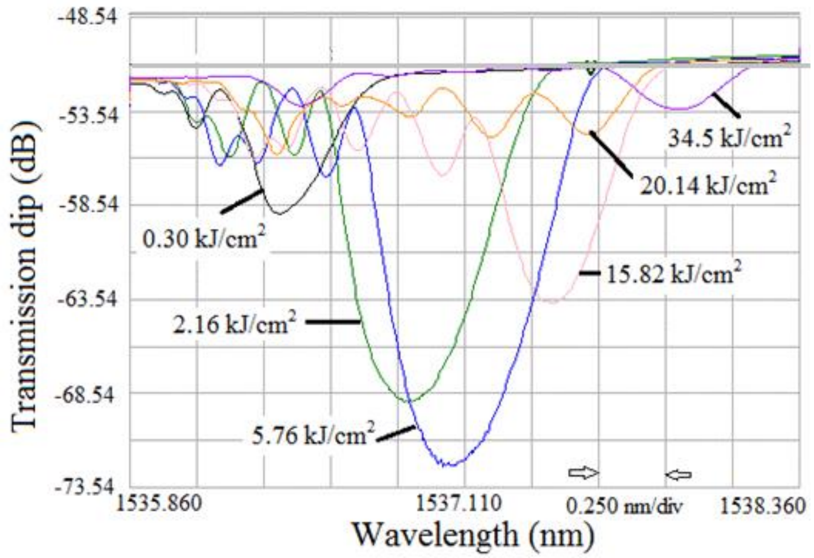

(a)

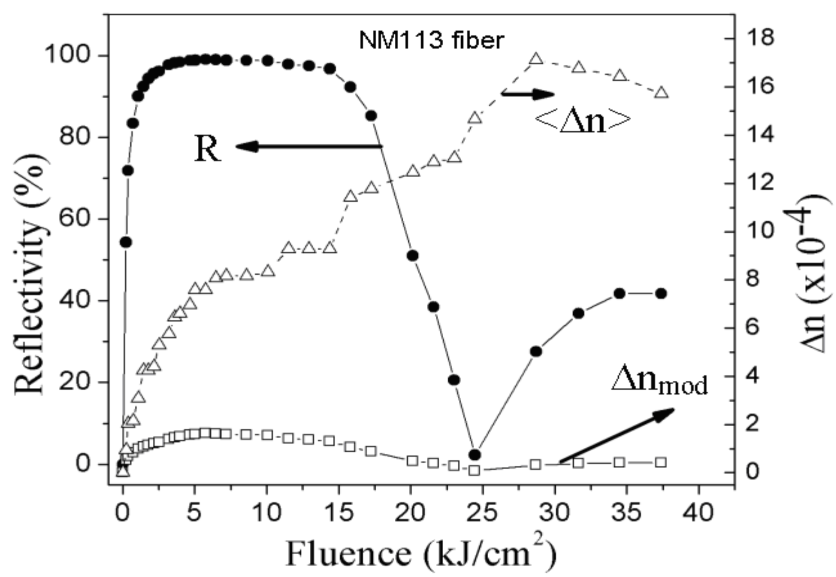

(b)

Figure 4.13: (a) Transmission spectrum at different fluence (b) Variation of reflectivity, average index, and index modulation with increase in accumulated fluence

The FBG length was about 10 mm. Single pulse energy density was 2.18 mJ/cm^2. The transmission spectrum of FBG in NM113 fiber at different accumulated fluence (marked in the figure) is shown in fig. 4.13a. The characteristic curve of variation of induced index modulation and the average index with accumulated fluence is shown in fig.4.13b. With continuous exposure, the reflectivity and refractive index modulation (Δn_{ac}) increased with the fluence and reached to maximum value of 99 % and 1.63×10^{-4} respectively, at the cumulative fluence of 5.76 kJ/cm^2. With further exposure, the reflectivity and index modulation reduced to 2.3 % and 0.08×10^{-4} respectively at the fluence of 24.45 kJ/cm^2. Thereafter reflectivity and refractive index modulation again increased and ultimately reached to 40 % and 0.42×10^{-4} respectively, at the fluence of 37.4 kJ/cm^2. However the average refractive index (Δn_{dc}) initially increases to 17×10^{-4} at the fluence of 28.7 kJ/cm^2 and then reduces to 15.7×10^{-4} at the fluence of 37.4 kJ/cm^2.

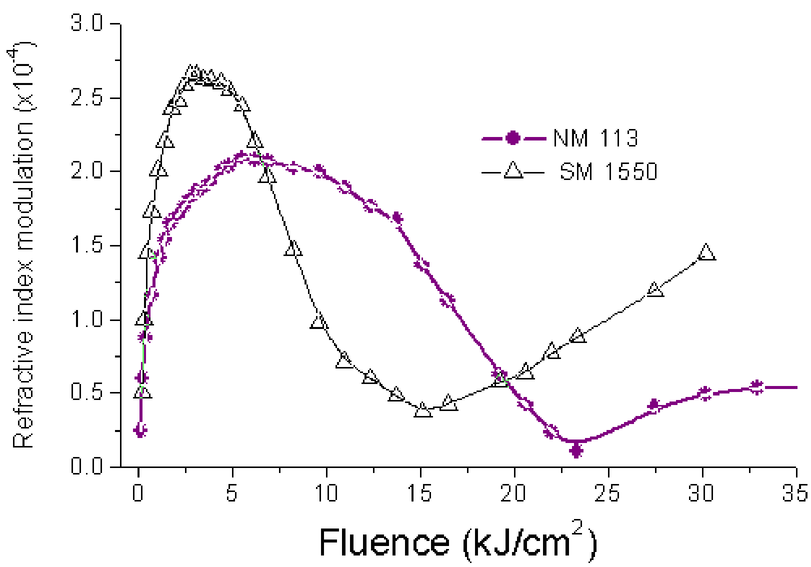

Figure 4.14: Variation of index modulation with increase in accumulated fluence

Fig. 4.14 shows the variation of refractive index modulation with accumulated fluence of FBGs written in NM 113 and SM 1500 fibers. The rollover in refractive index modulation (Δn_{ac}) was observed at much higher fluence of 24.45 kJ/cm^2 as compared to 7.39 kJ/cm^2 for 193 nm ArF laser [118] based writing. This is probably due to lower pulse energy of 2.18 mJ/cm^2 of 255 nm beam as compared to 133 mJ/cm^2 of 193 ArF laser. From the refractive index modulation (Δn_{ac}) and average refractive index (Δn_{dc}) curve, the inscribed FBG is a type IIA grating. The SM 1500 fiber photosensitive to UV wavelength of 255 nm is higher in compared to NM 113 fiber, due to higher concentration of germanium. Similarly, for SM1500 fiber, the re-growth of type IIA FBG started at lower fluence with higher growth rate. The observed FBG RI index modulation in type IIA phase was also higher.The refractive index growth on UV exposure is cumulative effect of change in absorption spectrum, induced stress and photo elastic effects [16]. The refractive index change attributed to stress change is positive. After saturation in type I phase, the refractive index modulation decreased due to wash out of modulation contrast. As the fluence increased further, the refractive index modulation again increased. It is believed that type IIA gratings involve stress relief, i.e., the gradual removal of the anisotropic difference between stresses, particularly by radial and axial components generated by UV irradiation during formation of type I gratings [137]. Due to stress relief, the modulation increases with decrease in photo induced average index. Niay *et al*. proposed a phenomenological model in which they suggested that the refractive index evolution with irradiation time results from two reactions with different rate constants [205]. The first reaction (with rate constant k_1) produces some defects which lead to a positive refractive index change whereas the second reaction (with rate constant $k_2 << k_1$), slower than the first, produces a negative refractive index change. The type IIA growth is attributed to second reaction [205].

4.5 Tilted Fiber Bragg gratings (TFBGs]

In a normal FBG, the grating planes are normal to fiber axis [87-89]. However, the Bragg resonant wavelength of a FBG is tuned in a limited range by tilting the fiber in the fringe plane. The induced index planes in the core of the fiber will be tilted. The tilt angle can be introduced by rotating the phase mask and cylindrical lens in the vertical plane by same angle so that the line focus remains on the fiber. In this case, the FBG length remains constant with change in tilt angle. Maximum tilt angle that could be applied in the writing system was about 10 degree.Figs.4.12b and 4.15 show the transmission spectra of a normal and atilted FBG respectively written in a single-mode fiber (PS 270) by UV3 beam. The observed transmission of normal FBG was -38 dB. The small resonance dips in the shorter wavelength side of the Bragg resonant wavelength are cladding modes (fig. 4.12b). These modes are excited by scattering light from the core of an optical fiber into the cladding. The strengths of these dips aresmall due to the limited overlap of the field of the cladding modes with the guided mode field and the refractive index change across the core. However, these cladding modes are excited with high efficiency [14-16] even with a small tilt, as seen in the spectrum of a FBG in which grating plane are slightly tilted ($\theta \sim 0.5^0$). The transmission of the tilt FBG is -30 dB.The transmission spectra consisted of a strong Bragg resonance and several narrow resonances, which are the cladding modes on the short wavelength side of the Bragg resonance. The transmitted spectrum of a tilted FBG is composed of numerous discrete dips which have two distinct origins. The dips at the longest wavelength originate from the self coupling of the core mode while the others are due to the backward coupling with the cladding modes.The resonance condition for self coupling of the core mode is given as [87]

$$\lambda_{Bragg} = 2n_{eff,co}\frac{_g}{\cos\theta} \tag{4.8}$$

where $n_{eff,co}$ is the refractive index of the fiber core and $_g$ represent the fringe period,θ is the angle between fringe planes and fiber axis. The resonance wavelength of the cladding mode is given by [87]

$$\lambda_{cl,i} = (n_{eff,co} + n_{eff,cl,i})\frac{_g}{\cos\theta} \tag{4.9}$$

where $n_{eff,cl,i}$ is the effective refractive index of i^{th} cladding mode. Thus the cladding modes appeared at wavelength shorter than the Bragg resonance wavelength (fig 4.15).

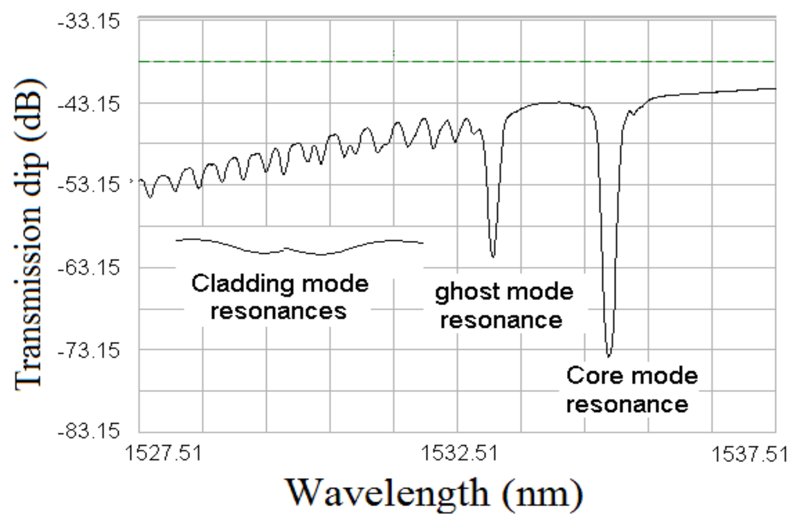

Figure 4.15: Transmission spectra of a FBG at $\theta = 0.5^0$

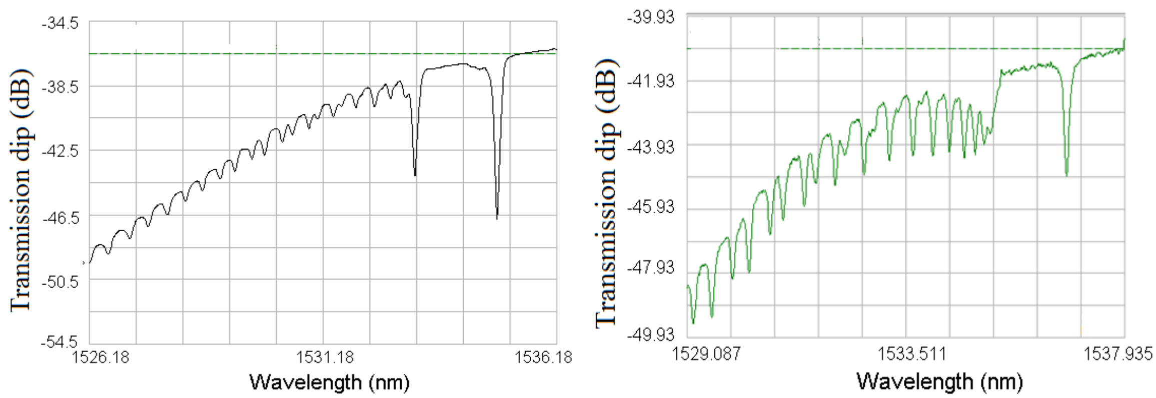

(a) (b)

Figure 4.16: Transmission spectra of tilted FBG (a) $\theta = 2^0$ (b) $\theta = 4^0$

The transmission loss in the ghost mode is about -16 dB. The ghost mode resonance corresponds to a group of low-order asymmetric cladding modes which are well confined in the core and less sensitive to the cladding external medium interface [87-89].The transmission dip at Bragg resonant wavelength decreased at higher tilt angle. The resonant wavelength shifted to longer wavelength with increase in tilt angle. However, the cladding mode resonances appeared at wavelengths shorter than the Bragg resonance wavelength. Figs.4.16a and 4.16b show the typical FBG transmission spectra at higher tilt angles of 2^0 and 4^0 respectively.

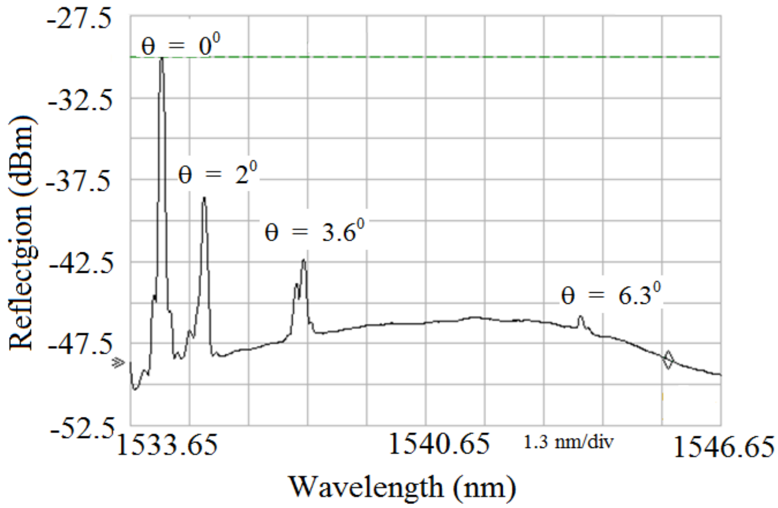

(a)

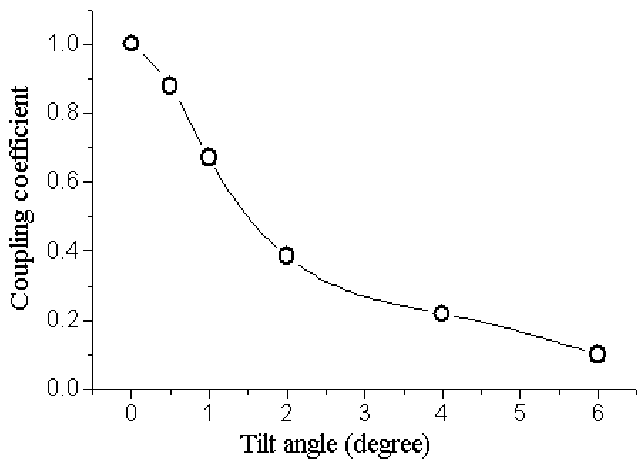

(b)

Figure 4.17 (a): Bragg wavelength tuning by tilting the fiber in the fringe plane (b) Variation in coupling coefficient with increase in tilt angle

Limited tuning is possible by tilting the fiber. Fig. 4.17 shows reflection spectrum of tilted grating arrays. The fiber was tilted (along horizontal plane) at different angles (marked) in the fringe plane, keeping one end fixed and rotating the other end within the fringe depth.The resonance wavelength shifted to longer wavelength with increase in tilt angle due to increase in effective grating period. The cladding mode peaks are not observed in the reflection spectrum since.The cladding modes are losses to surrounding media [14-16]. Fig.4.17 (a) shows the observed evolution of backward coupling coefficient (relative with respect to that at 0^0) with increase in tilt angle.The coupling coefficient of tilt gratings decreased from 1 for $\theta = 0^0$ (uniform FBG) to 0.25 for $\theta = 4^0$. The decrease in coupling coefficient is initially first with slow decrease at higher tilt angles.The grating reflectivity in main mode decreased with increase in tilt angle, due to decrease in backward coupling coefficient [213].

4.6 Effect of phase mask pitch on refractive index modulation

A phase mask of pitch 0.725 μm has been used to study FBG fabrication. The fiber (GF1) was placed at distance about 0.8 mm from the phase mask. The FBG was written by UV3 beam of diameter 7 mm.

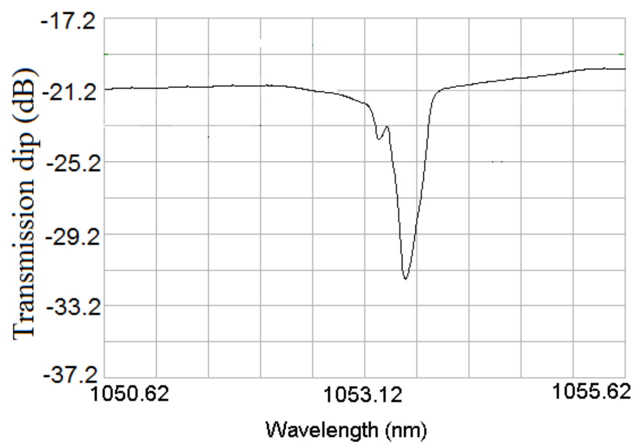

Figure 4.18: Transmission of FBGs written by phase mask of pitch 0.725 μm

The observed maximum transmission dip of a FBG was ~ 10.5 dB (R = 91%), at Bragg resonant wavelength of 1054 nm. Fig.4.18 shows the transmission spectrum. The induced refractive index modulation (Δn) saturation was about 0.9×10^{-4}. The observed saturated index modulation of the FBG written by the phase mask of pitch 0.725 μm was comparatively lower than the modulation (~ 2.2×10^{-4}) of a FBG written by the phase mask of pitch 1.06 μm in the same fiber, under similar conditions. The observed lower refractive index modulation may be attributed to cumulative effect of three important factors. First, the fringe contrast in a typical FBG writing plane (x) by the phase mask of lower pitch [d= 0.725 μm] will be lower in compared to that of a phase mask of higher pitch [d= 1.06 μm]. This could be explained as follows. The fringe contrast is given as [213, 183]

$$\gamma = \text{sinc}\,(k\ x\ \tan\theta\ \Delta\varphi) \tag{4.10}$$

where $k = 2\pi/\lambda_{uv}$, x is distance of the fiber position from the phase mask, $\Delta\varphi$ is beam divergence and θ [$\sin^{-1}(\lambda_{uv}/d)$] is diffraction angle. The fringe contrast decreases with increase in the angle of intersection (2θ) between +1 and -1 beam. This is due to larger separation between two points on the incident wavefront from which emanating +1 and -1 diffracted beam interfere at a point in the FBG writing plane. For d = 1.06 μm, $\theta = 13.9^0$ ($\tan\theta$ = 0.244) and for d = 0.725 μm, $\theta = 20.6^0$($\tan\theta$ = 0.35) at λ_{uv}= 255nm. For same λ_{uv} , x and $\Delta\varphi$, the induced refractive index modulation will be lower for FBGs written by phase mask of lower pitch (0.725 μm) in compared to that of a phase mask of higher pitch (1.06 μm) due to reduction in fringe contrast. Second, the fringe instability adversely affects FBG fabrication efficiency. The fringes of width 0.53 μm and 0.3625 μm are produced by the phase masks of pitch 1.06 μm and 0.725 μm respectively. The fringe stability decreases with decrease in fringe width (chapter 3). The time average fringe contrast dilution and therefore induced refractive index modulation will be lower for fringes of smaller width (0.3625 μm) in compared to those fringes of higher width (0.53 μm). Third, the fractional light present in residual orders affect the overall performance of the FBG fabrication efficiency. The phase mask of pitch 0.725μm diffracts up to ± 2 orders. The phase mask of pitch 1.06 diffract up to ± 4 orders with typical diffraction efficiency mentioned section 4.1. The small contribution from residual orders produces significant deviations in the fringe pattern as expected from ideal +1 and – 1 overlap only [182-183] which may affect the FBG fabrication efficiency [197, 182-185].

4.7 Conclusion

The type I, type IIA and tilted FBGs have been written in non-hydrogenated photosensitive fibers using low pulse energy, high repetition rate 255 nm pulsed UV beams. With continuous exposure of UV fringes, the refractive index modulation of type I FBGs increased to saturation. However the refractive index modulation contrast decreased with increase in accumulated fluence. The growth and saturation of refractive index modulation and required fluence to saturate was different for different fibers used in the study. The refractive index modulation of type I FBGs decreased after saturation. During growth and decay stage, the Bragg wavelength shifted to red side. With prolong exposure of UV fringes, the re-growth of FBG reflection (Type IIA regime) started after decay phase (of type I), at much higher fluence. The FBG growth rate in type IIA regime was slower in comparison to that in type I regime. The Bragg wavelength blue shifted during growth of type II FBG. Tilted fiber Bragg gratings have been written using highly coherent 255 nm radiation (UV3 beam). The reflectivity of FBGs decreased when written at higher phase mask to fiber distance. The appreciable type IIA growth of FBG was possible only when written by high contrast fringes. The Bragg wavelength tuning by tilting the grating planes from 0^0 (normal FBG) to and 6^0 were studied. The main Bragg peak shifted towards the higher wavelength accompanied by reduction of reflection power. With the increased in the tilt angle, the transmission in the cladding modes first decreased followed by increase after reaching a minimum.

The evolution of reflection spectrum, with continuous exposure of UV fringes, is dynamic. The side lobes on blue side of the spectrum evolved first. The side lobe strength increased with increase in grating strength. The side lobes on both sides appeared for saturated gratings. The FBGs were written by UV beams of different spatial characteristics. It is shown that the refractive index modulation growth is faster and saturated at higher value for UV beams of higher spatial coherence. By employing 255 nm UV beam of high degree of spatial coherence, obtained from SH of CVL in diffraction filtered resonator configuration, long gratings up to 10 mm length and of high reflectivity (> 99.9 %) were inscribed in different non-hydrogenated photosensitive fibers. Maximum transmission dip of 38 dB has been obtained. The importance of spatial coherence and pointing stability of the writing beam for damage free, phase mask based fiber Bragg grating has been demonstrated. These experimental results are suitably supported by theoretical analysis as presented in next chapter.

Publications based on this chapter

1. "Analysis on the saturation of refractive index modulation in fiber Bragg gratings (FBGs) written by partially coherent UV beams", **R. Mahakud**, O. Prakash , S.V. Nakhe and S.K. Dixit, Appl. Optics, **2012**, 51, 1828-1835.
2. "Analysis on the effect of UV beam intensity profile on the refractive index modulation in phase mask based fiber Bragg grating writing" **R. Mahakud**, J.Kumar, O. Prakash, S.V. Nakhe and S.K Dixit, Optics Commun., **2012**, 285, 5351-5358.
3. "Effect of the spatial coherence of ultraviolet radiation (255 nm) on the fabrication efficiency of phase mask based fiber Bragg gratings". O. Prakash, **R. Mahakud**, S.K. Dixit and U. Nundy, Optics Commun., **2006**, 263, 65-70.
4. "Enhanced temperature (~ 800 ^{0}C) stability of type IIa fiber Bragg grating written in Ge doped photosensitive fiber", O.Prakash, J. Kumar, **R. Mahakud**, S. K. Agrawal, S. K. Dixit and S. V. Nakhe, IEEE photonics technology letters, **2014**, 26, 93-95.

Chapter 5

Theoretical analysis of phase mask based FBG fabrication

5.1 Introduction

The refractive index change induced by UV photons in the photosensitive fibers is exploited for fabricating fiber Bragg gratings (FBGs) [26-33]. The photosensitive response depends upon the fiber composition and incident UV wavelength. The observed growth of refractive index modulation of type I FBGs is nonlinear [216-218]. The nonlinear growth of the induced refractive index modulation (Δn) during the grating writing has been described by the models of the form, $\Delta n \propto t^{\rho}$, [where t is time of exposure and ρ is a constant that increases with power density] [48, 219-221] and has the form $\Delta n \propto 1 - \exp(-t/\tau)$ [217, 222] for involving modulation saturation with τ as a fitting parameter. A grating with sinusoidal refractive index modulation has almost has no reflection at its second-order where as a grating with square modulation has reflections in second/higher orders. Xie *et al*. [223] first time observed second order Bragg reflection of FBGs, written by a Lloyd prism interferometer. The observed higher order reflection in FBG is attributed to non linear growth of induced refractive index with continuous exposure of sinusoidal UV fringes. To investigate the evolutions first and second order FBG reflectivity, Xie *et al.* proposed a phenomenological model described as [223]

$$\delta n(z,N) = \Delta n_{\max}[1 - e^{-kN(1+\cos(\frac{2\pi}{\Lambda}z))}] \tag{5.1}$$

where N is the number of incident UV pulses and k is a fitting parameter. Δn_{max} is the saturable (maximum) index change. According to eqn (5.1), the induced refractive index minimum [at z = (N+1/2)Λ, N-integer] is always zero. This is possible only when UV fringes' contrast is unity. For UV fringes of contrast less than unity, the induced refractive index at fringe minima points enhances with increase in accumulated fluence. In these models [221-223], the fringe contrast as a parameter is not considered.

In chapter 4, the FBG writing with partially coherent UV beams contrast less than unity are described. The experimental observations which need to be explained are trends on refractive index modulation with increase in UV fluence. Specifically, the FBG growth rate was faster for higher spatial coherent UV beam. Also, for higher the UV beam spatial coherence, the growth of induced refractive index modulation were higher and saturated at higher value. The FBG reflectivity decreased when written at larger distance from phase mask. The FBG growth rate and required fluence to saturate are different for different fiber types. The evolution of reflection spectrum was dynamic. Thus it is desirable to develop a model of refractive index modulation by incorporating fringe contrast to explain the observed trends on grating growth and saturation. With this in view, this chapter presents the theoretical analysis of FBG fabrication, by partially coherent UV beams, in terms of the refractive index modulation in the fiber core and its subsequent saturation of type I gratings, based on single photon absorption [213]. This analysis is further extended by evaluation of the reflection spectrum of the fiber Bragg gratings (FBGs) written by UV beams of non-uniform energy distribution [212].

5.2 Effect of UV beam spatial coherence on refractive index modulation

5.2.1 UV photon induced excitation

Upon exposure to UV radiation, GeO defect centers in the tetrahedral matrix of the silica host glass break, resulting in the evolution of new defects centers [6-11]. The depletion of GeO defects on UV illumination triggers formation of trapped states. The excitation of electrons from defect sites (D) induces forbidden transitions to the distribution of trap states (D_1) [called as defect induced defects (DIDs)] via an intermediate state (S^1) [217]. The transition of electron from state D to D1 depends on available energy bands with band gap energy corresponding to incidence UV wavelength. The UV beam intensity changes as it propagates in the fiber core due to absorption. The rate of change of intensity [I =I(ν)Δν]can be described as [224],

$$\frac{dI}{dx} = -\alpha(\nu)I - \rho_{tpa}(\nu)I^2 \tag{5.2}$$

where α is linear and ρ_{tpa} is the two-photon absorption coefficient. The intensity of UV beam (255 nm) used in FBG inscription is low (~ 0.1 MW/cm^2). It is assumed that the absorption is one photon (linear) in natureand attributed to GeO defect centers only. The absorption coefficient is given as, α (ν,t) = σ (ν)N_d(t), where σ (ν) is absorption cross section and N_d(t) is defect centre density. The rate of decay of defect centre density [N_d(t]) can be expressed as [224],

$$\frac{dN_d(t)}{dt} = -\sum_j B_j(\nu)u(\nu)\Delta\nu N_d(t) + \sum A_j N_j \tag{5.3}$$

where u(ν)Δν is incident UV energy density with bandwidth Δν, B_j(ν) is transition probability from ground state to jth excited state of oxygen-deficient germanium sites at frequency ν, N_j is jth excited state population, A_j is the sum of both radiative and non radiative relaxation probability from jth excited state to ground state. The main absorption of GODCs lies in 240 nm band. For the present case, the writing UV beam photon energy (4.87 eV, 255 nm) considered to overlap the 240 nm band. Relaxations to the original defect sites are ignored as the electron are trapped after excitation in intermediate states [217]. The eqn (5.3) is simplified as [213]

$$\frac{dN_d(t)}{dt} = -Bu(\nu)\Delta\nu N_d(t) = -B\frac{I}{c}N_d(t) = -\beta I N_d(t) \tag{5.4}$$

where $cu(\nu)\Delta\nu = I(\nu)\Delta\nu = I$ is the intensity of UV beam, c is velocity of light, B is the transition probability at ν = 255 nm and $\beta = B/c = \sigma(\nu)/h\nu$. By solving equation (5.4),

$$N_d(t) = N_d(0)\exp(-\beta It) = N_d(0)\exp(-\frac{t}{\tau_c}) \tag{5.5}$$

where $\tau_c = 1/\beta I$ is intensity dependent decay constant. N_{d0} is the initial (at t=0) GeO defect centers per unit volume. The decay constant τ_c determines how fast the GODC defects centers are depleted under UV exposure. The trapped states (D1) population density which is equal to depleted defect centers density is given as [213],

$$\Delta N_d(t) = N_{d0}[1-\exp(-\beta It)] \tag{5.6}$$

5.2.2 Induced refractive index change in the photosensitive fiber

The UV excitation induced refractive index change in the fiber core increases due to color-center [221] and compaction effects and decreases due to photo-elastic tensile strain [225-228]. The amount of each contribution might vary strongly as a function of fiber composition, pre-irradiation treatment, irradiation wavelength and UV beam intensity [207]. Taking the change in refractive index (δn), linearly proportional to depleted defect center population per unit volume, the induced refractive index is described as [213],

$$\delta n(t) = C\Delta N_d(t) = CN_{d0}[1-\exp(-\beta It)] \tag{5.7}$$

where C is proportionality constant which depends on fiber composition. In case of pulsed laser illumination, the total induced index change is sum of incremental index change (δn_j) of successive pulses given by [213]

$$\delta n = \sum \delta n_j = CN_{d0}[1-\exp(-\beta IN\tau)] = \Delta n_{\max}[1-\exp(-\beta F)] \tag{5.8}$$

where δn_j is the change in index on exposure of j^{th} pulse, N is the total number of pulses, τ is UV temporal pulse width, F (= $NI\tau$) is the accumulated UV fluence and Δn_{max} (= CN_{d0}) is termed as saturable index change. The UV induced growth of δn at a position approaches zero as δn approaches Δn_{max}.

5.2.3 UV fringes (sinusoidal) induced refractive index distribution

The overlapping of +1/-1 order of phase mask results the interference pattern half the period of phase mask. The fringe visibility [$\gamma_1(x)$] attributed to beam spatial coherence is given as $\gamma_1(x)$ = Sinc (k.x.tanα.Δϕ), where k (= $2\pi/\lambda_{uv}$), α (= $\sin^{-1}\lambda_{uv}/d$) is diffraction angle and Δφ is beam divergence (Chapter 3). The divergence and instantaneous intensity of CVL and thus the UV beam (255 nm) generated from second harmonic of CVL beam changes within the pulse (Chapter 2) [155, 167]. The UV beam can be considered to possess both coherent and chaotic part. The intensity and divergence of different pulses of the CVL and therefore its SHG beam fluctuates [181]. The beam pointing stability, fiber positional stability, thermo optic and acoustic fluctuations effects fringe stability and therefore reduces fringes average contrast. The time averaged fringe visibility can be thought of as $\gamma(x) = \gamma_1(x).\gamma_2(x)$ where the parameter, $\gamma_2(x) < 1$, encompasses all the additional fringe contrast diluting parameters as discussed except spatial coherence. The net fringe intensity distribution can be generalized as

$$I(z) = I_0[1 + \gamma(x)\cos(\frac{2\pi}{\Lambda}z + \varphi)] \tag{5.9}$$

where Λ is fringe period, I_0 is mean fringes intensity.$\gamma(x)$ is fringes contrast and φ(z) is phase due to local wave front distortion.Using equations (5.8) and (5.9), the induced refractive index distribution across FBG length is expressed as [213],

$$\delta n_n(z) = \Delta n_{\max}[1 - \exp[-\beta F_0\{1 + \gamma(x)\cos\frac{2\pi}{\Lambda}z\}] \tag{5.10}$$

The terms Δn_{max} and β depend on fiber photosensitivity at incidence UV wavelength, composition and molar concentration of defects that could be excited at UV wavelength. The analysis is generalized by normalizing induced refractive index and incidence fluence to make it independent on fiber specifics. The normalized induced refractive index [δn_n (z)] is defined as $\delta n_n (z) = \delta n (z)/\Delta n_{max}$ and normalized fluence (F_{n0}) is defined as, $F_{n0} = \beta F_0$. The modified form of eqn (5.11) becomes

$$\delta n_n(z) = [1 - \exp[-F_{n0}(1+\gamma(x)\cos\frac{2\pi}{\Lambda}z)] \quad (5.11)$$

The eqn. (5.11) is of same format as discussed in the phenomenological model [223] for γ =1. At low fluence, eqn (5.11) can be approximated as

$$\delta n_n(z) = F_{n0}\{1+\gamma(x)\cos\frac{2\pi}{\Lambda}z\} \quad (5.12)$$

The refractive index modulation in the fiber is sinusoidal. The photo induced period averaged refractive index change [$\langle\delta n\rangle$] is given as, $\langle\delta n\rangle = \Delta n_{max} F_{n0}$. The index modulation [$= \gamma\langle\delta n\rangle$] increases linearly with fluence and visibility. The refractive index contrast is equal to fringe visibility.

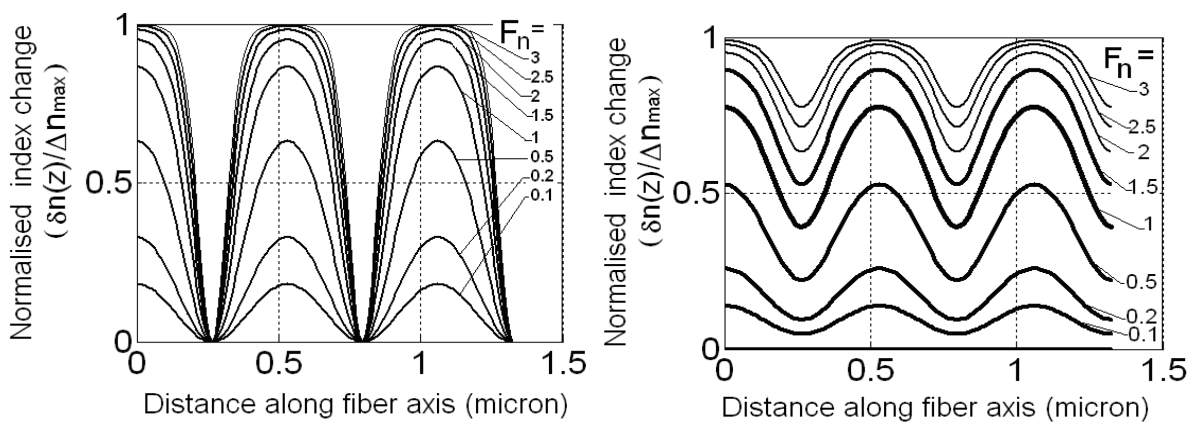

Figure 5.1: Simulated normalized RI change along FBG length for (a) γ (x) = 1 (b) γ (x) = 0.5 for different F_{n0}

The refractive index modulation will be higher for UV beams of higher fringe contrast. Figs.5.1a and5.1b show the variation normalized index change along FBG length in the core of the fiber for ideal value γ (x) = 1 and a typical experimental value of γ (x) = 0.5, for different values of F_{n0} varying from 0 to 3. At higher fluence, the normalized RI profile deviates from sinusoidal distribution.From eqn (5.12), the normalized index change at positions of fringe maxima (δn_n^{max}) and fringe minima (δn_n^{min}) are given by

$$\delta n_n^{max} = 1 - \exp\{-F_{n0}(1+\gamma)\} \tag{5.13}$$

$$\delta n_n^{min} = 1 - \exp\{-F_{n0}(1-\gamma)\} \tag{5.14}$$

Fig. 5.1c shows the variation of normalized index change δn_n^{max} and δn_n^{min} with fluence for γ =1 and γ = 0.5. For fringes of higher visibility (γ), the induced index change is higher at fringe maxima and lower at fringe minima in compared to that for fringes of low contrast.

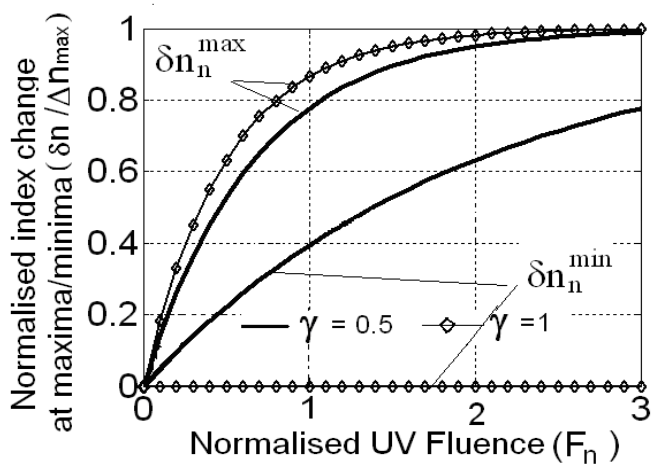

(c)

Figure 5.1: (c) Change δn_n^{max} and δn_n^{min} with F_{n0} for γ =1 and γ = 0.5

The induced refractive index δn_n^{min} is always zero for γ = 1 where as it increases with fluence for γ< 1. Thus it is clear that δn_n^{max} increases with increase of γ whereas δn_n^{min} increases with decrease of γ. This explains the experimental trends of observed lower refractive index modulation for FBGs written by low spatial coherent beams. The spatial distribution of $\delta n_n(z)$ and coefficients of its harmonic components will change with F_{n0} and γ.

5.2.4 Fourier harmonics of refractive index change

The normalized refractive index changes [$\delta n_n(z)$], expressed in Fourier series, is given as,

$$\delta n_n(z) = <\delta n_n> + \delta n_n^{(1)}\cos(\frac{2\pi}{\Lambda}z) + \delta n_n^{(2)}\cos(\frac{4\pi}{\Lambda}z) + \delta n_n^{(3)}\cos(\frac{6\pi}{\Lambda}z) + ... \quad (5.15)$$

where $<\delta n_n>$ and $\delta n_n^{(m)}$ represents period averaged and amplitude of m^{th} harmonic component of induced refractive index, $\delta n(z)$ respectively. By using the exponential series expansion and carrying out necessary integrations, the Fourier coefficients $<\delta n_n>$, $\delta n_n^{(1)}$, $\delta n_n^{(2)}$ and $\delta n_n^{(3)}$ eq. (5.10) of δn (z) are expressed as [213],

$$<\delta n_n> \approx 1 - a[1 + 0.25b^2 + 1.56\times10^{-2}b^4 + 4.34\times10^{-4}b^6 + 6.59\times10^{-6}b^8 + 5.71\times10^{-8}b^{10} + ...] \quad (5.16)$$

$$\delta n_n^{(1)} \approx ab[1 + 0.125b^2 + 5.2\times10^{-3}b^4 + 1.085\times10^{-4}b^6 + 1.356\times10^{-6}b^8 + 1.13\times10^{-8}b^{10} + ...] \quad (5.17)$$

$$\delta n_n^{(2)} \approx -a[0.25b^2 + 2.08\times10^{-2}b^4 + 6.51\times10^{-4}b^6 + 1.08\times10^{-5}b^8 + 1.13\times10^{-7}b^{10} + ...] \quad (5.18)$$

$$\delta n_n^{(3)} \approx a[4.17\times10^{-2}b^3 + 2.6\times10^{-3}b^5 + 6.51\times10^{-5}b^7 + 9.04\times10^{-7}b^9 + 8.07\times10^{-9}b^{11} + ...] \quad (5.19)$$

where $a = \exp(-F_{n0})$ and $b = \gamma F_{n0}$. It is clear from eqns (5.17-5.20) that the mean index change and refractive index modulation in different harmonics depend on both fluence and fringe contrast. The fringe contrast, $\gamma(x)$, may vary from 0 to 1 depending on x and $\Delta\phi$. The variation of $<\delta n_n>$, $\delta n_n^{(1)}$, $\delta n_n^{(2)}$ and $\delta n_n^{(3)}$ with Fn_0 and γ (x) are shown in figs.5.2(a-d) respectively. The growth and saturation of $\delta n_n^{(m)}$ and required fluence to saturate respective values are different for different γ. The amplitudes of higher harmonics of induced refractive index saturates at higher accumulated fluence. At specific value of γ (x), the refractive index modulation, $\delta n_n^{(1)}$, first increases and then decreases passing through a maxima. This is due to the fact that the induced index change undergoes differential growth before approaching saturation asymptotically.

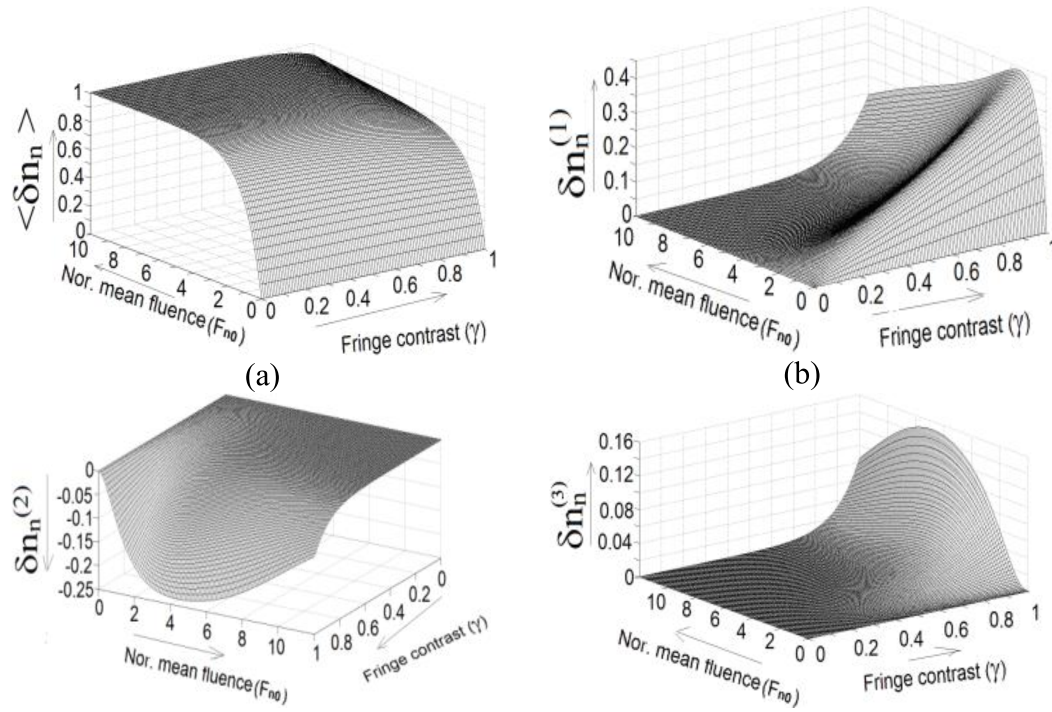

Figure 5.2: The variation of harmonic coefficients (a) $<\delta n_n>$ (b) $\delta n_n^{(1)}$ (c) $\delta n_n^{(2)}$ and (d) $\delta n_n^{(3)}$ with change in F_{n0} and γ (x).

While δn_n^{max} approaches saturation due to depletion of saturable defect sites, minimum index δn_n^{min} at location of fringe minima continues to grow with UV fluence resulting the variation of δn_n^{mod} passing through a maxima. The maximum fluence required for saturation of refractive index modulation is different at different fringe contrast. For low spatial coherent beams, maximum index change grows slower and minimum index change grows faster. Therefore the saturated index modulation is lower for lower γ in comparison to UV beams of higher fringe contrast (γ). The saturated value of $\delta n_n^{(1)}$ and required fluence to saturate decreases with decrease in fringe contrast.Figs.5.3a shows variation of $<\delta n_n>$, $\delta n_n^{(1)}$, $\delta n_n^{(2)}$ and $\delta n_n^{(3)}$ with normalized fluence for ideal value of γ (x) =1. The maximum of $\delta n_n^{(1)}$ ~

0.4382 occurs at $F_{n0} \sim 1.55$ where as $\delta n_n^{(2)}$ is in growth stage. The maximum of $(-)\delta n_n^{(2)} \sim 0.235$ occurs at $F_{n0} \sim 4.35$. For a typical value of $\gamma = 0.7$, the saturation values $\delta n_n^{(1)} \sim 0.2761$ and $(-)\ \delta n_n^{(2)} \sim 0.08$ occurs (figs. 5.3b) approximately at normalized fluence (F_{n0}) of 1.15 and 2.48 respectively.

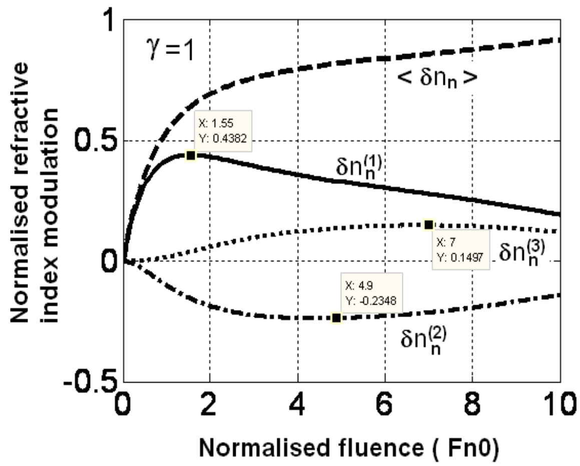

(a)

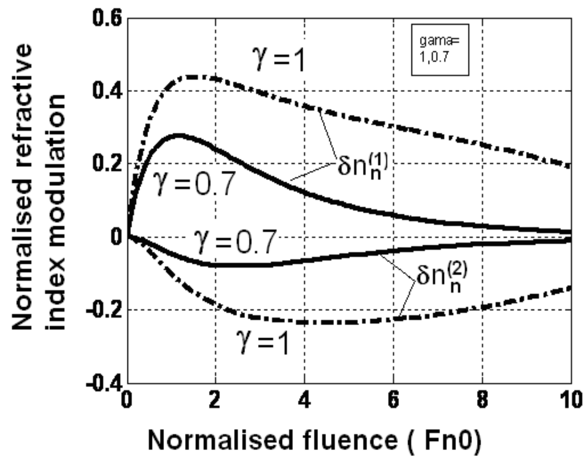

(b)

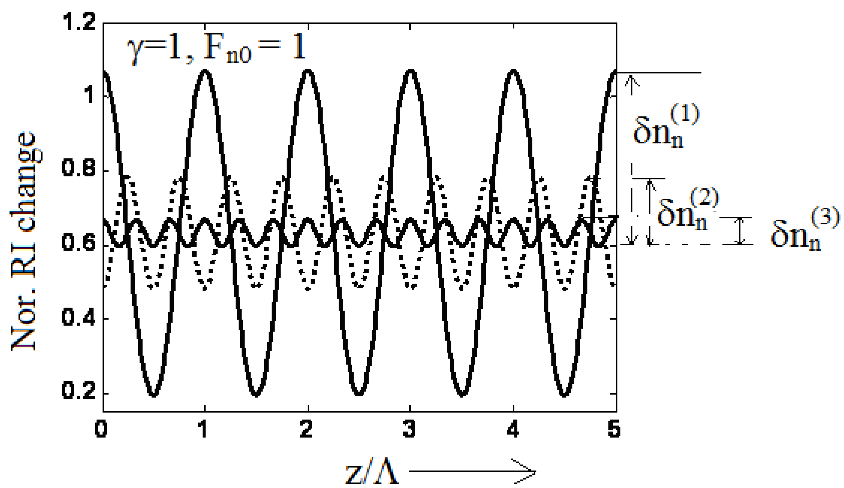

(c)

Figure 5.3: (a) Change of $<\delta n_n>$, $\delta n_n^{(1)}$, $\delta n_n^{(2)}$ and $\delta n_n^{(3)}$ with F_{n0} for γ (x) =1 (b) Change of $\delta n_n^{(1)}$ and $\delta n_n^{(2)}$ for γ (x) =0.7 and γ (x) =1 (c) Spatial variation of first three harmonics of normalized refractive index change [$\delta n_n(z)$]

The growth rate, required fluence to saturate and respective saturation coefficients of $\delta n_n^{(1)}$decreased with decrease in $\gamma(x)$. The ratio of saturated values of $\delta n_n^{(2)}$to$\delta n_n^{(1)}$ decreases with decrease in fringe contrast (γ). Typically, [max ($\delta n_n^{(2)}$)/ max($\delta n_n^{(1)}$)] = 0.53 for γ =1 and 0.28 for γ =0.7. Higher is the fringe visibility, higher the photo induced refractive index modulation, both in first and second order of FBG. Fig 5.3c shows spatial variation of first three harmonics with modulation amplitudes $\delta n_n^{(1)}$, $\delta n_n^{(2)}$ and $\delta n_n^{(3)}$, each around the mean value of $\langle \delta n_n \rangle$ for F_{n0} =1 and $\gamma(x)$ =1. The planes of maxima of the first and second harmonic terms of eqn (5.15) are

$$z = Nd/2 \quad \text{and} \quad z = (2N+1)d/8 \tag{5.20}$$

where N is an integer. The amplitude of these harmonic terms changes with F_{n0} and $\gamma(x)$. The amplitude of different harmonics decreases with decrease in fringe contrast. The ratio of amplitude of higher harmonics to the amplitude of first harmonic ($\delta n_n^{(1)}$) decreases with decrease in fringe contrast. The actual fluence required for saturation of refractive index modulation is different for different fiber types for same writing UV wavelength or different for same fiber but a different writing UV wavelength. Similarly for same induced normalized index modulation, the actual value of refractive index modulation may be different for different fiber composition and concentration of defects.

5.2.5 Fiber Bragg grating reflection in first order

The first harmonic component [$\delta n^{(1)}$] of refractive index change [δn (z)] contributes to FBG reflection at Bragg wavelength (λ_b), given as $\lambda_b = 2n_{eff}\Lambda$, where n_{eff} is effective refractive index of the fiber. The variation of reflectivity (R), resonant wavelength shift [$\Delta\lambda_b$ (shift)] and spectrum bandwidth [$\Delta\lambda$ (FWHM)] of the FBG with accumulated fluence (F_{n0}) during fabrication, is given as [14-16]

$$R(F_{n0},\gamma) = \tanh^2\left(\frac{\pi\eta\Delta n_{\max}\delta n_n^{(1)} L}{\lambda_b}\right) \tag{5.21}$$

$$\Delta\lambda(shift) = \lambda_b \Delta n_{\max} \eta < \delta n_n > / n_{eff} \tag{5.22}$$

$$\Delta\lambda(FWHM) = \sqrt{(\Delta n_{\max} \eta \delta n^{(1)} / n_{eff})^2 + (\lambda_b / n_{eff} L)^2} \tag{5.23}$$

where L is grating length.

For typical values (λ_B = 1550 nm, η = 0.85 and Δn_{max} = 1x 10^{-3}), the simulated FBG reflectivity with increase in normalized accumulated fluence (F_{n0}), for fringes of different contrast [$\gamma(x)$], is shown in fig.5.4a for grating length of 5 mm.

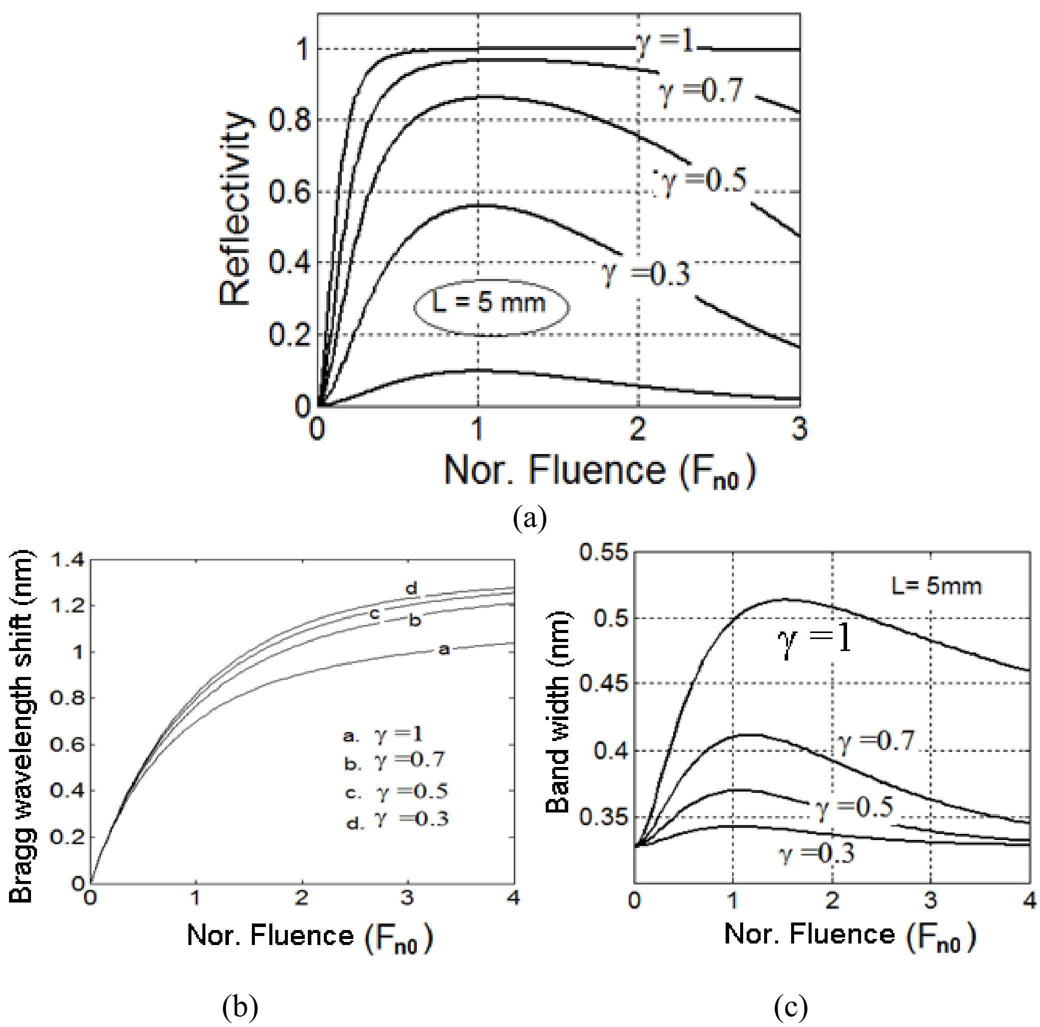

Figure 5.4: Simulated variation of (a) FBG reflectivity (b) Bragg wavelength shift (c) Bandwidth with increase in accumulated normalized fluence for a FBG of length 5 mm

The simulated FBG reflectivity decreases after saturation due to decrease in refractive index modulation. Fig.5.4b shows the Bragg wavelength shift with increase in accumulated fluence which is independent on FBG length. Fig.5.4c shows the simulated bandwidth of the FBG spectrum with increase in accumulated fluence. The FBG spectrum bandwidth (FWFZ) first increased to maximum at saturation followed by decrease due to decrease in RI modulation after saturation.

5.3 Effect of non-uniform UV beam profile on evolution of Bragg reflection spectrum

This section analyses the effect of beam profile on the evolution of FBG spectrum in view of non linearity in photo induced refractive index change. The shape of induced refractive index modulation profile is always uniform along the length of grating for a uniform writing UV beam. But when the fringe intensity is non uniform, saturation of index modulation at different sections of the FBG will occur at different exposure. Therefore the shape of index modulation profile along the length of the grating will dynamically change thus affecting FBG spectrum evolution while writing FBG. Different techniques are used for grating apodisation [229-231] including the technique fringe less UV [230-231]. However, the duration of UV pre/post exposure to obtain desired index profile must be related to UV beam profile, evolution dynamics and saturation affects. The present analytical study focuses on the effect of non-uniform energy distribution; specifically cylindrically focused UV beams of Gaussian and top hat energy distribution, on the dynamics of refractive index modulation and average index change (termed as AC and DC index further in the text) and their effect on FBG spectrum.

5.3.1 Fringe intensity distribution

Fig.5.5 shows the schematic of UV beam of intensity I(r), polarized parallel to grating grooves, incident normally on the zero order suppressed phase mask in the YZ plane. The interference at P (x, z) is due to +1 order from $P_1(0, z_1)$ and -1 order from P_2 $(0, z_2)$ separated by the distance Δz (= 2x tanψ).

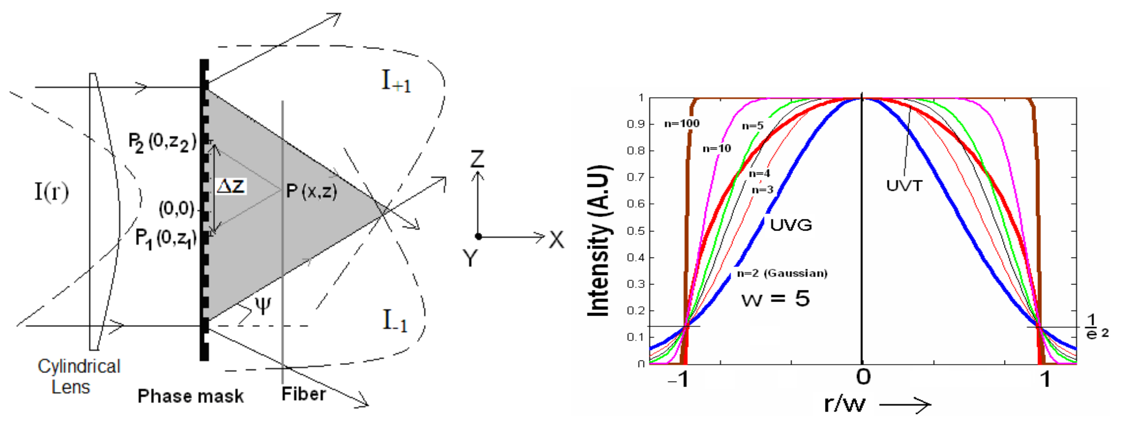

(a) (b)

Figure 5.5: (a) Schematic of FBG writing by phase mask technique with non uniform UV beam profile (b) Typical beam profiles

For an arbitrary UV beam profile, the phase and field amplitudes at P(x,z) are not same for both +1 and -1 order as they originate from different points of the incident wave front. The fringe intensity distribution due to superposition of +1 and -1 order (residual 0, ± 2, .. orders neglected) can be expressed as [212]

$$I_f(x,z) = I_m(x,z)[1+\gamma_1(x)g(x,z)\cos(\frac{2\pi}{\Lambda}z)] \tag{5.24}$$

$$\text{where } I_m(x,z) = I_{+1}(x,z) + I_{-1}(x,z) \ ; \quad g(x,z) = \frac{2\sqrt{I_{+1}(x,z)I_{-1}(x,z)}}{I_m(x,z)} \tag{5.25}$$

$\gamma_1(x)$ is spatial coherence function, $I_{+1}(x, z)$ and $I_{-1}(x, z)$ are intensity distribution of +1 and -1 order beam at P(x, z) . The expression $I_m(x, z)$ is the mean intensity of fringe pattern and g(x, z) is termed as fringe modulating parameter. The fringe visibility (γ) can be expressed as,$\gamma(x, z) = \gamma_1(x)\, g(x, z)$. The fringe intensity distribution in such cases can be expressed as in eqn (5.24) in which case the interferometer type will suitably modify $I_m(x, z)$ and g(x, z). For a uniform UV beam, I_m (x, z) is constant and g(x, z) = 1. If I(x, z) is the UV beam intensity distribution at P(x, z) on the fiber in the absence of phase mask, then the expression for I_m(x, z) and g(x,z) at P(x, z) in the presence of phase mask can be obtained by incorporating I_{+1}(x,z) and I_{-1}(x, z) in equation (5.24) as [212]

$$I_{+1}(x,z) = \eta_{+1} I(x, z - x\tan\psi) \tag{5.26}$$

$$I_{-1}(x,z) = \eta_{-1} I(x, z + x\tan\psi) \tag{5.27}$$

where η_{+1} and η_{-1} are diffraction efficiency of +1 and -1 order beams respectively. Fringes mean intensity and fringe modulating parameter, I_m(x, z) and g(x, z), change due to change in I_{+1} (x, z) and I_{-1}(x, z), based on typical UV beam profile used for FBG fabrication. The functional form of a continuous transition from a Gaussian to a top hat beam profile is given by the relation

$$I(r) = I(y,z) = \mathrm{I}_0 \exp(-2\left|\frac{r}{w}\right|^n) \qquad (n \geq 2) \tag{5.28}$$

where I(r) is intensity distribution at r and w is $1/e^2$ beam radius. The beam is Gaussian for n=2 and super Gaussian of order n for n >2. The beam profile broadens with increase in n, approaches top hat as n approaches infinity [232,212]. For specific, circular UV beams of Gaussian and top hat energy distribution are assumed for further analysis.

5.3.2 Fringe modulation due to beam focusing

A cylindrical lens focuses the beam to increase fluence in the fiber core. This cylindrical focusing leads to transformation of the +1/-1 beam profile incident on the fiber [233-234]. The cylindrically focused Gaussian and top hat beams are designated as UVG beam and UVT beam respectively. It is assumed that when the FBG writing position in the fringe depth is changed, the cylindrical lens also moved to keep laser spot size constant at each fiber position (x). In case of UVG beam, the intensity distribution in the focal plane of the cylindrical lens is Gaussian nature, both transverse (y-axis) to and along the fiber length (z-axis). The variation of average intensity (averaged over y-axis) along the fiber length compressed to a narrow strip (Δy) at the fiber position by the cylindrical lens, given as,

$$I(x,z) = \frac{1}{\Delta y}\int_{-\infty}^{\infty} I(x,y,z)dy = I_{0g}(x)\exp(-2z^2/w^2) \tag{5.29}$$

where $I_{0g}(x)$ is average intensity at z = 0. Similarly for UVT beam, the intensity distribution in the focal plane is a Sinc function transverse to y-axis. The variation of average intensity (averaged over y-axis) along fiber length (z-axis) is approximately

$$I(x,z) \approx I_{0t}(x)\sqrt{1-\left(\frac{z}{w}\right)^2} \quad (z \leq w) \tag{5.30}$$

where $I_{0t}(x)$ is average intensity (at z = 0). The thickness of focal strip [Δy] is assumed as same across the fringe depth. The length of the cylindrically focused strip at fiber position (x) depends on laser beam spot size at x. For a collimated beam, the beam expands due to diffraction divergence and therefore $I_{0g}(x)$ and $I_{0t}(x)$ will decrease with x. For typical fiber phase mask distances, the variation of length of the cylindrically focused strip can be neglected. Therefore for further computational analysis, $I_{0g}(x)$ and $I_{0t}(x)$ has been assumed as independent on x. The approximation in equation (5.30) is due to marginal change in shape of the intensity profile of a flat top beam with sharp boundary during propagation. Since the fringes of sub micron period are difficult to resolve in the 3D figure of fringe intensity distribution (I_{fe}) across whole fringe depth, the fringe intensity envelope were plotted that is bounded by surface of maximum and minimum fringe intensity and is defined as [212],

$$I_{fe}(x,z) = I_m(x,z)[1 \pm \gamma_1(x)g(x,z)] \tag{5.31}$$

This is obtained by putting z = mΛ (m integer) in eqn (5.24). Typically for w=2.5 mm, $\psi = \sin^{-1}(\lambda/d)$ [λ = 255nm, d = 1.06μm] and $\gamma_1(x)$ =1, the fringe intensity envelope due to UVG and UVT beam are shown in fig. 5.6a and 5.6b respectively where thickness of focused fringe strip [Δy] is assumed as same at each fiber position (x).

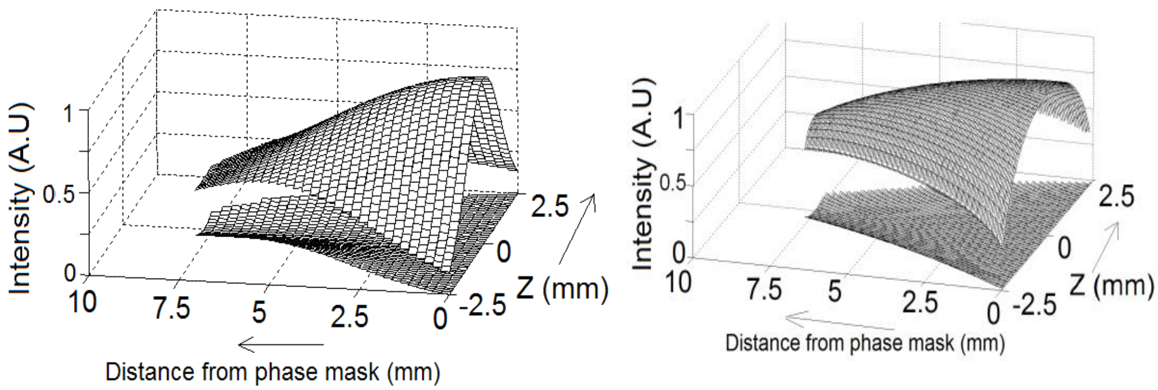

(a) (b)

Figure 5.6: Variation of maximum and minimum fringe intensity in the fringe depth by superposition of ±1 order of phase mask with (a) UVG (b) UVT beam illumination

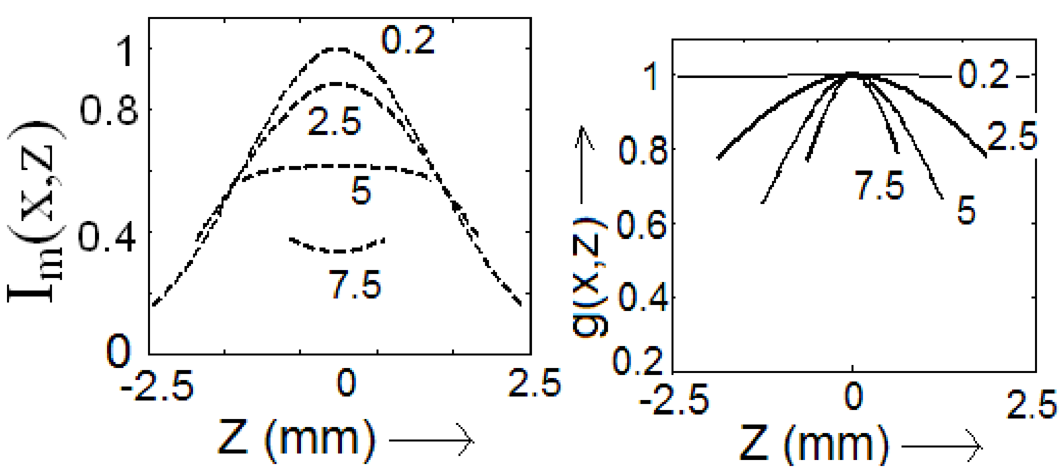

(a) (b)

Figure 5.7: Change of mean fringe intensity and (b) fringe modulating parameter along the fiber length at different phase mask fiber distance (indicated in mm) for UVG beam illumination.

The variation of mean fringe intensity, $I_m(x, z)$ vs. z and fringe modulating parameter, g(x, z) vs. z for UVG beam at different phase mask fiber distance x (indicated in fig. in mm) are shown in fig. 5.7a and 5.7b respectively. The intensity maxima and mean fringe intensity [$I_m(x, z)$] decreases both along x and z directions. The profile of $I_m(x, z)$ vs. z changes shape (convex to concave) as distance from phase mask (x) increases. At x=0.2 mm (close proximity), the profile is almost Gaussian. At the centre of overlap region (x ≈5 mm), the profile of $I_m(x, z)$ vs. z is nearly flat. The variation of g(x,z) vs. z also changes shape for different values of x. At z = 0, g(x, z) is always unity. It decreases both along ± z, the rate of decrease is higher with increase in distance from phase mask (x).

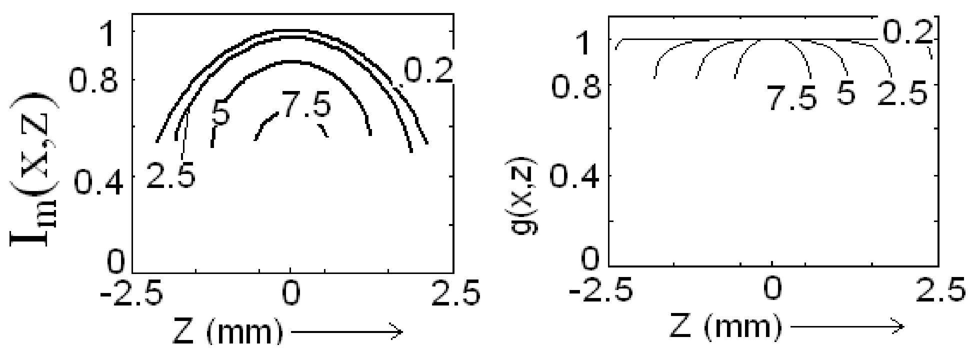

(a) (b)

Figure 5.8: (a) Change of mean fringe intensity and (b) Fringe modulating parameter along the fiber length at different phase mask fiber distance (indicated in mm) for UVT beam illumination.

For UVT beam, the profile of $I_m(x, z)$ vs. z and g(x, z) vs. z at different distance from the phase mask is shown in fig. 5.8a and 5.8b respectively. The profiles of $I_m(x, z)$ vs. z for different x are almost similar in shape, but the magnitude decreases with increase in distance from phase mask. The profile of g(x,z) vs. z is almost flat. It is clear from above discussion that different UV beam profiles affect fringe intensity and fringe modulation differently. Since induced refractive index change [δn(x, z)] is proportional to UV fluence, therefore AC and

DC index profile of the FBGs will be affected by the spatial distribution of fringe intensity which in turn depend on UV beam profile and beam coherence.

5.3.3 Dynamic evolution of refractive index modulation profile

The spatial profiles of Fourier coefficients [$<\delta n_n (x,z)>$] and [$\delta n_n^{(1)} (x,z)$] of refractive index change [$\delta n_n (x,z)$] are uniform across FBG length when written by uniform beams. When the beam profile is non-uniform, the refractive index change [$\delta n(x,z)$] distribution profile is no longer remains same with continuous fringe irradiation due to non-linear growth. The induced refractive index distribution [eqn (5.11)], modified to incorporate $I_m(x,z)$ and $g(x,z)$ at any point $P(x,z)$ is given as [213],

$$\delta n_n(x,z) = [1 - \exp[-F_{n0}(x,z).\{1 + \gamma(x,z).\cos\frac{2\pi}{\Lambda} z\}] \qquad (5.32)$$

where F_{n0} [$= \beta F_{m0}(x, z)$] is normalized fluence and γ [$= \gamma_1(x)\ g(x, z)$] is fringe visibility at $P(x, z)$. The $<\delta n_n (x, z)>$ and $\delta n_n^1(x, z)$ growth rate across the irradiated fiber length is not same because of variation of $I_m(x,z)$ and $g(x,z)$. Due to differential growth, the saturation of $\delta n^1(x,z)$ at different sections of the FBG occurs at different irradiation times. The induced index modulation, Δn [$= \eta\ \Delta n_{max}\ \delta n_n^{(1)}$] and average index change, $<\Delta n>$ [$= \eta \Delta n_{max} <\delta n_n>$] at different sections are also different due to different value of $\gamma(x,z)$. These two factors, $I_m(x, z)$ and $\gamma(x, z)$, lead to dynamic change in shape of $<\delta n(x, z)>$ and $\delta n^1(x, z)$ profile with increasing fluence due to differential growth of refractive index at different sections of the FBG. To illustrate it, typically FBG writing at distance (x) of 0.2 mm from the phase mask by a UVG/UVT beam of diameter 5 mm is considered. For $\gamma_1(x) =1$, the variation of normalized and $\delta n^1(x, z)$ and $<\delta n (x, z)>$ with normalized fluence, F_{n0} [$= (\eta_{+1}+\eta_{-1})\ \beta I_0 t$ where $I_0 = I_{0g}$ for UVG or I_{ot} for UVT beam at x=0 and z=0] are shown in figs. 5.9a and 5.9b respectively for UVG beam and in figs.5.9c and 5.9d that of for UVT beam. The $\delta n^1(x, z)$in an infinitesimal length passes through three regimes i.e. initial fast growth, saturation and decay with continuous irradiation. The $\delta n^1(x, z)$ at centre saturates earlier than that at edges. The required normalized fluence [F_{n0}] for $\delta n^1(x, z)$ saturation increases from centre to edges. The $\delta n^1(x, z)$ and $\langle \delta n\ (x, z)\rangle$ profiles of FBGs written in close proximity to phase mask, are tapered at low fluence, almost similar to fringes mean intensity/UV beam profile.

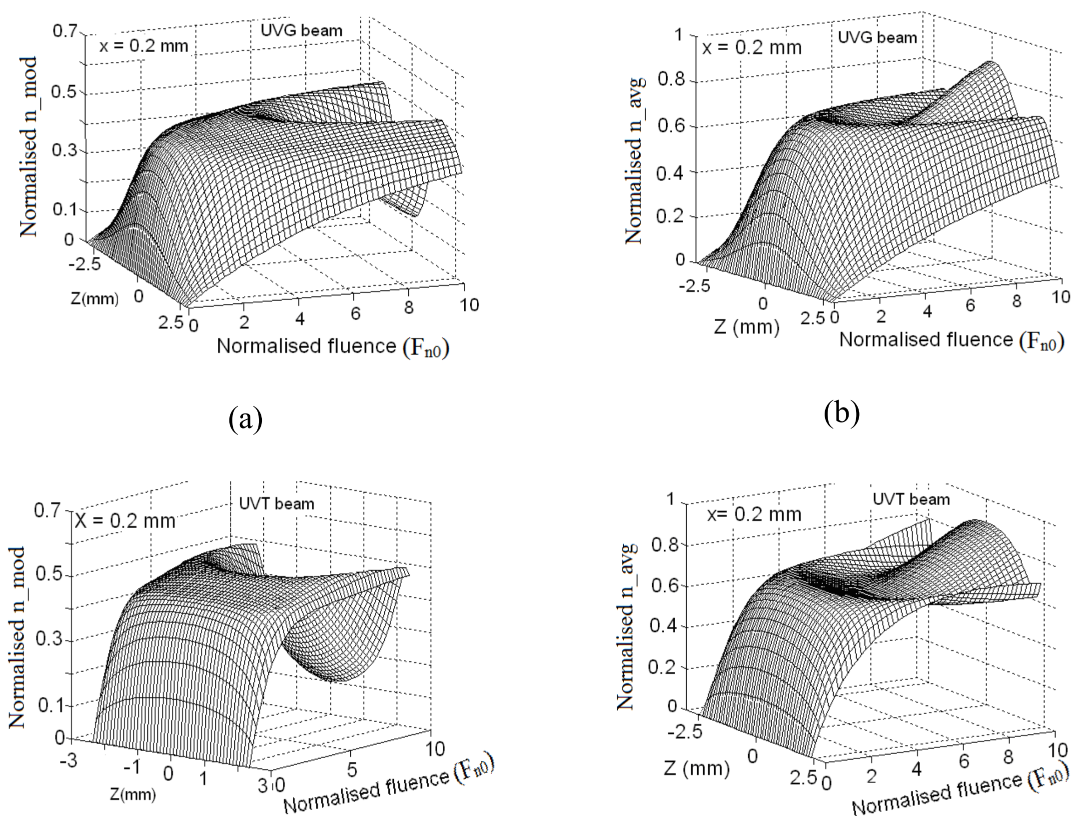

(a) (b)

(c) (d)

Figure 5.9: Variation of normalized (a) $\delta n^1(x,z)$ (b) $\langle \delta n\ (x,z)\rangle$ for UVG beam and (c) $\delta n^1(x,z)$ (d) $\langle \delta n\ (x,z)\rangle$ for UVT beam with normalized accumulated fluence

This is because when the $\delta n^1(x, z)$ at central portion of the FBG approaches saturation and that at the edges is still increasing leading to flatter profile. Beyond saturation, a dip in the $\delta n^1(x, z)$ profile first starts at the centre. The dip deepens and broadens with increasing fluence. This is because while at the central portion, the index changes at positions of fringe maxima approaches saturation that at positions of fringe minima continues to grow. As a consequence, index contrast at the central section goes on decreasing with increase in fluence while that at the edges increases up to saturation because of lower fringe intensity $I_m(x, z)$. At the same time, $\langle\delta n\ (x, z)\rangle$ grows assuming convex upward shape with decline of $\delta n^1(x, z)$ modulation. With continuous exposure, the normalized $\langle\delta n\ (x, z)\rangle$ continues to grow to the maximum value of unity causing complete erasure of index contrast, starting from central portion. The erasure time at different sections the grating are different. The$\delta n^1(x,z)$and $\langle\delta n\ (x,z)\rangle$ profile of UVT beam is flatter in comparison to UVG beam. For UVT beam, with continuous irradiation, the growth of rate of $\delta n^1(x,z)$and $\langle\delta n\ (x,z)\rangle$, their profile, required fluence for index modulation saturation will be different from that of UVG beam due to its different beam intensity distribution.

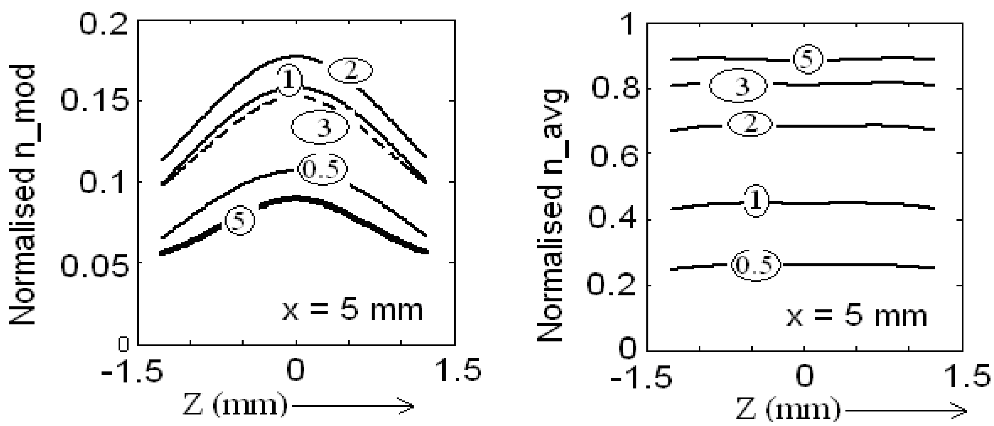

(a) (b)

Figure 5.10: Simulated (a) $\delta n_n^1(x, z)$ (b) $\langle\delta n_n\ (x, z)\rangle$ of the UVG beam written FBG at different normalized accumulated fluence for phase mask fiber distance of 5 mm.

If the phase mask fiber distance (x) is changed, magnitude and profile of $\delta n^1(x, z)$ and $\langle\delta n\ (x,z)\rangle$will be different from that of previous position even at same UV fluence due to differential variation of g(x,z) and $I_m(x, z)$ in different writing planes [figs.5.7 and 5.8]. For illustration, the FBG writing plane at x= 5 mm, about middle of the fringe depth is considered. The $\delta n^1(x,z)$ and $<\delta n\ (x,z)>$ profiles at different normalized fluence [value of Fn_0 indicated in the figure] with UVG as writing beam are shown in figs. 5.10a and 5.10b respectively. It is evident that at x = 5mm, the $\delta n^1(x, z)$ is always tapered for all fluence values unlike the FBG writing position at x=0.2 mm [fig.5.9a]. The saturated $\delta n^1(x,z)$ and required fluence to saturate at x =5 mm is less than that of at x= 0.2 mm. The $<\delta n\ (x, z)>$ profile is almost uniform due to flatness of $I_m(x,z)$ [fig.5.7a] at x = 5 mm. From the analysis it is clear that due to nonlinear growth of refractive index and saturation effects, the dynamics of $\delta n^1(x,z)$ and $<\delta n(x,z)>$ are different for different writing UV beam profiles and also are different in different writing planes for same writing UV beam.

5.3.4 Dynamic evolution of FBG reflection spectra

Bragg grating spectra is a function magnitude and profile of $\delta n^1(x,z)$ and $<\delta n\ (x,z)>$, grating length (L) and grating period (Λ) [14-16]. With continuous irradiation of non uniform UV fringes, the reflection spectrum of the FBGs changes due to change in magnitude and profile of $\delta n^1(x, z)$ and $<\delta n\ (x, z)>$. The FBG reflection was computed by Transfer matrix due to non uniformity of $\delta n^1(x, z)$ and $<\delta n\ (x, z)>$ profile [16] . Further discussion is limited to UVG/UVT beam. The simulated evolution of reflection spectra of an FBG written by UVG beam at different accumulated fluence (F_{n0}) are shown in fig.5.11a with typical parameters w = 2.5 mm, $\Delta n_{max}=10^{-3}$, x = 0.2 mm and $\gamma_1(x) = 1$. The ripple structure in the FBG spectrum changed with continuous exposure. At low fluence, the $\delta n^1(x, z)$ and $<\delta n\ (x, z)>$ profile is nearly Gaussian therefore diminishing side lobes. With increase in fluence, the first side lobe strength at the blue side of Bragg wavelength increased with increase of FBG reflectivity. As the irradiation continues, the AC index profile approached flatness [fig. 5.9a] thereby first side lobe strength at red side of the Bragg wavelength increased. Similarly the strength of other side lobes undergoes different evolution characteristics. As the irradiation continues further, the spectrum breaks up in to two individual peaks.

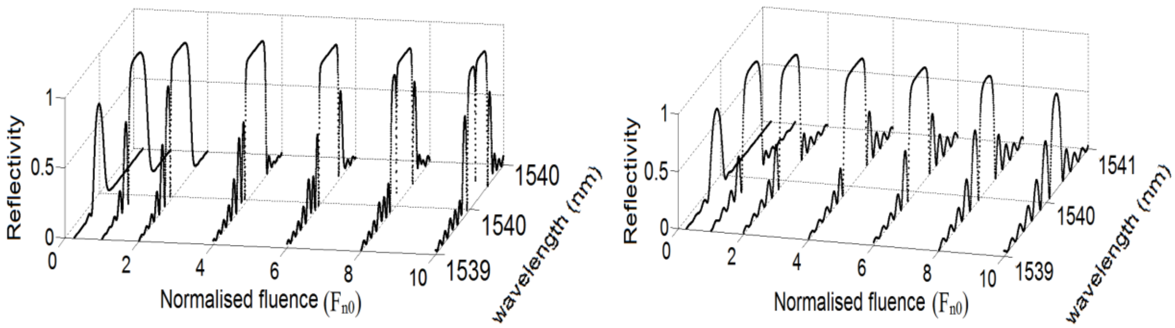

(a) (b)

Figure 5.11: Simulated reflection spectra of FBGs at different normalized fluence written by (a) UVG (b) UVT beam for phase mask fiber distance (x) of 0.2 mm.

Beyond saturation, $\delta n^1(x, z)$ decreases and $\langle \delta n\ (x, z)\rangle$ increases in the middle portion of the FBG. The $\langle \delta n\ (x, z)\rangle$ in the middle portion of the FBG length is higher than that of edges thus having two effective indexes leading to appearance of double peaks. The separation of two peaks is proportional to the difference between elevation and depression of induced average index ($\Delta\langle \delta n(x, z)\rangle$). Typically at $F_{n0}=10$, $\Delta\langle \delta n(x, z)\rangle = 0.25\ \Delta n_{max} = 2.5\text{x}10^{-4}$ which leads to separation of two peaks by about 0.25 nm. The simulated FBG reflection spectra at different accumulated fluence for UVT beam is shown in fig.5.11b. The side lobe suppression of FBGs written by UVT beam is less efficient due to flatter $\delta n^1(x,z)$ and $\langle \delta n\ (x,z)\rangle$ profile as compared to that of by UVG beam. If the FBG writing position is changed in the fringe depth, the dynamic evolution of grating properties changes due to change in fringe intensity distribution. With UVG writing beam, the evolution of grating spectra at different accumulated normalized fluence are shown in fig. 5.12 for typical fiber position of x = 5 mm. The ripples on both side of Bragg wavelength are almost absent due to tapered $\delta n^1(x,z)$ profile with almost uniform $\langle \delta n\ (x,z)\rangle$. The effect of beam profile on refractive index changes were discussed for γ_1 (x) = 1. This is justified for diffraction limited Gaussian/top hat UV beam, typically for diameter 5 mm, γ_1 (x) ≈ 1 for x=0.2 mm (typical position of proximity writing). However, γ_1(x) decreases with increase in fiber phase mask separation.

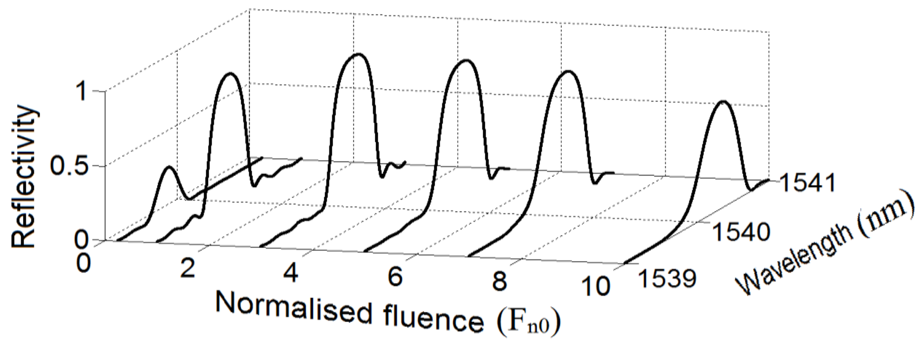

Figure 5.12: Simulated reflection spectra of FBG for phase mask fiber distance (x) of 5 mm.

The refractive index modulation profile of FBGs in proximity writing is mainly affected by UV beam intensity distribution.However with increase in phase mask fiber distance, γ_1 (x) decreases thus reducing refractive index modulation of FBGs written at larger distance from phase mask. Similarly for partially spatial coherent sources, γ_1(x) is less than unity. Beam pointing stability, thermo acoustic and ambient environmental vibration also dilute time average fringe contrast. In such a situation, FBG reflection spectrum at proximity writing will be affected by both UV beam intensity distribution and fringe contrast.

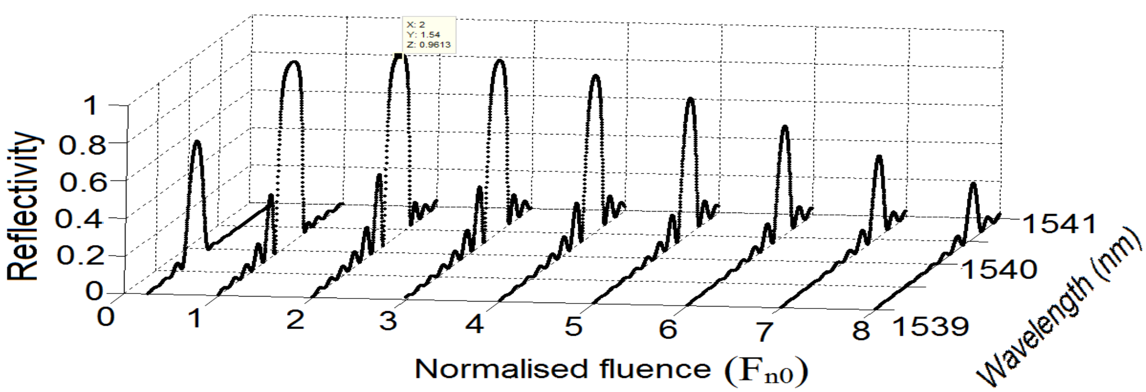

Figure 5.13: Simulated reflection fiber phase mask distance of 0.2 mm and γ_1(x) = 0.7

Fig.5.13 shows simulated reflection spectra of an FBG written by UVG beam at different accumulated fluence for typical values of $\gamma_1(x)$ = 0.7 at x=0.2 mm. The FBG reflectivity at same UV fluence will decrease with decease in $\gamma_1(x)$. The distribution of temperature profile also affects $\delta n^1(x, z)$ and $<\delta n (x, z)>$ besides photosensitivity thus affecting FBG spectrum during inscription. Due to higher UV beam power density, the typical temperature in the central portion of the FBG is higher in compared to edges thus tapering the $<\delta n (x,z)>$ profile by raising the index at the centre compared to edges. The refractive index modulation profile will decrease. However, the effect of temperature is significantly less in compared to photo induced change. The other factors that affects during writing process are hot spots in UV beam intensity, pointing stability, thermo-acoustic vibrations, fiber alignment, UV beam pulse power stability etc.

5.3.5 Effect of nonlinear growth on apodisation of grating profile

Grating apodisationis a technique of keeping $<\delta n (x, z)>$ constant along the grating length with gradually tapered $\delta n^1(x,z)$ profile which suppress side-lobes of FBG reflection spectrum [16]. The $\delta n^1(x, z)$ and $<\delta n (x, z)>$ profile depend on beam profile, fiber position in the fringe depth and duration of exposure. Particularly, when the grating is written by UVG beam at middle of fringe depth (x ~ 5 mm for w = 2.5mm), the $\delta n^1(z)$ profile is always tapered where as $<\delta n (z)>$ profile almost uniform [fig.5.10]. The ripples on both side of the resonant Bragg wavelength are almost absent [fig.5.12]. However, the grating reflectivity is less due to poor fringe contrast. Fibers with higher photosensitivity (high Δn_{max}) can used to increase FBG length to increase FBG reflectivity. Various techniques such as use of phase plate [230], multiple-exposure [231, 235], apodised phase mask with variable diffraction efficiency [236] etc have been used. The apodisation process requires controlled exposure.

The appropriate beam profile and irradiation time for pre/post fabrication illumination must be related to desired AC and DC index profile of the FBG due to non linear growth. The refractive index modulation and change in average index, due to additional fringe less exposure, can be obtained by replacing F_n (x,z) and γ(x,z) in equations (5.16-5.17) by F_t and γ_t, given as

$$F_t = F_n(x, z) + F_p(z) \quad \text{and} \quad \gamma_t = \gamma F_n(x, z) / [F_n(x,z) + F_p(z)] \tag{5.33}$$

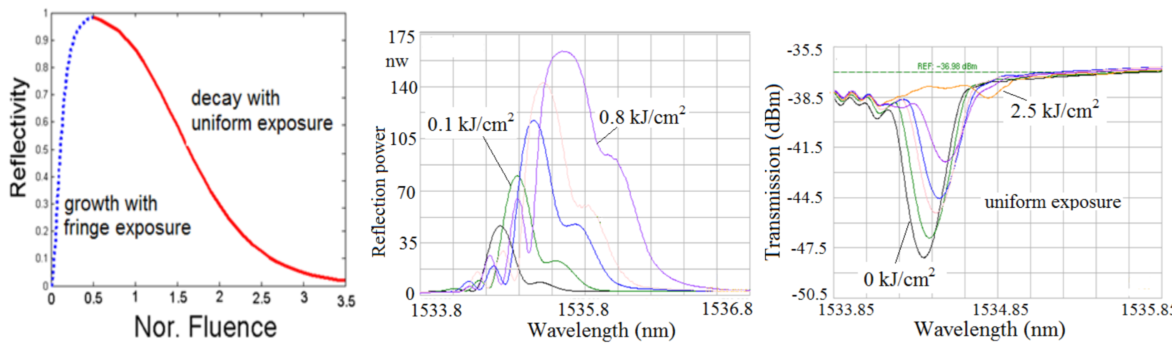

(a) (b) (c)

Figure 5.14: (a) Simulated growth of FBG reflectivity with fringe exposure and decay with fringeless UV illumination (b) Growth of a FBG reflection with fringe exposure (c) Decay of FBG transmission dip with uniform UV illumination

The additional exposure will reduce the refractive index modulation contrast thus reducing FBG reflectivity. Fig.5.14a shows the simulated growth of FBG reflectivity with uniform fringe exposure and decay with fringe less uniform illumination for typical value of Δn_{max} $=10^{-3}$ and L = 5mm as a typical example. As an illustration, fig.5.14b shows the growth of FBG reflection power with increase in accumulated fluence up to 0.8 kJ/cm^2. During growth, the Bragg wavelength shifted by ~ 0.6 nm which corresponds to increase in average refractive index by 5.65 x10^{-4}.The evolution of reflection spectrum of the FBG at different UV exposure times during fabrication was dynamic. During uniform UV illumination of same FBG with a total fluence of 2.5 kJ/cm^2, the Bragg wavelength shifted by ~ 0.5 nm which corresponds to increase in average refractive index by 4.7 $\times 10^{-4}$.Fringeless UV exposure on FBG reduced the refractive index modulation but average refractive index increased.

5.4 Effect of phase mask residual orders on fringe intensity distribution

In a standard phase mask maximized for diffraction in ± 1 order, residual orders (zero and higher orders) are not completely suppressed [16]. The complex refractive index structure with distinct Talbot diffraction pattern has been observed in the fiber core of a phase mask written FBG [202-204].By incorporating all the available diffracted orders, the fringe intensity distribution, can be expressed as [191],

$$I(x,z) = \sum_j I_j + \sum_{\substack{i,j \\ i\neq j}} \sqrt{I_i}\sqrt{I_j}\,\gamma_{ij}(x)\cos[(k_{ix}-k_{jx})x + (k_{iz}-k_{jz})z] \tag{5.34}$$

where I_j [= $f_j I_0$, where f_j is diffraction efficiency in j^{th} order and I_0 is intensity of the beam on phase mask] is the intensity of j^{th} order diffracted beam, k_{jx} and k_{jz} are the x (normal to phase mask) and z (along the phase mask) components of the wave vector, described as $k_{jx} = k \cos \alpha_j$; $k_{jy} = k \sin \alpha_j$ and $\alpha_j = \sin^{-1}(j\lambda/d)$. The coherence function [$\gamma_{ij}(x)$] is expressed as [191]

$$\gamma_{ij}(x) = \exp[-x^2(\tan\psi_i + \tan\psi_j)^2 / 2\sigma^2] \tag{5.35}$$

where σ is laser beam coherence width. The fringes intensity distribution can be written as

$$I(x,z) = I_0[1 + \sum_{\substack{i,j \\ i\neq j}} \frac{v_{ij}(x)}{2} \cos[\frac{4\pi}{\lambda_{uv}} \sin\alpha_{ij} \cos\beta_{ij}(z - x\tan\beta_{ij})] \tag{5.36}$$

where $\alpha_{ij} = (\alpha_i - \alpha_j)/2$ and $\beta_{ij} = (\alpha_i + \alpha_j)/2$

$$I_0(x,z) = \sum_j I_j(x,z) \quad ; \quad v_{ij}(x,z) = \frac{2\sqrt{I_i(x,z)}\sqrt{I_j(x,z)}\,\gamma_{ij}(x)}{I_0(x,z)}$$

The visibility, $v_{ij}(x, z)$, of the $(-1/+1)^{th}$ sinusoidal term in a plane, x, dominates over other terms and its maximums are separated by d/2 in the z- direction. The intensity distribution deviates from pure sinusoidal due to presence of residual orders. The spacing of stratification (maxima) lines of $(i, j)^{th}$ sinusoidal term is $\Lambda_{ij} = d \cos \beta_{ij}/|i-j|$ and are inclined at an angle β_{ij} with x-axis. The stratification lines, z = N d/2, of $(-1/+1)^{th}$ term are intersected at many specific points by stratification lines of $(i, j)^{th}$ sinusoidal terms ($i \neq -j$). The separation distance (Δx_{ij}) between two consecutive intersection points on the line z = N d/2 (N-integer) by $(i,j)^{th}$ sinusoidal stratification line is given by, Δx_{ij}=d/2 tan β_{ij}, which is also called as Talbot length [237]. The spatial profile of induced refractive index distribution in the core of fiber will depend on the net intensity distribution due to sum of all the sinusoidal terms which will be different if diffraction efficiency of different orders changes. Typically for $_{uv}$ =255 nm, there exist diffraction up to ± 4 orders for a phase mask period d = 1060 nm and up to ± 2 orders for a phase mask period d = 725 nm.

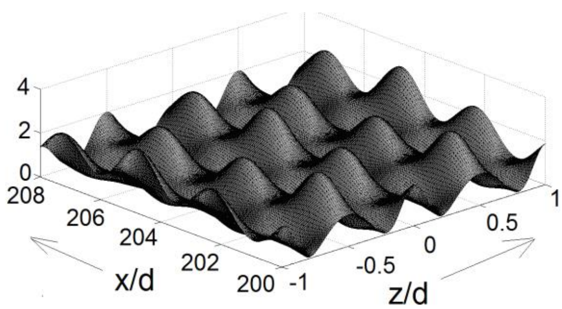

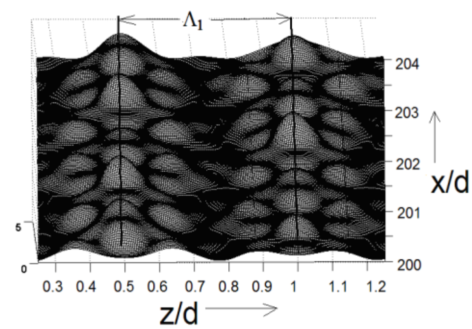

(a) (b)

Figure 5.15: Fringe intensity distributions for (a) $f_0 = 0.01$, $f_{\pm1} = 0.42$, $f_{\pm2} = 0.075$, $f_{\pm3} = 0$ and $f_{\pm4} = 0$ and for (b) $f_0 = 0.01$, $f_{\pm1} = 0.40$, $f_{\pm2} = 0.025$, $f_{\pm3} = 0.055$ and $f_{\pm4} = 0.015$

The simulated fringe intensity distribution in a small region at phase mask to fiber distance of x= 0.2 mm for typical diffraction efficiency of $f_0 = 0.01$, $f_{\pm1} = 0.42$, $f_{\pm2} = 0.075$, $f_{\pm3} = 0$ and $f_{\pm4} = 0$ [for a phase mask of pitch 0.725 μm, designated as PM1] is shown in fig.5.15a. The same due to $f_0 = 0.01$, $f_{\pm1} = 0.40$, $f_{\pm2} = 0.025$, $f_{\pm3} = 0.055$ and $f_{\pm4} = 0.015$ [for a phase mask of pitch 1.060 μm, designated as PM2] is shown in fig.5.15b. The intensity distribution is simulated assuming a uniform beam and $\gamma(x) = 1$. The intensity distribution for PM1 and PM2 are different. The intensity distribution for PM1 and PM2 are different.

However, the fringe periodicity of x- averaged (over the fiber core diameter, $\Delta x \approx 8$ μm) intensity profile along fiber axis is d/2 for both the fringe patterns PM1 and PM2. However, the fringe periodicity of x- averaged (over the fiber core diameter, $\Delta x \approx 8$ μm) intensity profile along fiber axis is d/2 for both the fringe patterns PM1 and PM2. The intensity distribution of PM1 is clearly defined. The period of modulation along phase mask (z which is the fiber axis) is d (0.725 μm). Such a fringe system may cause FBG reflection at about 2108 nm (~ n_{eff} d) and its harmonics. The observed reflection at 1054 nm is the second harmonic. In the intensity distribution of PM2, the fringe periodicities of d and d/2 along phase mask (z) co-exist.The intensity hills on line z = N d/2 are spitted unevenly. The fringe exposure of millions of UV pulses may dilute the sharp features due to fringe instability accompanied with nonlinear growth. The variation of intra pulse beam divergence, beam intensity and pointing fluctuation may further dilute the time average sharp features. Thus effectively the refractive index modulation period will be dominated by the periodicity of d/2 (0.53 μm). The Bragg reflection at ~ 1540 nm is first harmonic of refractive index change of periodicity 0.53 μm.

5.5 Conclusion

Based on one photon absorption, a model was developed to study the effect of spatial coherence of the writing UV beam on refractive index modulation saturation of type I FBG. The experimental trends of different rate of growth and refractive index modulation saturation of FBGs written by UV beams of different degree of coherence were explained theoretically.It is shown that the maximum reflectivity of a FBG written by a UV interference pattern of specific fringe visibility is obtained at specific fluence, beyond which the reflectivity of FBG decreases with an increase in exposure. This is attributed to a decrease in refractive index modulation after saturation. Further this model was extended to study the evolution of reflection spectrum of FBGs written by no uniform beam profile. The analysis takes into account UV beam energy distribution and non linear growth of refractive index for consideration. When the fringe intensity profile is no uniform, the average RI and refractive index modulation profile at a particular FBG writing plane changes shape, with continuous fringe irradiation. This is due to non linear growth and saturation affects at different sections of FBG occurring at different exposure times. It is analytically shown that RI modulation and average RI profiles of the FBGs written at different distances from the phase mask are also different due to different fringe intensity profile. In case of diffraction limited UV beams, the RI modulation and average RI of FBGs written in proximity to phase mask are mainly affected by UV beam intensity distribution rather than coherence. Thus, one advantage of the analysis is that it facilitates modeling and active control of the writing process. The analysis provides the trends on magnitude and loci of $\delta n^1(x,z)$ and $<\delta n (x,z)>$ and deviations from desired spatial index profiles which may facilitate choosing of parameters such as UV beam diameter, beam profile, beam focusing, length and position of fiber exposed to fringes, exposure time and fiber type for writing different type of FBGs of desired spectral characteristics. The knowledge of the profile is suitable for post fabrication processing such as fringeless post-irradiation for effective index correction.

Publications based on this chapter

1. "Analysis on the saturation of refractive index modulation in fiber Bragg gratings (FBGs) written by partially coherent UV beams", **R. Mahakud**, O. Prakash, S.V. Nakhe and S.K Dixit, Appl. Optics, **2012**, 51, 1828-1835.
2. "Analysis on the effect of UV beam intensity profile on the refractive index modulation in phase mask based fiber Bragg grating writing" **R. Mahakud**, J.Kumar, O. Prakash , S.V. Nakhe and S.K Dixit, Optics Commun., **2012**,285, 5351-5358.

Chapter 6

Studies on FBG fabrication and Bragg wavelength tuning by prism interferometers

6.0 Introduction

The fiber optic distributed sensing requires many FBGs, each of different Bragg wavelengths, in the fiber network [238-243]. Phase masks based writing is wavelength specific. Different methods were proposed to realize inscription of multiple FBGs at discrete wavelengths in an optical fiber [244–246]. Each method has own limitations. The prism interferometer route of FBG writing is a convenient choice of FBG inscription at different Bragg wavelengths.In addition, the fused silica prism-based FBG inscription is cost effective, with ease of fabrication/ handling. This is also inherently stable due to relatively high laser damage threshold in the absence of surface corrugations and/or coatings. The different refracting angle biprisms could be used to write FBGs at different wavelengths. The ease with which Bragg wavelength can be tuned could enable fabrication of more FBGs at different wavelengths to be serial multiplexed for distributive sensing.The FBGs have been written by single and biprism interferometers, using different UV sources [197-199]. The reportedmaximum reflectivity FBGs written by biprism interferometers are around 60% [197-200] and that by single prism (Lloyd prism) interferometers is around 80 % [223]. The observed reflectivity might be low for applications in telecommunication and fiber lasers. However, very high reflectivity is not essential for sensing applications as the sensing parameter is wavelength encoded. The comparatively low reflectivity of the FBGs written by biprism interferometer may be due to low fringe contrast at the FBG writing position. The second order reflection was observed by Xie *et al*. while writing FBG by Lloyd prism interferometer [223]. However, the link between nonlinear growth and writing UV beam spatial coherence on optimizing reflectivity of FBGs written by biprism and Lloyd prism interferometers are lacking. The Bragg wavelength tuning of biprism written FBGs was analyzed [247-248] assuming unity fringe visibility. However, the limitations on tuning, arising from finite coherence of the incidence UV beam and tilting of grating planes in the fiber core,is not paid sufficient attention.

In this chapter, the analysis on the FBG writing by prism interferometers using partially coherent 255 nm CVL UV beams of different spatialcharacteristics is carried out. The objective is to investigate the effect of beam spatial coherence and prism angle to determine the FBG writing position in case of biprism interferometer in order to optimize FBG reflection. The nature of beam overlap in single (Lloyd) prism and biprism are different. The different spatial variation of fringes contrast in two cases and their effect on the evolution and saturation refractive index modulation in first and second harmonics are discussed. The limit on Bragg wavelength tuning arising from finite coherence of the incidence UV beam is discussed. The comprehensive analysis incorporates the parameters such as fiber photosensitivity, prism angle, UV beam parameters such as coherence, beam diameter and beam collimation. Representative experimental results on FBG fabrication and wavelength tuning by biprism interferometer using UV1, UV2 and UV3 beams are presented. The FBG reflectivity up to ~ 12 dB (~ 93%) was observed with biprism based writing. The experimental trends on FBG writing agree with analytical results.

6.1 Analysis of FBG inscription by biprism interferometer

6.1.1 Optimization of FBG reflection

Fig 6.1a shows the schematic of a partially spatially coherent collimated UV beam (of wavelength λ_{uv}) and diameter 2W incident normally on the biprism of refracting angle A, width 2h and material refractive index n_p. The apex of the prism (O) is taken origin and x-axis taken as optical axis of the experimental set up. In the schematic, the fringes produced in the rhombus shaped overlap region OPQR.

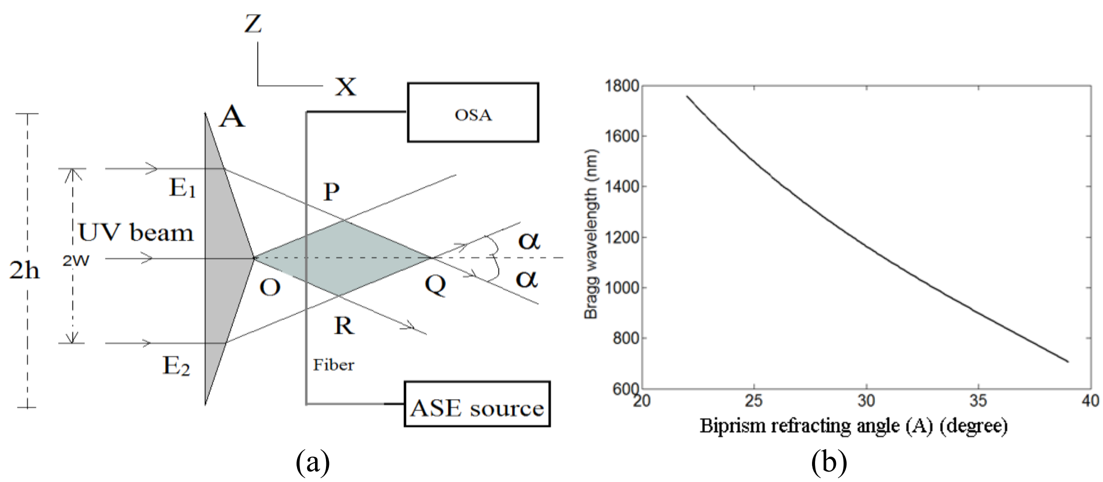

Figure 6.1: (a) Schematic of biprism interferometer for FBG inscription (b) Change in Bragg wavelength with change in refracting angle of the prism

The fringes are modulated along z direction (fiber axis). For the FBGs are written by this fringe system, the Bragg resonant wavelength is given as,

$$\lambda_b = 2\, n_{eff}\lambda_{uv}/2\sin\alpha \text{where } \alpha = \sin^{-1}[n_p \sin A] - A \tag{6.1}$$

The biprism of different refracting angle (A) could be used to write FBGs at different wavelengths. Fig.6.1b shows change in Bragg resonant wavelength with change in biprism refracting angle. The biprism fringes contrast [γ_{bp} (x, z)] in a FBG writing plane (along z), at a distance x from the biprism, is [eqn (3.8), ch.3)

$$\gamma_{bp}(x) = \mathrm{sinc}\,[k\, x\, \Delta\phi\, \eta_{bp}] \tag{6.2}$$

where η_{bp} = [sinα cosA/cos(α+A)].The UV fringes induced refractive index modulation of the FBG increases with increase in fringe contrast. The maximum value of refracting angle 'A' achievable by this set up is limited by the total internal reflection at the inclined face of the prism which is given as, $A_{max} = \sin^{-1}(1/n_p) = 41.8^0$ (for n_p=1.5). For $A \geq 41.8^0$, the FBG can't be written. To compare the effect of refracting angles on FBG fabrication, A = 24^0 and A = 32.5^0 are assumed as representative values for which the Bragg wavelengths are at about 1540 nm and 1054 nm respectively.Fig.6.2a shows the variation of fringe contrast [γ_{bp} (x)] with change in biprism to fiber distance (x) for a diffraction limited uniform UV beam of diameter 10 mm. The fringe contrast at a particular plane (x) decreases with increase in refracting angle (A) of the prism.

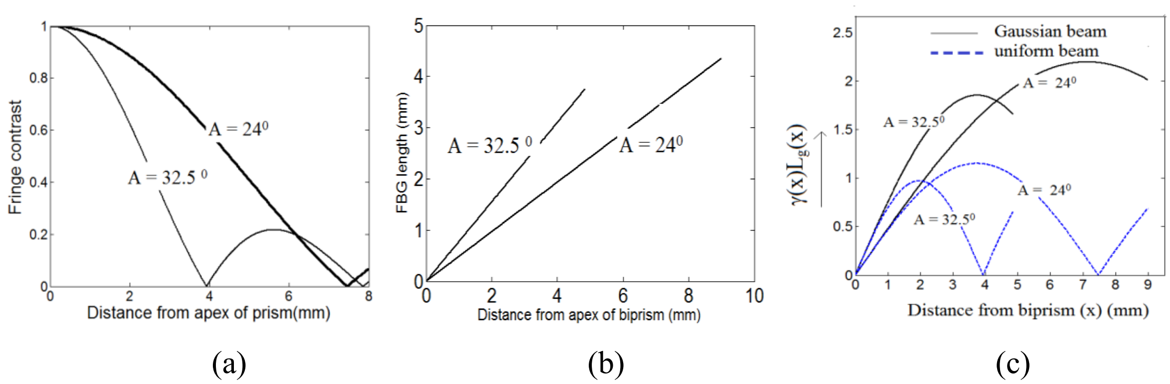

Figure 6.2: Variation of (a) fringe contrast [γ_{bp} (x)] (b) FBG length (L_g) (c) product of fringe contrast and FBG length [γ_{bp} (x). L_g] with distance (x) from the biprism

The FBG length depends on fiber position in the fringe depth. Using geometry, the position of maximum overlap ($x = x_m$) of refracted wavefronts is given as,

$$x_m = 0.5W (\cot \alpha - \tan A) \tag{6.3}$$

When the FBG is written at x_m, the grating length will be maximum, given as,

$$L_g (max) = W (1- \tan \alpha \tan A) \tag{6.4}$$

The inscribed FBG length (L_g), when the fiber is placed at a distance x (< x_m), is given as,

$$L_g = 2 x \tan \alpha \;\; [\text{for } x<x_m] \tag{6.5}$$

The FBG reflectivity (R) increases with increase in the product of refractive index modulation [Δn] and grating length (L_g) (eqn 5.21). The refractive index modulation is proportional to fringe contrast (eqn 5.17). For $x \le x_m$, the fringes contrast decreases and FBG length increases with increase in biprism to fiber distance (x). However, both the FBG length and fringes contrast decrease with increase in x for x > x_m. Thus choosing a FBG writing position beyond x_m is not appreciated. Therefore, the analysis on FBG reflection is confined for x ≤x_m. The maximum overlap position (x_m) for A = 24^0 is 9.2 mm and that for A=32.5^0 is 4.85 mm. The variation of FBG length with change in fiber position (x) up to x = x_m is shown in fig.6.2b. The rate of increase in FBG length (L_g) with x is higher for higher A. However, the maximum fringe overlap distance (x_m) decreases with increase in A. It is not necessary that the FBG reflectivity (R) will be maximum when written at x_m, rather than somewhere in between x=0 to x= x_m. The FBG reflectivity maximizes approximately for the position (x) where the product of fringe contrast [γ_{bp} (x, z)] and grating length (L_g) is maximum. Fig.6.2c shows the variation of [γ_{bp}(x). L_g(x)] vs. x for A = 24^0 and 32.5^0 and for Δϕ = 63 μrad and 33 μrad [which correspond to diffraction limited divergence of a 10 mm diameter uniform and Gaussian beam and beam of wavelength 255nm].

The amplitudes of first [$\delta n^{(1)}$] and second [$\delta n^{(2)}$] harmonic components in the Fourier expansion of δn(z) can be expressed as [213] (Eqns 5.17-5.18, chapter 5)

$$\frac{\delta n^{(1)}}{\Delta n_{\max}} \approx ab[1+0.125b^2+5.2\times10^{-3}b^4+1.085\times10^{-4}b^6+1.356\times10^{-6}b^8+1.13\times10^{-8}b^{10}+.......] \qquad (6.6)$$

$$\frac{\delta n^{(2)}}{\Delta n_{\max}} \approx -ab[0.25b^1+2.08\times10^{-2}b^3+6.51\times10^{-4}b^5+1.08\times10^{-5}b^7+1.13\times10^{-7}b^9+.......] \qquad (6.7)$$

where a = exp(-F_{n0}), b (x) = F_{n0} γ(x); F_{n0} = normalized mean fluence, γ (x) is fringe contrast and Δn_{max} is saturable index change. The reflectivity (R_m) of a uniform FBG at λ_m due to m^{th} harmonic component of refractive index change [called as m^{th} order] is described as [16,197]

$$R(F_{n0},\lambda_m,x) = \tanh^2\left(\frac{\pi\eta(\lambda_m)\Delta n_{\max}\delta n_n^{(m)}(x)L_g(x)}{\lambda_m}\right) \qquad (6.8)$$

where λ_m = 2 n_{eff} (λ_m) Λ /m ; m = 1 (first order), m = 2 (second order).

n_{eff} (λ_m) is the effective index of the fiber at wavelength λ_m andΛ is fringe period.Fig.6.3 shows variation of simulated reflectivity (R_1) of uniform FBGs at Bragg resonance wavelength [$\lambda_b = \lambda_1 = 2\ n_{eff}\ (\lambda_1)\ \Lambda$] for typical values A =$24^0$, λ_1 = 1540 nm, F_{n0}= 1, W = 5 mm, Δn_{max} = 1.5 x 10^{-3}. The typical beam divergence values are marked in the figure. The fiber positions of maximum reflectivity will move towards the apex of the prism and the maximum reflectivity will increase for UV beams of lower divergence. The zeros in the plot of reflectivity vs. distance, for higher divergence ($\Delta\varphi$ = 125 μrad, 180 μrad in figure), are due to zero of fringe contrast (Sinc function).

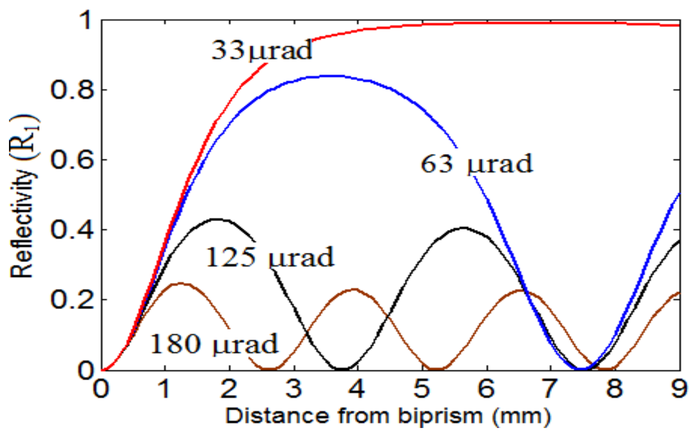

Figure 6.3: Variation of simulated FBG reflectivity with distance from the apex of the biprismfor different divergence angles

Figs 6.4b and 6.4c show the simulated FBG reflectivity R_1 (m=1, first order) and R_2 (m=2, second order) with change in fiber position (x) [for typical values A =24^0, λ_1 = 1540 nm, W = 5 mm, λ_2 =λ_1 /2, Δn_{max} = 1 x 10^{-3}] for $\Delta\phi$ = 63 μad and $\Delta\phi$ = 33 μad respectively. The different accumulated normalized fluence (F_{n0}) values are marked in figure. The typical divergence values are for diffraction limited uniform beam ($\Delta\phi$ = 63 μrad) and Gaussian beam ($\Delta\phi$ = 33 μrad) of diameter 10 mm.For a diffraction limited uniform beam (fig. 6.4a), R_1 is maximum ($R_1 \sim 0.54$ at $F_{n0} \sim 1.5$) at x ~ 4 mm. At same fluence, R_2 is ~ 0.17 at x ~ 4 mm.

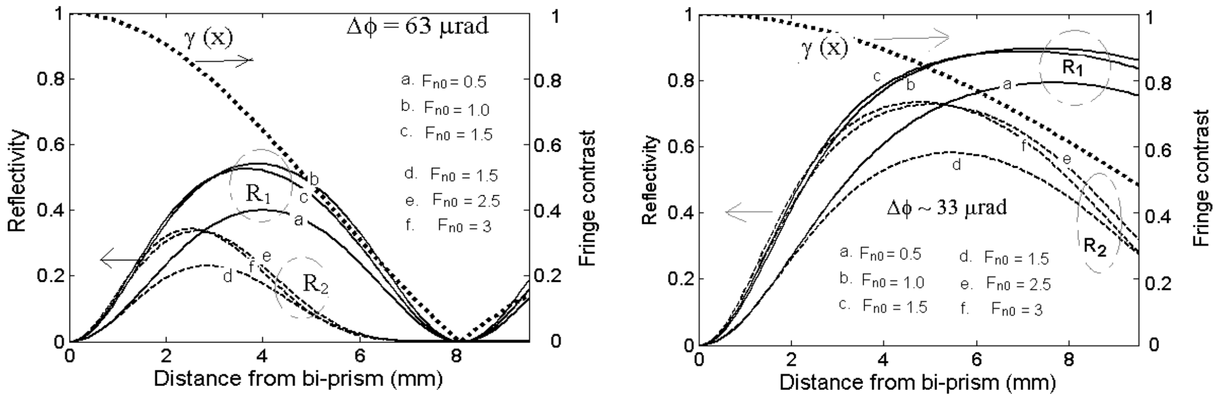

(a) (b)

Figure 6.4: Variation of simulated FBG reflectivity with distance from the apex of the biprism for (a) Diffraction limited uniform beam and (b) Gaussian beam

At $F_{n0} = 2.5$, R_1 decreases to ~ 0.34 and R_2 increases to ~ 0.23. The inscribed grating length at this position is ~ 2 mm. Maximum of R_2 (~ 0.32 at F_{n0} ~ 2.5) occurs at fiber position x ~ 2.5 mm which is comparatively nearer to the biprism. The inscribed grating length at this position is ~ 1.25 mm. Thus the positions of maximum reflectivity of R_1 and R_2 are different. Similarly, for the Gaussian beam, R_1 is maximum (R_1 ~ 0.9) at x ~ 7 mm and R_2 is maximum (R_2 ~ 0.72) at x ~ 4.5 mm. The maximum reflectivity position (x) is still less than the maximum overlapping position (x_m) [249].

6.2 Bragg wavelength tuning

6.2.1 By incidence angle tuning of incident collimated UV beam

The Bragg wavelength FBG is fixed for UV beam normally incidence on the biprism. The specific wavelength is decided by design specifics. For inscription of FBG at different wavelengths, separate biprisms with appropriate refracting angle are required. However, it is also possible to write FBGs at different Bragg wavelengths using a single biprism by changing the UV beam incidence angle. For this purpose, the biprism and the fiber mounts should be fixed on a single platform and the platform will be rotated about an axis, passing through point C and perpendicular to the plane. Fig.6.5a shows the schematic of a uniform beam incident on the biprism at angle,θ (with x-axis). The axes are shown in figure. The refracted wavefronts from upper and lower parts of the biprism are inclined at angles α_1 and α_2 with x-axis (fig. 6.4a) respectively, given as,

$$\alpha_1 = \sin^{-1} [n \sin \{A - \sin^{-1}(\sin\theta / n_p) \}] - A \tag{6.9a}$$

$$\alpha_2 = \sin^{-1} [n \sin (A + \sin^{-1}(\sin\theta / n_p))] - A \tag{6.9b}$$

For $\theta = 0$, the fringes are parallel to x-axis. For $\theta \neq 0$, the fringe lines will be inclined at angle $(\alpha_1-\alpha_2) / 2$ with x-axis. The fringe separation (Λ) is given as, $\Lambda = [\lambda_{uv} / 2 \sin (\alpha_1+ \alpha_2)/2]$.

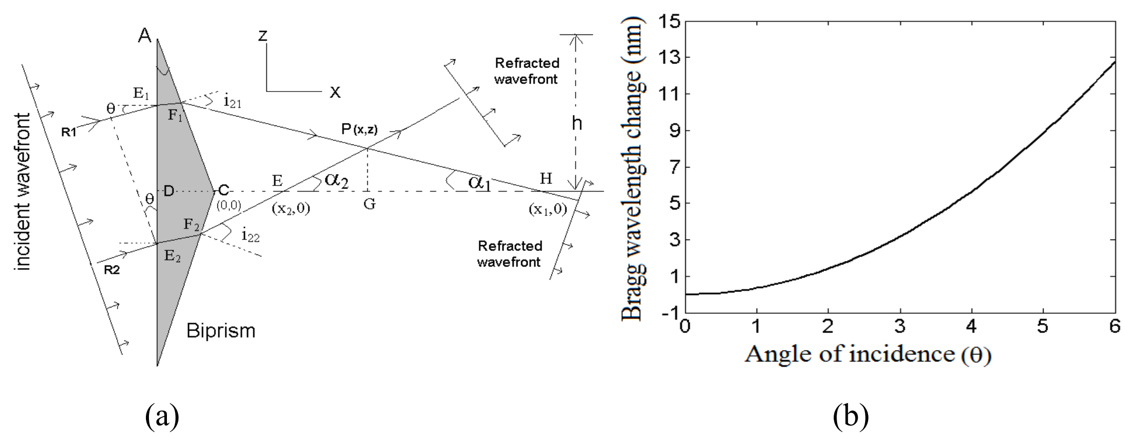

Figure 6.5: (a) Schematic of UV beam incidence at anlge θ on the biprism (b) Bragg wavelength change with increase in incidence angle (θ)

The fiber is usually placed along z-direction in a plane x (= constant) for FBG writing. The fringe separation along the fiber axis (z-direction) and thus Bragg resonant wavelength of the FBG imprinted in the fiber core by exposure of fringes are given as,

$$\Lambda_z = \Lambda / \cos \{(\alpha_1- \alpha_2)/2\} \quad ; \quad \lambda_b (\theta) = 2\, n_{eff} \Lambda / \cos \{(\alpha_1- \alpha_2)/2\} \tag{6.10}$$

With increase in incidence angle (θ), the Bragg wavelength ($\lambda_b (\theta)$) decreases from the designed value (for $\theta = 0$). Fig.6.5b shows the change in Bragg wavelength [$\lambda_b (\theta)$] with increase in incidence angle in degrees. The ratio, ($\Delta\lambda_b/\Delta\theta$), increases with increase in incidence angle, θ. The theoretical limit for tuning may be obtained for the critical angle of incidence on one of the inclined surface of the prism. As the angle of incidence increases, a point is reached at which the incident angle for one of the interfering beams on the inclined surface suffers total internal reflection. For typical values $A=24^0$, $n=1.5$, $n_{eff}=1.45$, this limit occurs at about 27.2° for which $\Delta\lambda_b \sim 400$ nm. However, in practice, the tuning range is limited by tilt of the grating planes with the fiber axis. The angle of inclination $[= (\alpha_1-\alpha_2)/2]$ of fringe lines increases with increase in input angle (θ). The core mode coupling will decrease with increase in tilt angle. The tolerable tilt angle is about 8^0 beyond which all the power in the core mode will lose to cladding. Thus the tunable Bragg wavelength in practice is of about 23 nm for varying of θ from 0 to 8^0.

6.2.2 Bragg wavelength tuning by a diverging UV beam

Fig. 6.6a shows the schematic of ray transfer when geometrically diverging UV beam incident on the biprism. The laser beam symmetrically diverges about the x-axis with divergence envelope of 2φ.

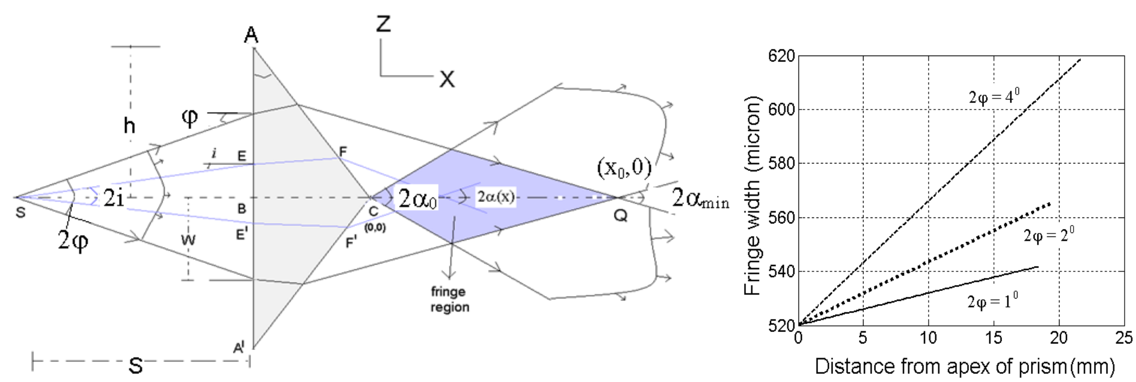

(a) (b)

Figure 6.6: (a) Schematic of the interference by geometrically diverging UV beam (b) Change in fringe width with increase in distance from the apex of the prism

The half width of the beam on the hypotenuse of the prism in the plane of figure is W. The source, from where the laser beam starts diverging, is located at a distance S from the input face of the prism. The interference fringes are perpendicular to the plane of the figure.

The apex (C) of the prism is the origin C (0, 0). The incident angle (i) on the prism changes from 0 to φ as the point of incidence on the biprism moves from B to E. For angle on incidence I (ray SE), the distance of intersection point from apex of prism on x-axis is x(i) and the angle of intersection α (i), are given as,

$$\alpha(i) = \sin^{-1}[n_p \sin\{A - \sin^{-1}((\sin i)/n_p)\}] - A \qquad (6.11a)$$

$$x(i) = x_F + y_F \cot \alpha(i) \qquad (6.11b)$$

$$\text{where } x_F = -(S.\tan i + h \tan A.\tan r_1)\tan A/(1+\tan A.\tan r_1) \qquad (6.11c)$$

$$\text{and } y_F = (S.\tan i + h \tan A.\tan r_1)/(1+\tan A.\tan r_1) \qquad (6.11d)$$

The fringe width in the plane x is given as, $\Lambda(x) = \lambda_{uv}/2\sin\alpha(x)$ and the Bragg resonant wavelength of the inscribed FBG is given as [249],

$$\lambda_b(x) = 2 n_{eff} \Lambda(x) \qquad (6.12)$$

On the x-axis, the angle of intersection of the refracted wave fronts [2α (x)] changes from $2\alpha_0$ at x= 0 to $2\alpha_{min}$ at x = x_0 (maximum beam overlap length on x-axis) where $\alpha_0 = \{\sin^{-1}(n_p \sin A) - A\}$ for $i = 0$ and $\alpha_{min} = \sin^{-1}[n_p \sin\{A - \sin^{-1}((\sin\varphi)/n_p)\}] - A$ for $i = \varphi$.

For small geometrical divergence envelope ($\varphi \sim 2^0$),$\alpha_{min} = \sin^{-1}[n_p \sin(A-\varphi/n)] - A$ and $x_m = [d(\cot\alpha_{min} - \tan A).\{\varphi/(2 n_p.\tan A) + W/h\}/\{\varphi/(2 n_p.\tan A) + 1\}]$. For typical values n_p=1.505, A=24 ^{0}, h=10 mm and W= 5 mm; $x_0 \sim 18.5$ mm for φ = 0. The beam overlap region from the apex of the prism marginally increases with increase in cone angle from (φ = 0 to 4^0). The Bragg wavelength increases from λ_1 [$= n_{eff}\lambda_{uv}/\sin\alpha_0$] at x = 0 to λ_1^{max} [$= n_{eff}\lambda_{uv}/\sin\alpha_{min}$] at x = x_0. Fig 6.6b shows variation of fringe width with distance from apex of the prism (x) for 2φ = 1^0, 2^0 and 4^0. The fringe width increases with increase in distance from the apex of the prism. This is because the fringe lines are hyperbolic due to superposition of spherical wave fronts. The tuning can be achieved by simple translation of the fiber in the fringe depth and/or by changing the cone angle. Fig. 6.7a shows the change in Bragg wavelength with change in distance (x) from the biprism for different cone angles (2φ). Thus Bragg wavelength [λ_b (x)] of inscribed FBG will increase with increase in prism to fiber distance (x). The rate of change of Bragg wavelength [$d\lambda_b$ (x) /dx] with distance from the apex of prism for small cone angles is almost linear. However, in a particular plane, [$d[\lambda_b(x)]/dx$] increases with increase in cone angle (2φ). The fringe width, in plane x= 4 mm, changes from 0.52 μm for $2\varphi = 0^0$ to 0.62μm for $2\varphi = 4^0$, a change of about 0.1μm (fig.6.6b) for which the possible Bragg wavelength tuning is of the order of 300 nm (fig.6.7a), a large tuning range. The Bragg resonant wavelength is tuned towards longer wavelength unlike the situation in incidence angle tuning of a collimated UV beam.

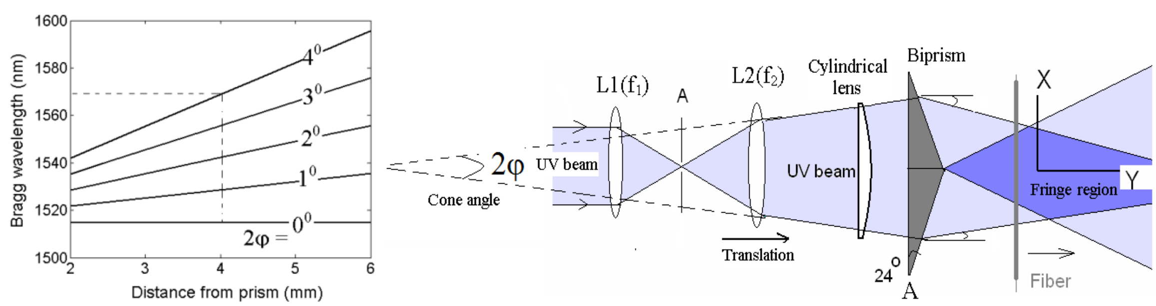

(a) (b)

Figure 6.7: (a) Variation of Bragg wavelength with increase in fiber to biprism distance for different cone angles (b) Schematic of FBG fabrication by using a diverging beam incidence on the biprism

Large tuning range is possible by changing the biprism to fiber distance. However, the limitation to tuning range is attributed to fringe contrast affecting FBG reflectivity. As shown in fig. 6.3, appreciable reflectivity is obtained for fiber positions varying between x = 2 mm to 6 mm for which the wavelength tuning is of about 55 nm for $2\varphi = 4^0$ and 25 nm for $2\varphi = 2^0$.

Alternatively, by keeping the fiber at same position (approximately at the position of maximum reflectivity), the collimating lens L2 (fig. 6.7b) could be horizontally translated. The UV beam is collimated for L = f_1+f_2, where L is separation distance between two spherical lenses L1 of focal length f_1 and L2 of focal length f_2, as shown in fig 6.6b. The beam is diverging for L< (f_1+f_2) and converging L > (f_1+f_2). The Bragg wavelength can be tuned by about 60 nm by increasing the cone angle from 0 to 4^0. For a geometrically diverging incidence beam, the chirp grating will be formed when the fiber is tilted in the fringe plane. The reflectivity may be less in this case. In another technique, a series of gratings, each of small length (~ 1mm), could be written on the same fiber by moving the fiber slowly in the fringe depth so that the reflection band width of each grating will partially overlap with other. As a result, the bandwidth of adjacent gratings will have appreciable reflectivity with larger bandwidth.

6.3 Analysis of FBG inscription by single (Lloyd) prism interferometer

The schematic of Lloyd prism based FBG writing is shown in fig.3.5a. The fringe modulation contrast, [γ_{lp} (x, z)], is given as, [249] (eqn 3.11, chapter 3)

$$\gamma_{lp}(x, z) = \text{Sinc}\,[k\, z\, \Delta\phi\eta_{lp}] \qquad (6.13)$$

The fringe contrast varies along the fiber length (z). With increase in irradiation time, the saturation of refractive index modulation and required fluence will decrease from z = 0 to z = L as the fringe contrast decreases along FBG length (eqn 6.13, Fig 3.5b). For typical $\alpha = 45^0$, $\theta \sim 58^0$, n_p=1.5, $\Delta\phi$ = 63 μrad, W= 5 mm and λ_{uv} = 255 nm, the simulated fringe intensity and induced refractive index distribution in a small section at z = 0.2 mm and z = 2.5 mm along the fiber length (z) is shown infig. 6.8 (solid line in figure is for intensity and dotted lines marked as a, b and c are for normalized fluence values 0.25, 1.5 and 3 respectively). The peak index regions flattened and minima regions are sharpened at z = 0.2 mm, at higher fluence. However at z = 2.5 mm, the $\delta n(z)$ profile even at higher fluence is almost sinusoidal with comparatively small modulation contrast with high average index change.

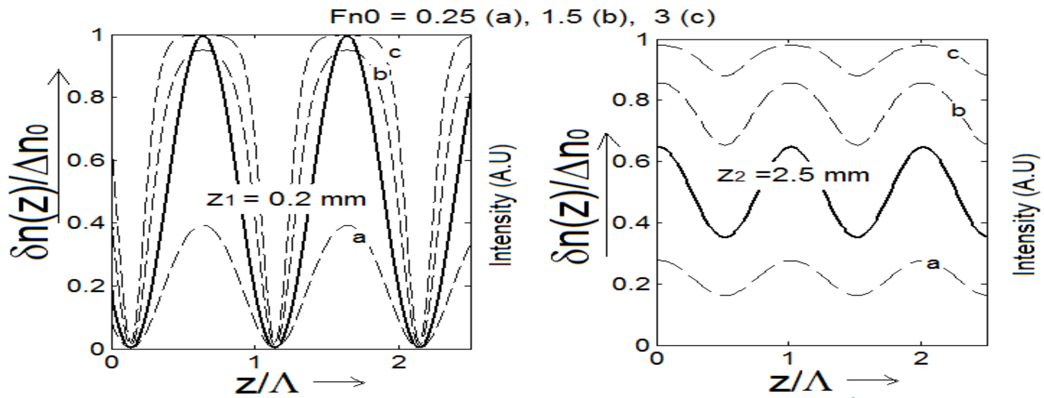

Figure 6.8: Refractive index distribution at positions z = 0.2 mm and 2.5 mm

Due to differential growth of induced refractive index along FBG length, the magnitude and profile of $\delta n_n^{(1)}$ and $\delta n_n^{(2)}$ along FBG length (z = 0 to L) will change with continuous irradiation. Fig.6.9a shows simulated variation of fringe contrast and refractive index modulation with different cumulative normalized fluence (F_{n0}) (normalized fluence marked as a , b and c are at z=0). The $\delta n^{(1)}$ and $\delta n^{(2)}$ profiles are tapered and approaches zero for $\gamma(z) = 0$ i.e. at $z = z_0 = (\lambda_{uv} /2\ \Delta\phi\ \eta_{lp})$. The refractive index modulation for $z \geq z_0$ is very small. Due to π phase shift in the fringe position after $z \geq z_0$, the light reflected from refractive index planes for $z \geq z_0$ will be out of sync with light reflected for $z \leq z_0$. Thus the fiber exposure length should be restricted to less than or equal to z_0 instead of beam overlap length (L) if $z_0< L$. For diffraction limited UV beam of radius (w) 5 mm, $z_0 \sim 3.25$ mm even if the beams overlap length is about 7mm. The effective grating length (L_g) can be defined as $L_g = z_0$ (for $z_0< L$) or $L_g = L$ (for $z_0> L$). The effective FBG length will be reduced with increase in beam divergence. The grating profiles will be apodised due to tapered refractive index modulation. Figs.6.9b and 6.9c show simulated [by T-matrix approach] reflection spectrum of a FBG in first (R_1) and second (R_2) order respectively at different F_{n0} with typical parameters; L_g= 3.25 mm, $\Delta\phi$ = 63 μrad, Δn_{max} =0.001, n_{eff} =1.4524 and λ_b = 1540 nm. The inscribed grating length and reflectivity will be higher in case the low divergence Gaussian beam is used as writing beam.

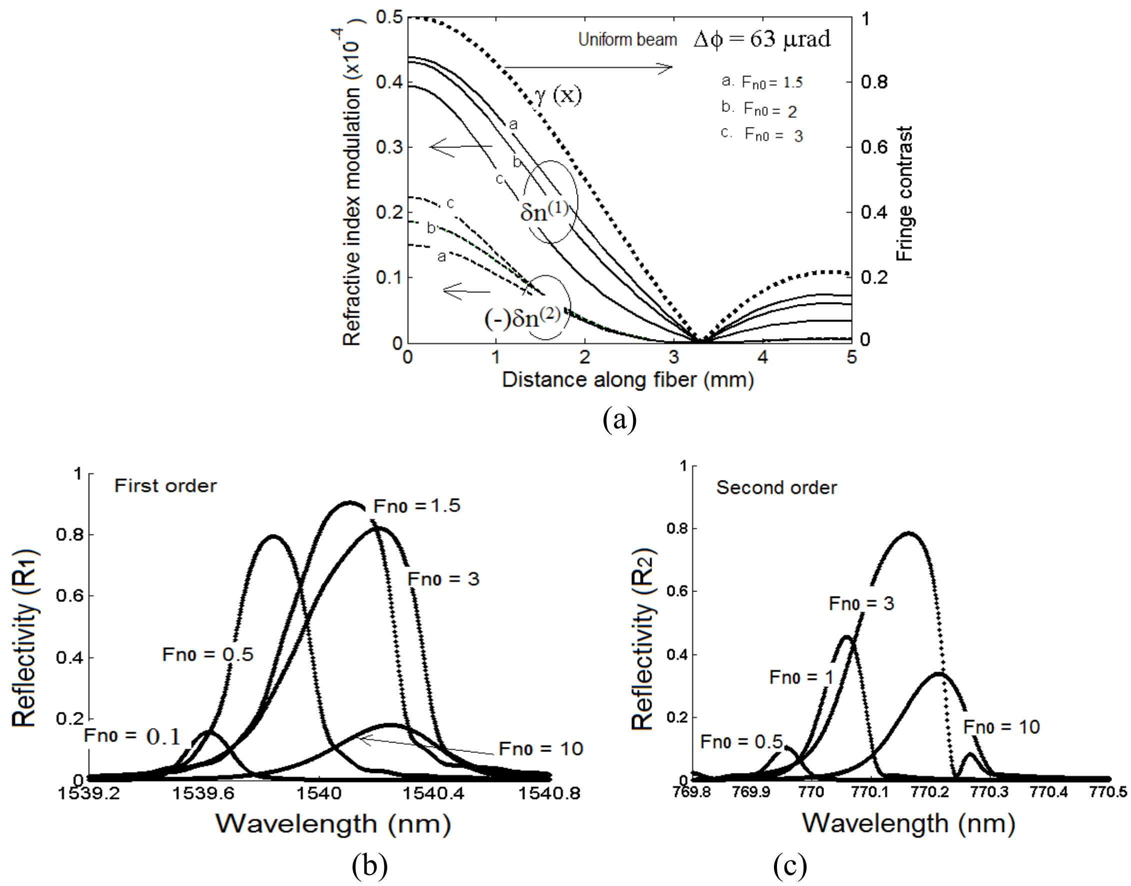

Figure 6.9: Simulated (a) fringe contrast and refractive index modulation along FBG length (b) reflection spectrum of a FBG in (b) first (R_1) and (b) second (R_2) order

Bragg wavelength tuning: - Bragg wavelength can be tuned by changing the angle of incidence. The fringe lines are always parallel to x-axis in this case unlike the case of biprism. The Bragg wavelength is given as [249]

$$\lambda_b = \lambda_1 = n_{eff}\lambda_{uv}\left[\frac{1}{n_p \cos\{\alpha + \sin^{-1}(\sin\theta / n_p)\}}\right] \tag{6.14}$$

A large change in Bragg wavelength ($\Delta\lambda$) is possible y the small change in UV beam incidence angle (θ) on the Lloyd prism.In particular, for a Lloyd prism designed to write FBG in C band, $\Delta\lambda \sim 130$ nm for $\Delta\theta = 35$ mrad. Fig.6.10a shows the Bragg resonant wavelength shift ($\Delta\lambda_b$) with change in incidence angle ($\Delta\theta$). The wavelength is tuned towards longer wavelength. When FBG are written by a diverging beam, a chirp grating will be formed as the fringe width in the FBG writing plane are not uniform.

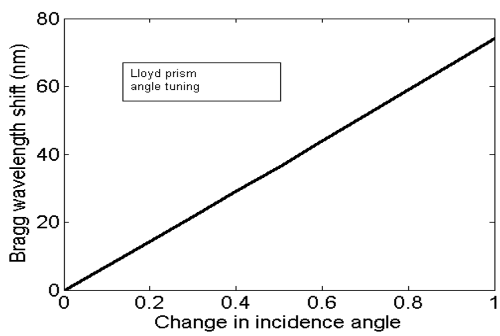

(a)

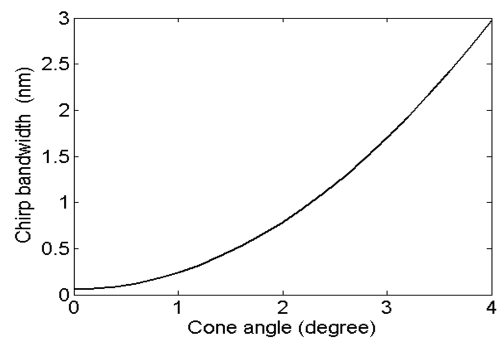

(b)

Figure 6.10: (a) Bragg resonant wavelength shift with change in incidence angle (b) Chirp band width with change in incidence beam cone angle

Fig.6.10b shows the change in chirp bandwidth with change in cone angle of the diverging UV beam. In Lloyd prism based FBG writing, the Bragg wavelength repeatability is critical as 2 mrad changes in angular beam pointing will shift the Bragg wavelength by ~ 7 nm. The deviation from beam collimation will introduce chirp in the FBG spectrum and reduce the reflectivity. The gratings of large length would not be written for by this interferometer. In the Lloyd prism interferometer, path difference is introduced for which temporal coherence is another factor in diluting fringe contrast. The UV beam must be spatially and temporally coherent with a uniform intensity for production high quality gratings. In the present work, the biprism based FBG writing, beings more convenient, is chosen for experimental demonstration.

6.4 Experimental method, results and discussion

A biprism interferometer is used to study the effect of spatial coherence and pointing stability of UV1, UV2 and UV3 beams on FBG fabrication efficiency. The schematic is shown in fig.6.10a. The FBGs were written in the fiber (PS-RMS-50, core dopants: B_2O_3 and GeO_2; non hydrogen loaded) by using a 24^0 refracting angle biprism.

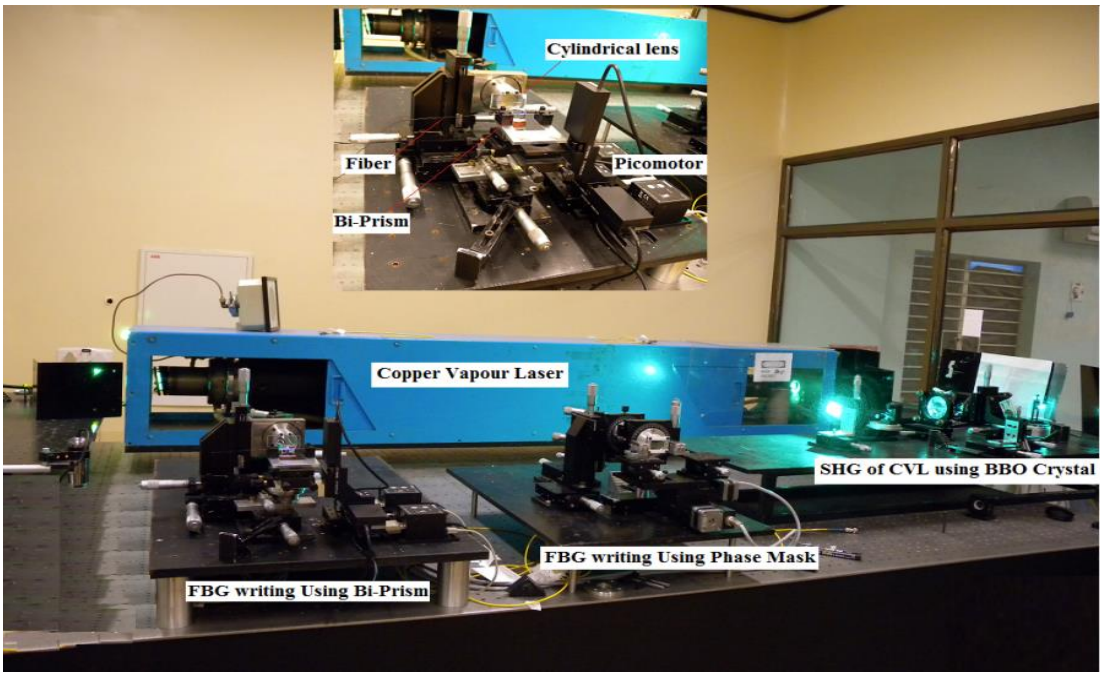

Figure 6.11: Biprism based FBG writing set up

The schematic of writing set up and procedure is same as described in figure 4.1a (in chapter 4) for phase mask technique, except that the phase mask was replaced by the biprism. Fig. 6.11 shows the photograph of the set up. The incidence UV beam diameter was 10 mm. The average power for each of the three UV beams of different spatial coherence was kept constant at 220 mW. The FBGs were written at maximum overlap position (x ~ 9.5 mm) at which the inscribed FBG length are maximum (~ 5 mm). Fig.6.12 (a-c) shows the observed transmission spectrum of FBG written by UV1, UV2 and UV3 beam respectively. The observed transmission dip (reflectivity) of FBGs written by UV1, UV2 and UV3 beam were 0.25 dB (5 %), 2.2 dB (39%) and 3.5 dB (55 %) respectively.

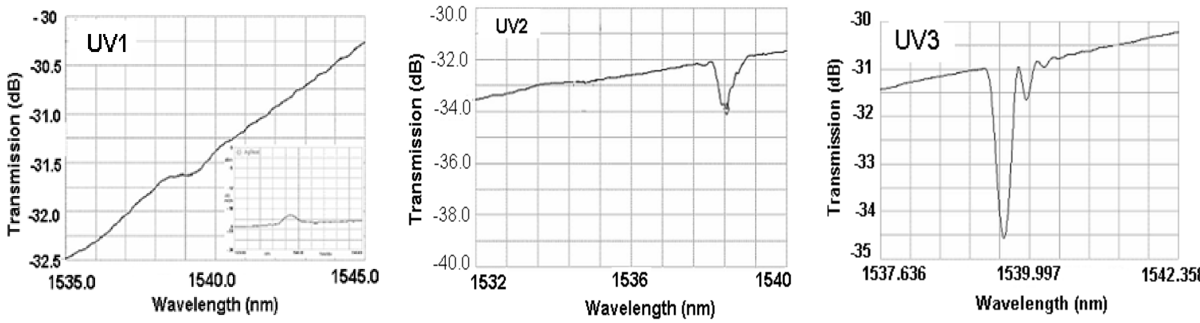

(a) (b) (c)

Figure 6.12: Transmission spectrum of FBGs written by (a) UV1 (b) UV2 and (c) UV3 beams

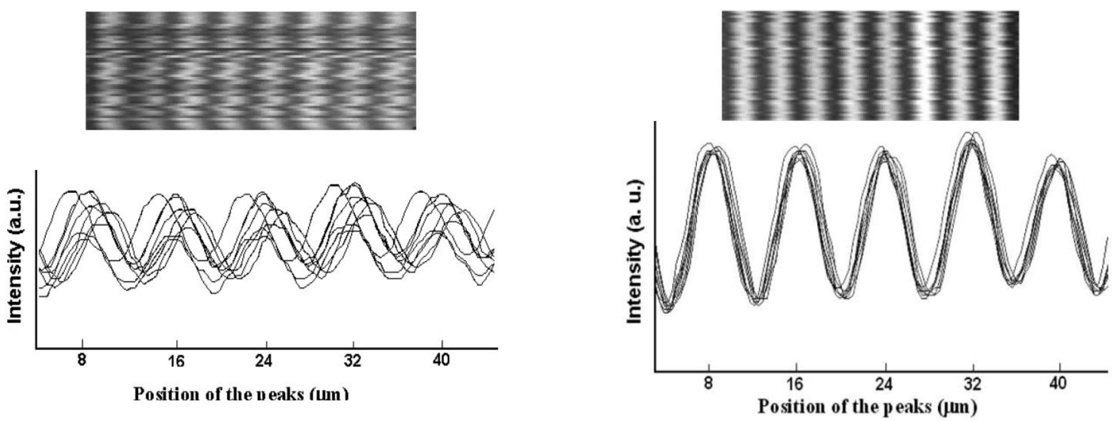

(a) (b)

Figure 6.13: Composite picture and intensity profile of a 2° biprism fringes for (a) UV1 beam (b) UV3 beam

The induced refractive index modulation was higher for FBGs written by the UV beams of higher the spatial coherence and lower beam pointing stability. The coherence and fringe stability are expected to affect FBG fabrication as the FBGs are written at larger distance from the beam splitter. Figs. 6.13a and 6.13b show the pulse to pulse stacked picture of image line (horizontal cursor position) and fringe intensity profile of a 2° biprism, produced by UV1 and UV3 beams respectively. These stacked pictures are recorded in the same way (section 2.3d) except replacing CVL beam by the UV beam. The visible fluorescence of UV fringes on LUMI glass was captured on gated CCD. For the UV1 beam, the fringes have large positional jitter and low contrast. The stacked pictures in the same fringe plane are indicative of positional stability and fringe contrast [185-186]. The observed overall situation improved with UV2 beam (not shown in fig). The best results were for the UV3 beam, where fringes of much better contrast and positional stability were obtained. The fringe instability parameter (S), defined as, $S_{bp} = \Delta\Lambda/\Lambda$, values are, 0.45 for the UV1 beam, 0.22 for the UV2 beam, and 0.10 forthe UV3 beam. In particular, the UV3 source based on the GDFR CVL produced UV fringes of maximum contrast and minimum fringe instability. This is due to highest coherence and lowest beam pointing instability over the FBG writing period and also excellent power stability (fig. 2.15 in chapter 2) leading to optimized FBG fabrication.

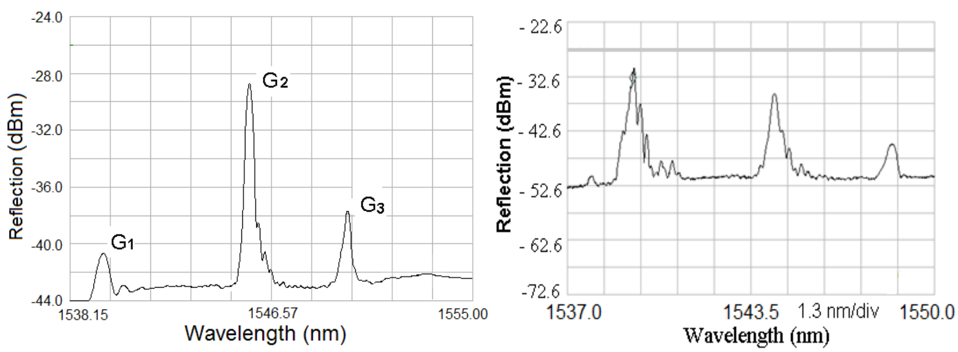

(a) (b)

Figure 6.14: Reflection spectra of gratings written at 2 mm (G1), 5 mm (G2) and 7.5 mm (G3) from biprism

Since the best results were obtained for UV3 beam, further study on optimizing FBG writing was carried out for UV3 beam. A representative experimental result on the effect of fiber position in the biprism fringe depth on the FBG spectrum, written by UV3 beam, is shown in the fig.6.14a. The UV beam was slightly geometrically diverging (~ 0.5^0) to discriminate Bragg wavelengths at different fiber position. The UV beam width incidence on thebiprism was ~ 10 mm. The refracted beams maximum overlap position (x_0) was approximately at about 9.2 mm from the biprism. The FBG reflection spectra marked as G_1, G_2 and G_3 in the fig.6.14a were written by placing the fiber approximately at distance (x) of 2 mm, 5 mm and 7.5 mm from the biprism respectively. The reflection powers of G_1, G_2 and G_3

are 3.2 dBm, 14 dBm and 5 dBm respectively. Due to higher value of $\{\gamma(x).L_g(x)\}$, the observed reflection power of the FBG written at x = 5 mm was higher than that obtained for positions of 2 mm and 7.5 mm [249]. The reflectivity of G_1 is lower due to smaller L_g where as that of G_3 is lower due to lower γ (x). The experimental results follow the simulated trends (fig.6.7a). Thus it was established that the FBG reflectivity is maximized not at maximum overlap position but at a position closer to the apex of the biprism, where product of fringe contrast and inscribed grating length is maximum. Fig. 6.14b shows the reflection spectrum of FBGs arrays, written at same positions of the same fiber. The Bragg wavelength was angle tuned. The reflection power decreased due to tilting of the grating planes.

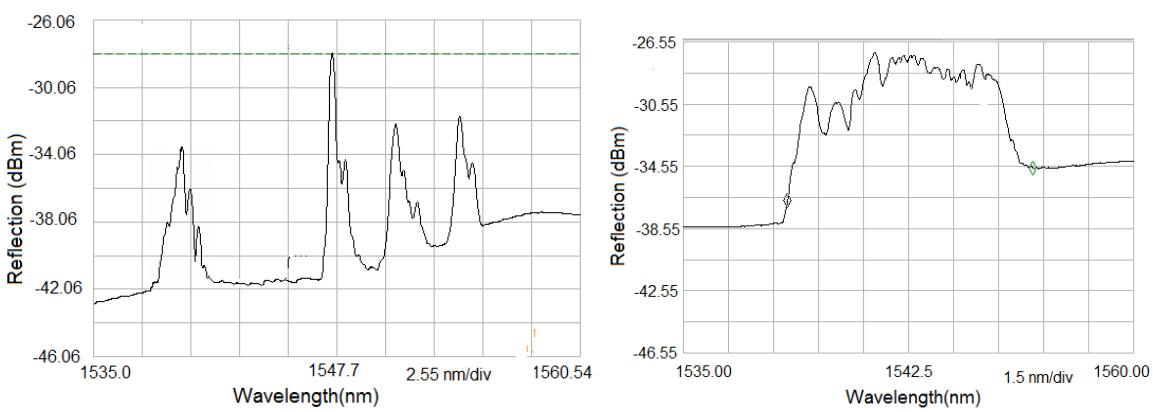

(a) (b)

Figure 6.15: Reflection spectrum of grating arrays (a) written by moving the collimating lens (b) with partial overlap of their spectrum bandwidth

Fig.6.15a shows the reflection spectrum of FBG arrays. The gratings were written by positioning the fiber at x ~ 5 mm from the biprism for which the FBG length is ~ 2.5 mm. In this case (fig. 6.15a), Bragg wavelength was tuned by moving the collimating lens (L_2 in fig. 6.7b) which changed the divergence envelope of the incident UV beam on the phase mask. The chirp gratings have been written by using a diverging UV beam and tilting the fiber in the fringe plane. In this case the observed reflection power was low. The reflection loss increased due to tilting of grating planes. In another technique, a series of gratings, each of small length, could be written on the same fiber. The fiber was placed at 4 mm from the biprism for which FBG length is ~ 2 mm. At this position the fringe contrast is appreciable. Once the FBG reflection was saturated, the exposure stopped. Then the fiber was translated by about 1 mm along horizontal direction. A small distance (~ 0.1 mm) translated along x-axis. The UV exposure again started. The new grating was formed by moving the fiber in steps in the fringe depth so that the reflection band width of each grating partially overlaps with other. The gratings of small length with increasing period could be formed by continuing this process. As a result, a comb of gratings with a net band width of about 6 nm was formed. Fig.6.14b shows the reflection spectrum of such a gratings comb. The maximum reflectivity observed was 93.7 % (T_d=12 dB) for an FBG written in GF1 (Neufern) fiber. The fiber was placed at a distance of about 5 mm from the biprism. For FBGs written in PS270 fiber, the maximum observed reflectivity was 90 % (T_d=10 dB).

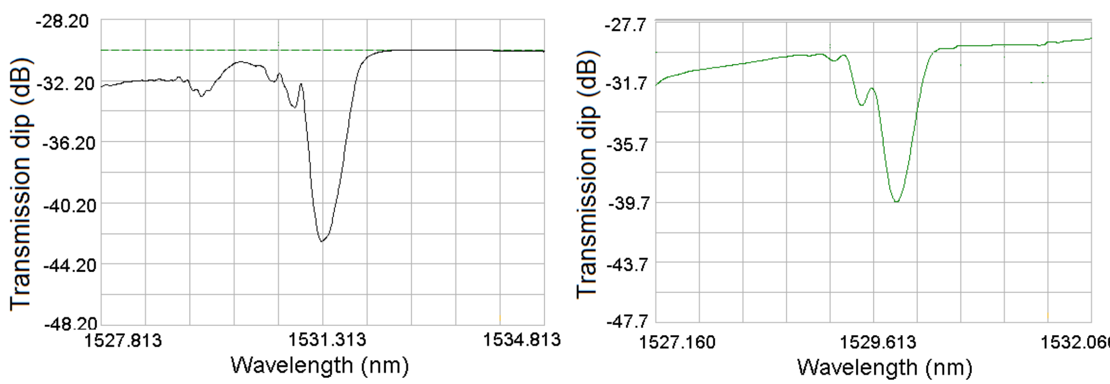

(a) (b)

Figure 6.16: Transmission spectra of FBG written by UV3 beam in (a) GF1 (b) PS270 fibers

Figs. 6.16a and 6.16b show the transmission spectrum of the FBGs written in GF1 and PS270 fiber. The usual observations were that the refractive index modulation increased nonlinearly with accumulated fluence followed by decrease after saturation. The Bragg resonance wavelength shifted towards right during writing. While the observed reflectivity of a FBG written in GF1 fiber, placed at maximum beam overlap position (~ 10mm), was 55% (T_d = 3.5 dB), that increased to 93 % when the fiber placed at a distance of about 5 mm from the biprism.It would be worth comparing the present data on biprism based FBG writing from different UV sources so far published. It is noticed with the frequency doubled (244 nm) Ar^+ laser source, the net FBG reflectivity was lower (44%) while the exposure time is much longer (60 min). This is despite the fact that the CW Ar^+ UV source is supposed to possess good spatial coherence and pointing stability and hence quality UV fringes characteristics. Lower performance of the 244 nm source is probably due to lower UV power (average 125mW). On the other hand, extremely fast FBG writing has been carried out in a single pulse of Excimer laser (248 nm) of energy density 1 J/cm^2. The FBG reflectivity of 62% was observed. In the present study, the FBG reflectivity is 95%, with a 255 nm beam energy density of 0.0032 J/cm^2. The comparable FBG reflectivity in these two set ups, despite the fact that the UV energy density for the UV3 beam is about 300 times lower, is probably due to the better quality of UV fringes achieved in our setup. Additionally, proper selection of fiber position is one of the criteria in deciding FBG reflectivity as found out from the analysis.

6.5 Conclusion

This chapter analyses refractive index modulation, grating length, FBG reflectivity, wavelength tuning of FBG inscription by prism interferometers. The biprism fringes contrast decreases along fringe depth but uniform along fiber length whereas the Lloyd prism fringes contrast decreases along fiber length. The effective grating length of prism interferometer written FBG is limited by divergence rather than beam overlap length. It was analytically shown that in biprism based FBG writing, the fiber position of maximum FBG reflectivity in biprism based writing is dictated by beam divergence and is less than the distance of maximum beam overlap position. The FBG reflectivity is maximized not at maximum overlap position but at a position closer to the apex of the biprism, where product of fringe contrast and inscribed grating length is maximized. This chapter also throws the light on the role of UV beam spatial coherence, long term pointing and power stability in influencing the net reflectivity achieved in an interferometric way of writing FBG. Pulsed UV beams (255 nm, 5.6 kHz, 30 ns) based SH of copper vapor laser were chosen for the study. In comparative study with UV1, UV2 and UV3 beam, the highest coherence UV3 beam resulted in achieving 55 % reflectivity FBG as compared to 5% for UV1 beam and 39 % for UV2 beam, in a biprism based writing, with fiber positioned at maximum overlap position. The experimental results followed analytical trends. The maximum observed reflectivity of the FBG written in non-hydrogenated fiber by biprism method was about 93 %, written by the highly spatial coherent UV3 writing beam. This is one of the highest reported FBG reflectivity by biprism method.

Publications base on this chapter

1. “Analysis of ultraviolet fringes contrast on first and second order Fiber Bragg gratings written by prism interferometers” **R. Mahakud**, J. Kumar, O.Prakash, S.K. Dixit, Optical Engg, **2013**, 52, 0761141-6.

2 “Study on quality of interference fringes from a pulsed UV source for application in a biprism based fibre Bragg grating writing”, O. Prakash, **R. Mahakud**, R. Biswal, S. Gurram, H.S. Vora and S.K. Dixit, Appl. Optics, **2007**, 46, 6210-6216.

Chapter 7

Studies on temperature sensitivity and stability for FBG based temperature sensing

7.0 Introduction

The temperature sensitivity and thermal stability are two most important parameters for use of FBG in high temperature sensing [250-255]. The temperature coefficient of effective refractive index of FBGs reported in the literature varies considerably [256-258]. This will affect the uniformity of temperature sensitivity of a FBG based temperature sensor [258]. The temperature sensitivity of an embedded FBG [258-261] is higher than that of a bare FBG. The refractive index modulation of a FBG decays at elevated temperatures [264-265]. Annealing improves thermal stability. Several studies, both experimental and theoretical, pointed out that the thermal stability of FBGs is affected by fiber composition, hydrogenation, and UV sensitization, writing condition and annealing.

This chapter presentsthe experiment and analysis on the factors affecting nonlinearity of temperature sensitivity of bare and embedded FBG, in order to express temperature as a function of Bragg wavelength shift. The analysis shows that uniformity of temperature sensitivity is mainly affected by thermo optic coefficient of the fiber material. In addition, the strain transfer coefficient and thermal expansion of the substrate affect the non linear evolution of Bragg wavelength with temperature.The thermal stability of type I and type IIA FBGs written in Ge- and Ge-B codoped fibers are compared. The thermal regeneration of type-I FBGs written in Ge-doped fibers was observed.The experimental results show that the factors such as initial grating strength, UV exposure, temperature variation of effective index and fiber photosensitivity affect the FBG thermal stability. The experimental results are supported by analysis.

7.1 Experimental methodology

7.1.1 For investigation of temperature sensitivity in bare FBG

The evolution of FBG centre wavelength due to change in temperature of the FBG was recorded by heating them in a programmable, in-house built, PID controller based oven working up to 1000 ^{0}C. Fig.7.1a shows the schematic of experimental set up to measure Bragg wavelength shift and observe reflection/transmission spectrum with change in temperature. Fig.7.1b shows the photograph of temperature controlled tubular oven.

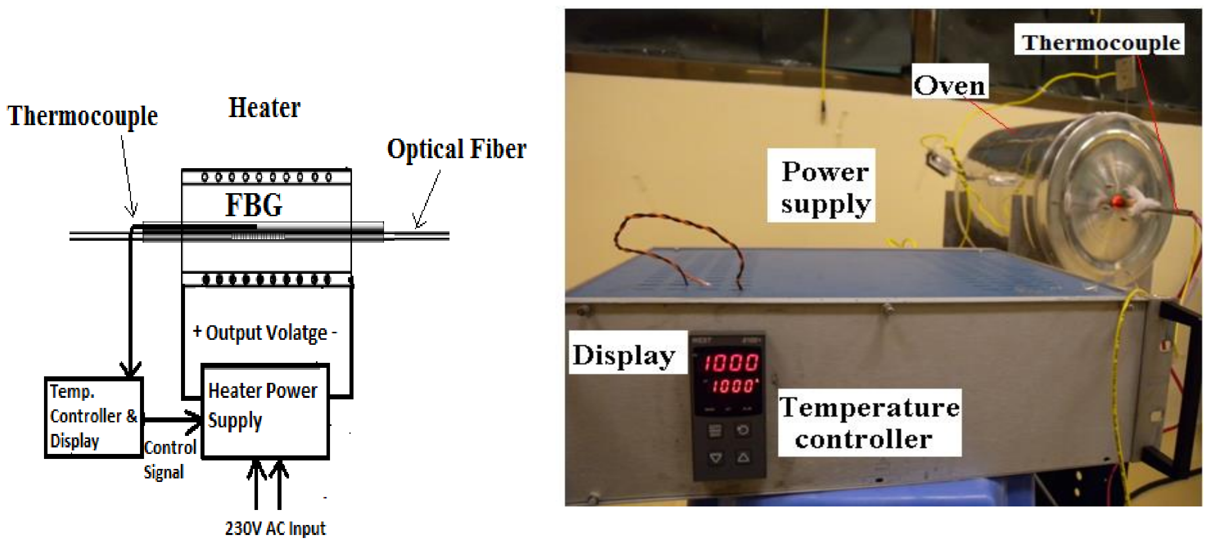

(a) (b)

Figure 7.1: (a) Schematic of temperature controlled oven (b) Oven photograph

The centre wavelength was recorded from the Bragg peak detection by the FBG interrogation system. The minimum resolution of thermocouple was 0.5^0 C. For improving the measurement precision of temperature sensitivity, FBGs of sharp reflection peak are required for which unsaturated gratings could be used. But the reflectivity of a FBG decays at high temperature [264]. In the present work, strong gratings with flat topped spectral exhibit flat-topped response are studied. The study on variation of temperature sensitivity was carried out in two steps. In the first step, the saturated FBGs written in different fibers were annealed at high temperature (700-850 ^{0}C). In the subsequent round of temperature elevation, the Bragg wavelength at different temperature was recorded from 25 ^{0}C to 525 ^{0}C in steps of 25 ^{0}C for temperature sensitivity analysis. The individual gratings were very carefully placed in the oven, so that there was no excess strain on the gratings. In each step, the Bragg peak was recorded after temperature stabilization for about 10 minutes. The estimation of temperature sensitivity [S (T)] required precise recording of Bragg wavelength in very small temperature intervals. The errors may occur due to local temperature fluctuation, error in peak detection, resolution of thermocouple and optical spectrum analyzer. Therefore, the average temperature sensitivity [<S(T)>] was estimated as the ratio of wavelength shift ($\Delta\lambda$) to change in temperature (T-T_0) from reference.

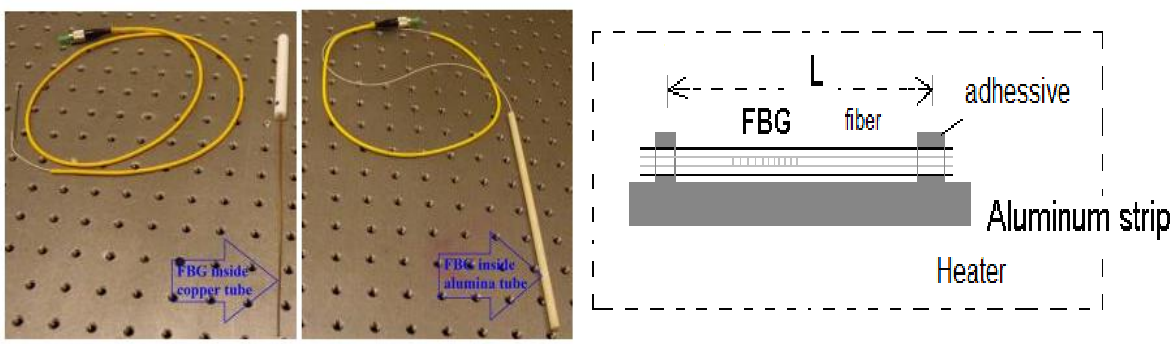

(a) (b)

Figure 7.2: (a) Bare FBG sensor (encapsulated) (b) Schematic of embedded FBG sensor

To use the FBG as single point temperature sensor, the fiber incorporating FBG was kept inside a capillary tube. The ceramic or the metallic capillary tubes such as copper or stainless steel could be used. The pass-through type FBG sensor housing was like that of a thermocouple (fig.7.2a). The encapsulated FBG was without strain. The FBGs written in fibers CMS-1550-R1 (Stocker Yale), GF1 (Nufern) and SM-1550 (CGCRI) designated as fiber A, B and C respectively were employed in the temperature sensitivity study.

7.1.2 For investigation of temperature sensitivity in embedded FBG

In the present experiment, we attached the fiber incorporating FBG to a single metal strip (aluminum) at two ends, as shown in schematic (fig.7.2b). The bonded length at each point was ~ 1mm. The temperature to wavelength response of the embedded FBG was recorded from 30 ^{0}C to 90 ^{0}C in steps of 10 ^{0}C, recorded after due stabilization for about 10 minutes in each step. We could not go for higher temperature as the epoxy adhesive used could withstand temperatures only up to 100 °C. The length of fiber between fixed points is termed as sensor length (L).The Bragg wavelength shift was recorded for three different sensor lengths of 20 mm, 40 mm and 80 mm. The FBGs (T_d ~ -6 dB) used in the study were written in fiber A [CMS-1550-R1 (Stocker Yale)]. The tensile load on the fiber was exerted by thermal expansion of the aluminum strip.

7.1.3 For study on thermal sustainability

The studies on thermal stability of the FBGs written in Ge- and Ge-B codoped fibers were carried out. The thermal behavior was studied for two different processes i.e. the temperature elevation as function of time (termed as TFT process) and in isothermal process. The rate of temperature elevation in TFT process was 5 ^{0}C /minute. During thermal annealing, the Bragg resonant wavelength shift and the transmission dip were recorded for FBGs written in different fibers. A comparative study on thermal sustainability of type I and type IIA FBG written in a typical photosensitive fiber was carried out. The normalized integrated coupling constant (NICC) was calculated by the relation [262]

$$\eta(t,T) = [\tanh^{-1}(R\ (t,T))^{1/2} / \tanh^{-1}(R\ (t = 0,T_0))^{½}] \qquad (7.1)$$

where R (t, T) and R(0, T_0) are the FBG reflectivity at temperature T and time t and initial (t=0) reflectivity at room temperature T_0 .

7.2 Non-uniformity of sensitivity of FBG based temperature sensors

The Bragg wavelength shift ($\Delta\lambda$) of a FBG subjected to temperature and axial strain is given as [250-251]

$$\Delta\lambda = \lambda(\kappa_T + \alpha_f)\Delta T + \lambda k \varepsilon_g \tag{7.2}$$

where λ is Bragg wavelength, ΔT is change in temperature, ε_g is axial strain, κ_T [= $(dn_{eff}/dT)/n_{eff}$)] is thermo-optic coefficient of the fiber material, n_{eff} is effective refractive index, α_f is fibers thermal expansion coefficient and k = 1-P_e where P_e (~ 0.22) is the effective photo elastic constant of the fiber. Typically, for α_f ~ 0.55x10^{-6} /^{0}C and κ_T ~ 8.5 x 10^{-6} /^{0}C, the contribution of thermal expansion coefficient of the fiber (α_f) to the wavelength shift of a bare FBG is comparatively small (~ 9%). The temperature sensitivity will be constant provided κ_T and α_f are constants. However, the temperature sensitivity will change if thermo optic coefficient changes with temperature.

(a) Bare FBG

When the FBG is not subjected to axial strain (ε_g=0), the Bragg wavelength at temperature T is given as [16],

$$\lambda(T) = 2n_{eff}(T)\Lambda(T) \tag{7.3}$$

where Λ(T) is grating period and n_{eff} (T) is effective refractive index. The temperature dependence of fiber's thermal expansion coefficient ($d\alpha_f/dT$) in the operating temperature range and wavelength dependence of refractive index ($dn_{eff}/d\lambda$) in the measured wavelength range are ignored. The Taylor's series of temperature variation of effective refractive index around a reference temperature (T_0) can be expressed as [269],

$$n_{eff}(T) = c_0 + c_1\Delta T + c_2\Delta T^2 + c_3\Delta T^3 + ... \tag{7.4}$$

where $\Delta T = (T-T_0)$ and $c_m = (1/m!)\ (d^m n_{eff}/dT^m)$ at T_0 $(m = 0,1,2, \ldots)$.The coefficient c_m depends on fiber glass and reference temperature (T_0). The temperature dependence of grating period can be expressed as,

$$\Lambda(T) = \Lambda_0\,(1+\alpha_f \Delta T) \tag{7.5}$$

Using eqns. (7.4) and (7.5), the Bragg wavelength [λ (T)] can be expressed as,

$$\lambda(T) \approx \lambda(T_0) + a_1(T-T_0) + a_2(T-T_0)^2 + a_3(T-T_0)^3 + \ldots. \tag{7.6}$$

where $\lambda(T_0)=2n_{eff}(T_0)\ \Lambda(T_0)$. The coefficient a_m in eqn.(7.6) is given as, $a_m = (c_m+\alpha_f c_{m-1})\ \lambda(T_0)/n_{eff}(T_0)$. The temperature sensitivity [S (T)] of bare FBG at temperature T is given as,

$$S(T) = \frac{d\lambda}{dT} = a_1 + 2a_2(T-T_0) + 3a_3(T-T_0)^2 + \ldots \tag{7.7}$$

The average temperature sensitivity [<S(T)>] is given as

$$< S(T) >= a_1 + a_2(T-T_0) + a_3(T-T_0)^2 + .. \tag{7.8}$$

From eqns. (7.6) and (7.7), it is clear that the evolution of Bragg wavelength is nonlinear. The temperature sensitivity in bare FBG is a combined effect of thermal expansion effect of fiber and temperature derivatives of the effective refractive index.

(b) Embedded FBG

The temperature sensitivity of an embedded FBG is enhanced due to induced axial strain in the FBG transferred from host. However, the fractional strain transfer from the host to the FBG depends on bonding between substrate and fiber which in turn depends on elastic modules of fiber, protective coating, adhesive and bonded length etc [266-267]. The strain in the FBG may be expressed as,

$$\varepsilon_g = \xi\,(\varepsilon_s - \alpha_f\,\Delta T) \tag{7.9}$$

where ε_s is thermally induced strain in the substrate ($=\alpha_s\Delta T$), ξ is strain transfer coefficient, α_s is thermal expansion coefficient of the substrate and ΔT (= $T-T_0$) is change in temperature from reference. The strain transfer from the substrate depends on design specifics. For perfect bonding, $\xi=1$. The temperature sensitivity increases with increase in α_s and ξ. The variation of thermal expansion coefficient (α_s) is given as,

$$\alpha_s(T) \approx \alpha_{s0} + \alpha_{s1}(T-T_0) \tag{7.10}$$

whereα_{s0} is thermal expansion coefficient of the host at T_0 and α_{s1} is its coefficient. Using eqns (7.2), (7.6), (7.9) and (7.10); the Bragg wavelength shift of an embedded FBG can be expressed as,

$$\Delta\lambda = b_1(T-T_0) + b_2(T-T_0)^2 + a_3(T-T_0)^3 + .. \tag{7.11}$$

Where b_1= a_1+ $\xi\lambda k$ (α_{s0}-α_f) and b2= a_2 + $\xi\lambda k\alpha_{s1}$. The average temperature sensitivity, [<S (T)>], can be expressed as,

$$S(T) = b_1 + 2b_2(T-T_0) + 3a_3(T-T_0)^2 + .. \tag{7.12}$$

The temperature sensitivity will increase with increase in coefficient thermal expansion of the fiber and strain transfer coefficient. The nonlinearity in wavelength shift in embedded sensors depends on first and second derivatives of effective refractive index, temperature derivative of thermal expansion coefficient (α_{s1}) of the substrate and strain transfer coefficient (ξ).

7.2.1 Experimental results and discussion on bare FBG temperature sensitivity

The type I FBGs written in fibers CMS-1550-R1 (Stocker Yale), GF1 (Nufern) and SM-1500 (Fiber core), designated as fiber A, B and C respectively, were employed in the sensitivity study. Fibers A and C are Ge-doped. Fiber B was Ge-B codoped. Fig.7.3a show the reflection spectrum of a FBG (in fiber A, T_d= 26 dB) during annealing. The annealing sharpened the reflection spectrum thereby improving the precision in Bragg peak detection in the subsequent round of data recording. The FBG bandwidth decreased due to decay of refractive index modulation. After annealing, the stable portion of UV induced index, up to annealing temperature, remained [264]. The annealing eliminated the effect of decay of UV induced average index on the variation of temperature sensitivity below the annealed temperature. Fig. 7.3b show the Bragg wavelength shift with increase in temperature of annealed FBG.The same procedure was applied for FBG in fiber B and C.

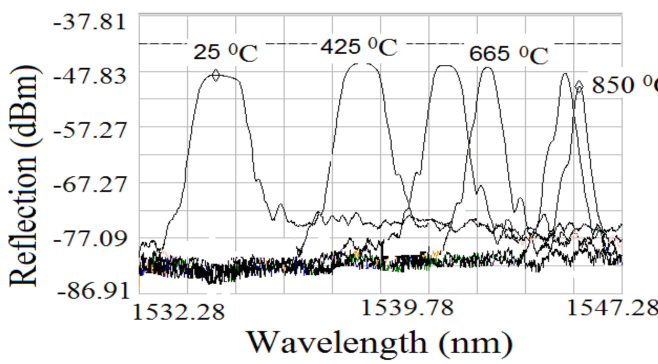

(a)

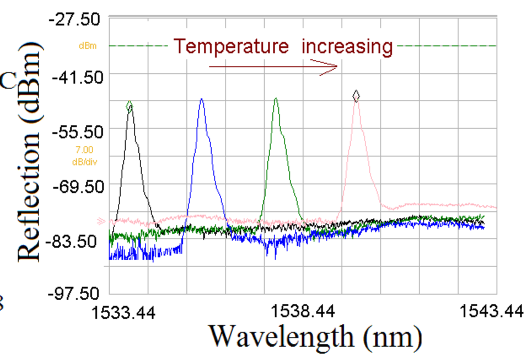

(b)

Figure 7.3: Reflection spectrum of FBG (a) during annealing (b) during data recording

The wavelength shift with change in temperature was no uniform. Figs.7.4(a-c) show the observed Bragg wavelength [λ(T)] at different temperature (T) for FBGs in fiber A, B and C respectively. The temperature sensitivity of the FBG increased with temperature elevation. Figs.7.3 (d-e) show the variation of average temperature sensitivity [< S (T)>] with change in temperature (T-T_0) from reference for fibers A, B and C respectively. For FBG in fiber A, the Bragg wavelength shift was 0.5 nm in the temperature interval of 25 ^{0}C to 75 ^{0}C and 0.78 nm in the temperature interval of 475 ^{0}C to 525 ^{0}C. The observed average temperature sensitivity in the temperature range of 25 ^{0}C to 125 ^{0}C was 10.4 pm/^{0}C and that between 25 ^{0}C to 525 ^{0}C was 12.4 pm/^{0}C. The experimentally observed variation of average temperature sensitivity with temperature is almost linear [figs.7.3 (d-e)]. Hence, the contribution terms containing the coefficients a_3, a_4… in eqn.(7.8) are negligible.

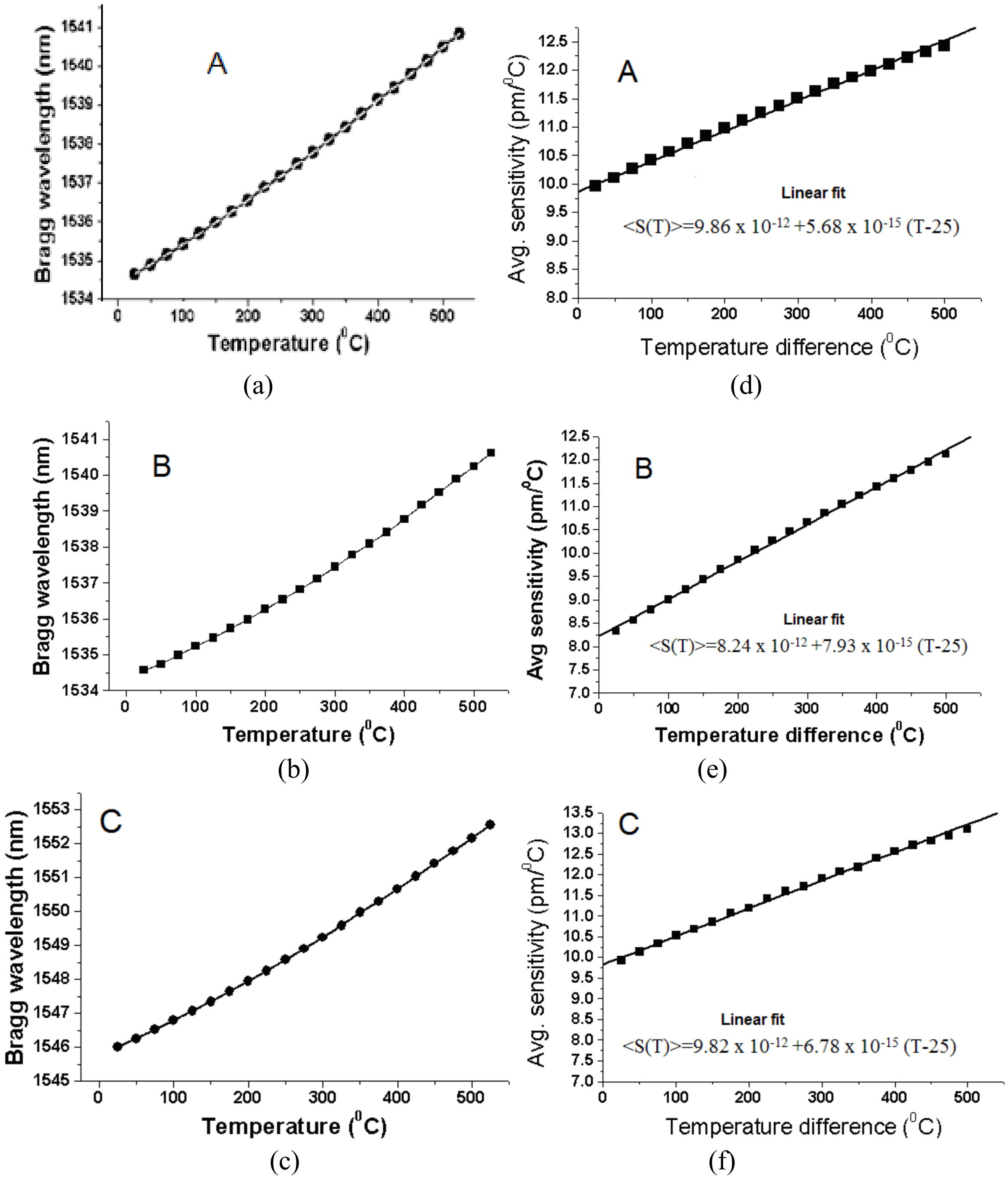

Figure 7.4: (a) Bragg wavelength at different temperature for FBG in fiber (a) A (b) B (c) C and variation of average temperature sensitivity [<S(T)>] with change in temperature ($T-T_0$) for FBG in fiber (d) A (e) B (f) C

The coefficient a_2 which depends on first and second derivatives of refractive index and thermal expansion effect of the fiber is mainly responsible for non-uniformity of temperature sensitivity. The coefficients a_1 and $a_2$are evaluated by assuming average temperature sensitivity as the linear fit (figs.7.4 (d-e)) of the observed data. The coefficients $a_1$and a_2 were estimated from the linear fit of <S (T)>. With the typical values of λ (T_0), n_{eff} (T_0) and α_f, the estimated first and second derivatives of effective refractive index for fibers A, B and C, given in table 7.1, are different. The effective thermo-optic coefficient increased with temperature elevation differently for fibers A, B and C. The reduced visibility of nonlinearity in fig.7.4a is due to lower value of second derivative of effective refractive index for fiber A (table 7.1) in compared to that for fibers B and C.

Table 7.1: Coefficients of temperature sensitivity and effective refractive index for fibers A, B and C

Fiber	A	B	C
a_1 (pm/^{0}C)	9.86	8.24	9.82
a_2 pm/(^{0}C)^2	5.68 x10^{-3}	7.93 x10^{-3}	6.782 x10^{-3}
dn_{eff}/dT	8.55 x 10^{-6}/(^{0}C)	6.94 x 10^{-6} /(^{0}C)	8.46 x 10^{-6} /(^{0}C)
d^2n_{eff}/dT^2	1.07 x 10^{-8} /(^{0}C)^2	1.46x10^{-8} /(^{0}C)^2	1.28 x10^{-8} /(^{0}C)^2

Thus it is clear from the experimental results that the temperature sensitivity of type I FBGs increases with temperature elevation.The response also depends on fiber composition. In a model for the thermo-optic coefficients of standard optical glass, it is shown that the excitonic and isentropic optical band gap energy and the thermal expansion coefficient contribute to the thermo-optic coefficients [266-268]. The refractive index change with temperature (dn/dT) is positive and increases with the quantity, H, given as [266-267]

$$H = - (1/E_g)\, d\, (E_{eg})/dT \qquad (7.13)$$

where E_{eg} is excitonic band gap energy. The excitonic band gap energy decreases with increase in temperature and therefore dn/dT increases with temperature [268-269]. The experimental trends of nonlinear change in Bragg wavelength with change in temperature are in agreement with this model. Due to difference in fiber composition, the excitonic band gap energy and its variation with temperature are different for different fibers. Since the material composition in the core is usually different from that of cladding, the differential change in the core and the cladding refractive index, subjected to temperature, may affect the thermal variation of effective refractive index.

Temperature Evaluation

In order to permit accurate measurement by a FBG temperature sensor, the wavelength dependence of the FBG on temperature must be known. It is difficult to know the exact values of temperature variation of effective refractive index of the FBGs written in different fiber types. It is rather convenient to evaluate the temperature derivatives of refractive index from the experimental data to express temperature as function of Bragg wavelength shift. With the linear approximation of <S (T)>, the Bragg wavelength response to temperature change is quadratic. By solving eqn (7.6) by keeping terms up to quadratic power of ($T-T_0$), the temperature (T) calculated from Bragg wavelength shift ($\Delta\lambda$) can be expressed as,

$$T = T_0 + p[\sqrt{1 + q\Delta\lambda} - 1] \tag{7.14}$$

where $p = a_1/2a_2$, $q = 4a_2/a_1^2$. The constants p and q, involved in the temperature function, are different for different fibers. Figs.7.5 (a-b) show the simulated temperature as a function of Bragg wavelength shift ($\Delta\lambda$). The change in temperature is approximately linear for small shift in Bragg wavelength [$dT/d\lambda \approx 1/a_1$]. The estimated temperature for a FBG in a particular fiber marginally deviates from actual temperature for large wavelength shift. This is due to dropping of higher order terms in eqn.(7.6), particularly the term containing the coefficient a_3. The coefficient, a_3, depends on both second and third derivative of the effective refractive index.

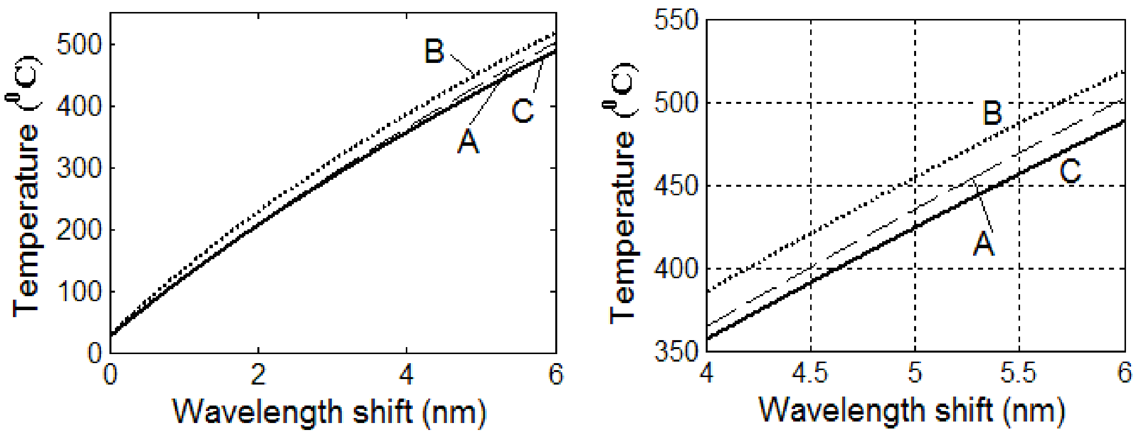

(a) (b)

Figure 7.5: Simulated Bragg wavelength shift vs. temperature change for typical FBGs written in fiber A, B and C (a) Bragg wavelength shift from 0 to 6 nm (b) Bragg wavelength shift 4 to 6 nm

By retaining up to cubic terms of (T-T$_0$) in eqn. (7.6), the estimated error (δT_{er}) is given as [269]

$$\delta T_{er} \approx \frac{a_3(T - T_0)^3}{a_1 + 2a_2(T - T_0)} \tag{7.15}$$

where δT_{er} is the difference in temperature obtained from solution of eqn (7.6) by keeping up to quadratic and cubic exponent of (T-T$_0$). The error increases at high temperature and for fibers having higher value of (d^3n/dT^3). For a_3 ~ - 1.1 x10^{-6}pm/ (^{0}C)^3 [obtained from the polynomial fit (of order 3) to the Bragg wavelength vs. temperature change for fiber A] , ($d^3 n/dT^3$) ~ - 6.18 x10^{-12}/(^{0}C) which is in the typical range. For above a_3, δT_{er} ~ - 0.5 ^{0}C for $\Delta\lambda$ = 2 nm and δT_{er} = - 6 ^{0}C for $\Delta\lambda$ = 6 nm for FBG in fiber A. The deviation increases with temperature elevation. The quadratic response of Bragg wavelength shift to temperature change was considered for calculation of temperature within the reasonable error limit. But a more precise algorithm may be applied, by retaining higher order terms in eqn (7.6), to evaluate the temperature encountered by FBG from the Bragg wavelength shift.

7.2.2 Results and discussion on embedded FBG temperature sensitivity

Eqns (7.11) and (7.12) are for Bragg wavelength shift and average sensitivity with change in temperature for an embedded FBG sensor. With aluminum as substrate, $\alpha_{s0} = 23.2 \times 10^{-6}$ and $\alpha_{s1} \approx 1.66 \times 10^{-8}$ [272]. For typical values such as $\lambda = 1535$ nm, $a_1 = 9.86$ pm/^{0}C, $a_2 = 5.68 \times 10^{-3}$ pm/(^{0}C)^2 (for fiber A), the simulated Bragg wavelength shift ($\Delta\lambda$) and temperature sensitivity (S(T)) with change in temperature ($T-T_0$) are shown figs.7.6a and 7.6b respectively, for $\xi = 0.5$ and 1.

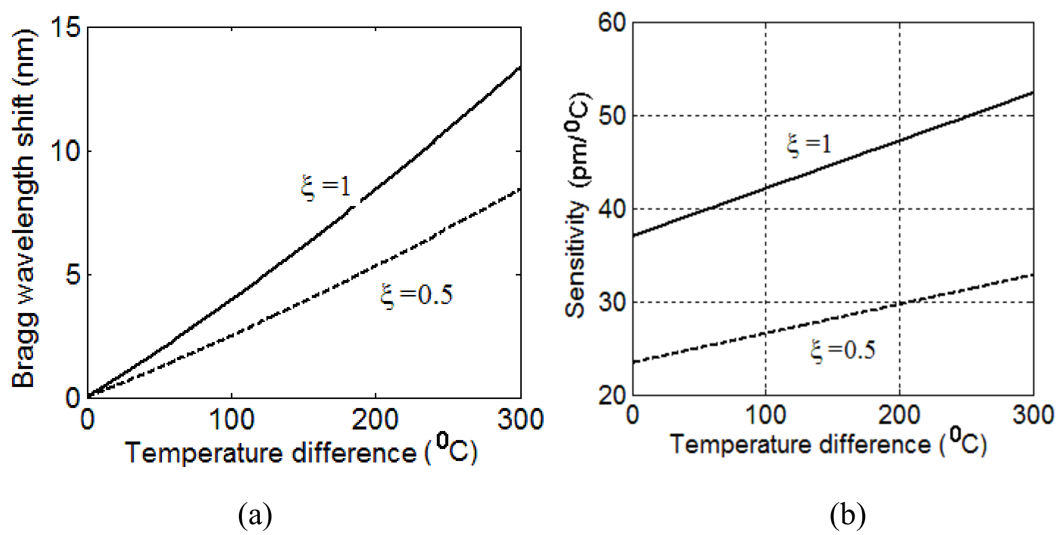

Figure 7.6: Simulated (a) Bragg wavelength shift (b) Sensitivity with change in temperature for different strain transfer coefficient

The third and higher order terms in eqn (7.11) are neglected. For the temperature change from 0 to 300 ^{0}C, the simulated Bragg wavelength shifts by 13.39 nm for $\xi = 1$ and 8.341 nm for $\xi = 0.5$. The simulated sensitivity increased with increase in strain transfer coefficient and temperature elevation. In small temperature interval ($\Delta T = 100$ ^{0}C) as carried out in the experimental study, the simulated temperature sensitivity increased from 37 pm/^{0}C (at 25 ^{0}C) to 42 pm/^{0}C (at 125 ^{0}C), an increase of 5 pm/^{0}C for $\xi = 1$ and that increased from 23.35 pm/^{0}C (at 25 ^{0}C) to 26.5 pm/^{0}C (at 125 ^{0}C), an increase of 2.65 pm/^{0}C for $\xi = 0.5$. The rate of increase of sensitivity [$(d^2\lambda/dT^2)$] is 4.4 (for ξ=1) and 2.2 (for ξ= 0.5) times higher than that of bare FBG.

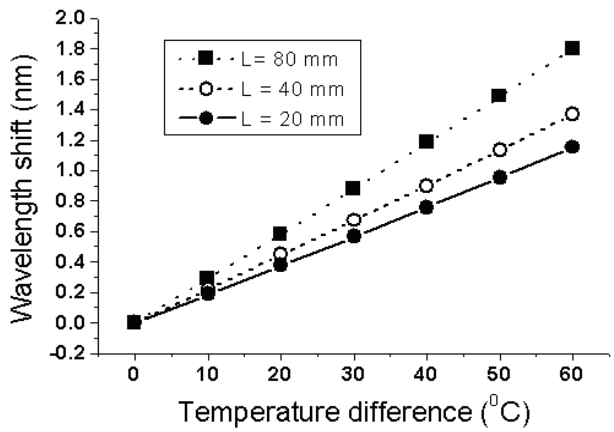

Figure 7.6: (c) Experimentally observed Bragg wavelength shift with change in temperature for embedded length 20 mm, 40 mm and 60 mm

The experimentally observed Bragg wavelength shift with increase in temperature is shown in fig.7.5c. In the temperature interval of 30 ^{0}C to 90 ^{0}C, the average temperature sensitivity increased from 19.2 pm/^{0}C for L= 20 mm to 29.9 pm/^{0}C for L= 80 mm. The temperature sensitivity increased with increase in fastened length. By using the typical values of a_1 and a_2 (fiber A), α_{s0}, α_{s1} (aluminum), and λ (1535 nm), the estimated strain transfer coefficient are approx. 0.32, 0.45 and 0.68 for fastened lengths of 20, 40 and 80 mm respectively. These results imply that the fractional strain transfer from substrate to FBG increased with fastened length. Higher strain transfer coefficient might be obtained if stronger adhesive to tightly fix the fiber and metal strip more tightly is used.From the experimentally observed results in this study, it is clear that the fastened length is an important parameter in fractional strain transfer from substrate to the the FBG.

It is noteworthy to cite the similar results observed in ref [265] in which the average temperature sensitivity increased from 14.4 pm /^{0}C to 29.6 pm/^{0}C with the increase of fastened length 20 mm to 100mm. However, the FBG sensors were fabricated by attaching the FBG to two fixed metal strips (lead and tantalum) of different temperature expansion coefficients instead of a substrate of single metal strip. In the structure, the tension due to thermal expansion of a lead metal concentrated on the FBG and the sensitivity was enhanced.

The experimental results may be explained as follows. The axial force (F) in the fiber due to tensile load exerted by substrate is given as, $F = A_f Y_f \varepsilon_g$, where Y_f is Young's modulus and A_f is cross section area of the fiber.The axial elongation (ΔL_f) of the fiber is given as $\Delta L_f = L\varepsilon_g$. As the bulk modulus of adhessive and arcylate coating is much smaller than that of the fiber, the linear displacement of the fiber-adhessive interface subjected to force F is due to shear deformation only. The displacement will depend on shear modulus, length and thickness of the coating and adhesive layers. For a simple discussion, here we assume that the two layers are lumped into an effectively one layer of shear modulus (G), thickenss (h) and interface area A between the substrate and fiber. The two embeded sites are considered identical. The total linear displacement of the fiber–adhesive interfaces can be expressed as $\Delta L_a = \chi\varepsilon_g$, where the propertionality constant (χ) is given as $\chi \sim (2Y_f A_f h/GA)$. Estimating χ requires rigourous analysis which is beyond the scope of this work. The objective is to investigate the the relative trends. The thermal expansion (ΔL) of the substrate along fiber axis is sum of axial elongation of the fiber induced by strain and temperature and the displacement of fiber-adhesive interface, given as

$$\Delta L = \varepsilon_g [L + \chi] + L\alpha_f \Delta T \tag{7.16}$$

The strain in the substrate (ε_s) is equal to ΔL/L. The strain in the FBG can be expressed as

$$\varepsilon_g = (\alpha_h - \alpha_f)\Delta T / (1 + \chi / L) \tag{7.17}$$

It is clear from eqn. (7.17) that the strain experienced by FBG is different from the strain in the substrate. The strain transfer coefficient (ξ) is given by

$$\xi = 1/(1 + \chi / L) \tag{7.18}$$

Since $\chi \neq 0$, the strain transfer coefficient and therefore temperature sensitivity increases with increase in fastened length which explains the experimental trends qualitatively.

Thus the non-uniformity of temperature sensitivity of embedded FBG sensors is twofold. First, the sensitivity is different for different strain transfer coefficient, as observed for different fastened lengths. Secondly, for a particular fastened length, the temperature sensitivity increased with temperature elevation. For fastened length of 80 mm, the temperature sensitivity increased from 29 pm/^{0}C to 30.9 pm/^{0}C, an increase of 1.9 pm/^{0}C (~ 6%) as the temperature increased from 30 ^{0}C to 90 ^{0}C. This figure was about 1.1 pm (5.7%) for the fastened length of 20 mm. For this small temperature difference ($\Delta T = 60\ ^0C$), the contribution of second term to wavelength shift [eqn (7.11)] is comparatively very small. The increase in temperature sensitivity will be higher when the change in temperature ($T-T_0$) from reference is large. However, the sensor operation at high temperature will subject to availability of high temperature tolerant adhesive which will affect fiber- adhesive and adhesive- substrate bonding rigidity thus affecting strain transfer coefficient. The breaking stress of the fiber is another limitation. If the FBG can be strained up to ε_g (max) for safe operation, then the operating temperature range (ΔT_{op}) is ~ ε_g (max)/ $\xi(\alpha_s-\alpha_f)$. Typically ΔT_{op} ~ 115 ^{0}C for ξ =1 and about 230 ^{0}C for ξ =0.5 with ε_g (max) = 2500 $\mu\varepsilon$. The operating temperature range of the sensor could be increased for smaller strain transfer coefficient though the sensitivity decreases with decrease in strain transfer coefficient. This work is about a dual end embedded FBGs fastened to single metal strips of different length. But it is clear from the discussion that besides other factors, the temperature measurement is a function of strain transfer which requires either a design specific numerical analysis or experimental determination to calibrate typical embedded FBG based temperature sensors.

7.3 Studies on thermal sustainability of FBG

On UV illumination, the GODC defects (D_1) in the fiber core transform to the continuous distribution of trap energy states [called defect induced defects (D_2)], responsible for UV induced index change in the fiber core. The trapped population density is a measure of photo induced index change. The thermal decay of trapped population is characterized by an energy barrier called as demarcation energy, given as [262],

$$\varepsilon_d = k\,T \ln (\nu_0\, t) \tag{7.19}$$

where ν_0 (~ 10^{15} Hz) is initial release rate and k is Boltzman constant and t is time (in sec). The demarcation energy couples the two parameters, time and temperature, into one parameter. The population in all the states with trap depth energy $\varepsilon_i<\varepsilon_d$ are depleted thus resulting in decay of photo-induced induced refractive index. To analyze FBG thermal stability, Erdogan et.al proposed empirical power law for normalized integrated coupling coefficient (NICC) [7], given as [262],

$$\eta\,(t,T) = 1/\,(1+A\,t^{\alpha}) \tag{7.20}$$

WithA (T) = $A_0 \exp (aT)$; α (T) = T / T_r where $\eta(t,T)$ is NICC, T is temperature (in Kelvin) , t is time (in minutes) and A_0, a and T_r characteristic constants. Most of the studies on thermal stability are based on analysis of isothermal annealing experimental plots of η (t) vs. t (time) at several different temperatures, requiring several FBGs for the experiment. Since η depends only on $\varepsilon_d$and not separately on t and T, plotting η (t) vs. t (at fixed temperature) or η (T) vs.

T (for fixed t) will lead to the same curve of η (ε_d) vs. ε_d [7.24]. In this study, we have analyzed the FBG thermal sustainability by annealing the FBG with temperature elevation as a function of time (TFT).

7.3.1 Experimental results

Fig.7.7a shows the decay in transmission dip of a FBG, in a typical fiber, with increase in temperature as a function of time. The Bragg wavelength shifted due to change in effective index and the transmission dip decreased due to decay in refractive index modulation. Fig.7.7b shows the variation of transmission dip of a FBG with time, when isothermally annealed at higher temperature. The Bragg wavelength blue shifted due to decay in average effective index. Further, the results for particular studies are presented from subsection (A to D).

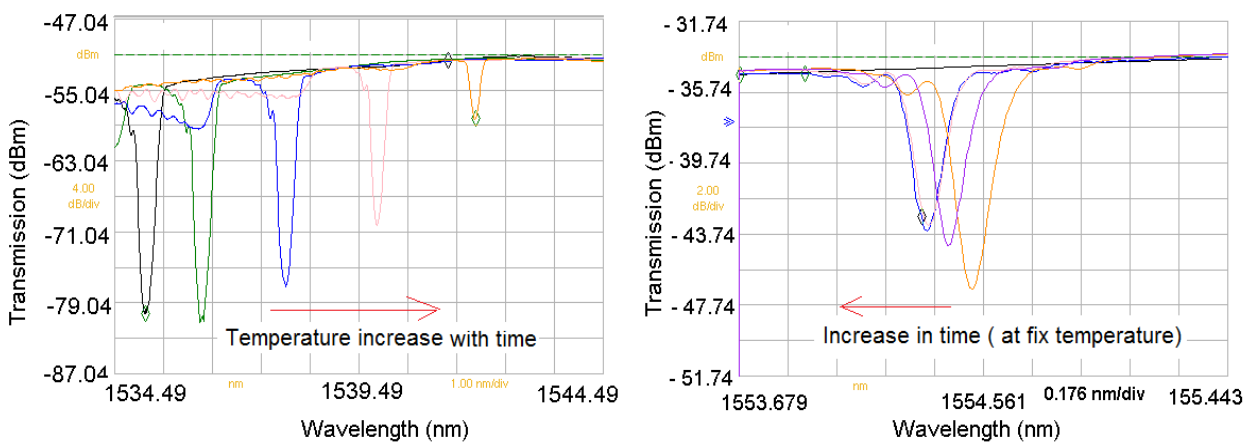

(a) (b)

Figure 7.7: Change in FBG transmission with (a) increase in temperature (b) increase in time at fixed temperature

A) Studies on thermal behavior of FGBs with temperature elevation

Type I FBG growth with UV fluence and thermal decay with temperature elevation as a function of time were studied for germanium doped CMS-1550-R1 (Stocker Yale, fiber A) and germanium–boron codoped PS 270 (CGCRI, doping 8% Germanium, 6 % Boron, fiber D) fibers. Fig.7.8a and 7.8b show the growth of index modulation [Δn] and average index [<Δn>] with UV fluence (F). The photosensitivity fiber A is lower in compared to fiber D. The Bragg wavelength shift and the transmission dip were recorded with temperature elevation two FBGs of reflectivity 92.7% (Td= 11.4 dB, in fiber A), and 93.4 % (Td= 11.8 dB, in fiber D) designated as G_1, and G_2 respectively. The reflectivity of gratings G_1 and G_2 marginally increased to maximum followed by decay with temperature elevation. The temperature of maximum reflectivity was about 250 ^{0}C for G_1 and 100 ^{0}C for G2. Typically the transmission dip of G_1 increased from 11.4 dB at 25 ^{0}C to 12.36 dB at 250 ^{0}C and then decreased 11.2 dB at 450 ^{0}C.

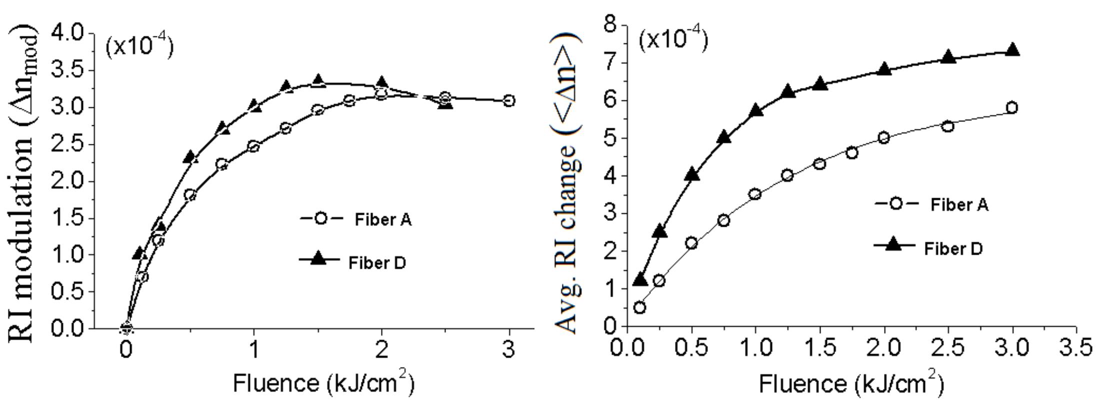

(a) (b)

Figure 7.8: Growth of (a) refractive index modulation (b) average index with UV fluence.

Fig.7.9a shows the variation of NICC [η (t, T)] at different temperature. The NICC decay rate with temperature elevation was lower for FBG in fiber A as compared to that of in fiber B. The NICC of grating G_1 increased to 1 to 1.057 as the temperature increased from 25 ^{0}C to 250 ^{0}C and then decreased to 0.98 at T= 450 ^{0}C. The decay of NICC was enhanced after 550 ^{0}C and approached to ~ 0.12 at 1000 ^{0}C. Similarly, the NICC of G_2 increased to 1.011 as the temperature increased to 100 ^{0}C and then decreased to 0.98 at 250 ^{0}C. The NICC of G_2 approached 0.1 at 700^{0} C. The NICC decay rate of G_2 was faster in compared to grating G_1.

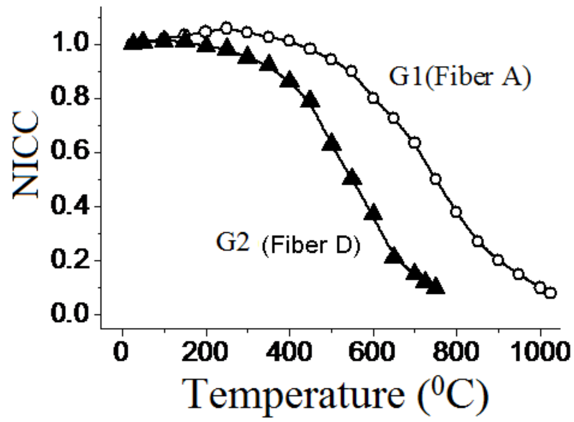

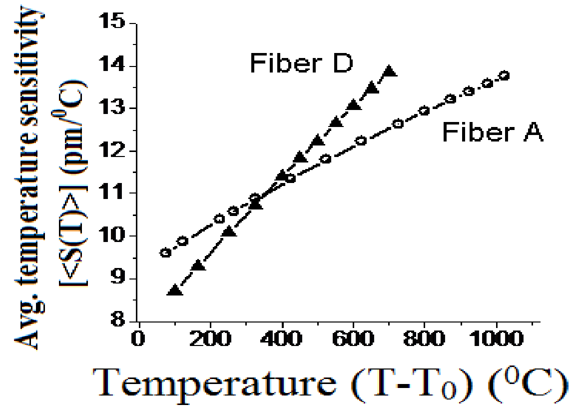

(a) (b)

Figure 7.9: (a) Decay of NICC [η (t, T)] (b) increase of average temperature sensitivity with temperature elevation

After the thermal cycle, the initial Bragg wavelength (of residual reflection) decreased by about 0. 3 nm as the FBGs is cooled to room temperature. Fig.7.9b shows the change of average temperature sensitivity [<S (T)>] with increase temperature. The average temperature sensitivity increased from 9.6 pm/^{0}C to 13.2 pm/^{0}C as temperature increased to 1025 ^{0}C for grating G_1 (in fiber A) and that from 8.7 pm/^{0}C to 13.86 pm/^{0}C as temperature increased from to 700 ^{0}C for grating G_2 (in fiber D). The temperature sensitivity increased at higher rate for G_2 (in high photosensitive fiber D) in compared to G_1 (in low photosensitive fiber A). The analytical discussion about the implication of the results is in section 7.4.

B) Thermal decay of FBGs for high and low reflectivity (in same fiber)

The decrease of FBG reflectivity with temperature elevation was lower for FBGs with higher initial index modulation. Typically the reflectivity of a saturated FBG in fiber A decreased from 99.7 % (T_d = 26 dB, Δn_{mod}= 2.65x10^{-4}) to 84 % (Td ~ 8 dB, Δn_{mod}= 1.1x10^{-4}), a change of ~ 16 %, as the temperature increased from 25 ^{0}C and 850 ^{0}C. At same temperature interval, the reflectivity of an unsaturated FBG of reflectivity 92.7 % (T_d = 11.4 dB) decreased to 29.2 % (T_d ~ 1.5 dB), a change of 63 %. Similarly the reflectivity of a 35.2 dB FBG in fiber D decreased from 99.97 % to 78 % as the temperature increased from 25 ^{0}C and 650 ^{0}C, a change of ~ 22% while that for 11.2 dB FBG was 67%. It was observed the refractive index modulation contrast of post annealed FBGs was almost same as pre annealed FBG.

C) Studies on thermal decay of Type I and Type IIA FBG

The thermal decay characteristics were studied for Type I and Type IIA FBGs written in germanium doped (10 mole %) fiber (NM113, fiber E). Initial reflectivity of type I and type IIA FBGs were 40 % and 99.9 % respectively. Fig.7.10a shows the variation of reflectivity with change in temperature which was varied in steps (red trace).

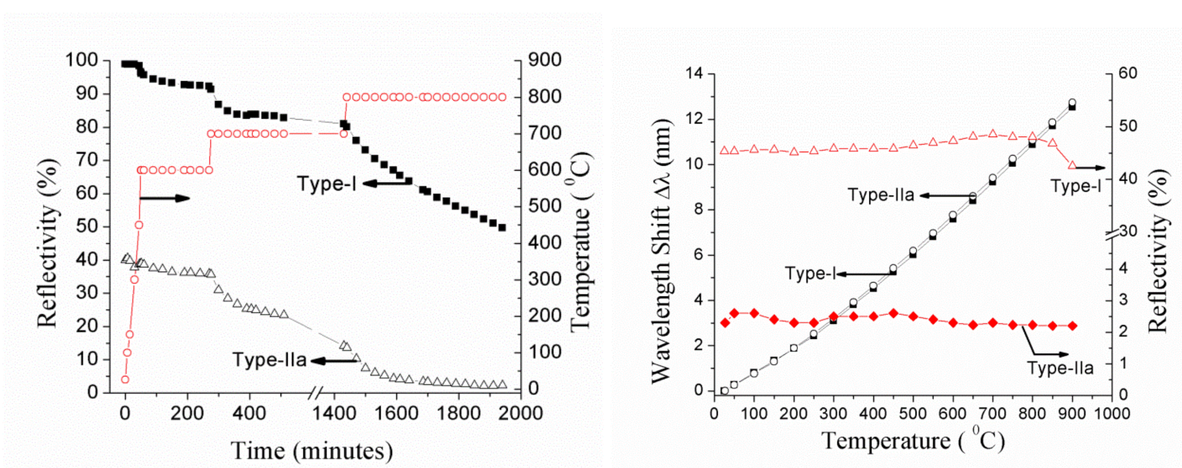

(a) (b)

Figure 7.10: (a) Variation of temperature and FBG reflectivity with time during annealing (b) Variation of Bragg wavelength shift and reflectivity of post annealed FBG with temperature

The temperature increased to 600 ^{0}C within 50 minutes and kept at 600 ^{0}C for four hours. The reflectivity of type-I and type-IIa gratings reduced by about 4 % from the maximum reflectivity after 4 hours of heating at 600 ^{0}C. The reflectivity of both type-I and type IIA grating decreased when the temperature rose to 700 ^{0}C. However, at fixed temperature of 700 ^{0}C, the type-I grating reflectivity increased slightly (~ 0.8 %) before decay.The marginal increase in the reflectivity at this temperature may be due to the thermal regeneration [215]. No such thermal regeneration is noticed for the type-IIA gratings. The reflectivity of type-I and type-IIA grating reduced to 81 % and 14% respectively after 19 hours of continuous heating at 700 ^{0}C. In third step, the temperature of the oven was increased to 800 ^{0}C and kept constant for about 9 hours. The reflectivity of type-I gratings reduced from 80 % to 50 % and that of type-IIa grating reduced from 13 % to 2.5 %. Then the FBGs are cooled down to room temperature. The Bragg wavelength shift and variation of reflectivity of post annealed FBGs with increase in temperature is shown in figure 7.10b.The reflectivity of type-I grating decreased after 800 ^{0}C. In contrast for type-IIa gratings, the reflectivity remained almost constant up to 900 ^{0}C [215]. The evolution of Bragg wavelength with increase in temperature of type I and type IIA FBG almost followed the same trend as shown in fig.7.10b.

D) Studies on thermal regeneration of FBG reflection

The thermal regeneration of FBG reflection studied for type-I FBGs written in fibers SM-1500 (doping: Ge ~ 18 mol %, fiber C), PS-270(doping: B ~ 6 mol %, Ge ~ 8 mol %, fiber D) and NM-113 (doping: Ge ~ 10 mol %, fiber E). The FBGs of length 10 mm were written under similar conditions at same fluence. The initial reflectivity of FBGs in fibers C, D and E were 96.9 %, 99.7 % and 99.6 % respectively. Fig. 7.11a shows the variation in the normalized reflectivity with time at different temperatures. The temperature varied in three steps as shown (marked as T) in fig 7.11a. During annealing at 600 ^{0}C for four hours, the reflectivity of FBGs in fiber C, D and E reduced due to decay of effective refractive index modulation. However, when annealed subsequently at 700 ^{0}C for 19 hours, thermal regeneration was observed for the seed FBGs written in Ge doped fiber C and E whereas no such regeneration was observed for Ge-B codoped fiber D.

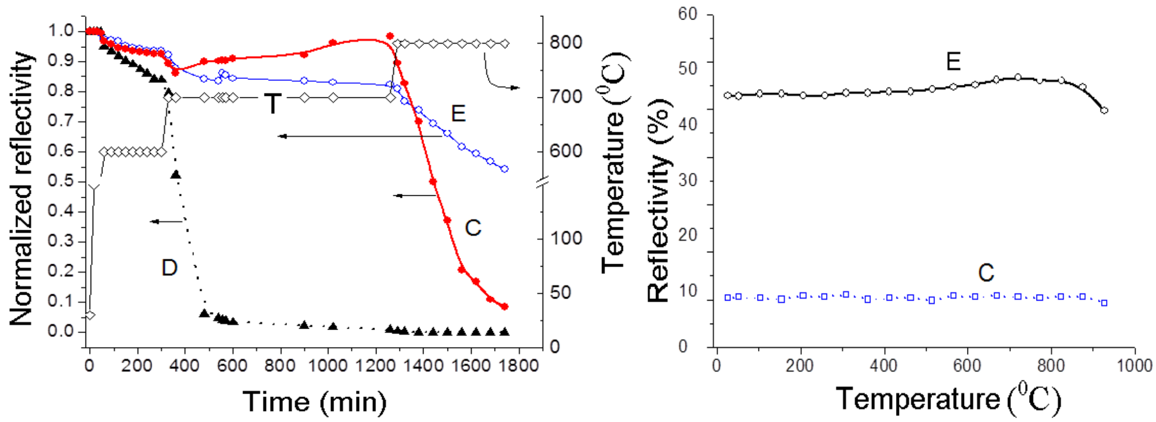

(a) (b)

Figure 7.11: (a) Variation of temperature and FBG reflectivity with time during annealing (b) Variation of post annealed FBG reflectivity with temperature

The normalized reflectivity of the FBG in fiber E first reduced from 92.2% to 83.55% within 210 minutes and then increased marginally by about 3 %. The increase in the reflectivity of the FBG in fiber C is around 10 %. Thus the FBGs written in C and E fibers show a sign of regeneration at temperature 700 ^{0}C. The degree of thermal regeneration was different and observed at different time for FBGs in fiber C and E. In fiber E, the thermal regeneration was observed after 210 minutes and for about 30 minutes. In case of FBG in fiber C, the regeneration was for the entire time at 700 ^{0}C. The strength of thermal regeneration was higher for the FBGs in the fiber having higher Ge- doping concentration. The FBG in Ge-B co-doped fiber decayed substantially at 700 ^{0}C. The reflectivity of the post annealed FBG written in Ge doped fiber was stable up to 800 ^{0}C in successive round of temperature elevation (fig 7.11b) [272].

7.4 Discussion on FBG temperature stability

The observed experimental results may be summarized as follows. The thermal decay with temperature elevation is initially slow with fast decay at higher temperature. However, in isothermal annealing at high temperature, the decay of a pristine FBG was initially fast with slow decay afterwards. During thermal relaxation, the Bragg wavelength shifted to blue side and spectrum band width decreased with decay of FBG reflectivity. The temperature sustainability of FBGs written in Ge-doped fiber was higher in compared to Ge-B doped fiber. The observed decay of average refractive index was higher than decay of modulation after thermal annealing. Based on concept of demarcation energy, Edrogan *et al.* provided an empirical law [262] for decay of NICC. However, the small increase in FBG reflectivity as observed in the present experiment and reported results in the low temperature range [257], could not be explained by this law. The FBG reflection at a particular temperature is higher for high reflectivity FBG. The thermal regeneration was observed for FBGs in Ge-doped fiber when annealed at 700 ^{0}C. However, no thermal generation was noticed for seed FBG written in B-Ge doped fiber [272].

To explain the effect of fiber composition and FBG strength on FBG temperature sustainability, initial distribution of trapped population may be expressed in Gaussian form [46, 272]

$$f(\varepsilon) = f(\varepsilon_0)\ \exp(-2(\varepsilon-\varepsilon_0)^2/\Delta\varepsilon^2) \tag{7.21}$$

where $f(\varepsilon_0)$ is fractional population at the distribution peak (at $\varepsilon = \varepsilon_0$) and $2\Delta\varepsilon$ is $1/e^2$ bandwidth.Fig.7.12a shows typical distributions designated as d_1 and d_2 [(d_1: ε_0 = 2 eV, $\Delta\varepsilon$ =1eV; d_2: ε_0 = 3eV, $\Delta\varepsilon$ = 1.5 eV). The induced refractive index linearly proportional the trapped state population density.The change photo induced index normalized to it's pre-anneal value [η (ε_d)] can be expressed as,

$$\eta(t,T)=\eta(\varepsilon_d)=[\int_{\varepsilon_d}^{\infty} f(\varepsilon)d\varepsilon]/[\int_{0}^{\infty} f(\varepsilon)d\varepsilon] \tag{7.22}$$

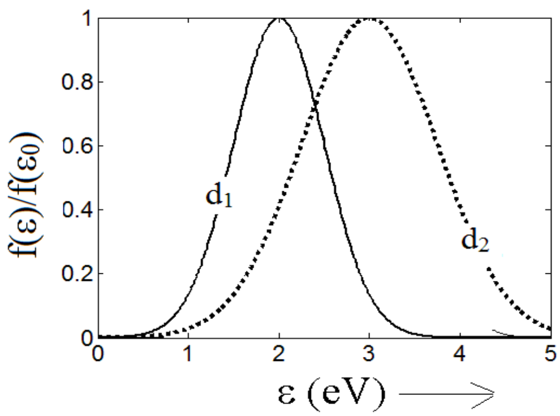

(a)

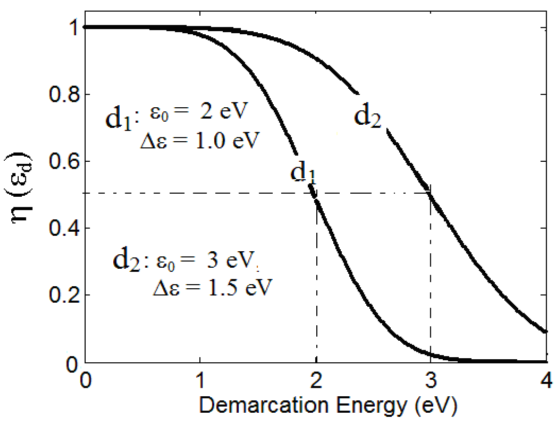

(b)

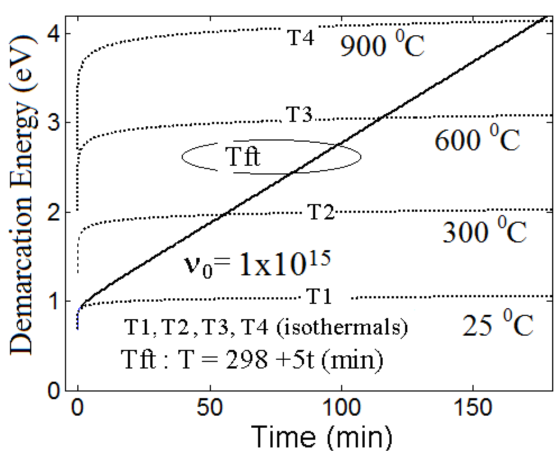

(c)

Figure 7.12: Simulated (a) typical distributions of d_1 and d_2 [(d_1: ε_0 = 2 eV, $\Delta\varepsilon$ =1eV; d_2: ε_0 = 3eV, $\Delta\varepsilon$ = 1.5eV] (b) η (ε_d) vs. ε_d for d_1 and d_2 (c) Change in demarcation energy with time in Tft and isothermal process

With assumption of the distribution function independent on duration of UV exposure (trapped state population density), the η (ε_d) will be same as NICC. Fig.7.12b shows simulated η (ε_d) vs. ε_d for typical distributions of d_1 and d_2.Thus the NICC decreases with increase in demarcation energy (increase in time and/or temperature). The UV induced growth of refractive index is cumulative effect of change in absorption spectrum, stress and photo-elastic changes. The irreversible thermal decay may be linked to similar reverse change in these factors. The growth of refractive index with continuous UV illumination is initially fast with slow growth towards saturation. The thermal decay with increase in demarcation energy is initially slow with fast decay at higher demarcation energy. During FBG writing, the reflection spectrum bandwidth increases and Bragg resonant wavelength shifts towards red. During thermal relaxation, the Bragg wavelength shift to blue side and spectrum band width decreases with decay of FBG reflectivity.As the modulation contrast of the FBG before annealing is less than unity, the thermal decay of average refractive index will be always higher than decay of modulation. For a uniform FBG, the refractive index modulation at demarcation energy (ε_d) is expressed as,

$$\Delta n\,(t,T) = \Delta n(0)\,\eta(\varepsilon_d) \tag{7.23}$$

The reflectivity [$R = \tanh^2(\pi\,\Delta n\,L/\lambda)$] of the grating increases with grating length (L) and refractive index modulation (Δn). The remnant reflectivity of a FBG kept at temperature T for time t will be higher for a FBG of higher initial strength [$\Delta n\,(0)\,L$]. Thus the thermal stability of a high reflectivity grating at any temperature will be higher, as found in the experimental results.Fig.7.12c shows the variation of activation energy with temperature elevation as a function of time (Tft process) and in isothermal process, for typical values mentioned. In isothermal annealing at high temperature, the demarcation energy increases vary fast with very slow increase in longer times. The decay of FBG refractive index modulation in isothermal annealing followed the same pattern. In Tft process, the increase of demarcation energy with time is almost linear with temperature. As observed experimentally, the refractive index modulation decay in Tft process will be initially slow with fast decay as ε_d approaches ε_0 (distribution peak). When $\varepsilon_d = \varepsilon_0$, $\eta\ (\varepsilon_d = \varepsilon_0) = 0.5$ (half of the species D2 deplete) as apparent from fig.7.12b. From the symmetry of the distribution, for certain $\Delta\varepsilon_d$ (marked for d_2 and d_3)

$$\eta\ (\varepsilon_0-\Delta\varepsilon_d) - \eta\ (\varepsilon_0) = \eta\ (\varepsilon_0) - \eta\ (\varepsilon_0+\Delta\varepsilon_d) \tag{7.24a}$$

Thus if $\varepsilon_0 = kT_c \ln\nu_0 t_c$; $(\varepsilon_0-\Delta\varepsilon_d) = kT_1 \ln\nu_0 t_1$ and $(\varepsilon_0+\Delta\varepsilon_d) = kT_2 \ln\nu_0 t_2$ where ($t_2 > t_c > t_1$ and $T_2>T_c>T_1$) , then the initial release rate (ν_0) from eqn (7.24a) can be expressed as,

$$\nu_0 = (t_1^{T_1} t_2^{T_2} / t_c^{2T_c})^{1/(2T_c-T_1-T_2)} \tag{7.24b}$$

Thus $2\Delta\varepsilon_d \approx \varepsilon_0 \Delta T/T_C$ [where $\Delta T = T_2-T_1$].It was experimentally observed that $\eta\ (t,T) = 0.5$ at $T = T_C$ (= 750 ^{0}C for G_1 and 550 ^{0}C for G_2). The grating G1 has higher thermal stability either for (i) $\varepsilon_{0A} > \varepsilon_{0B}$ (trap depth of $G_1$is higher) $\nu_{0A} = \nu_{0B}$ or (ii) $\nu_{0A} < \nu_{0B}$ (release rate of G_1 is lower) for $\varepsilon_{0A} = \varepsilon_{0B}$ then or combination of two.The observed temperature interval (ΔT) in which the NICC decayed from 0.85 to 0.15 for G_1 and G_2 are ~ 400 ^{0}C and ~ 300 ^{0}C respectively. The bandwidths of the distribution for G_1 and G_2, for this interval, are approximately 0.53 ε_{0A} and 0.66 ε_{0B} respectively.For $\nu_{0A} \sim (5.3 \pm 0.53)\ \mathrm{x}10^{11}$ Hz and $\nu_{0B} \sim (9 \pm 0.9)\mathrm{x}10^{15}$ Hz, the temperatures T_1,T_c, T_2 for equal change NICC from T_C approximately lies on the ε_d vs. T plot for G_1 and G_2 respectively. The estimated energy peak and bandwidth of the distribution are [ε_{0A} ~ 3.15 eV, $\Delta\varepsilon_{0A}$ ~ 1.1 eV], [ε_{0B} ~ 2.8 eV and $\Delta\varepsilon_{0B}$ ~ 1.2 eV]. Fig.7.13a shows the simulated η (t, T) vs. T based on the concept of demarcation energy for typical values ε_{0A} ~ 3.15 eV, $\Delta\varepsilon_{0A}$ ~ 1.1 eV for fiber A and ε_{0B} ~ 2.8 eV and $\Delta\varepsilon_{0B}$ ~ 1.2 eV for fiber B.

The concept of demarcation energy could not explain the reversible but small growth of FBG reflectivity in the low temperature regime. This may be related to variation of effective index with temperature elevation. The change of refractive index of the UV illuminated glass is the cumulative effect of reversible response (increase in refractive index with temperature) and the irreversible response (decrease in refractive index due to thermal relaxation). The change of index modulation with temperature implies that the change effective indices in bright and dark fringe regions are not same.Thus UV exposure (population density of DID) affects the temperature derivatives of UV induced refractive index. Taking the effective indices in high and low index regions as n_h (T) and n_l(T) respectively, the average effective refractive index of the FBG can be expressed as, n_{eff} (T)= [n_h (T)+n_l(T)]/2. The effective index modulation can be expressed as, Δn_{eff} (T) = [n_h(T)- n_l(T)]/2. The refractive index of the fiber glass, expressed in Taylor's series, is given in eqn (7.3). Using eqn (7.3), n_{eff} (T) and Δn_{mod} (T) and average temperature sensitivity <S(T)> are given by,

$$n_{eff}(T) = <n_0(T_0)> + <c_1>(T-T_0) + <c_2>(T-T_0)^2 + <c_3>(T-T_0)^3 + ... \quad (7.25)$$

$$\Delta n_{eff}(T) = \Delta n_{\text{mod}}(T_0) + \Delta c_1(T-T_0) + \Delta c_2(T-T_0)^2 + \Delta c_3(T-T_0)^3 + ... \quad (7.26)$$

$$<S(T)> = <d\lambda(T)/dT> = a_1 + a_2(T-T_0) + a_3(T-T_0)^2 + ... \quad (7.27)$$

where $<c_m> = (c_{mh}+c_{ml}) / 2$; $\Delta c_m = (c_{mh}-c_{ml}) / 2$; $a_m = \lambda(T_0)\,[\,<c_m>/(<n_0>) + \alpha <c_{m-1}>/]$; α is thermal expansion coefficient of the fiber. Δc_1 and Δc_2 will also depend on rate of temperature elevation (dT/dt). We have $\Delta a_m \neq 0$ (modulation changed with temperature). Let Δn_{mod} (T) passes through a maximum at temperature T_m. This (T_m) was about 250 ^{0}C for grating G1 (in fiber A) and 100 ^{0}C for grating G2 (in fiber B).The temperature sensitivity [<S(T)>] was approximately linear [fig. 7.9b].Thus the effect of a_m and Δa_m for $m \geq 3$ were neglected and further discussion on variation of modulation is now limited up to quadratic in (T-T_0) [in eqn (12)] to analyze the qualitative trends. At, T= T_m(> T_0), (dn_{eff}/dT) = 0 and (d^2n_{eff}/dT^2) < 0 which gives (T_m -T_0) = -$\Delta c_1/\Delta c_2$; Δc_2< 0 and Δc_1> 0. Thus we have c_{1h} >c_{1l} and c_{2h}<c_{2l}. At reference temperature, the refractive index first derivative is higher and second derivative is lower in bright fringe region. The highest temperature (T_h) at which modulation will be zero can be obtained from equation (7.26) by putting Δn_{eff} (T_h) = 0. By retaining terms up to quadratic of (T_h-T_0) in equation (7.26), T_h is expressed as,

$$T_h = T_m + \sqrt{(T_m - T_0)^2 - \frac{2\Delta n_{\mathrm{mod}}(T_0)}{\Delta c_2}} \tag{7.28}$$

From eqn (7.28), we have $T_h \geq 2T_m - T_0$. The value of T_h in eqn (7.28) is not exact as higher order derivatives have been ignored. If T_m and T_h are constants for a typical material, then Δc_1 and Δc_2 increases with increase of initial modulation. In the temperature interval from T_0 to T_m, the positive growth due to reversible material response is higher than the negative growth due to DID thermal relaxation induced.

For grating G_1, the average growth rate of modulation ($<d\Delta n_{mod}/dT>$) from T_0 (25 ^{0}C) to T_m (= 250 ^{0}C) was ~ $3.5\text{x}10^{-8}$ [$<(d\eta/dT)> = +2.56\text{x}10^{-4}$]. By ignoring thermal relaxation, the refractive index modulation of grating G_1 will increase from initial value of $1.39\text{x}10^{-4}$at 25 ^{0}C to 1.66 $\text{x}10^{-4}$at 800 ^{0}C. For grating G_2 in fiber B, $<(d\eta/dT)> = +\ 1.15\text{x}10^{-4}$ between 25 ^{0}C to 100 ^{0}C (=T_m). Above T_m, the decay of modulation due to thermal relaxations is higher than the growth attributed to variation reversible growth. The UV exposure dependent refractive index change with temperature effectively raised the demarcation energy barrier and thus improved the thermal sustainability. For grating G_1 in fiber A, the typical values : $<c_1> \sim 8.55$ $\text{x}10^{-6}$, $<c_2> \sim 9\ \text{x}10^{-9}$ (estimated from observed average temperature sensitivity); the typical $\Delta c_1 \sim 10\text{x}10^{-4}\Delta n_{mod}$ (25 ^{0}C), $\Delta c_2 \sim -\ 4.4\text{x}10^{-6}\Delta n_{mod}$ (25 ^{0}C) [estimated from T_m and fromη (T) = 0.5]. Since Δn_{mod}(T) is a polynomial of (T-T_0) and depends on difference in higher order derivatives (eqn 12), η (T) = 0.5 has been chosen to evaluate Δa_1 and Δa_2, as average representations. Similarly, for grating G_2 in fiber B, the typical values are $<c_1> \sim 7.1 \times 10^{-6}$, $<c_2> \sim 13.3 \times 10^{-9}$, $\Delta c_1 \sim 4.8 \times 10^{-4} \Delta n_{mod}$ (25 ^{0}C), $\Delta c_2 \sim - 4.8 \times 10^{-6} \Delta n_{mod}$(25 ^{0}C).

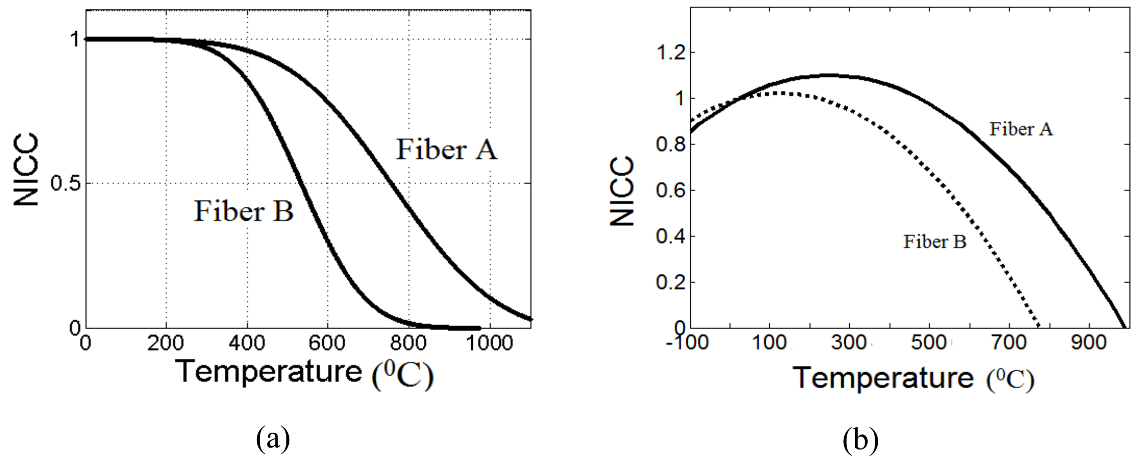

Figure 7.13: Simulated η (ε_d) vs. T (a) for typical distributions [A: $\varepsilon_{0A} \sim 3.15$ eV, $\Delta\varepsilon_{0A} \sim 1.1$ eV], [B: $\varepsilon_{0B} \sim 2.8$ eV, $\Delta\varepsilon_{0B} \sim 1.2$ eV]. (b) Based on different variation of effective refractive index in bright and dark fringe regions

Fig. 7.13b shows simulated variation of NICC with temperature for FBGs in fiber A and B, as relative trends. FBGs written in Ge-doped fiber are able to tolerate higher temperature in compared to FBGs written in Ge-B codoped fiber. The boron doping enhanced photosensitivity. However, the same reduced the thermal sustainability. The probable reasons are that the boron co-doping reduced the demarcation energy required to depopulate the trapped states population. Boron co-doping either lowered the trap depth or increased the release rate or the combination of both. Besides, the different variation of effective index with change in temperature in high and low index regions which effectively decelerated the degradation of refractive index modulation. The enhancement of temperature sustainability was higher for Ge-doped fiber. The degree of enhancement was reduced when boron was codoped. The thermal regeneration of FBG at 700 ^{0}C may be attributed to stress relaxation of the fiber core between high exposed and less exposed region by the UV or due to crystallization of fused silica fiber [16]. However doping of Boron lowers the softening temperature of glass. This may lead to no thermal regeneration and FBG decayed at lower temperature as compared to only Ge doped fibers.

7.5 Conclusion

It was experimentally observed that the temperature sensitivity of both bare and embedded FBG increases with temperature elevation. The average temperature sensitivity increased by about 20% as bare FBG temperature was elevated from 25 ^{0}C to 525 ^{0}C. The temperature sensitivity of embedded FBG sensor, investigated in temperature range of 30 to 90 ^{0}C, was a factor of 2 to 3 larger than bare FBG, depending on its fastened length with substrate. The theoretical analysis shows that the increase in temperature sensitivity of bare FBG at elevated temperature depends on temperature derivatives of effective refractive index, especially second derivative of refractive index and thermal expansion of the fiber material. Additionally, the non-uniformity of temperature sensitivities of embedded FBG sensors depends on strain transfer coefficients from substrate to FBG and thermal expansion of the substrate. In typical FBG based temperature sensors; it is rather convenient to experimentally determine the required constants to express temperature as function of Bragg wavelength shift.The experimental study on thermal sustainability of type I FBGs written by high repetition rate 255 nm UV beam showed that the observed decay of refractive index modulation with temperature elevation was faster for the FBG (fiber) in which its growth with UV fluence was faster. The FBGs written in the comparatively low photosensitivity (to 255 nm) fiber was able to tolerate higher temperature (up to 800 ^{0}C). With temperature elevation, the reflectivity marginally increased to maximum and decayed at elevated temperature. The type IIA FBGs and regenerated FBGs showed comparatively higher thermal stability. Thermal regeneration was observed when the FBGs written in Ge-doped fibers were annealed at 700 ^{0}C. The thermal sustainability of type I FBGs were analyzed using key concepts, thermal relaxation of trapped population based on demarcation energy, trap depth/release rate of trapped population and different rate of increase of effective index in UV fringes induced high and low index regions. The experimental results qualitatively agree with the analysis.

Publications based on this chapter

1. "Studies on thermal regeneration and temperature stability of type-I FBGs written in Ge–B codoped and Ge-doped fibers by a kHz repetition rate nanosecond 255nm beam" J. Kumar , **R.Mahakud**, A.Mokhariwale, O.Prakash, S.K.Dixit and S.V.Nakhe, Optics Commun. **2014**, 320, 109–113.
2. "Enhanced temperature (~ 800^{0} C) stability of type IIa fiber Bragg grating written in Ge doped photosensitive fiber", O.Prakash, J. Kumar, **R. Mahakud**, S. K. Agrawal, S. K. Dixit and S. V. Nakhe, IEEE photonics technology letters ,**2014**, 26, 93-95.
3. "A study on the non-uniform behavior of temperature sensitivity of bare and embedded fiber Bragg gratings: Experimental results and analysis"**R.Mahakud**, J. Kumar, O.Prakash and S.K. Dixit, Appl. Optics, **2013,** 52, 7570-7579.

Chapter 8

Summary and future scope

8.1 Summary of the thesis

The present thesis is a comprehensive study on the fabrication, analysis and utilization of fiber Bragg gratings manufactured by kHz repetition rate, ns duration, 255 nm UV pulsed sources, generated from second harmonic of CVL 510 nm beams. The whole work consisted of closely interlinked sections such as development of UV source based on second harmonic of CVL, extensive UV/CVL beam characterization, studies on the contrast and stability of UV fringes, development of FBG writing setup, extensive FBG writing by phase mask and biprism techniquesby UV beams of various degree of spatial coherence and pointing stabilities, theoretical analysis on the effect of contrast and stability of UV fringes on FBG reflectivity and induced refractive index modulation and study on the developed FBGs as temperature sensorsboth experimentally and analytically.

The first presented work, in the thesis, is the development of second harmonic UV source at 255 nm from the 510 nm CVL radiation at 5.6 kHz repetition rate. For the efficient second harmonic conversion as well for ascertaining the beam characteristics of generated UV appropriate for writing FBG, it was very important to thoroughly characterize the CVL source for spatial coherence, pointing stability, line-width, average power, intensity profile and pulse shape. These characteristics were thoroughly studied with three different CVL optical resonators such as confocal unstable resonators of magnification 12.5 (PBUR1) and 100 (PBUR2) as well as an intra-cavity spatial filtering resonator (GDFR). The spatial coherence measurements, of these partially coherent CVL beams, were carried out by in house proposed and developed compact reversal shear interferometer. The single pulse and pulse to pulse characteristics were measured by a gated CCDin a sequential data acquisition system. The CVL beam quality improved with increase in unstable resonator magnification from 12.5 to 100. However the best CVL spatial coherence and pointing stability was obtained in spatial filtering (GDFR) resonator which was suitably explained. The beam divergence (in terms of diffraction limit) and pointing stability of PBUR1, PBUR2 and GDFR CVL beams were, 3.0 DL & 45 μrad, 2.2 DL & 22 μrad and 1.1 DL & 8 μrad. The next logical step was to frequency convert (second harmonic) these CVL beams to UV (255 nm) radiations in a homemade set up. The UV beams (UV1, UV2 and UV3) characteristics such as average power, spatial coherence, and pulse shape and power stability are studied in detail. The UV beam characteristics are correlated with that of fundamental CVL beam. The beam quality of UV3 was best among the three beams. The maximum UV power obtained were 600 mW (UV1) at 2.1 W GDFR CVL, 650 mW (UV2) at 3.5 W PBUR2 CVL and 325 mW (UV3) at 4.5 W PBUR1 CVL. Thepower and beam quality of investigated UV beams were appropriate to write high reflectivity FBGs as aptly demonstrated.

Inching towards the FBG fabrication, the next step was to study the UV fringes' contrast and stability, made by a FBG writing interferometer, due to widely differing spatial coherence and pointing stability characteristics of UV1, UV2 and UV3 beams.The FBG fabrication by kHz repetition rate but low energy (10s μJ) 255 nm pulses require millions of UV pulses in typical writing period of 2 to 10 minutes. Hence it is the average fringe contrast over the writing period that decides the FBG parameters. Three FBG writing interferometers namely, Phase mask. Phase mask-Talbot and biprism were analyzed for average fringe contrast as a function of incident UV beam divergence and pointing angle. The fringe contrast was theoretically estimated as a function of distance (in millimeter) from the phase mask surface/biprism apex. It is concluded that the fringe contrast is significantly affected by the spatial coherence of the UV beam. Poorer the incident UV spatial coherence, larger will be the fringe contrast dilution at a given fiber plane. Also for a fixed UV beam divergence, the fringe contrast dilution is higher for the larger distance of fiber from the interferometer. The fringe contrast distribution is much more complex for UV beams generated from CVL. The UV pulse characteristics which follows the CVL pulse contains different beam divergence components due to evolution of CVL divergence within a pulse. This is due to self-terminating, short inversion time, high gain nature of CVL (510 nm) transition. It is concluded that for CVL based UV pulse, that the weighted average fringes contrast dictates the FBG writing. For a given fiber location, higher the fraction of power in larger divergence angle (within a UV pulse), poorer was the UV fringes contrast. The strong role of UV beam spatial coherence is demonstrated both in phase mask and biprism based FBG writing, in the continued work.

The fringes' contrast dilution is also calculated, for all the three interferometers, as a function of pointing instability of the incident UV beams. This effect is analyzed by considering the set of parallel rays incident on the beam splitting optical element, with incident angle fluctuating within pointing angle envelope, with uniform distribution of pointing angles. Larger the UV beam pointing instability and/or larger the FBG writing distance form beam splitter, poorer was the average fringe contrast. The fringes contrast dilution was compared for all the interferometers, for the typical FBG writing distances of 1mm (for phase mask), 10 mm (for biprism) and 24 mm (for phase mask-Talbot). For these distances, the calculated fringe instability (fringe width/fringe pitch) &averaged fringes contrast were 3.7% & 0.98, 42% & 0.73 and 99.8% & 0.07 for phase mask, biprism and Talbot interferometers respectively for incident UV beam pointing stability of 20 μrad. The theoretical analysis is verified experimentally, in a test set up, by studying the instability of

14.6 μm spacing fringes formed by a 2^0biprism with GDFR, PBUR2 and PBUR1 CVL (510 nm) beamsof pointing instability 8 μrad, 22 μrad and 45 μrad respectively. The whole work on fringe contrast analysis provided guidelines for the effective FBG fabrication by UV1-UV3 beams.

Next, UV1-UV3 beams of repetition rate 5.6 kHz, pulse width 20-30 ns, average power 200-400 mW and energy density 1.4-2.8 mJ/cm^2 were utilized in a study on FBG fabrication by phase mask technique, in an in-house developed setup. The Ge and Ge-B doped photosensitive fibers from commercial manufactures such as Stocker Yale, Nufern, Fiber core and CGCRI of different Germanium (3-18 %) and Boron (6-8%) doping are studied for type – I, type-IIA and tilted FBG inscriptions. The type-IIA gating was written for the first time with CVL based UV source. The C-band (~ 1550 nm) FBG reflectivity upto 99.98 % (T_d = 38 dB) for typeI, tilted FBGs of reflectivity up to 30 dB (99.9 %), type IIA gratings up to 9.9 dB (89.7 %) are achieved. The bandwidth of the fabricated FBGs varied in 0.3 – 1.0 nm range. The results are very impressive as none of the fibers were hydrogen loaded. The writing time & cumulative UV fluence were in range 3-10 minutes & 0.5 -5 kJ/cm^2 for type-I gratings and 15-35 minutes&15-35 kJ/cm^2 for type-IIA gratings. In one of the studies, about 10.5 dB (91%) type-I FBG reflectivity was demonstrated at ~ 1054 nm by using a phase mask of different pitch 0.725 μm. The best FBG performances were achieved with highest spatial coherence and least pointing stability UV3 beam.

On the finer level, the FBG growth characteristics such as reflectivity, refractive index modulation and spectrum were studied with accumulated UV1-UV3 beams' fluence with continued exposure of fringes. The growth and saturation of refractive index modulation and required fluence to saturate was different for different fibers. These trends were also different for UV beams of different spatial coherence. The refractive index modulation growth was faster and saturated at higher value for UV beams of higher spatial coherence. In a particular, for a fixed average UV power (~220 mW), beam diameter (~10 mm), phase mask to fiber distance (~ 0.8 mm) and single mode photosensitive fiber (PS-RMS-50, Stocker Yale, core dopants: B_2O_3 and GeO_2), the type I FBG reflectivity in first 50 seconds, were 6 dB, 10 dB and 16 dB for UV1, UV2 and UV3 beams respectively. Beyond 50 s, the grating growth rate slowed down for UV1 beam, reaching maximum transmission of 13 dB in 400s. For UV2 beam, maximum 21 dB was obtained in 300 s. For UV3 beam, the highest transmission of 30.5 dB was observed in 210 s. In every case, with continuous exposure, the growth rate reduced as the induced refractive index modulation approached saturation. The evolution of reflection spectrum, with continuous exposure of UV fringes, was dynamic. The side lobes on blue side of the spectrum evolved first. The side lobe strength increased with increase in grating strength. The side lobes on both sides appeared for saturated gratings.

With prolong exposure of UV fringes, the re-growth of FBG reflection (Type IIA regime) started after decay phase (of type I), at much higher fluence. The FBG growth rate in type IIA regime was slow in comparison to that in type I regime. The Bragg wavelength blue shifted during growth of type IIA FBG.The appreciable type IIA growth of FBG was possible only when written by high contrast UV3 fringes. The Bragg wavelength tuning by tilting the grating planes from 0^0 (normal FBG) to and 6^0 were studied. The main Bragg peak shifted towards the higher wavelength accompanied by reduction of reflection power.

The preceding work on phase mask based FBG fabrication was further extended by theoretical analysis. This was mainly with a focus to explain the different experimental trends in the growth and saturation of refractive index modulation (with increase in UV fluence) for the writing UV beams of different spatial coherence. This necessitated the incorporation of reduced fringe contrast of the partially coherent UV beams in the existing models which are based on unity fringe contrast. Such arevised model is proposed. It is based on single photon absorption with change in refractive index of photosensitive fiber core, in the UV illuminated region, considered proportional to depleted GeOdefect centers per unit volume. Then, the sinusoidal refractive index modulation expression, along the FBG length, was corrected for reduced UV fringes contrast for partially coherent beams. The variation in refractive index change along FBG length was evaluated for different fringe contrast with respect to increasing UV fluence.It was observed that at higher fluence, the spatial distribution of refractive index modulation δn (z) deviates from sinusoidal distribution with progressively flattening of peaks. This makes it necessary to consider higher harmonics of index modulation. The spatial variations of index modulation, of first three harmonics, were evaluated for different UV beam contrast and fluence. This theoretical analysis clearly indicated that growth of 1st harmonic of refractive index modulation (hence FBG reflectivity) is faster and saturation of refractive index modulation is higher when written by UV beams higher contrast (due to higher spatial coherence), explaining the observed experimental results.

This analysis is further extended to study the reflection spectrum of the fiber Bragg gratings written by the UV beam profiles of different intensity distributions, particularly cylindrically focused top hat and Gaussian beams. It is analytically shown that while writing FBG by UV fringes of non-uniform intensity distribution, the refractive index distribution envelope evolves with exposure time. The average refractive index and refractive index modulation profiles change due to nonlinear growth and saturation of UV induced refractive index, at different sections of the grating occurring at different times of exposure. Effect of average refractive index and refractive index modulation profile dynamics on the reflection spectra of fiber Bragg gratings, are discussed. The analysis explained the observed experimental trends on FBG spectral characteristics as well as its post fabrication erasure by fringeless (uniform) UV exposure for effective index correction. Also the effect of residual phase mask orders in FBG fabrication is analyzed and their effect on experimental results is brought out.

The thesis work is further continued to study prism interferometer based FBG fabrication. This technique is simple, cost effective, damage free and highly suitable for multi-wavelength FBG writing. However, in view of large path length involved, the requirement on UV beam coherence and pointing stability are very stringent which is facilitated by UV3 beam in the present work. In the first part, theoretical analysis is carried out on refractive index modulation, grating length, reflectivity and wavelength tuning of FBG written by prism interferometers (Biprism and Lloyd mirror). The fringe contrast and the FBG reflectivity with varying fluence was estimated as function of distance from the prism. It is shown that the fringe contrast, evolution and saturation of reflectivity and the spectrum of the FBGs will be affected by the interferometer design, UV beam divergence and profile besides the fiber photosensitivity. The biprism fringes contrast decreases along fringe depth but uniform along fiber length whereas the Lloyd prism fringes contrast decreases along fiber length. The fiber position of maximum FBG reflectivity in biprism based writing is dictated by beam divergence and is less than the distance of maximum beam overlap position where inscribed FBG length is largest. The FBG wavelength tuning is also analyzed with change in beam incidence angle, geometrical divergence and distance of fiber from interferometer. This analytical study helps in design and synthesis of the FBGs written by prism interferometers.

In the second part, an experimental study is carried out on writing C-band FBGs with a 24^0 biprism with UV1, UV2 and UV3 beams in different fibers. However prior to FBG writing, in a test setup, about 8 μm spacing UV fringes formed by a 2^0 biprism and characterized for positional stability and fringe contrast. This is implemented by recoding the visible fluorescence of UV1-UV3 fringes (incident on luminescent glass) on the gated CCD. As expected, the UV3 fringes were of best quality. With incidence UV1, UV2, UV3 beams of same diameter of 10 mm and same average power of 220 mW, type-I FBGs are written by the 24^0 biprism interferometer. The fiber was placed at the same maximum beam overlap position at which inscribed FBG length is largest. The FBGs reflectivity (at~ 1550 nm) were 0.25 dB (5.6 %), 2.2 dB (39.7 %) and 3.5 dB (55 %), for UV1, UV2 and UV3 respectively. It is clear that in contrast to phase mask based writing, the effect of UV beam spatial coherence and pointing stability are much stronger in prism based FBG writing, as expected. The FBG reflectivity was also studied for different location for fiber from the biprism apex. The maximum FBG reflectivity of about 10 dB (90%) in PS270 fiber and 12 dB (~ 93.7 %) GF1 fiber was achieved by the writing UV3 beam.These are one of the highest reflectivity achieved in prism based FBG writing. The wavelength tuning of FBG is also studied. The overall experimental results closely matched with that predicted from the analysis.

The final thesis work was utilizing the written FBGs for high temperature sensing where two important parameters are FBG temperature sensitivity and thermal stability. The experimental results and analysis on the factors affecting nonlinearity of temperature sensitivity of bare and embedded FBGs are presented. It was experimentally observed that the temperature sensitivity of both bare and embedded FBG increased with temperature elevation. The average temperature sensitivity increased by about 20% (from 10.4 pm/^{0}C to 12.4 pm/^{0}C) as bare FBG temperature was elevated from 25 ^{0}C to 525 ^{0}C. The temperature sensitivity of embedded FBG sensor, investigated in temperature range of 30 to 90 ^{0}C, was a factor of 2 to 3 larger than bare FBG, depending on its fastened length with substrate. The theoretical analysis shows that the increase in temperature sensitivity of bare FBG at elevated temperature depends on temperature derivatives of effective refractive index, especially second derivative of refractive index and thermal expansion of the fiber material. In addition, the non-uniformity of temperature sensitivities of embedded FBG sensors depends on strain transfer coefficients from substrate to FBG and thermal expansion of the substrate.

The thermal stability of performance of type I and type IIA FBGs was studied during and after the multistep annealing process. These steps were, heating the FBG to 600 ^{0}C in 50 minutes, 600 ^{0}C maintained for four hours, further heating to 700^0 C for 19 hours and finally 800^0 C for 9 hours. Then the FBGs were cooled down to room temperature. The reflectivity of type-I and type-IIA grating reduced to 81 % and 14% respectively after 19 hours of heating at 700 ^{0}C. At this temperature (700 ^{0}C), the type-I grating reflectivity increased slightly (~ 0.8 %) possibly due to thermal regeneration. The reflectivity of type-I and type-IIA gratings reduced from 80 % to 50 % and 13 % to 2.5 %, respectively after 9 hours heating at 800 ^{0}C. The Bragg wavelength shift and reflectivity of post annealed FBGs was studied with increase in temperature upto 900^0 C. The reflectivity of type-I grating decreased after 800 ^{0}C. In contrast for type-IIA gratings, the reflectivity is almost constant up to 900 ^{0}C, demonstrating its high temperature sensor capabilities. In general, the experimental study showed that decay of refractive index modulation with temperature elevation was faster for the FBG with faster growth during fabrication. The FBGs written in the comparatively low photosensitivity fiber was able to tolerate higher temperature. The factors such as initial grating strength, UV exposure, temperature variation of effective index and fiber photosensitivity affected the FBG thermal stability. The thermal stability of FBGs were analyzed using key concepts such as thermal relaxation of trapped population based on demarcation energy, trap depth/release rate of trapped population and different rate of increase of effective index in UV fringes induced high and low index regions. The analysis qualitatively explained the experimental results.

It is worth mentioning that present thesis work, in addition to being a detailed study on the CVL based UV source utilization in the field of FBG, is also of very high significance in the field, in general. This is due to several reasons. First, a very limited literature was available in FBG fabrication using high repetition rate 255 nm UV sources, that too without any detailed experimental study or analysis. Second, the detailed UV beam characterization (spatial coherence, divergence, beam profile, pulse shape, pointing and power stability) and their implication in FBG writing is highly relevant, in general to any way of FBG fabrication with pulsed or CW UV sources. Third, the CVL based kHz repetition rate, ns pulse width and kW range peak power UV sources are very interesting complimentary sources for FBG fabrication among most common low repetition rate, nano second, high pulse energy Excimer lasers, low average power CW and also recently investigated IR fs laser sources. Fourth, the extensive theoretical analysis on FBG fabrication in terms of induced refractive index modulation, its subsequent saturation and evolution of FBG spectrum are of general importance.

In summary, the overall thesisstarting from the review in the field and going through stages such as UV beam generation, characterization, UV fringes studies, FBG fabrication, analysis, temperature sensing, and ending with future scope of work, is a comprehensive and meaningful document on the thesis "Studies on fabrication of fiber Bragggratings using high repetition rate ultraviolet radiation from frequency converted copper vapour laser".

8.2 Future scope of work

The present work has an excellent future scope for research and development as very limited literature is available in utilization of high repetition rate UV sources for fabrication of fiber gratings. These high repetition rate sources can be CVL or solid state laser based. For CVL based UV source, the present FBG study can be further extended to hydrogen loaded fibers. Very interesting results in terms of FBG reflectivity, spectral and sensing characteristics are expected in hydrogen loaded photosensitive fibers. The thermal regenerated gratings, mainly produced in hydrogen loaded fibers, are currently very potential for high temperature (> 1000^0 C) sensing. Now, the advanced CVL sources based on HBr or HCl additive are available which operation at much repetition rate 15-20 kHz with much higher average power. Accordingly, another possible extension of present work may be in direction of utilizing, higher repetition rate/higher power CVL based UV sources (255, 271, 289 nm) for studies in FBG, LPG, tilted or chirped fiber gratings fabrication in hydrogen free or loaded photosensitive fibers. The high power partially coherent UV beams, as generated from advanced CVL sources, may also lead to significant self- annealing of FBG, being fabricated. Thisin-situ stress relief issue, not being paid sufficient attention so far, may lead to FBG with higher thermal stability. The future scope also include comprehensive studies on the utilization of q-switched, high repetition rate, diode pumped solid state laser based UV sources for FBG fabrication such as frequency quadrupled 257 nm Yb:YAG laser and 266 nm Nd:YAG laser with hydrogen loaded fibers. However, special attention needs to be paid to beam quality and pulse width characteristics of solid state lasers.

REFERENCES

[1] K. O. Hill, Y. Fujii, D. C. Johnson and B. S. Kawasaki, Appl. Phys. Lett. **32**, 647 (1978).

[2] B. S. Kawasaki, K. O. Hill, D. C. Johnson and Y. Fujii, Opt. Lett. **3**, 66 (1978).

[3] D. K. W. Lam and B. K. Garside, Appl. Opt. **20**, 440 (1981).

[4] J. Bures, J. Lapiere and D. Pascale, Appl. Phys. Lett. **37**, 860 (1980).

[5] G. Meltz, W. W. Morey and W. H. Glenn, Opt. Lett. **14**, 823 (1989).

[6] J. Stone, J. Appl. Phys. **62**, 4371 (1987).

[7] T. Tamura, G.H. Lu, M. Kohyama and R. Yamamoto, Physical Rev. B **70**, 153201 (2004)

[8] J. M. Yeun, Appl. Opt. **21**, 136 (1982).

[9] B. Poumellec, P. Guenot, I. Riant, P. Sansonetti, P. Niay, P. Bernage and J. F. Bayon, Opt. Materials. **4**, 441 (1995).

[10] D. L. Williams, S. T. Davey, R. Kashyap, J. R. Armitage and B. J. Ainslie, Electron. Lett. **28**, 369 (1992).

[11] R. M. Atkins and V. Mizrahi, Electron. Lett. **28**, 1743 (1992).

[12] R. Kashyap, J. R. Armitage, R. Wyatt, S. T. Davey and D. L. Williams, Electron. Lett. **26**, 730 (1990).

[13] P. Lemaire, R. Atkins, V. Mizrahiand and W. Reed, Electron. Lett. **29**, 1191(1993).

[14] A. Othonos, Rev. Sci. Instrum. **68**, 4309 (1997).

[15] K. O. Hill and G.Meltz, J. of Light wave Technology **15**, 1263 (1999).

[16] R. Kashyap, Fiber Bragg Gratings, Academic Press, New York, 2012.

[17] A. Othonos and K. Kalli, Fiber Bragg Gratings: Fundamentals and Applications in Telecommunications and Sensing, Artech House, Norwood, Mass. (1999).

[18] M. M. Broer, C. L. Cone and J. R. Simpson, Opt. Lett. **16**, 1391 (1991).

[19] F. Bilodeau, D. C. Johnson, B. Malo, K. A. Vineberg and K. O. Hill, Opt. Lett. **15**, 1138 (1990).

[20] Y. Kondo, K. Nouchi, T. Mitsuyu, M. Watanabe, P. G. Kasansky and K. Hirao, Opt. Lett. **24,** 646 (1999).

[21] K. A. Zagorul’ko, P. G. Kryukov, Y. V. Larionov, A. A. Rybaltovskii, E. M. Dianov, N. S. Vorob’ev, A. V. Smirnov, M. Y. Shchelev and A. M. Prokhorov, Quantum Electron. **31**, 999 (2001).

[22] A. Dragomir , D. N. Nikogosyan, K. A. Zagorulko, P. G. Kryukov and E. M. Dianov, Opt. Lett., **28**, 2171 (2003).

[23] A. Dragomir, J. G. McInerney and D. N. Nikogosyan, Appl. Opt. **41**, 4365 (2002).

[24] A. Dragomir, J. G. McInerney, D. N. Nikogosyan and P. G. Kazansky, Appl. Phys. Lett. **80**, 1114 (2002).

[25] A. Dragomir, D. N. Nikogosyan, A. A. Ruth, K. A. Zagorulko and P. G. Kryukov, Electron. Lett. **38**, 269 (2002).

[26] S.Nagel, J. B.MacChesney and K. L. Walker, IEEE J. Quantum Electron. **18,** 459 (1982).

[27] Y. Hibino and H. Hanafusa, J. Appl. Phys. **60**, 1797 (1986).

[28] Y. Hibino and H. Hanafusu, Jap. Journ. Appl. Phys. **22**, 766 (1983).

[29] P. Kaiser, J. Opt. Soc. Am. **64**, 475 (1974).

[30] N. M.Lawandy, Opt. Commun. **74**, 180 (1989).

[31] P. J. Kaiser, J. Opt. Soc. Am. **64**, 475 (1974).

[32] E. J. Friebele, C. G. Askin, M. E. Gingerich and K. J. Long, Nucl. Instrum. Methods Phys. Res. B **1**, 355 (1984).

[33] H. Kawazoe, Y. Watanabe, K. Shibuya and K. Muta, Mater. Res. Soc. Symp. Proc. **61**, 350 (1986).

[34] E. J. Friebele and D. L. Griscom, Mater. Res. Soc. Symp. Proc. **61**, 319 (1986).

[35] T. E. Tsai and D. L. Griscom, Proc. SPIE **1516**, 14 (1991).

[36] D. L. Griscom and E. J. Friebele, Phys. Rev. B **24**, 4896 (1981)

[37] P. St. J. Russell, L. J. Poyntz-Wright and D. P. Hand, Proc. SPIE **1373**, 126 (1990).

[38] R. M. Atkins, V. Mizrahi and T. Erdogan, Electron. Lett. **29**, 385 (1993).

[39] R. M. Atkins, P. J. Lemaire, T. Erdogan and V. Mizrahi, Electron. Lett. **29**, 1234 (1993).

[40] K. Awazu, H. Kawazoe and M. Yamane, J. Appl. Phys. **68**, 2713 (1990).

[41] K. Noguchi, N. Shibata, N. Uesugi and Y. Negishi, J. Lightwave Technol. **3**, 236 (1985).

[42] F. Bilodeau, B. Malo, J. Albert, D. C. Johnson and K. O. Hill, Opt. Lett. **18**, 953 (1993).

[43] D. L. Williams, B. J. Ainslie, R. Armitage, R. Kashyap and R. Campbell, Electron. Lett. **29**, 45 (1993).

[44] D. L. Williams, B. J. Ainslie, R. Kashyap, G. D. Maxwell, J. R. Armitage, R. J. Campbell and R. Wyatt, Proc. SPIE **2044**, 55 (1993).

[45] I. Camlibel, D. A. Pinnow and F. W. Dabby, Appl. Phys. Lett. **26**, 185 (1975).

[46] B. Poumellec, J. of Non-Crystalline Solids **239**,108 (1998).

[47] Y. H. Li, C. R. Liao, D. N. Wang, T. Sun and K. T. V. Grattan,Opt. Exp. 16, 21239 (2008)

[48] L. Dong, J. L. Archambault, L. Reekie, P. St. J. Russell and D. N. Payne, Appl. Opt. **34**, 3436 (1995).

[49] D. P. Hand and P. St. J. Russell, Opt. Lett.**15**, 102 (1990).

[50] W. X. Xie, P. Niay, P. Bernage, M. Douay, J. F. Bayon, T. Georges, M. Monerie and B. Poumellec, Opt. Commun. **104**, 185 (1993).

[51] H. Mueller, J. Am. Ceram. Soc.**21**, 27 (1938).

[52] S. A. Slattery, D. N. Nikogosyan and G. Brambilla, J. Opt. Soc. Am. B **22**,354 (2005).

[53] K. A. Zagorulko, P. G. Kryukov, Y. V. Larionov, A. A. Rybaltovsky, E. M. Dianov, S. Chekalin, Y. A. Matveets and V. O. Kompanets, Opt. Express **12**, 5996 (2004).

[54] L. B. Fu, G. D. Marshall, G. A. Bolger, P. Steinvurzel, E. C. Mägi, M. J. Withford, and B. J. Eggleton, Electron. Lett. **41**, 638 (2005).

[55] D. N. Nikogosyan, A. A. Oraevsky and V. I. Rupasov, Chem. Phys. **77**, 131 (1983).

[56] J. Albert, B. Malo, K. O. Hill, F. Bilodeau, D. C. Johnson and S. Thériault, Appl. Phys. Lett. **67**, 3529 (1995).

[57] D. N. Nikogosyan, Meas. Sci. Technol. **18**, R1 (2007).

[58] P. Y. Fonjallaz, H. G. Limberger, R. P. Salathé, F. Cochet and B. Leuenberger, Opt. Lett. **20**, 1346(1995).

[59] H. G. Limberger, P. Y. Fonjallaz, R. P. Salathé and F. Cochet, Appl. Phys. Lett. **68**, 3069 (1996).

[60] F. Dürr, H. G. Limberger, R. P. Salathé, F. Hindle, M. Douay, E. Fertein and C. Przygodzki, Appl. Phys. Lett. **84**, 4983 (2004).

[61] H. G. Limberger, C. Ban, R. P. Salathé, S. A. Slattery and D. N. Nikogosyan, Opt. express, **15**, 5610 (2007)

[62] C. Fiori and R. A. B. Devine, Material Research Society Symp. Proc. **61**, 187 (1986).

[63] J. P. Bernardin and N. M. Lawandy, Opt. Commun. **79**, 194 (1990).

[64] E. M. Dianov, V. G. Plotnichenko, V. V. Koltashev, Y. N. Pyrkov, N. H. Ky, H. G. Limberger and R. P. Salathé, Opt. Lett. **22**, 1754 (1997).

[65] M. G. Sceats and S. B. Poole, Aust. Conf. Opt. Fiber Technol. **302** (1991).

[66] B. C. Stuart, M. D. Fiet, A. M. Pubenchick, B.W. Shore and M.D. Parry. Phys. Rev. Lett., **74**, 2248 (1995)

[67] K. O. Hill, B. Malo, F. Bilodeau, D. C. Johnson and J. Albert, Appl. Phys. Lett. **62**, 1035 (1993).

[68] R. Kashyap, Electron. Lett. **34**, 2025 (1998).

[69] A. Othonos and X. Lee, IEEE Photon. Technol. Lett. **7**, 1183 (1995).

[70] P. E. Dyer, R. J. Farley, R. Giedl, C. Ragdale and D. Reid, Appl. Phys. Lett. **64**, 3389 (1995).

[71] Q. Zhang, D. A. Brown, L. Reinhart and T. F. Morse, Opt. Lett. **19**, 2030 (1994).

[72] N.H. Rizvi and M. C. Gower, Appl. Phys. Lett. **67**, 739 (1995).

[73] B. Malo, K. O. Hill, F. Bilodeau, D. C. Johnson and J. Albert, Electron. Lett. **29**, 1668 (1993).

[74] H. Kogelnik and C. W. Shank, J. Appl. Phys. **43**, 2327 (1972).

[75] H. Kogelnik, Bell.Syst. Tech. J. **55**, 109 (1976).

[76] A. Yariv, in Optical Electronics, 4th ed. Saunders College Publishing (1991).

[77] H. H. Chia, in Coupled Mode Theory. VNU Science Exp., the Netherlands (1984).

[78] M. Matsuhara, K. O. Hill and Watanabe, J. Opt. Soc. Am. **65**, 804 (1975).

[79] D. Gloge, Appl. Opt. **10**, 2252 (1971).

[80] D. Marcuse, in Theory of Dielectric Optical Waveguides. Academic Press, New York, 1994.

[81] M. Yamada and K. Sakuda, Appl. Opts. **26**, 3474 (1987).

[82] M.P. Rouard, Annal. Phys (Paris). Ser. **II7,** 291, (1937).

[83] P. St. J. Russell, J. Mod. Optics. **38**, 1599 (1994).

[84] V. Bhatia and A. M. Vengsarkar, Opt. Letters, **21**, 692 (1996)

[85] S. W. James and R. P Tatam, Meas. Sci. Technol. **14**, 49 (2003)

[86] L. Drozin, P.Y. Fonjallaz and L. K.Stensland, Electron. Lett. **36,** 742 (2000)

[87] T. Erdogan and J. E. Sipe, J. Opt. Soc. Am. A **13**, 296 (1996).

[88] T. Erdogan, J. Opt. Soc. Am. A **14**, 1760 (1997).

[89] W. W. Morey, G. Meltz, J. D. Love and S. J. Hewlett, Electron. Lett. **30**, 730 (1994).

[90] R. Kashyap, S. Hornung, M. H. Reeve and S. A. Cassidy, Electron. Lett. **19**, 1039 (1983).

[91] R. Kashyap, R. Wyatt and P. F. Mckee, Electron. Lett. **29**, 1025 (1993).

[92] K. O. Hill, F. Bilodeau, B. Malo and D. C. Johnson, Electron. Lett. **27**, 1548 (1991).

[93] K. C. Byron, K. Sugden, T. Bircheno and I. Bennion, Electron. Lett. **29**, 1659 (1993).

[94] B. Eggleton, P. Krug and L. Poladin, Tech. Digest of Opt. Fib. Comm. Conf., OFC '94, 227.
[95] M. C. Farries, K. Sugden, D. C. J. Reid, I. Bennion, A. Molony and M. J Goodwin Electron. Lett. **30**, 891(1994).
[96] K. O. Hill, F. Bilodeau, B. Malo, T. Kitagawa, D. C. Johnson and J. Albert, in Technical Digest of Post-Deadline Papers, PD2-1, Opt. Fib. Comm. Conf., OFC '94.
[97] T. Stephens, P. A. Krug, Z. Brodzeli, G. Doshi, F. Ouellette and L. Poladin, Electron. Lett. **32**, 1559 (1996).
[98] R. Kashyap, P. McKee, R. Campbell and D. Williams, Electron. Lett. **30**, 996 (1994).
[99] S. Okude, T. Sakai, A. Wada and R. Yamauchi, in Proc. of OFC '96, paper Tu07' 68.
[100] M. A. Putnam, G. M. Williams and E. J. Friebele, Electron. Lett. **31**, 309 (1995).
[101] W. H. Loh, R. I. Laming, N. Robinson, A. Cavaciuti, C. Vaninetti, C. J. Anderson, M. N. Zervas and M. J. Cole, IEEE Photon. Technol. Lett. **8**, 944 (1996).
[102] A. Boskovic, M. J. Guy, S. V. Chernikov, J. R. Taylor and R. Kashyap, Electron. Lett. **31**, 877 (1995).
[103] P. Gunning, R. Kashyap, A. S. Siddiqui and K. Smith, Electron. Lett. **31**, 1066 (1995).
[104] A. D. Kersey and M. A. Davis, Proc. OFS '94, 319, Glasgow, UK (1994)
[105] J. A. R. Williams, I. Bennion and N. J. Doran, Opt. Commun. **116**, 62 (1995).
[106] M. C. Farries, G. M. Ragdaleand and D. C. J. Reid, Electron. Lett. **28**, 487 (1992).
[107] R. Kashyap, R. Wyatt and P. F. McKee, Electron. Lett. **29**, 1025 (1993).
[108] I. Zhang, K. Sugden, J. A. R. Williams and I. Bennion, Opt. Lett. **20**, 1927 (1995).
[109] M. Matsuhara and K. O. Hill, Appl. Opt.**13**, 2886 (1974).
[110] V. Mizrahi, J. E. Sipe, J. Lightwave Technol.**11**, 1513 (1993).
[111] R. J. Campbell and R. Kashyap, Opt. Lett.**16**, 898 (1991).
[112] M. J. Cole, W. H. Loh, R. L. Laming, M. N. Zervas and S. Barcelos, Electron. Lett. **31**, 92(1995).
[113] A. Othonos, X. Lee and R. M. Measures, Electron. Lett. **30**, 1972 (1994).
[114] B. J. Eggleton, P. A. Krug, L. Poladian and F. Quellette, Electron. Lett. **30**, 1620 (1994).
[115] R. Kashyap, P. F. McKee and D. Armes, Electron. Lett. **30**, 1977 (1994)
[116] J. Canning and M. G. Sceats, Electron. Lett. **30**, 1344 (1994).
[117] D. Uttamchandani and A. Othonos, Opt. Commun. **127**, 200 (1996).
[118] N. Groothoff and J. Canning, Opt. Lett. **29,** 2360 (2004).

[119] J. L. Archambault, L. Reekie and P.St.J. Russell, Electron.Lett. **29,** 453 (1993).

[120] C. Chojetzki, M. Rothhardt, S. Ommer, S. Unger, K. Schuster and H.R. Mueller, Opt. Eng. **44,** 060503 (2005).

[121] P. St. J. Russell, J.L. Archambault and L.Reekie, Phys. World **41**, (1993).

[122] W. W.Morey, G.Meltz and W.H.Glen, Opt. photon. News **1**, 8 (1994).

[123] H. Patrick and S. L. Gilbert, Opt Lett **18**, 1484 (1993)

[124] J. R. Armitage, Electron.Lett. **29,**1181 (1993)

[125] C. J. Paddison, J. M. Dawes, D. J. W. Brown, M. J. Withford and R. I. Trickett, Electron. Lett. **34**, 2407 (1998).

[126] H. J. Booth, E. K. Illy, M. R. H. Knowles, G.T. Purves and A. J. Kearsley, in Proceedings of the ICALEO, Laser Institute, America, paper M203 (2001).

[127] B. F. Johnston, A. J. Lee, M. J. Withford and J. A. Piper, Opt. Express **10**, 818 (2002).

[128] O. Prakash, R. Mahakud, S.K. Dixit and U. Nundy, Optics Commun. **263,** 65 (2006).

[129] M.J. Kushner, IEEE J. of Quantum Electron **17**, 139 (1981)

[130] C. E. Little; Metal Vapour Lasers: Physics, Engineering and Applications, ISBN, Wiley-VCH (1999).

[131] P. A. Bokhan, V. A. Gerasimov, V. I. Solomonov and V.B. Scheglov, Sov. J. Quantum electron 8, 1220 (1978)

[132] M. J. Withford, D. J. Brown and J.A. Piper, IEEE Quant. Electron, **7**, 1310 (1997)

[133] B. Singh, P. Badhani, J. Mittal and R. Bhatnager, Rev. of Scientific Instru. **55**, 1542 (1984)

[134] G.T. Kanellos, G. Papaioannou, D. Tsiokos, C. Mitrogiannis and G. Nianios , N. Pleros, Opt. express **18,** 179 (2010)

[135] B. J. Eggleton, P. S. Westbrook, R. S. Windeler, S. Spalter and T. A. Strasser, Opt. Lett. **24**, 1460 (1999).

[136] M.P. Huy, G.Laffont, V. Dewynter, P. Ferdinand, L. Labonté, D. Pagnoux, P. Roy, W. Blanc and B. Dussardier, Opt. Express **14**, 10359 (2006).

[137] N. Groothoff, J. Canning, E. Buckley and J. Zagari, Opt. Lett. **28**, 233 (2003).

[138] J. Canning, N. Groothoff, E. Buckley, T. Ryan, K. Lyttikainen and J. Digweed, Opt. Express **11**, 1995 (2003).

[139] N. Groothoff and J. Canning, Opt. Lett. **29**, 2360 (2004).

[140] D. Grobnic, S. Mihailov, C. Smelser and H. Ding, IEEE Photon. Tech. Lett. **16**, 2505 (2004).

[141] O. V. Butov, E. M. Dianov and K. M. Golant, Meas. Sci. Technol. **17**, 975 (2006).

[142] M. Fokine, J. Opt. Soc. Am. B **19**, 1759(2002).

[143] J. Canning, M. Stevenson, S. Bandyopadhyay and K. Cook, Sensors **8**, 6448 (2008).

[144] S. Bandyopadhyay, J. Canning, M. Stevenson and K. Cook, Opt. Lett. **33**, 1917 (2008)

[145] D. Grobnic, C. W. Smelser, S. J. Mihailov and R. B. Walker, Meas. Sci. Technol. **17**, 1009 (2006).

[146] D. Grobonic, S. J. Mihailov, C.W. Smelser and H. Ding, IEEE Photo. Techno. Lett., **16**, 2505 (2011)

[147] Y. Liu, Z. Guo, Y. Zhang, K. Chiang and X. Dong, Electronics Lett., **36**, 564 (2000).

[148] J. W. Arkwright, N. G. Blenman, I. D. Underhill, S. A. Maunder, M. M. Szczesniak, P. G. Dinning and I. J. Cook, Opt. Express **17**, 4500 (2009).

[149] K. Krebber, H. Henschel and U.Weinand, Meas. Sci. Technol. **17,** 1095 (2006).

[150] W. Liang, Y. Huang, Yong Xu, Reginald K. Leeand and A. Yariv , Appl. Phys. Lett. **86**, 151122 (2005)

[151] S. C. Tjin, Y. Wang, X. Sun, P. Moyo and J. M. W. Brownjohn, Meas. Sci. Technol. **13**, 583 (2002).

[152] W. Du, X. M. Tao, H. Y. Tam and C. L. Choy, Compos. Struct. **42**, 217 (1998).

[153] D. W. Coutts, IEEE J. Quantum Electronics, **31**, 330 (1995).

[154] J. J. Chang, Appl. Opt. **33**, 2255 (1994).

[155] O. Prakash, S. K. Dixit and R. Bhatangar, IEEE J. Quantum Electron. **38,** 603 (2002).

[156] T.Omatsu, K.Kuroda, T. Shimura, M.Chihara, M.Itoh and I. Ogura, Opt. Commun., **79**,125 (1990)

[157] J. W. Chen, A. Luches, V. Nassisi and M. R. Perrone, Opt. Commun. **72,** 225 (1989).

[158] V. V. Atezhev, S. K. Vartapetov, A. N. Zhukov, M. A. Kurzanov and A. Z. Obidin, Quantum Electron. **33**, 689 (2003).

[159] P. Michel, C. Labaune, H. C. Bandulet, K. Lewis, S. Depierreux, S. Hulin, G. Bonnaud, V. T. Tikhonchuk, S. Weber, G. Riazuelo and H. A. Baldis, A. Michard, Phys. Rev. Lett. **92**, 175001 (2004).

[160] S. Kawata, I. Hikima, Y. I. chihara and S. Watanabe, Appl. Opt. **31**, 387 (1992).

[161] K. A. Valiev, L. V. Velikov, G. S. Volkov and D. Y. Zaroslov, Sov. J. Quantum Electron. **17**, 806 (1987).

[162] K. A. Valiev, L. V. Velikov, G. S. Volkov and D. Y. Zaroslov, Microelectron. Eng. **11**, 173 (1990).

[163] T. Omatsu, K. Kuroda, T. Shimura, K. Chihara, M. Itoh and I. Ogura, Opt. Quantum Electron. **23**, 477 (1991).

[164] S. Chatterjee and O. Prakash, Opt. Laser Technol. **35**, 133 (2003).

[165] O. Prakash, R.Mahakud and S.K.Dixit, Optical Eng., 50**,** 114201 (2011).

[166] H. S. Vora and N. Singh, Opt. Commun. **282,** 4259 (2009)

[167] S. K. Dixit, R. Mahakud, O. Prakash, R. Biswal and J. K. Mittal, Optics Commun. **281**, 2590 (2008)

[168] R. S. Hargrove, R. Grove and T. Kan, IEEE J. Quantum Electron, **16**, 1108 (1980).

[169] P. G. Gobbi and G. C. Reali, Opt. Commun. **52**, 195 (1984).

[170] S.K. Dixit, in Filtering Resonators, Nova Science Pub Inc (2001)

[171] S. K. Dixit, J. K. Mittal, B. Singh, P. Saxena and R. Bhatnagar, Opt. Commun. **98,** 91 (1993).

[172] J. K. Mittal, P. K. Bhadani, B. Singh, L. Abhinandan and R. Bhatnagar, J. Phys. E **21**, 388 (1988).

[173] A.A. Isaeve, G.Y. Lemmerman and G. L. Malafeeva, Soviet J. Q. Electron, **10**, 983 (1980).

[174] G. S. Evtushenko, V. O. Troitskii and J. Russ. Laser Res., **15,** 28 (1994).

[175] O. Prakash, S. K. Dixit and R. Bhatnagar , Appl. Opt., **44**, 1719 (2005)

[176] D. W. Coutts and D. J. W. Brown, IEEE Sel. Top. Quantum Electron. **1,** 768 (1995).

[177] A. A. Isaev, D. R. Jones, C. E. Little, G. G. Petrash, C. G. Whyte and K. I. Zemskov, Opt. Commun. **132,** 302 (1996).

[178] D.W. Coutts, IEEE J. Quantum Electronics **31**, 2208 (1995).

[179] A.Yariv, Quantum electronics, 3rd ed. New York: John Wiley and Sons, 393 (1989).

[180] G.D Boyd, A. Ashkin, J.M. Dziedzic and D.A. Kleinman, Phys. Rev.**137**, A1305 (1965)

[181] O.Prakash, R. Mahakud, S.V. Nakhe and S. K. Dixit, Opt. & Laser Techno. **50**, 43 (2013).

[182] P. E. Dyer, R. J. Farley and R. Gied, Opt. Commun. **115**, 327 (1995)

[183] P. E. Dyer, R. J. Farley and R. Giedl, Opt. Commun. **129,** 98 (1996).

[184] J. Solymar and D. J. Cooke in Vol. Holography and Vol. Gratings, Academic Press, New York, 1981

[185] R. Mahakud, O. Prakash, S. K. Dixit and J. K. Mittal, Opt. Commun. **282,** 2204 (2009).

[186] O. Prakash, R. Mahakud, R. Biswal, S. Gurram, H. S .Vora and S. K .Dixit, Applied optics **46,** 6210 (2007).

[187] C. Li, Y. Lu, S. Wu, Q. Su and C. Huang, Opt. Laser Technol. **36** (2004) 459

[188] E. Lindner, M. Becker, M. Rothhardt and H. Bartelt, Opt. Commun. **281**, 4612 (2008)

[189] M. Tebaldi, P. E. Rueda and N. Bolognini, Opt. Commun. **185**, 65 (2000)

[190] Max Born and Emil Wolf, Principles of Optics, 4th.ed. Pergamon Press (1970)

[191] L. Xiong and J. Albert, J. Opt. Soc. Am. *B* **26**, 2136 (2009).

[192] Y.Cai Y and S. He, J. Opt. Soc. Am. A **23**, 2623 (2006)

[193] G. S. Agrawal, Phys. Rev. A **23**, 1863 (1981).

[194] M. S. Zubairy and J. K. McIver, Phys. Rev. A **36**, 202 (1987).

[195] N. A. Ansari and M. S. Zubairy, Opt. Commun. **59**, 385 (1986).

[196] R. Mahakud, J. Kumar, O. Prakash and S.K. Dixit, Opt. Engg., **52,** 0761141 (2013).

[197] C. M. Rollinson, S. A. Wade, B. P. Kouskousis, D. J. Kitcher, G. W. Baxter and S. F. Collins, J. Opt. Soc. Am. A **29**, 1259 (2012)

[198] M. G. Moharam, E. B. Grann, D. A. Pommet and T. K. Gaylord, J. Opt. Soc. Amer. A**12**,1068 (1995)

[199] G. Pakulski, R. Moore, C. Martian, F. Shepard, M. Fallahi and I. Templton, Appl. Phy. Lett. **62**, 222, (1993).

[200] Y. Qiu, Y. Sheng and C.Beaulieu, J. Light wave Technol. **17**, 2366 (1999)

[201] C. Smelser, S. Mihailov and D. Grobnic, Opt. Express **13,** 5377 (2005).

[202] J. Canning, Lasers Photonics, Rev. **2,** 275 (2008).

[203] T. Erdogan, J. Light wave Technol.**15**, 1277 (1997)

[204] Y. Zhao and J. C. Palais, J. Light wave Technol. **15**, 154 (1997).

[205] P. Niay, P. Bernage, S. Legoubin, M. Douay, W. X. Xie, J. F. Bayon, T. Georges, M. Monerie and B. Poumellec, Opt. Commun. **113,** 176 (1994).

[206] E. Lindner, J. Canning, C. Chojetzkic, S. Brückner, M.Becker, M. Rothhardt and H. Bartelt, Opt. Commun. **284** 183 (2011)

[207] H. Ky. Nguyen, H.G. Limberger, R.P. Salathe´, F. Cochet and L. Dong, Opt. Commun. **225,** 313 (2003).

[208] L. Dong, J. L. Archambault, L. Reekie, P. St. J. Russell and D. N. Payne, Electron. Lett. **29,** 1577 (1993).

[209] C. G. Askins, M. A. Putnam, G. M. Williams and E. J. Friebele, Opt. Lett. **19,** 147 (1994).

[210] C. G. Askins, G. M. Williams, M. Bashkansky, E. J. Friebele, FiberOptic Smart Structures and Skins V, Proc. SPIE **1798,** 66 (1992).

[211] A. K. Ghatak and K. Tyagarajan in "Introduction to fiber optics" Cambridge University press Pvt. Ltd (2007)

[212] R. Mahakud, J. Kumar, O. Prakash, S.V. Nakhe and S.K. Dixit, Opt. Commun. **285**, 5351 (2012).

[213] R. Mahakud , O. Prakash , S.V. Nakhe and S.K Dixit, Appl. Opt., **51**,1828 (2012)

[214] T. E. Sai, G.M.Williams and E.J. Freebie, Opt. Lett, **22**, 224 (1997)

[215] O. Prakash, J. Kumar, R. Mahakud, S. K. Agrawal, S. K. Dixit and S. V. Nakhe, IEEE Photo. Techno. Lett. **26**, 93 (2013).

[216] J. Canning, Optical Fiber Techno **6**, 275 (2000).

[217] M. Kristensen, Phy, Review B **64**, 144201 (2001).

[218] J.A. Besley, L. Reekie, C. Weeks, T. Wang and C. Murphy, J. Lightwave Tech. **27**, 3123 (2009).

[219] M. Douay, W. X. Xie, T. Taunay, P. Bernage, P. Niay, P. Cordier, B. Poumellec, L. Dong, J. F. Bayon, H. Poignant and E. Delevaque, J. Lightwave Technol. **15**, 1329 (1997).

[220] P. I. Jensen and A. Sudbo, IEEE Photon. Technol. Lett, **7**, 783 (1995)

[221] D. Z. Anderson, V. Mizrahi, T. Erdogan and A. E. White, Electron. Lett. **29**, 566 (1993).

[222] T. A. Strasser, T Erdogan, A. E. White, V Mizrahi and P. J. Lemaire, Appl. Phys. Lett. **65,** 3308 (1994).

[223] W. X. Xie, M Douay, P. Bernage, P. Niay, J. F. Bayon and T. Georges, Opt. Commun. **101**, 85 (1993).

[224] R. Menzel in Photonics: Linear and Nonlinear Interactions of Laser Light and Matter, Springer ISBN-10: 3540670742, 1st edition (2001)

[225] P. Cordier, S. Dupont, M. Douay, G. Martinelli, P. Bernage, P. Niay, J.F. Bayon and L. Dong, Appl. Phys. Lett. 70, **1204** (1997).

[226] B. Poumellec, P. Niay, M. Douay and J.F. Bayon, J. Phys. **D29**, 1842 (1996).

[227] H.G. Limberger, P.Y. Fonjallaz, R.P. Salath and F. Cochet, Appl. Phys. Lett. **68,** 3069 (1996).

[228] P.Y. Fonjallaz, H.G. Limberger, R.P. Salath, F. Cochet and B. Leuenberger, Opt. Lett. **20**, 1346 (1995)

[229] H.G.Froohlich and R.Kashyap, Opt. Commun. **157,** 273 (1998).

[230] C. Martinez, S. Magne and P. Ferdinand, Appl. Opt **41**, 1733 (2002).

[231] S.Abdulina, S.Babin, S.Kablukov and A.Vlasov, Proc. of SPIE **6612**, 661201 (2007)

[232] M. Santarsiero and R. Borghi, J. Optical soc. America A, **16**, 188 (1999)

[233] D.L shealy and S.H.Chao, Opt. Engg., **42**, 3123 (2003)

[234] D.L. Shealy and J. A. Hoffnagle, SPIE Conf. Laser Beam Shaping VI, Proc. **5876** (2005)

[235] C. Yang and Y. Lai, Opt. and laser Techno. **32**, 307 (2000).

[236] T. Osuch and Z. Jaroszewicz, Opt. Commun. **284,** 567 (2011)

[237] C. M. Rollinson, S. A. Wade, N. M. Dragomir, G.W. Baxter, S.F. Collins and A. Roberts, Opt. Commun. **256**, 310 (2005)

[238] E. J. Friebele, C. G. Askins, M. A. Putnam, A. A .Fosha, J. J. Florio, R. P. Donti and P. G. Blosser Electron. Lett.**30,** 1783 (1994)

[239] E. J. Friebele, C. G. Askins, M. A. Putnam, P. E. Heider, R. G. Blosser, J. Florio, R. P. Donti and P. G. Blosser, *Proc. SPIE* **2721,** 118 (1996)

[240] V. Bhatia, D.Campbell and R.O. Claus , Optics letters, 22, 648 (1997)

[241] C.G Lin, L.Wang, C.C.Yang, M. C. Shih and T. J. Chuang, IEEE Photon. Technol.Lett,**10,** 406 (1998)

[242] S.E Baldini, D.J. Tubbs and W.A. Stange , Proc. SPIE**1370,** 162 (1990)

[243] M. Reid, Opt. Engg. **37,** 237 (1998)

[244] Y. J. Rao, Meas. Sci. Technol. **8**, 355 (1997).

[245] M. L. Dockney, S. W. James and R. P. Tatem, Meas. Sci. Technol. **7**, 445 (1996).

[246] Q. Zhang, D. A. Brown, L. Reinhart, T. F. Morsé, J. Q. Wang and X. Gang, IEEE Photo. Technol. Lett. **6**, 839 (1994).

[247] S. Gurram and A. K. Nath, Appl.Opt **46**, 2197 (2007).

[248] G Srikanth , Appl. Opt, **47**, 3092 (2008)

[249] R. Mahakud, J. Kumar, O. Prakash and S.K. Dixit, Opt. Eng., **52**, 0761141 (2013).

[250] A. D. Kersey, M. A. Davis, H. J. Patrick, M. LeBlance, K. P. Koo, C. G. Askins, M. A. Putnam and E. J. Friebele, J. Light wave Technol. **15**, 1442 (1997).

[251] S. J. Mihailov, Sensors **12**, 1898 (2012).

[252] Y. Shen, J. He, T. Sun and K. T. V. Grattan, Opt. Lett. **29**, 554 (2004).

[253] H. Bartelt, K. Schuster, S.Unger, C. Chojetzki, M. Rothhardt and I. Latka, Appl. Opt. **46**, 3417 (2007).

[254] G. J. de Villiers, J.Treurnicht and R. T. Dobson, Appl. Thermal Eng. **38**, 143 (2012).

[255] V. de Oliveira, M. Muller and H. J. Kalinowski, Appl. Opt. **50**, E55 (2011).

[256] A. Hidayat, Q.Wang, P. Niay, M. Douay, B. Poumellec, F. Kherbouche and I. Riant, Appl. Opt. **40**, 2632 (2001) .

[257] M. H. Gordon, R. J. M. Flockhart, J. S. Barton, W. N. MacPherson, J. D. C. Jones, K. E. Chisholm, L. Zhang, I. Bennion, I. Read and P. D. Foote, Appl. Opt. **43,** 2744 (2004).

[258] R. Mahakud, J. Kumar, O. Prakash and S. K. Dixit, Appl. Opt**. 52,** 7570 (2013).

[259] L. Yuan and L. Zhou , Sensors and Actuators A **69**, 5 (1998)

[260] S.C. Her and C.Y. Huang, Sensors, **11**, 6926 (2011).

[261] J. Jung, H. Nam, B. Lee, J. OhByun and N. S. Kim, Appl. Opt. **38**, 2752 (1999).

[262] T. Erdogan, V. Mizrahi, P. J. Lemaire and D. Monroe, J. Appl. Phys. **76**, 73 (1994).

[263] S. Pal, T. Sun, K. T. V. Grattan, , S. A. Wade, S. F. Collins, G. W. Baxter, B. Dussardier and Ge´rard Monnom, J. Opt. Soc. Am. A **21**, 1503 (2004).

[264] S. Her and C. Huang, Sensors**11**, 6926 (2011).

[265] J. Jung, H. Nam, B. Lee, J. Byun and N. S. Kim , Appl. Opt. **38**, 2752 (1999).

[266] G. Ghosh, M. Endo and T. Iwasaki, J. Lightwave Technol. **12**, 1338 (1994).

[267] G. Ghosh, Appl. Opt. **36**, 1540 (1997).

[268] J.H. Wray and J.T. Neu, J. Opt. Soc. Am. **59**, 774, (1969).

[269] R.Mahakud, J. Kumar, O.Prakash and S.K. Dixit, Appl. Opt.52, 7570 (2013).

[270] F. C. Nix and D. MacNair**,** Phy. Review **60**, 597 (1941).

[271] D. Razafimahatratra, P. Niay, M. Douay, B. Poumellec and I. Riant, Appl.opt. **39,** 1924 (2000).

[272] J. Kumar, R. Mahakud, A. Mokhariwale, O. Prakash, S. K. Dixit and S. V. Nakhe, Opt. Commun. **320** 109 (2014).

[273] B. Poumellec, P. Niay and T. Taunay, “Photosensitive Optical Materials and Devices”, San Jose`, CA, USA, p. 36 (1997).